

Causal Viscous Hydrodynamics
for Relativistic Heavy Ion Collisions

DISSERTATION

Presented in Partial Fulfillment of the Requirements for
the Degree Doctor of Philosophy in the
Graduate School of The Ohio State University

By

Huichao Song

Graduate Program in Physics

The Ohio State University

2018

Dissertation Committee:

Ulrich W. Heinz, Advisor

Richard J. Furnstahl

Michael A. Lisa

Junko Shigemitsu

ABSTRACT

The viscosity of the QGP is a presently hotly debated subject. Since its computation from first principles is difficult, it is desirable to try to extract it from experimental data. Viscous hydrodynamics provides a tool that can attack this problem and which may work in regions where ideal hydrodynamics begins to fail.

This thesis focuses on viscous hydrodynamics for relativistic heavy ion collisions. We first review the 2nd order viscous equations obtained from different approaches, and then report on the work of the Ohio State University group on setting up the equations for causal viscous hydrodynamics in 2+1 dimensions and solving them numerically for central and noncentral Cu+Cu and Au+Au collisions at RHIC energies and above. We discuss shear and bulk viscous effects on the hydrodynamic evolution of entropy density, temperature, collective flow, and flow anisotropies, and on the hadron multiplicity, single particle spectra and elliptic flow. Viscous entropy production and its influence on the centrality dependence of hadron multiplicities and the multiplicity scaling of eccentricity-scaled elliptic flow are studied in viscous hydrodynamics and compared with experimental data. The dynamical effects of using different versions of the Israel-Stewart second order formalism for causal viscous fluid dynamics are discussed, resolving some of the apparent discrepancies between early results reported by different groups. Finally, we assess the present status of constraining the shear viscosity to entropy ratio of the hot and dense matter created at RHIC.

ACKNOWLEDGMENTS

First I would like to express my deepest gratitude to my advisor Prof. Ulrich Heinz, for his thoughtful guidance during my graduate study in the past five years. I enjoy to work with him very much. He led me to a fantastic research area, which made me busy and fruitful; he provided me with all kinds of opportunities to broaden my horizon and allow me to grow up as a scientist. Especially, I thank him for his patience, encouragement and continuous support even during the hardest times of my research without which my early research would not have found its proper direction. I also enjoy the research atmosphere he created for us, through which I learned a lot from other group members. Here I especially thank Evan for many technical discussions on hydrodynamics, and Guang-You and Abhijit for discussions beyond hydrodynamics.

For work covered in this thesis, I gratefully acknowledgement the fruitful and enlightening discussions with S. Bass, K. Dusling, R. Fries, P. Huovinen, P. Kolb, M. Lisa, D. Molnar, P. Petreczky, S. Pratt, P. Romatschke and D. Teaney. I especially thank K. Dusling and P. Romatschke for their close collaborations during the code verification. I am also grateful for many thought-stimulating discussions and debates with N. Demir, S. Jeon, J. -Y. Jia, V. Koch, Y. Kovchegov, R. Lacey, R. Neufeld, J. Noronha-Hostler, J. Randrup, R. Snellings, P. Steinberg, A. Tang, I. Vitev, X. -N. Wang, X. Zhe, and many others (This includes numerous people in the RHIC community, whom I met at conferences, workshops and seminars – I apologize for not listing all of them here individually).

I also thank my B. S. and M. S. thesis advisors Prof. Guo-Mo Zeng and Prof. Yu-Xin Liu, who gave me early scientific training and encouraged me to switch to new research areas to further explore my potentials.

Last but not least, I thank my husband Yulu Che for the life I could enjoy with him together and for a warm home where I could rest with peace of mind. I thank my parents for their unconditional love and support.

TABLE OF CONTENTS

	Page
Abstract	ii
Acknowledgments	iii
Chapters:	
1. Introduction	1
1.1 The Quark Gluon Plasma and Relativistic Heavy Ion Collisions	1
1.1.1 From weakly coupled QGP to strongly coupled QGP	1
1.1.2 Stages of a heavy ion collision and theoretical tools	2
1.1.3 QGP signatures	6
1.1.4 “RHIC scientists serve up the perfect liquid ”	10
1.2 Transport coefficients for non-relativistic fluids	11
1.3 Transport coefficients for relativistic fluids: weak vs. strong coupling	13
1.4 Shear and bulk viscosity for QCD matter	14
1.5 Shear viscosity and bulk viscosity from $N = 4$ SYM and AdS/CFT	17
1.6 Notation and outline of this thesis	18
2. Relativistic Viscous Hydrodynamics: the Formalism	20
2.1 From ideal to viscous hydrodynamics	20
2.2 Navier-Stokes formalism	22
2.3 Israel-Stewart formalism from the 2nd law of thermodynamics	22
2.4 Israel-Stewart formalism from kinetic theory	24
2.5 Israel-Stewart formalism from conformal symmetry constraints	26
2.6 Öttinger-Grmela formalism	27
2.7 Final comments on the state of the formalism	27
3. Causal Viscous Hydrodynamics in 2+1 Dimensions	29
3.1 Viscous hydrodynamic equations in 2+1 dimensions	29
3.2 Initial conditions	30

3.2.1	Initializations for the energy density	30
3.2.2	Initializations for π^{mn} and Π	32
3.3	The equation of state (EOS)	32
3.4	Freeze-out procedure and calculation of spectra	34
3.5	Additional viscous inputs: shear, bulk viscosity and relaxation times	35
4.	Generic Viscous Effects: Shear Viscosity	37
4.1	Introduction	37
4.2	Hydrodynamic evolution	38
4.3	Final particle spectra and elliptic flow v_2	44
4.4	Sensitivity to relaxation time and π^{mn} initialization	47
4.5	Dependence on system size and collision energies	49
4.6	Breakdown of viscous hydrodynamics at high p_T	51
4.7	Conclusions	51
5.	Multiplicity Scaling of v_2/ε and Shear Viscosity Effects	53
5.1	Introduction	53
5.2	Multiplicity scaling of v_2/ε in ideal and viscous hydrodynamics	54
5.2.1	EOS I: conformal fluids with $e = 3p$	54
5.2.2	Phase transition effects: EOS Q vs. EOS L	56
5.2.3	A look at the experimental data	57
5.3	Multiplicity scaling of entropy production in viscous hydrodynamics	58
5.4	Concluding Remarks	59
6.	Generic Viscous Effects: Bulk Viscosity	61
6.1	Introduction	61
6.2	Shear viscosity vs. bulk viscosity effects	61
6.2.1	Hydrodynamic evolution	61
6.2.2	Spectra and elliptic flow	63
6.3	Sensitivity to relaxation time and bulk pressure initialization	64
6.4	Validity of I-S viscous hydrodynamics and upper limits for ζ/s	66
6.5	Extracting η/s from experimental data: uncertainties from bulk viscosity	67
6.6	Summary	68
7.	Recent Developments in Viscous Hydrodynamics	70
7.1	Introduction	70
7.2	System size, EOS and different I-S equations	70
7.3	Detailed comparison of different I-S equations	71

7.3.1	“Simplified” and “full” I-S equations	72
7.4	Code verification and comparison between I-S and O-G equations	75
7.5	Conclusions	76
8.	Extracting η/s from Experimental Data: Uncertainty Analysis	77
8.1	Introduction	77
8.2	Dynamical freeze-out and effects from late hadronic viscosity	77
8.3	EoS	78
8.4	Bulk viscosity	80
8.5	Glauber model vs. CGC initialization	80
8.6	Numerical viscosity	81
8.7	Conclusions	81
9.	η/s from Other Considerations and Extraction Methods	83
9.1	Shear viscosity and Knudsen number	83
9.2	Shear viscosity from the parton cascade model	84
9.3	Shear viscosity and radiative energy loss	85
9.4	Shear viscosity and heavy quark diffusion	86
9.5	Summary and comments	87
10.	Summary and Concluding Remarks	90
Appendices:		
A.		92
A.1	Coordinates and Transformations	92
A.2	Details of the viscous hydro code VISH2+1	92
A.2.1	Expressions for $\tilde{\pi}^{mn}$ and $\tilde{\sigma}^{mn}$	92
A.2.2	Velocity finding	93
A.3	Tests of the viscous hydro code VISH2+1	93
A.3.1	Testing the ideal hydro part of VISH2+1	93
A.3.2	Comparison with analytical results	94
A.3.3	Reduction of VISH2+1 to relativistic Navier-Stokes theory	95
A.4	Hydrodynamics vs. blast wave model	96
A.5	Cooling rates for ideal and viscous heavy-ion fireballs	97
B.	Glossary	99
	BIBLIOGRAPHY	101

Chapter 1: Introduction

1.1 The Quark Gluon Plasma and Relativistic Heavy Ion Collisions

Shortly after the discovery of the asymptotic freedom of QCD, people realized that common nuclear matter, confining quarks and gluons within individual protons and neutrons, could transform into a new de-confinement phase (at high energy densities) – the quark gluon plasma (QGP) [1, 2], a form of matter that once existed in the very early universe or some variant of which possibly still exists in the inner core of a neutron star. It was theoretically conjectured that such extreme conditions can also be realized on earth through colliding two heavy nuclei with ultra-relativistic energies [3], which transform a fraction of the kinetic energies of the two nuclei into heating the QCD vacuum within an extremely small volume. However, it actually took more than 25 years of efforts to reach the threshold for the QGP phase transition, from the first relativistic heavy ion program at the Bevalac at LBL (with beam energies of up to 1GeV/nucleon) in the early 1980s [4], to the AGS at BNL (with center of mass energies per nucleon pair $\sqrt{s} \sim 5\text{GeV}$) and the SPS at CERN (with $\sqrt{s} \sim 17\text{GeV}$) in the late 1980s [5], to the RHIC at BNL (with $\sqrt{s} = 200\text{GeV}$), starting in 2000 [6, 7, 8, 9], and to the impending heavy ion program at the LHC at CERN (with $\sqrt{s} = 5.5\text{TeV}$), which will probably start towards the end of next year [10].

At AGS and SPS energies and below, there was no unambiguous evidence for QGP formation, although a number of signals found at the SPS strongly suggested the formation of a “new state of matter” [11]¹. Only after the beginning of the RHIC program during the summer of 2000, more and more evidence showed that the QGP had been discovered [6, 7, 8, 9, 12, 13, 14]. Before discussing these QGP signatures, we will first explain the concept of the QGP and how its features have become richer during the past few years.

1.1.1 From weakly coupled QGP to strongly coupled QGP

The quark gluon plasma is defined as a thermalized state of quarks and gluons without color confinement. It was originally conceived as a weakly coupled gas, motivated by the asymptotic freedom of QCD at high energies. Using the statistics of relativistic massless fermions and bosons, one obtains the equation of state (EOS) for a free massless QGP gas [15]:

$$p = \left[g_g + \frac{7}{8}(g_q + g_{\bar{q}}) \right] \frac{\pi^2}{90} T^4, \quad e = \left[g_g + \frac{7}{8}(g_q + g_{\bar{q}}) \right] \frac{\pi^2}{30} T^4. \quad (1.1)$$

Here, $g_g + \frac{7}{8}(g_q + g_{\bar{q}})$ is the total degeneracy of the QGP. For gluons with 8 colors and 2 polarizations, $g_g = 8 \times 2$. For quarks with 3 colors, 2 spins and N_f flavors, $g_q = 3 \times 2 \times N_f$. The 7/8 factor comes from Fermi-Dirac statistics. The above equations give the ideal EOS for a non-interaction massless QGP, $p = e/3$. If one assumes that the phase transition happens at $e \approx 1\text{GeV}/\text{fm}^3$, roughly seven times that of normal nuclear matter, then one finds a critical temperature of $T_c \approx 160\text{ MeV}$ for a massless 2 flavor (u, d) QGP.

In principle, the free energy and the EOS of the weakly coupled QGP can be perturbatively calculated order by order in thermal QCD. However, the QCD free energy shows bad convergence of the perturbative expansion in powers of the strong coupling constant g [16, 17]. To solve this problem, one needs to reorganize the perturbation theory. This led to the recent developments of hard thermal loop (HTL) perturbation theory, the so called ϕ -derivable approach, dimensionally reduced screened perturbation theory, and others

¹The SPS measurements indicate that the plasma was already created there, but was very short lived.

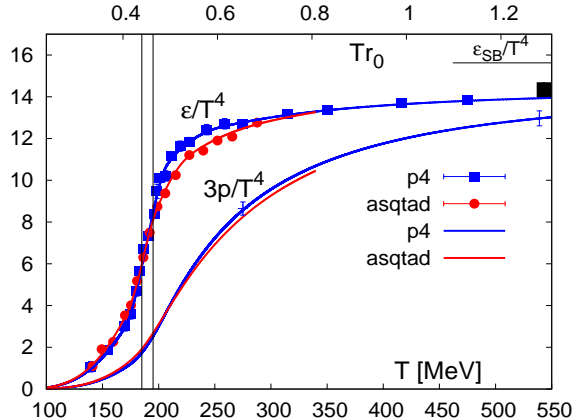


Figure 1.1: Energy density and three times the pressure as a function of temperature, calculated from lattice QCD with asqtad and p4 action [21].

(see the review article [18] for details), all of which yield much improved convergence for the QCD free energy and an improved EOS at high temperature. Still, the calculation needs non-perturbative input, due to the existence of a non-perturbative magnetic mass scale $m_{mag} \sim g^2 T$, which enters the EOS at order g^6 [19, 20]. On the other hand, even the most sophisticated weakly coupled QCD methods fail near the phase transition where non-perturbative effects become dominant.

Lattice QCD offers a non-perturbative approach to study the QCD properties at finite temperature. Recent developments in this field have made available quite precise lattice calculations of the EOS with almost physical quark masses [21, 22]. Fig 1.1. shows the Lattice EOS (at zero chemical potential) from Bazavov et al., using two different improved staggered fermion actions (the asqtad and p4 action, respectively) [21]. They found that both deconfinement and chiral symmetry restoration happen in a narrow temperature region: $185 \text{ MeV} < T_c < 195 \text{ MeV}$, which is indicated by the narrow band in Fig 1.1. At higher temperature $T > 300 \text{ MeV}$, one finds that the lattice EOS approaches 85-90% of the Stefan-Boltzmann limit for an ideal non-interacting QGP gas. But this does not necessarily mean that the QGP is already weakly coupled there. From the EOS alone, lattice QCD simulations can not distinguish a weakly coupled QGP from a strongly coupled QGP. Indeed, the concept of a strongly coupled QGP, which behaves like an almost perfect liquid with very low viscosity [24, 12, 13, 25], came from the strong collective flow observed in RHIC experiments and its very successful descriptions by ideal hydrodynamics [26, 27]. However, why the QGP is strongly coupled at RHIC energies is still a theoretical challenge³, and it is also unknown whether the QGP created in the future LHC experiments will continue to be a strongly coupled liquid or behave more like a weakly coupled gas.

1.1.2 Stages of a heavy ion collision and theoretical tools

Stages of a heavy ion collision

In this subsection, we introduce different stages of a heavy ion collision and the main theoretical tools to describe or simulate these stages. After a discussion of these theoretical tools, we will list several experimental probes and signatures to detect the transient QGP phase.

² Other groups found a lower transition temperature $155 \text{ MeV} < T_c < 174 \text{ MeV}$ [23].

³ Some models trying to explain the strongly coupled nature of the QGP at RHIC energies can be found in Refs. [28, 29]. Other authors explore the possibility that the strongly coupled dynamics can be obtained through weak coupling expansions using HTL resummation [30, 31].

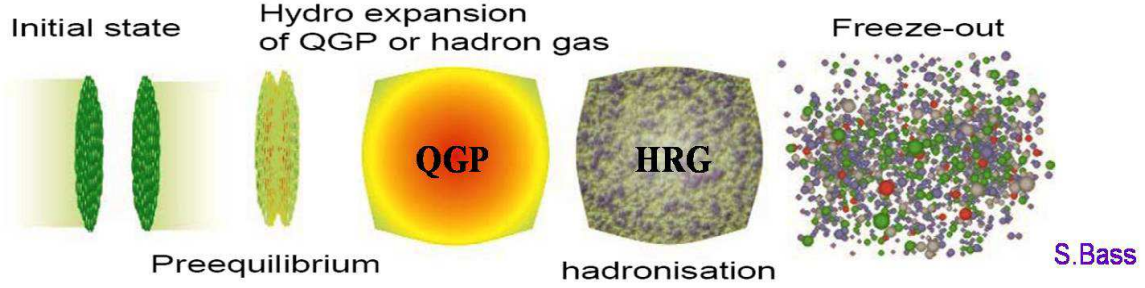


Figure 1.2: Different stages for relativistic heavy ion collisions [33].

The different stages for an ultra-relativistic heavy ion collision ($\sqrt{s} \gtrsim 100$ GeV) are schematically illustrated in Fig 1.2 and 1.3. The initial stage before the collision is followed after impact by a pre-equilibrium stage, an expanding QGP and hadron resonance gas (HRG) stage and a final freeze-out/decoupling stage. In more detail, these stages are characterized as follows [32]:

1. Initial stage at $\tau < 0$: Two Lorentz contracted heavy nuclei approach each other with more than 99.9% of the speed of light. At sufficiently high collision energy (possibly reached at RHIC), this initial stage can be described by dense gluon walls known as the Color Glass Condensate (CGC) (this is further explained in the theoretical tools below).
2. Pre-equilibrium stage and thermalization: The energetic collision of the two heavy nuclei excites the QCD vacuum and produces a dense pre-equilibrium matter consisting of quarks, anti-quarks and gluons. It takes around 1 fm/c for the pre-equilibrium bulk matter to achieve local thermalization and form the quark-gluon plasma. In this very early pre-equilibrium stage, the primary collisions between fast partons inside the colliding nuclei also generate “hard probes” with either large mass or large transverse momentum, such as heavy quark pairs ($c\bar{c}$ and $b\bar{b}$), pre-equilibrium real or virtual photons, and very energetic quarks and gluons with large transverse momentum (from which jets are formed after hadronization).
3. QGP expansion and hadronization: After thermalization, the quark-gluon plasma (QGP), driven by thermal pressure gradients, expands and cools down very quickly. After reaching the critical temperature $T_c \simeq 170$ MeV, it hadronizes and turns into hadronic matter, consisting of a mixture of stable and unstable hadrons and hadron resonances. Hadronization happens continuously at the edge of the

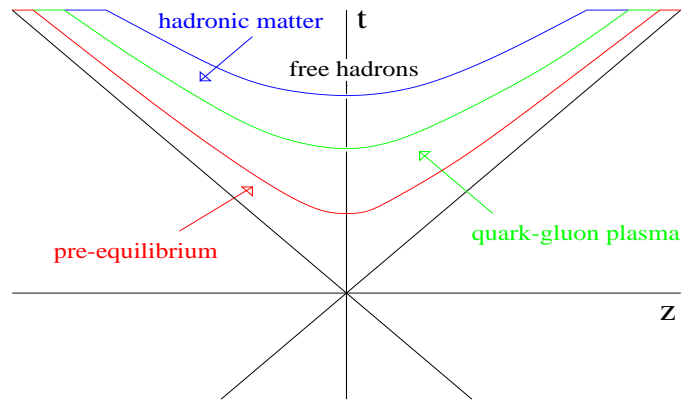


Figure 1.3: The space-time picture of a heavy ion collision [34].

QGP fireball during the whole QGP expansion period. In central Au+Au collisions at RHIC, it takes around 10 fm/c for the QGP fireball to expand and fully convert to hadronic matter.

4. Hadronic expansion and decoupling: The hadronic matter continues to expand until the system becomes very dilute. Then individual hadrons decouple from the system (kinetic freeze-out) and free-stream to the detector. Like the QGP hadronization process, the hadronic decoupling happens continuously at the edge of the fireball, where the density is low. After complete hadronization, it takes another 5 – 10 fm/c for the hadronic matter to completely freeze-out.

Theoretical tools for different stages of a heavy collisions

There does not exist a unique theoretical tool to describe the whole heavy ion collision process from the very beginning till the end. The different energy and time scales during different collision stages imply dramatic changes of the effective physical degrees of freedom and their interactions, which thus require different tools for their description. A complete description requires matching these tools to each other, generating so-called hybrid approaches. For example, the results from the Color Glass Condensate (CGC) theory can be used as initial conditions for dynamical evolution models such as hydrodynamics or the parton cascade. Hydrodynamics or parton cascade models are then connected with a hadron cascade model for a description of the late hadronic stage. The hadron cascade model is equipped with an afterburner to generate quantum statistical or final-state interaction induced 2-particle correlations. Fig 1.4 shows the different theoretical approaches and their ranges of applicability. Although plotted by S. Bass as early as 2001, it still very nicely illustrates our present understanding, in spite of several new theoretical developments in the past years⁴.

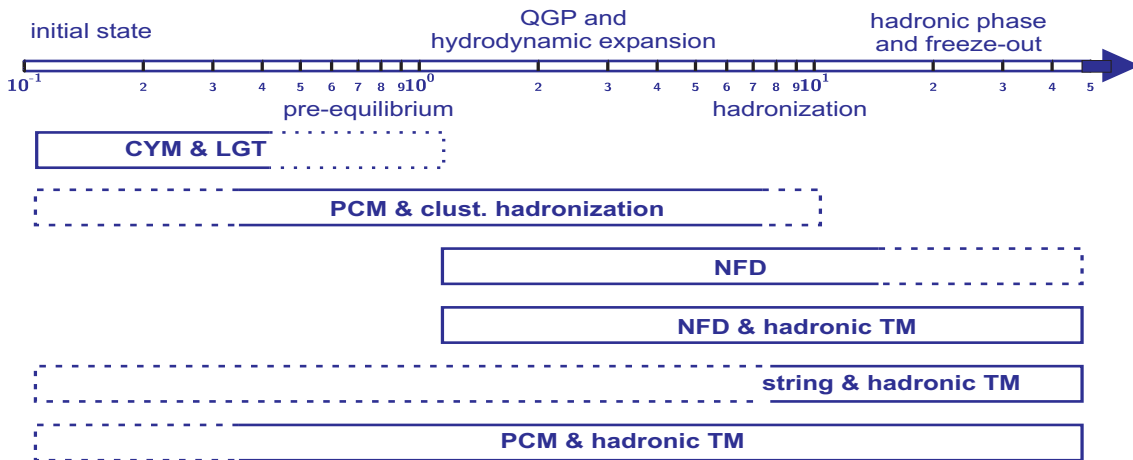


Figure 1.4: Theory tools for RHIC and their range of applicability [39]. Solid bands denotes the safe range to apply respective theoretical tools, while the dashed and dotted bands refer to the region where the approach is still applied, but may be questionable or unsafe. CYM: Classical Yang-Mills Theory [40, 41], LGT: Lattice Gauge Transport [42, 43], PCM: Parton Cascade Model [44], NFD: Nuclear Fluid Dynamics or Hydrodynamics [45, 26, 27]. String and Hadronic TM: String and Hadronic Transport Model [46, 47, 48].

⁴These new developments include new ideas to understand thermalization [35, 36] as well as first numerical implementations of hybrid approaches, such as hydrodynamics+hadron cascade [37, 38].

Color Glass Condensate: At very high collision energies, particle production at mid rapidity probes the nuclear structure functions in the small- x regime (x is the fraction between parton momentum and beam momentum). It is well known that the gluon distribution function $xG(x, Q^2)$ increases dramatically with decreasing of x , for large enough probe resolution Q^2 . When the gluon density becomes high enough, two gluons start to recombine to one. This leads to gluon saturation below some momentum scale Q_s^2 . At this momentum scale, each gluon mode has macroscopic occupation number $\sim \frac{1}{\alpha_s}$, which is why this state has been called a condensate. These small- x gluons are generated by radiation corrections from gluons at large x , whose natural evolution time scale is Lorentz dilated. This time dilation is transferred to the small- x degrees of freedoms, making them evolve very slowly compared to other natural time scales: their behavior is “glassy”. Considering these factors, together with the color nature of gluons, this initial stage has been named Color Glass Condensate (CGC) [40, 41, 49]. The production of the pre-equilibrium secondary soft gluons is related to breaking the phase coherence in this initial CGC wave function [50].

Parton cascade model: After the initial parton production, one needs to describe the pre-equilibrium stage and its thermalization. For dilute systems with incoherent parton configurations, the classical motion of on-shell partons can be described by the Parton Cascade Model (PCM) [44, 51, 52], which solves the Boltzmann equation with a leading order PQCD collision term. Initially, the PCM was assumed to work for the pre-equilibrium stage, the subsequent thermalization period and the succeeding QGP expansion stage. However, the typical thermalization time obtained from PCM with 2-body ($gg \leftrightarrow gg$) PQCD scattering cross sections is of the order of 5 fm/c [52], which is too long for the fast thermalization (< 1 fm/c) required by RHIC data [24, 53]. The recent development of a PCM with $2 \leftrightarrow 3$ ($gg \leftrightarrow ggg$) processes leads to faster thermalization and indeed reproduces the large observed elliptic flow [54, 55]. However, it is applied to a dense system, which creates tension with the assumptions under which the Boltzmann equation is valid. In a very dense system (such as the very early pre-equilibrium stage at RHIC and LHC energies) the partons scatter so frequently that they are no longer on shell. To treat partons with off-shell energies requires the use of quantum transport theory. The theoretical framework for quark-gluon quantum transport was developed by Heinz more than 20 years ago [56, 57, 58, 59], but its numerical demands are exorbitant, and it has not yet been implemented numerically.

Thermalization: The formation of the quark gluon plasma requires two aspects: local equilibrium (thermalization) and local momentum isotropy. Generally, it is believed that the system achieves momentum isotropy before completing thermalization, which is assumed to happen at a time scale of ~ 0.6 fm/c at RHIC energies as indicated by the validity of ideal hydrodynamic simulations [24, 53]. Elucidating the mechanism for fast isotropization and thermalization has been a theoretical challenge. Although much progress has been made during the past years, the thermalization mechanism is still not fully understood. Recently, people realized that the Weibel instability, which is known from traditional electromagnetic plasmas [60], might help to understand the fast isotropization and thermalization of the QGP [61, 62, 35, 36]. The presence of a Chromo-Weibel instability in the early parton plasma, which is characterized by strong momentum anisotropies, has been confirmed by numerical simulations in 1+1-dimensional [35, 36, 63] and 3+1-dimensional [64, 65] hard thermal loop effective theory and in a 3+1-dimensional expanding Glasma⁵ [66, 67]. However, non-Abelian saturation effects temper the exponential growth of the Chromo-Weibel instability, leading to significantly larger time scales even for isotropization than those required for the fast thermalization approximately observed at RHIC [64, 66].

Hydrodynamics: If thermalization is achieved and can be locally maintained during the subsequent expansion, the further evolution of the QGP and hadronic matter can be described by hydrodynamics [45]. Hydrodynamics is a macroscopic approach which describes the system by macroscopic variables, such as local energy density, pressure, temperature and flow velocity. It requires knowledge of the equation of state, which

⁵ *Glasm*a is the name introduced for initially highly coherent gluon matter that makes the transition from the Color Glass Condensate to the Quark Gluon Plasma [50].

gives a relation between pressure, energy and baryon density, but no detailed knowledge of the microscopic dynamics. The simplest version is ideal hydrodynamics [26, 27], which totally neglects viscous effects and assumes that local equilibrium is always perfectly maintained during the fireball expansion. Microscopically, this requires that the microscopic scattering time is very much shorter than the macroscopic expansion (evolution) time and that the mean free path is much smaller than the system size. If this is not satisfied, viscous effects come in, and one can apply viscous hydrodynamics as long as the deviation from local equilibrium remains small [68, 69]. If the system is far away from equilibrium, one has to switch to a kinetic theory approach, such as parton [44] or hadron [47] cascade models.

Hadron cascade model and hybrid approaches: The hadron cascade model [46, 47, 48], which solves the Boltzmann equation for a variety of hadron species with flavor-dependent cross-sections, is a successful tool to describe the hadronic matter created at AGS and SPS energies. At these collision energies, the hadron cascade model is initialized by a superposition of hadrons and hadronic strings, produced in the primary nucleon-nucleon collisions. At RHIC energies and above, hybrid approaches that combine a parton cascade model or hydrodynamics with a hadron cascade, provide a “unified” description of the evolution of the QGP and the succeeding hadronic matter. However, some caution must be taken for the transition between the models. Parton + hadron cascade hybrids must deal with the problem of converting partons to hadrons without violating the second law of thermodynamics (i.e. without losing entropy), and they have difficulties to incorporate the change in the structure of the QCD vacuum during the phase transition⁶. Hydrodynamics + hadron cascade hybrids [37, 38] can more easily accommodate these, by employing a realistic EOS from lattice QCD. One generally stops hydrodynamics at a switching temperature slightly below T_c , converting the fluid to hadrons using a Cooper-Frye prescription (see Chap. 3.4) for phase-space distributions to generate (via Monte-Carlo) initial momentum and spectra profiles for the hadron cascade simulations. However, this procedure can not deal with a potential feed-back from cascade hadrons to the hydrodynamics fluid along space-like parts of the matching freeze-out hypersurface.

1.1.3 QGP signatures

Possible signals and probes for the quark-gluon plasma have been investigated for around 30 years since the birth of the field. Such signatures include: collective flow [72, 73, 26, 27], strangeness enhancement [74, 75], charmonium suppression [76, 77], thermal photon and dilepton emission [78, 79], jet quenching [80, 81, 82, 83], critical fluctuations [84], and others. Some of the predicted signature were already found in earlier heavy ion experiments at AGS and SPS energies [11]. However, none of these signatures allow individually to prove QGP formation, as they are contaminated by the dynamical evolution of the fireball through various stages, usually from the very early pre-equilibrium stage through (perhaps) a QGP phase to the late hadronic stage. The combination of three observations at RHIC, that finally convinced the community that the QGP has been successfully created, were the measurements of strong anisotropic collective flow, valence quark number scaling of the elliptic flow v_2 , and jet quenching [85, 86]. This led to the announcement in 2005 that the QGP had been discovered at RHIC [12, 13, 85, 87].

Collective flow:

The hadron momentum spectra, their angular distribution (flow patterns) and the particle yield ratios are primary observables for the bulk medium created in heavy ion collisions. One of the main discoveries of RHIC is that the medium displays strong collective dynamics [88, 89, 90, 91], which, for the first time in the history of particle and nuclear physics, could be quantitatively well described by ideal hydrodynamics⁷. In the language

⁶Some development try to solve this problem can be found in [70, 71]

⁷Although large collective flow was also observed in heavy ion collisions at AGS and SPS energies, the corresponding data can not be quantitatively described by hydrodynamics models [92].

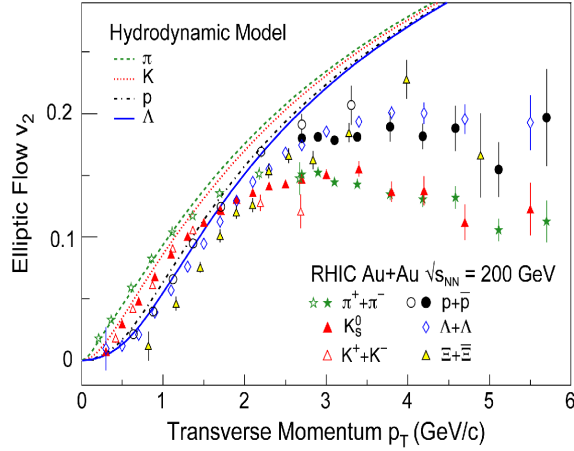


Figure 1.5: Elliptic flow v_2 for different hadron species [94, 90, 95], plotted as a function of transverse momentum, compared with ideal hydrodynamics predictions [96, 97].

of hydrodynamics, the collective flow is driven by pressure gradients, thus providing access to the equation of state (EOS) of the medium. Whereas the azimuthally averaged radial flow receives contributions from all expansion stages, the anisotropic “elliptic” flow seen in non-central collisions is generated mostly during the hot early stage, and thus provides the information about the QGP phase, namely its thermalization and its EOS [26, 27, 93].

The elliptic flow v_2 is defined as the 2nd Fourier coefficient of the azimuthal distribution of hadron spectra:

$$v_2(p_T) = \langle \cos(2\phi_p) \rangle \equiv \frac{\int d\phi_p \cos(2\phi_p) \frac{dN}{dy p_T d p_T d\phi_p}}{\int d\phi_p \frac{dN}{dy p_T d p_T d\phi_p}}, \quad (1.2)$$

where $\frac{dN}{dy p_T d p_T d\phi_p}$ is the angular distribution of the transverse momentum (p_T) dependent spectra, and $y = \frac{1}{2} \ln[(E + p_L)/(E - p_L)]$ is the rapidity of the particles.

Fig 1.5 compares the experimental elliptic flow data $v_2(p_T)$ with ideal hydrodynamic predictions [94, 90, 95, 96]. For $p_T < 1.5$ GeV, where most (more than 98%) of the particles are produced, ideal hydrodynamics shows excellent agreement with the experimental data and correctly predicts the observed splitting for different hadron species. This strongly indicates that the bulk of the matter is strongly coupled and behaves like an almost perfect fluid [85].

For a successful description of the RHIC data, especially for the elliptic flow, ideal hydrodynamic requires a fast thermalization of the system, which must happen on a time scale of about 0.6 fm/c [24, 53]. Around that time, the early matter has a peak temperature of ~ 350 MeV – about twice the QGP phase transition temperature. Although this gives indirect evidence for QGP formation, the success of ideal hydrodynamics is primarily evidence for the formation of a *thermalized* new form of matter at $T \sim 2T_c$ [24, 12, 13].

Quark degrees of freedom and partonic collectivity:

The success of the statistical model in analyzing of the measured hadron abundances [98, 99] gives additional evidence for the QGP phase transition. Particle ratios including a large number of hadron species are well described by a thermal model with just two parameters, T and μ , yielding a chemical freeze-out temperature $T_{ch} = 160 - 170$ MeV, which is approximately equal to the QCD phase transition temperature as determined by lattice QCD simulations. This strongly indicates that hadrons are born during the QGP to

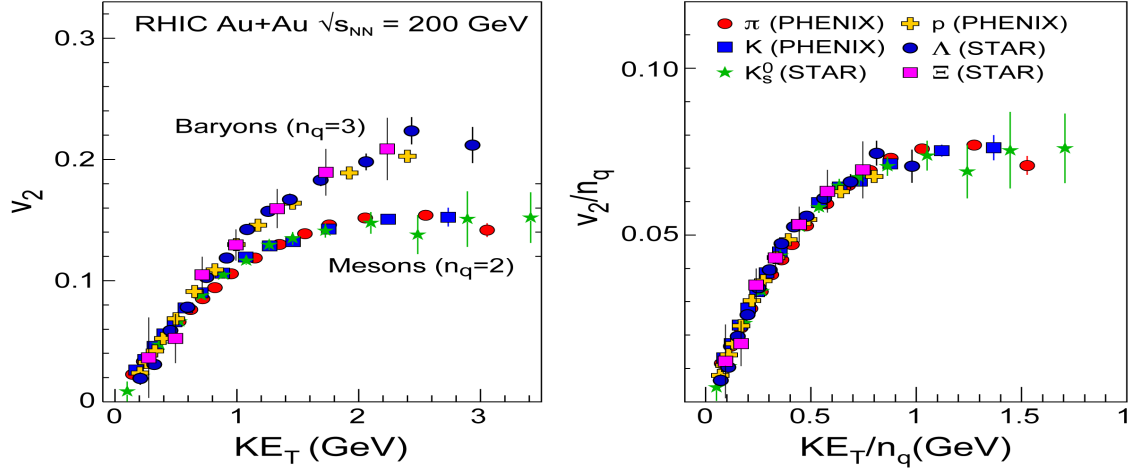


Figure 1.6: left: The transverse kinetic energy KE_T dependence of v_2 for various hadron species. Mesons and baryons fail to different universal curves respectively. right: v_2 and KE_T are scaled by the number of valence quarks. All of the hadron species fail to the same universal curve: the differential elliptical flow per quark. [100]

hadron phase transition, and that flavor changing interactions (from inelastic collisions) quickly cease right after the phase transition [32].

Direct evidence for quark degrees of freedom in the newly formed matter can be extracted from detailed measurements of the p_T -differential elliptic flow $v_2(p_T)$ for a large variety of mesons and baryons. This observable, shown in Fig. 1.5, shows a characteristic splitting between mesons and baryons at intermediate transverse momentum $p_T = 2-5$ GeV. Even though this is above the p_T range where hydrodynamics is valid, the underlying collective flow of the fireball still affects hadron production at this p_T [32]. After replacing the transverse momentum p_T by the transverse kinetic energy $KE_T = \sqrt{p_T^2 + m^2} - m$, the mass splitting at $p_T < 1.5$ GeV disappears. Fig. 1.6 left shows, as a result of this procedure, two universal v_2 scaling curves for baryons and mesons, respectively [100]. Baryons, which contain three valence quarks, show stronger v_2 at intermediate transverse momentum than mesons, containing only two valence quarks. This phenomenon can be well explained by the quark recombination model [101,102,103,104], in which collectively flowing baryons and mesons are generated by the coalescence of quarks that collectively flow with the medium. According to the recombination model, the baryon and meson elliptic flow coefficients are expressed in terms of the quark elliptic flow in the following way [105]:

$$v_2^{(M)}(p_T) = 2v_2^{(q)}(p_T/2); \quad v_2^{(B)}(p_T) = 3v_2^{(q)}(p_T/3). \quad (1.3)$$

As the right panel in Fig. 1.6 shows, a corresponding rescaling of both v_2 and KE_T by the number of valence quark (2 for mesons and 3 for baryons) leads to a universal v_2 scaling curve for *all* hadron species. In short, the universal valence quark number scaling v_2 suggests that the collectively flowing matter directly involves quarks, and that the quark collective properties are transferred to those of hadrons by quark recombination.

Jet quenching:

At the very beginning of a heavy ion collision, hard scatterings of incoming quarks and gluons every now and then create a pair of energetic fast partons with large transverse momentum. Each of the two fast partons will finally fragment into a spray of hadrons, forming what is called a jet. The rates for such hard process are small but grow rapidly with increasing collision energy. At RHIC energies, the fast partons for the first time became sufficiently abundant as useful probes for the hot medium. Their production rates are well understood, both experimentally from pp collision at the same energy or theoretically via PQCD. What

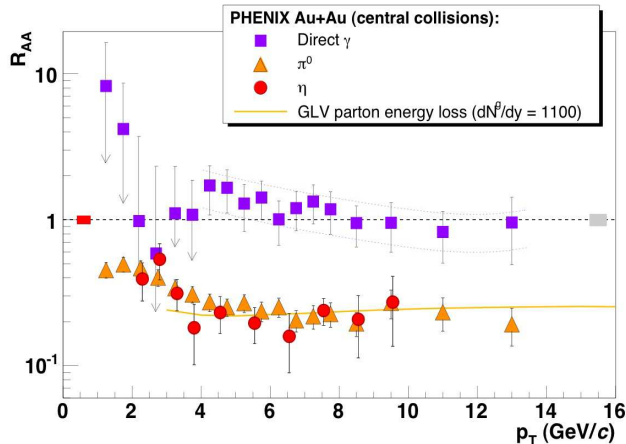


Figure 1.7: The nuclear modification factor R_{AA} as a function of transverse momentum p_T for direct photons γ , as well as π^0 and η mesons in central Au + Au Collisions [106]. R_{AA} is defined as the ratio of the cross section per nucleon-nucleon collision measured in a heavy ion collision divided by the cross section measured in p + p collisions. $R_{AA} = 1$ if the heavy collisions can be viewed as a simple superposition of p + p collisions.

makes them useful for heavy ion collisions is that, before hadronization to jets, they have to travel through the hot fireball medium formed in the collision, which modifies their initial energy and momentum.

One of the most exciting results from RHIC, right after the discovery of strong elliptic flow, was the observation of a strong suppression of high- p_T hadrons in central Au+Au collision, compared with the scaled results from the pp collisions [109, 110, 111]. The experimentally observed suppression by a factor 4-5 agrees qualitatively with theoretical predictions for jet quenching [80, 112, 82, 83], which argued that the QGP formation could lead to large energy loss of fast partons by collision induced gluon radiation and thus suppresses the production of high p_T hadrons fragmented from such partons. The discovery of jet quenching is illustrated in Fig 1.7. The strong suppression of pions and η mesons is distinctly in contrast to that of direct photons, which show no suppression since they interact only electro-dynamically and thus directly escape from the medium without further interactions.

Angular correlations between a high- p_T leading (trigger) hadron with other energetic hadrons provide additional strong support for the picture of significant parton energy loss in the QGP medium [81]. Energy momentum conservation requires that fast partons are always generated in pairs, moving along opposite directions in the pair center of mass frame. This leads to back-to-back correlations between the resulting jets, as shown by two peaks in the azimuthal angle correlation separated by 180° . Such a back-to-back correlation is clearly seen in p+p and d+Au collisions (see left panel of Fig. 1.8 [107, 113]). In central Au+Au collisions, however, one sees only one such peak in the direction of fast trigger hadron (blue stars in the left panel of Fig. 1.8). This can be understood if one assumes that the energetic parton pair is created near the surface of fireball: the near-side outgoing parton quickly escapes from the medium and fragments into the leading hadron and other softer hadrons correlated in angle with the leading hadron, while its inward-traveling partner at 180° loses most of its energy through interactions with the QGP medium and no longer contributes to energetic hadrons in the away-side (recoiling) direction [81]. The energy carried by the away-side fast parton is deposited in the medium, which leads to an enhancement of soft hadron production in the away-side hemisphere, as shown in the right panel of Fig 1.8 [108]. Soon, people realized that the much broadened away-side correlations may be related to a possible collective “hydrodynamic” response of the medium to the energy and momentum deposition from the fast parton, called Mach Cone [114, 115, 116].

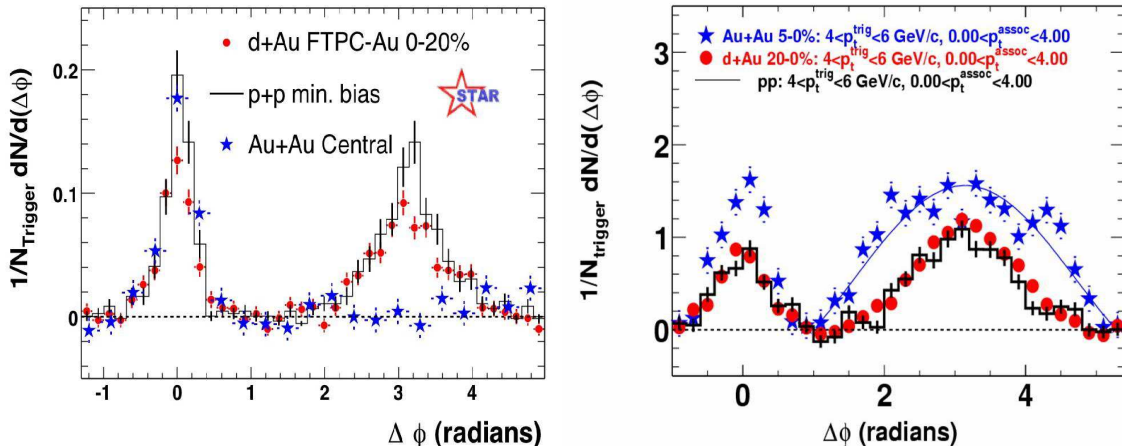


Figure 1.8: Azimuthal angular correlations between high momentum hadrons in $p + p$, $d + Au$, and central $Au + Au$ collisions. In both cases, the trigger particle of the pair has high-momentum ($p_T > 4\text{ GeV}$). Left: Associated particles recoiling with high momenta ($p_T > 2\text{ GeV}$) exhibit strong suppression in $Au + Au$ [107]. Right: Associated particles with low recoil momenta ($p_T > 0.15\text{ GeV}$) are strongly enhanced in $Au + Au$ collisions [108].

1.1.4 “RHIC scientists serve up the perfect liquid ”

The 2007 NSAC Long Range Plane for Nuclear Physics States that “The experiments performed at RHIC since it began operation in 2000 have provided spectacular evidence that the QGP does exist” [85], but its properties are quite different from the earlier expectation based on PQCD, which had suggested that the QGP should behave like a dilute gas. In fact, the strong collective flow together with the very good description from ideal hydrodynamics indicates that the quark gluon plasma created at RHIC is strongly coupled and behaves like a nearly perfect liquid with very low viscosity [85].

The discovery of the strongly coupled QGP is intellectually exciting since it surprisingly connects superstring theory with relativistic heavy ion experiments. Mapping strongly coupled quantum field theories to weakly coupled gravity by the AdS/CFT correspondence [117, 118], string theorists have developed tools for gaining (at least) qualitative insights into the strongly coupled QCD-like systems [119, 120] where traditional PQCD methods fail to apply. Meanwhile, insights from other strongly coupled systems may help us to understand the nature of the strongly coupled QGP. An example comes from strongly interacting fermion systems, created in optical traps at extremely low temperatures, which show similar hydrodynamic behavior [121, 122]. The advantage of such cold atom experiments lies in the tunable coupling strength, via Feshbach resonances, which allows to switch between strongly and weakly coupled fermion systems and thus may help us to understand the transition between strongly and weakly coupled QGP.

With these exciting developments in the past years, the next phase of the RHIC physics program and of the incoming heavy ion program at the LHC will focus on detailed investigations of the QGP, “both to quantify its properties and to understand precisely how they emerge from the fundamental properties of QCD” [85]. Fundamental questions that need to be addressed include (see Ref [123] for details):

- *What is the mechanism of the unexpectedly fast thermal equilibrium?*
- *What is the initial temperature and thermal evolution of the produced matter?*
- *What is the energy density and equation of state of the medium?*
- *What is the viscosity of the produced matter?*
- *Is there direct evidence for deconfinement, color screening, and a partonic nature of the hot dense medium? What is the screening length?*

- *Is the chiral symmetry restored by QCD?*
- *How does the new form of matter hadronize at the phase transition?*

In this thesis, I will concentrate on one of the above questions, the viscosity of the QGP. To answer it requires continuous progresses on both theoretical and experimental sides, especially the development of viscous hydrodynamics and future high statistics flow measurements for a variety of identified hadrons species. This thesis will focus on viscous hydrodynamics for relativistic heavy collisions⁸. The transport coefficients (such as shear viscosity and bulk viscosity) are free parameters in viscous hydrodynamic calculations. The hope is that by tuning these parameters for best fits of a sufficiently large set of sensitive experimental observables, the QGP viscosity can be extracted phenomenologically from experimental data. This requires not only the development of a practical and accurate viscous hydrodynamics code, but a careful investigation of other ingredients (EOS, initial and final conditions, etc.), which may affect the viscosity-sensitive observables. Some of these issues will be addressed in this thesis. (Of course, the QGP transport coefficients are not just simple numbers, but depend on the thermodynamics properties of the fireball, which evolve with time). We should therefore use, as much theoretical knowledge as available, to constrain the the temperature dependence of these variables, at least at the qualitative level. In the rest of this chapter we will briefly review the present status of theoretical understanding and knowledge of the transport coefficients for QCD matter and other strongly coupled systems.

1.2 Transport coefficients for non-relativistic fluids

There are several transport coefficients that characterize the internal "friction" in a fluid. For example, the shear viscosity (dynamic viscosity) η measures the fluid's resistance to flow, the bulk viscosity (volume viscosity) ζ measures the fluid's resistance to expansion, and the thermal conductivity (heat conductivity) λ measures the fluid's ability to conduct heat. In this section, we will discuss shear and bulk viscosity in some detail, since they will be used in later parts of this thesis.

Shear viscosity

Classically, the shear viscosity is defined as the ratio between the friction force F per area and the transverse flow gradient $\nabla_y v_x$,

$$\frac{F}{A} = \eta \nabla_y v_x. \quad (1.4)$$

Microscopically, shear viscosity is associated with momentum transfer between particles in different fluid cells. For a dilute gas of non-relativistic particles, the shear viscosity η and shear viscosity to entropy density ratio η/s are estimated as [147]:

$$\eta \sim nm\bar{v}l_{\text{mfp}} \sim \frac{m\bar{v}}{\sigma}, \quad \frac{\eta}{s} \sim \frac{m\bar{v}}{\sigma n}, \quad (1.5)$$

where n is the particle density, m is the particle mass, \bar{v} is the mean velocity, $l_{\text{mfp}} = \frac{1}{n\sigma}$ (where σ is the transport cross section) is the mean free path, and the entropy density s is proportional to the particle density $s \sim n$. The shear viscosity of a non-relativistic dilute gas increases with temperature $\eta \sim \sqrt{mT}$ (taking $\bar{v} \sim \sqrt{T/m}$) and is approximately independent of density⁹. The $1/n$ density dependence of η/s

⁸ *This thesis mainly covers work done and results obtained by the author [124, 125, 126, 127, 128, 129, 130]. Results from other groups published over the same time period can be found in Ref [131, 132, 133, 134, 135, 136, 137, 138, 139, 140, 141, 142, 143, 144]. We will refer to these papers for comparison when needed or useful.*

⁹ *This estimate agrees qualitatively with results derived from the Chapman-Enskog expansion [147].*

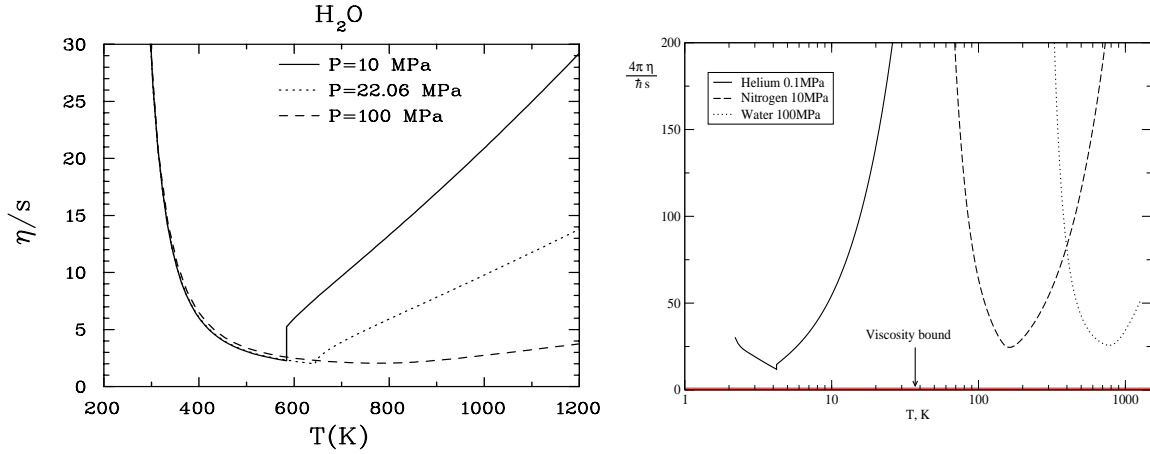


Figure 1.9: left: η/s as a function of temperature for water at different pressures [145]. right: η/s for helium, nitrogen and water [146].

translates into a pressure dependence of η/s , as shown in the left panel of Fig 1.9. Using the ideal gas EOS $p = nk_B T$, one finds that, for fixed pressure, η/s increases with temperature approximately as

$$\eta/s \sim T^{3/2} \quad (1.6)$$

in the high temperature gas phase.

For a liquid, the momentum transfer between different fluid cells involves the motion of voids. The density of voids decreases with temperature, which leads to an increase of shear viscosity due to the growth of mean free path. Detailed calculation [148] shows that

$$\eta \simeq h n e^{E/(k_B T)} \quad \frac{\eta}{s} \sim h e^{E/(k_B T)}, \quad (1.7)$$

where E is an activation energy and h is the Planck constant, and again $s \sim n$. This result shows that for a liquid η/s increases with decreasing temperature.

Taking the liquid phase and gas phase together, Eq.(1.6) and Eq.(1.7) imply that η/s is likely to reach a minimum during the liquid-gas phase transition. This is confirmed by experimental results shown in Fig 1.9 which plots in the right panel η/s as a function of temperature for three different fluids (helium, nitrogen and water) [146], and for water at different pressures in the left panel [145]. In all of these cases, η/s reaches a minimum near the phase transition.

Bulk viscosity

In non-relativistic fluid dynamics, the bulk viscosity ζ is defined as a combination of shear viscosity η and volume viscosity¹⁰ ν : $\zeta = \nu + \frac{2}{3}\eta$. Bulk viscosity vanishes for a scale invariant system. For a dilute monatomic gas, experimental data and kinetic theory show that bulk viscosity is vanishingly small or zero [149]. The bulk viscosity of a dilute diatomic gas, however, has an appreciable value due to the exchange of energy between translational and rotational degrees of freedom during collisions [150]. In a dense gas, bulk viscosity is associated with the internal friction force arising from the change of volume at constant shape [151]. In a liquid, bulk viscosity is related to the rearrangement of molecules during acoustic compression and rarefaction [151].

Experimentally, bulk viscosity is generally determined from measuring the sound absorption coefficient. In contrast to shear viscosity, there are no comprehensive bulk viscosity data sets for many varieties of fluids over a wide range of temperature and density, and the existing bulk viscosity data have large error bars.

¹⁰The volume viscosity (also known as “second viscosity”) ν measures the resistance to expansion; it determines the dynamics of a compressible fluid.

The phase transition behavior of the bulk viscosity of spherical molecules was studied by Meier, Laesecke and Kabelac using molecular-dynamics simulations with Lennard-Jones potentials. They found that the bulk viscosity shows a peak in the vicinity of the gas-liquid phase transition [152] (see also Fig.6 and related comments in Ref. [153]).

In short, the shear (bulk) viscosity to entropy ratio reaches a minimum (maximum) near phase transitions for common non-relativistic fluids. As we will see in Sec. 1.4, the same holds for relativistic QCD matter. This is not a rigorous statement from first principles calculations, but appears to be supported by specific examples of both experimental data and theoretical results.

1.3 Transport coefficients for relativistic fluids: weak coupling vs. strong coupling

Relativistic hydrodynamics can be viewed as an effective theory for quantum field systems at large distance and time scales. The dynamics of long wavelength, low frequency fluctuations are characterized by transport coefficients (shear viscosity η , bulk viscosity ζ and heat conductivity λ , electric conductivity σ etc.). For a relativistic fluid, the transport coefficients define the leading order corrections of the energy momentum tensor $T_{\mu\nu}$ and charge current N_μ from their local equilibrium forms. For example, in the local rest frame the stress tensor reads at leading order in gradients: $T_{ij} = p_{eq}(e)\delta_{ij} - \eta(\partial_i u_j + \partial_j u_i + \frac{2}{3}\delta_{ij}\partial_k u_k u_j) - \zeta\delta_{ij}\nabla \cdot u$. In this section, we will briefly review methods for calculating these transport coefficients (especially shear and bulk viscosity) in both weak and strong coupling regimes.

For a weakly coupled system, the transport coefficients can be calculated from kinetic theory or from linear response theory. The kinetic theory approach [154,155,156,157,158,159] starts from local equilibrium distribution functions and expands the full distribution function order by order in terms of gradients of the four-velocity, temperature and chemical potential. The viscosity coefficients are associated with the first order terms in velocity gradients, and can be determined from the Boltzmann equations if the collision term is known explicitly (they depend on the transport cross section in the collision term).

In linear response theory, the transport coefficients can be rigorously expressed by Kubo formulae [160], that relate the transport coefficients to the slope of associated spectral functions at zero frequency. For example,

$$\eta = \lim_{\omega \rightarrow 0} \lim_{\mathbf{k} \rightarrow 0} \frac{\rho^{12,12}(\omega, \mathbf{k})}{2\omega}, \quad \zeta = \frac{1}{9} \lim_{\omega \rightarrow 0} \lim_{\mathbf{k} \rightarrow 0} \frac{\rho^{ii,jj}(\omega, \mathbf{k})}{2\omega}, \quad (1.8)$$

where the spectral functions are given by the imaginary part of the retarded green functions, $\rho(\omega, \mathbf{k}) = 2\text{Im}G_R(\omega, \mathbf{k})$, for certain components of the energy-momentum tensor:

$$G_R^{\mu\nu,\kappa\sigma}(\omega, \mathbf{k}) = -i \int d^4x e^{i(\omega t - \mathbf{k}\mathbf{x})} \langle [T^{\mu\nu}(\mathbf{x}, t) T^{\kappa\sigma}(0, 0)] \rangle.$$

The Kubo formulae can be applied to both weakly and strongly coupled systems (see Chap. 1.5) and can be generalized for lattice simulations. In lattice QCD, the spectral function $\rho(\omega)$ is obtained from the Matsubara (imaginary time) Green function G_E , instead of the retarded Green function G_R . (Both of them have spectral representation in terms of ρ ¹¹.) The calculation of shear and bulk viscosity on the lattice [161,162,163,164] starts with the calculation of the corresponding imaginary time correlators of the

¹¹ G_R is obtained from G_E by replacing $i\omega_n$ with $\omega - p_0 + i\varepsilon$:

$$G_E(i\omega_n) = \int \frac{d\omega}{2\pi} \frac{\rho(\omega)}{\omega - i\omega_n}, \quad G_R(p_0) = -i \int \frac{d\omega}{2\pi} \frac{\rho(\omega)}{\omega - p_0 - i\varepsilon}.$$

Here $\omega_n = 2\pi nT$ ($n \in \mathbb{Z}$) are bosonic Matsubara frequencies, and T is the temperature of the medium.

energy momentum tensor in Euclidean time $0 \leq \tau < 1/T$, which is related to the spectral function by

$$G_E(\tau) = T \sum_n e^{-i\omega_n \tau} \int \frac{d\omega}{2\pi} \frac{\rho(\omega)}{\omega - i\omega_n} = \int \frac{d\omega}{2\pi} \frac{\cosh[\omega(\tau - 1/(2T))]}{\sinh[\omega/(2T)]} \rho(\omega). \quad (1.9)$$

In principle, one can obtain the spectral function $\rho(\omega)$ by inverting eq.(1.9), and then use eq.(1.8) to calculate the transport coefficients. In practice, one can only compute a finite number of points for $G_E(\tau)$ on the lattice, which makes the unique extraction of an analytical spectral function $\rho(\omega)$ impossible. Generally, one makes an ansatz for $\rho(\omega)$ with a small number of parameters, motivated by (usually somewhat model-dependent) considerations on the expected behavior of $\rho(\omega)$ at small and large ω , and then fits these parameters to the Monte Carlo data [161, 162, 163, 164].

1.4 Shear and bulk viscosity for QCD matter

Shear viscosity

Attempts to calculate the QGP shear viscosity using weakly coupled QCD started more than 20 years ago [165, 166]. Using kinetic theory in the relaxation time approximation and using a simple perturbative estimate for the latter, one found that the shear viscosity of the QCD matter behaves as $\eta \sim \frac{T^3}{\alpha_s^2 \ln(1/\alpha_s)}$ [165, 166]. A first calculation of the leading logarithmic contribution from the Boltzmann equation was performed in [167], with a complete result finally published in [156]. A full leading order calculation that also computed the coefficient under logarithm was performed by Arnold, Moore and Yaffe using effective kinetic theory in the hard thermal loop approximation [157]. For a weakly coupled QGP with three massless quark flavors, the shear viscosity to entropy ratio is [157]:

$$\frac{\eta}{s} = \frac{5.12}{g^4 \ln(2.42/g)}. \quad (1.10)$$

This result is shown as the solid line in the left panel of Fig. 1.10, using the two-loop renormalization group expression for the running coupling $g(T)$ [145]. (Note that using Eq.1.10 with a running coupling is phenomenological and beyond the order of accuracy at which Eq.1.10 was derived.)

In principle, the QGP shear viscosity can also be non-perturbatively calculated by lattice QCD using Kubo formulae. However, such calculations are highly non-trivial in the standard Monte-Carlo simulations due to the large noise to signal ratio for the relevant operators and the ill-posed inversion problem for the spectral function $\rho(\omega)$, given the finite number of data points for the Euclidean correlators [163]. A first attempt to calculate the shear viscosity of SU(3) gluonic matter on an $8^3 \times 4$ lattice comes from the pioneering work of Karsch and Wyld [161], using a three-parameter ansatz for the spectral function $\rho(\omega)$. This method was later implemented by Nakamura and Sakai to calculate both shear and bulk viscosity on larger lattices ($16^3 \times 8$ and $24^3 \times 8$) with improved Iwasaki action [162]. They found that the shear viscosity to entropy density ratio is less than one, $\eta/s < 1$, and that the bulk viscosity is zero within errors for the temperature range $1.4 \leq T/T_c \leq 1.8$. A new evaluation of the shear viscosity for SU(3) gluon dynamics was performed by Meyer [163] using a two-level algorithm [168], which dramatically improves the statistical accuracy of the relevant Euclidean correlators. He derived a robust upper bound $\eta/s < 1.0$ for the shear viscosity entropy ratio and estimated that:

$$\eta/s = \begin{cases} 0.134(33) & (T = 1.65T_c), \\ 0.102(56) & (T = 1.24T_c). \end{cases} \quad (1.11)$$

Early calculations of the shear viscosity for the hadronic matter started from a theory of massless pions in the low-energy chiral limit, giving [170]

$$\frac{\eta}{s} = \frac{15}{16\pi} \frac{f_\pi^4}{T^4}, \quad (1.12)$$

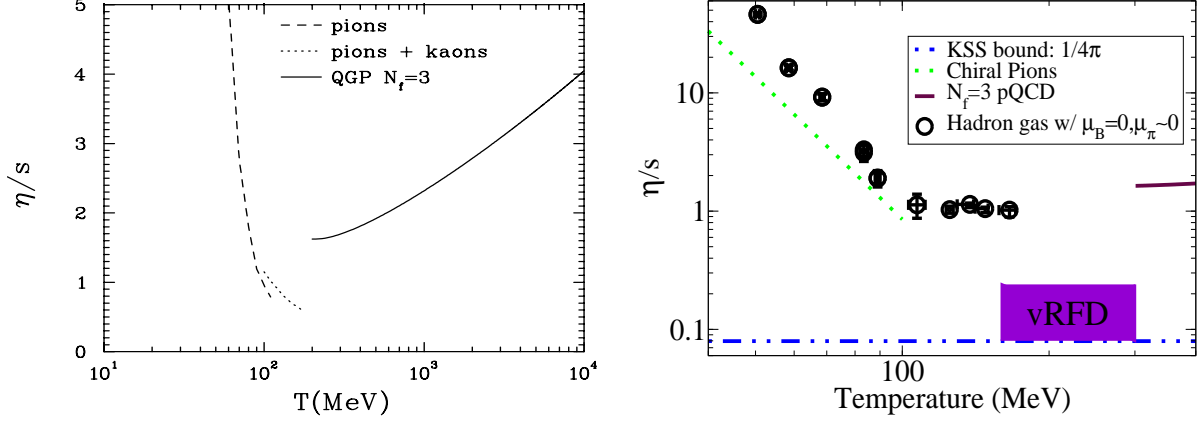


Figure 1.10: left: η/s for low temperature hadronic phase and high temperature QGP phase [145]. right: η/s for hadron resonance gas in chemical and kinetic equilibrium [169].

where $f_\pi = 93$ MeV is the pion decay constant. The ratio η/s diverges at zero temperature; together with the logarithmic perturbative results discussed above, η/s is seen to reach a minimum near the QGP phase transition. A more detailed calculation of η/s for hadronic matter with both pions and kaons can be found in Ref. [170]; it goes beyond the chiral approximation and includes intermediate resonances such as the ρ meson (see also [171]). The left panel of Fig. 1.10 shows these two results, which qualitatively agree with each other at low temperature but gradually deviate from each other above $T > 100$ MeV due to kaon excitations.

Recently, η/s for a hadron resonance gas including a large set of hadron species up to 2 GeV was extracted from UrQMD¹² simulations, using the Kubo formula [169]. Fig. 1.10 shows the extracted η/s as a function of temperature T for a chemically equilibrated hadron resonance gas with zero chemical potential. Below $T < 100$ MeV, η/s quickly rises with decreasing temperature, in qualitative agreement with the chiral pion result [170]. Between 100 MeV and 160 MeV, η/s saturates at a value ~ 1 . For a hadron resonance gas out of chemical equilibrium, a similar tendency was demonstrated in Fig. 4 of Ref. [169], where it is shown that at fixed temperature T , a non-zero baryon chemical potential reduces η/s . For $\mu_B/T = 3.0 - 3.4$ (an unrealistically large chemical potential for RHIC energies), η/s can decrease to 0.3-0.4 near the phase transition, and the plateau structure between 100 MeV and 160 MeV is replaced by a tendency that η/s continues to decrease with increasing T .

It is worthwhile to point out that Ref. [172] argued that including Hagedorn states¹³ can significantly reduce η/s in the hadronic phase near T_c since the highly degenerate Hagedorn states could dramatically increase the entropy density. The authors of Ref. [172] investigated Hagedorn state effects on η/s for a gas of pions and nucleons [173] and for a hadron-resonance gas with excluded volume corrections [174] and found that near T_c , η/s can be significantly reduced to values close to the KSS bound $\eta/s = 1/4\pi$ (see Chap. 1.5).

Bulk viscosity

At sufficiently high temperature, the equation of state of a massless QGP satisfies $p = e/3$ which, on the classical level, leads to a vanishing bulk viscosity for the weakly coupled QGP. However, quantum corrections break the conformal symmetry and result in a non-zero bulk viscosity. Detailed calculations from Arnold,

¹²UrQMD: Ultra-relativistic Quantum Molecular Dynamics, a hadron cascade model [46, 47, 48].

¹³Hagedorn states are highly unstable, massive hadronic resonances that exist close to T_c . These states are not included in the above UrQMD simulation.

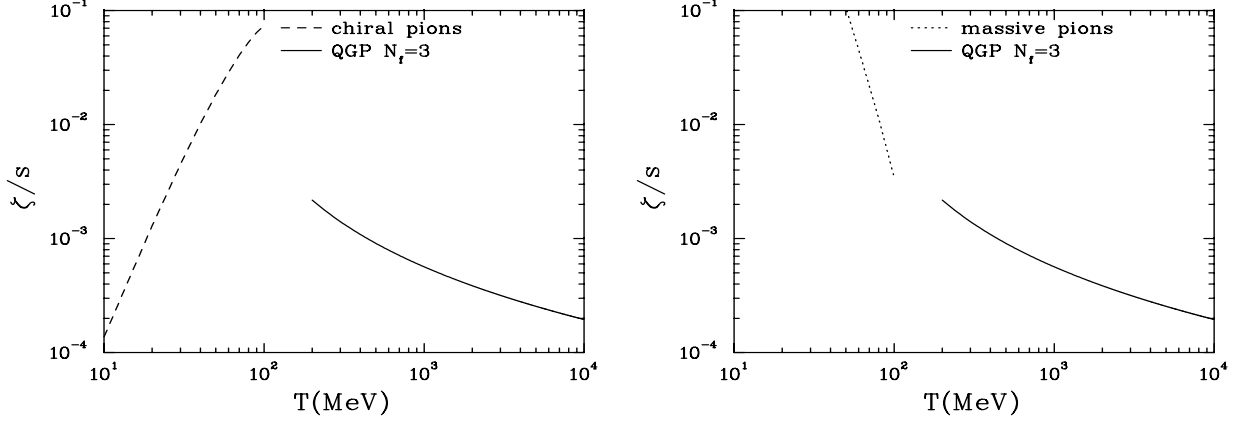


Figure 1.11: left: ζ/s for high temperature QGP and for massless (left) and massive (right) pions [153].

Dogan and Moore [175] showed:

$$\zeta = \frac{A\alpha_s^2 T^3}{\ln[\mu^*/m_D]} . \quad (1.13)$$

Here, A , μ^* and m_D^2 depend on the number of quark flavors in QCD. For QCD with three massless quark flavors, $A = 0.657$, $\mu^* = 7.77T$ and $m_D^2 = 1.5g^2T^2$. Relating Eq. (1.13) with the shear viscosity calculated within weakly coupled QCD [156,157] one finds an approximate, but simple relationship between shear and bulk viscosity:

$$\zeta \simeq 15\eta(c_s^2 - 1/3)^2. \quad (1.14)$$

While this relation does not hold exactly [175], it gives the right order of magnitude of ζ/η .

The bulk viscosity of interacting massless pions was calculated by Chen and Wang in the framework of kinetic theory, combined with chiral perturbation theory. They found that ζ/s monotonically increases with temperature below $T = 120$ MeV: $\frac{\zeta}{s} \sim \frac{T^4}{f_\pi^4}$. The bulk viscosity for massive pions was calculated by Prakash et al. in the 1990's, using kinetic theory with experimental elastic scattering cross sections as inputs [170,171]. In contrast to the case of massless pions, one finds that ζ/s is a decreasing function of temperature. The bulk viscosity to entropy density ratio $\frac{\zeta}{s}$ for massless and massive pions, together with the result for a weakly coupled QGP, are illustrated in Fig. 1.11.

The behavior of bulk viscosity near the QCD phase transition was first investigated by Paech and Pratt within the linear sigma model [176]. Their work showed qualitatively that ζ/s reaches a maximum near the phase transition. This behavior was confirmed in later research by Kharzeev et al. [177,177] and Meyer [164], respectively. Using low energy theorems, Kharzeev et al. connected the bulk viscosity with the lattice interaction measure $e - 3p$ and extracted a temperature dependent ζ/s from lattice data for pure SU(3) gluon dynamics [177] and for full QCD [178]. Meyer directly extracted ζ/s from lattice QCD simulations by calculating the corresponding correlation function for a pure SU(3) gluon plasma. He showed that the peak value of ζ/s near T_c can reach as high as 0.73 [164] (a value that is around 10 times larger than the string theory estimates from holographical models [179,180]). Both of these methods involve an ansatz for the spectral function. However, the parameterized spectral functions used by these authors were challenged by Moore and Saremi [181], who examined the behavior of the spectral function with analytical methods both near the QCD phase transition and in the weak coupling regime.

1.5 Shear viscosity and bulk viscosity from $N = 4$ SYM and the AdS/CFT correspondence

The transport coefficients calculated from weakly coupled QCD are valid at sufficiently high temperature where the running coupling constant becomes small. However, the temperature reached in relativistic heavy ion collisions is not very high (top RHIC energies: $T \sim 350$ MeV, and LHC energies: $T \sim 600$ MeV). It is thus questionable to directly apply the weakly coupled QCD results at LHC/RHIC temperatures. Some insights for this problem can be gained from studies of $N = 4$ supersymmetric Yang-Mills theory (SYM), where the shear viscosity can be calculated in both the strong coupling [182, 183] and weak coupling regimes [184]. Without too much effort, one can parameterize the behavior at intermediate coupling by interpolating between the two limits [184].

For $N = 4$ SYM theory with infinite N_c and large, but finite t'Hooft coupling $g^2 N_c$ (strongly coupling regime), η/s was calculated by Buchel, Liu and Starinets (using the gauge/gravity correspondence, see below). They found [183]

$$\frac{\eta}{s} = \frac{1}{4\pi} \left[1 + \frac{135\zeta(3)}{8(2g^2 N_c)^{3/2}} + \dots \right]. \quad (1.15)$$

The η/s of $N = 4$ SYM theory in the weakly coupled regime was investigated by the McGill group using the kinetic theory approach. They found a much smaller η/s than what was previously found in weakly coupled QCD at the same value of the coupling constant. However, good agreement can be achieved after re-scaling each result by a combination of Debye screening mass and the number of degrees of freedom in the theory. Extending this mapping between weakly coupled QCD and weakly coupled $N=4$ SYM to lower temperature or into the strongly coupled regime, one finds that $\alpha_s = 0.5$ in QCD corresponds to $\lambda = 4.7$ in $N=4$ SYM, where η/s from $N=4$ SYM is still relatively large, of the order of 1 [184].

The finite temperature version of the gauge/gravity (AdS/CFT) correspondence [185, 186], which maps finite temperature gauge field theory at strong coupling onto weakly coupled gravity in a curved space with a black hole, provides a new method to study strongly coupled systems and helps us to gain insights for the properties of a strongly coupled QGP¹⁴. One example is the shear viscosity in the strong coupling limit. In the language of black holes gravity, the shear viscosity, defined by the Kubo formula, is connected with the absorption cross section of the black hole: $\eta \propto \lim_{\omega \rightarrow 0} \sigma_{BH} = A$, where the last equality comes from the general theorem on black holes [187] which states that the cross section $\sigma_{BH} = A$ is equal to the horizon area A for a broad class of black holes. On the other hand, the horizon area A also represents the entropy of the black hole: $s_{BH} = \frac{A}{4G}$. This shows that the shear viscosity to entropy ratio η/s is a constant [188]. The constant was found by Kovtun, Son, and Starinets [146], who showed that

$$\frac{\eta}{s} = \frac{1}{4\pi} \quad (1.16)$$

is a universal value for a large class of black holes or branes. Given that the corresponding dual gauge field theories are very different, they conjectured that $1/4\pi$ is an absolute low bound for η/s , now known as the KSS bound¹⁵.

The bulk viscosity vanishes in conformal field theories such as $N = 4$ SYM. To apply string theory techniques to the calculation of the bulk viscosity in the strongly coupled regime thus requires investigating non-conformal deformations of the original AdS/CFT correspondence. Some recent developments can be found in Ref [179, 191, 192, 193]. Based on various holographical model computations, Buchel proposed a lower bound for the bulk viscosity to entropy ratio [194]:

$$\frac{\zeta}{s} \geq 2\left(\frac{1}{3} - c_s^2\right)\frac{\eta}{s}. \quad (1.17)$$

¹⁴The AdS/CFT correspondence can not be directly applied to QCD since QCD is not a Conformal Field Theory, and its gravity dual (if it exists) is not known.

¹⁵Some possibilities to violate the KSS bound are discussed in [189, 190].

(Note the different dependence on $\frac{1}{3} - c_s^2$ from the weakly coupled result (1.14)). Using a scalar potential tuned to reproduce the lattice equation of state, Gubser et al. calculated the bulk viscosity via gravity duals of non-conformal gauge theories [179, 180]. They found that ζ/s rises sharply near T_c , with $\zeta/s|_{T_c} \simeq 0.05$.

1.6 Notation and outline of this thesis

Throughout thesis we adopt units in which $\hbar = c = k_B = 1$. The metric tensor is always taken to be $g^{\mu\nu} = \text{diag}(+1, -1, -1, -1)$. $\Delta^{\mu\nu} = g^{\mu\nu} - u^\mu u^\nu$ is the projector onto the space transverse to the fluid velocity u_μ , $\Delta^{\mu\nu} u_\mu = 0$. The partial derivative ∂^μ can then be decomposed as:

$$\partial^\mu = \nabla^\mu + u^\mu D,$$

where, $\nabla^\mu = \Delta^{\mu\nu} \partial_\nu$ is the transverse component of the partial derivative ∂_μ , and $D = u^\mu \partial_\mu$ is the corresponding longitudinal component. In the fluid rest frame, D reduces to the time derivation and ∇^μ reduces to the spacial gradient. One therefore also uses the denotation $\dot{f} = Df$.

We also frequently use the symmetric, anti-symmetric and the $\langle \rangle$ brackets in Chap. 2, following Ref. [195, 196, 197, 198]:

$$\begin{aligned} A_{\langle\mu} B_{\nu\rangle} &= \frac{1}{2} (A_\mu B_\nu + A_\nu B_\mu), \\ A_{[\mu} B_{\nu]} &= \frac{1}{2} (A_\mu B_\nu - A_\nu B_\mu), \\ A_{\langle\mu} B_{\nu\rangle} &= \frac{1}{2} \left(\Delta_\mu^\alpha \Delta_\nu^\beta + \Delta_\nu^\alpha \Delta_\mu^\beta - \frac{2}{3} \Delta^{\alpha\beta} \Delta_{\mu\nu} \right) A_\alpha B_\beta. \end{aligned}$$

Using the above notations, the commonly used local fluid rest frame variables in dissipative viscous hydrodynamics are expressed in terms of the energy momentum tensor $T^{\mu\nu}$, charge current N^μ and entropy current S^μ as following (see Chap. 2.1 and Ref. [195, 196, 197] for details):

$n \equiv u_\mu N^\mu$	net density of charge;
$V^\mu \equiv \Delta_\nu^\mu N^\nu$	net flow of charge;
$\varepsilon \equiv u_\mu T^{\mu\nu} u_\nu$	energy density;
$p + \Pi \equiv -1/3 \Delta_{\mu\nu} T^{\mu\nu}$	p: thermal pressure, Π : bulk pressure;
$\pi^{\mu\nu} \equiv T^{\langle\mu\nu\rangle}$	shear stress tensor;
$W^\mu \equiv u_\nu T^{\nu\lambda} \Delta_\lambda^\mu$	energy flow;
$q^\mu \equiv W^\mu - h V^\mu$	heat flow;
$s \equiv u_\mu S^\mu$	entropy density;
$\Phi^\mu \equiv \Delta_\nu^\mu S^\nu$	entropy flux.

In the 1st and 2nd order formalisms for viscous hydrodynamics (Chap. 2) one also frequently encounters the following scalar and tensors constructed from the gradients of the four velocity u^μ :

$\theta \equiv \partial \cdot u$	expansion rate,
$\nabla^{\langle\mu} u^{\nu\rangle} \equiv \sigma^{\mu\nu} = \frac{1}{2} (\nabla^\mu u^\nu + \nabla^\nu u^\mu) - \frac{1}{3} \nabla^{\mu\nu} \partial_\alpha u^\alpha$	velocity stress tensor,
$\Omega^{\mu\nu} \equiv -\nabla^{[\mu} u^{\nu]}$	vorticity tensor.

Note that the above notations are for Cartesian coordinates $x^\mu = (t, x, y, z)$. In Chap. 3, we change to curvilinear coordinates $x^m = (\tau, x, y, \eta)$ for the convenience of describing a longitudinally boost invariant system (i.e. viscous hydrodynamics in 2+1 dimensions). To express the above variables in (τ, x, y, η) coordinates, one can notationally replace μ, ν by m, n , but must also replace the partial derivative ∂_μ by the

covariant derivative d_m , see Chap. 3.1 and Appendix A. 1 for detail.

Outlines:

This thesis focuses on viscous hydrodynamics for relativistic heavy ion collisions. Chapter 2 outlines the 2nd order formalism for viscous hydrodynamics, obtained from different approaches. Chapter 3 sets us up for numerical calculations in (2+1)-dimension, assuming exact longitudinal boost invariance. The discussion there includes explicit transport equations in (2+1)-dimension, the initial conditions, the EOS, final conditions and the transport coefficients used in viscous hydrodynamic simulations. Generic shear and bulk viscosity effects are studied in Chapter 4 and Chapter 6, respectively, by comparing runs with ideal and viscous hydrodynamics using identical initial and final conditions. Chapter 5 focuses on the system size dependence of the shear viscous effects and investigates the multiplicity scaling of the elliptic flow coefficient v_2 for both ideal and viscous hydrodynamics. In Chapter 7, we report on some of the most recent developments in viscous hydrodynamics, including the search for the optimized I-S equations for numerical implementations and recent efforts on code verifications among different groups. Chapter 8 assesses the current uncertainties for extracting the QGP viscosity from experimental data and briefly comments on some future directions for viscous hydrodynamics. Chapter 9 briefly outlines other methods for estimating the QGP shear viscosity. Our conclusions are summarized in Chapter 10.

Chapter 2: Relativistic Viscous Hydrodynamics – the Formalism

In this chapter we introduce the formalism for viscous (dissipative) hydrodynamics. Initial attempts to formulate relativistic dissipative fluid dynamics started as a relativistic generalization of the Navier-Stokes (N-S) equations [199,200]. Unfortunately, it turned out that the relativistic N-S equations are unsuited for numerical implementation since they developed instabilities due to exponentially growing modes, in particular at high frequencies, and violate causality (the N-S formalism will be briefly described in Chap. 2.2.). These difficulties are largely avoided in the 2nd order formalism developed 30 years ago by Israel and Stewart [201,198,202], which goes beyond the so-called 1st order Navier-Stokes approach by expanding the entropy current to 2nd order in dissipative flows, replacing the instantaneous identification of the dissipative flows with their driving forces multiplied by some transport coefficient (as is done in Navier-Stokes theory) by a kinetic equation that evolves the dissipative flows rapidly but smoothly towards their Navier-Stokes limit. The deduction of the I-S equation from the entropy current expansion and the 2nd law of thermodynamics will be introduced in Chap. 2.3. The I-S formalism can also be derived from the Boltzmann equation [131,203,159], by expanding the distribution function around local equilibrium. The most general form of 2nd order viscous hydrodynamics was derived in [204,159] for systems with conformal symmetry and in [203] for systems without such symmetry (i.e. which also feature bulk viscosity and heat conductivity). Some of this will be discussed in Chap. 2.5. All versions of the I-S formalism directly solve evolution equations for the dissipative flows. In contrast, another type of 2nd-order formalism, developed by the Ottinger and Grmela (O-G formalism) [205,206,207], uses evolution equations for auxiliary fields, rather than the dissipative flows (see Chap. 2.6). The standard dissipative flows can be approximately reconstructed from the auxiliary fields [208].

2.1 From ideal to viscous hydrodynamics

Hydrodynamics is a macroscopic tool to describe the expansion of the QGP and hadronic matter. It starts from the conservation laws for the conserved charge currents $N_i^\mu(x)$ and the energy momentum tensor $T^{\mu\nu}(x)$ (x denotes the 4-dimensional space-time coordinates (t, \mathbf{x})) [209]:

$$\partial_\mu N_i^\mu(x) = 0, \quad i = 1, \dots, k; \tag{2.1a}$$

$$\partial_\mu T^{\mu\nu}(x) = 0. \tag{2.1b}$$

For simplicity, one sets $k = 1$ and only considers the conserved net baryon number current. This leaves 14 independent variables: 10 from the symmetric energy momentum tensor $T^{\mu\nu}$ and 4 from the charge current N^μ . However, this system of equations is unclosed since (2.1) only offers 5 independent equations. To solve this problem, one needs either to reduce the number of independent variables through physically assumptions, or to provide more equations.

Ideal hydrodynamics [26, 27] solves this problem via the first route. By assuming perfect local thermal equilibrium, one can decompose the charge current and energy momentum tensor as follows:

$$N^\mu = nu^\mu, \tag{2.2a}$$

$$T^{\mu\nu} = eu^\mu u^\nu - p\Delta^{\mu\nu}, \quad (\Delta^{\mu\nu} = g^{\mu\nu} - u^\mu u^\nu), \tag{2.2b}$$

where $n(x)$, $e(x)$, $p(x)$ are the local net baryon density, energy density and pressure, respectively, and $u^\mu(x)$ is the 4-flow velocity which is time like and normalized: $u^\mu u_\mu = 1$. The above ideal fluid decomposition

reduces the 14 independent variables into 6 (1 each for e , n and p and 3 independent components in u^μ). With one additional input – the equation of state (EOS) $p = p(n, e)$ – the system of equations is closed and can be solved to simulate the evolution of the system. Using the fundamental thermodynamic identity $e + p = Ts + \mu n$, it is easy to show that, in the absence of shocks (i.e. discontinuity in e , n or p), Eqs. (2.1) conserve entropy, $\partial_\mu S^\mu = 0$, with $S^\mu = su^\mu$.

In classical kinetic theory, N^μ and $T^{\mu\nu}$ are associated with the microscopic phase-space distribution function $f(x, p)$ as follows [209, 210]:

$$N^\mu = \sum_i n_i \int \frac{d^3p}{E} p^\mu f_i(x, p), \quad (2.3a)$$

$$T^{\mu\nu} = \sum_i \int \frac{d^3p}{E} p^\mu p^\nu f_i(x, p). \quad (2.3b)$$

Here n_i are the baryon charges per particle of species i (particles and anti-particles count as separate species). Plugging in the equilibrium distribution function $f_{i, eq}(x, p) = \frac{1}{e^{[p \cdot u(x) + \mu_i(x)]/T(x)} \pm 1}$ (where $\mu_i(x)$ and $T(x)$ are the local chemical potential of particle species i and the temperature, respectively) into eq.(2.3), one directly obtains the ideal fluid decomposition (2.2). Local thermal equilibrium is thus the basic assumption behind ideal hydrodynamics. In kinetic theory, it requires that the microscopic mean free path is much smaller than the system size and the microscopic collision time scale is much shorter than the macroscopic evolution time scale. The concept of local thermal equilibrium is, however, more general and can be formulated without recourse to kinetic theory. Ideal fluid dynamics always applies if local thermal equilibrium is ensured.

If microscopic processes are not fast enough to satisfy the above conditions, the system is no longer in local equilibrium. For a near-equilibrium system, the distribution function can be decomposed into an equilibrium part plus a small deviation:

$$f(x, p) = f_{eq}(x, p) + \delta f(x, p), \quad (\delta f \ll f) \quad (2.4)$$

Putting eq. (2.4) into eq. (2.3) one finds

$$N^\mu = N_{eq}^\mu + \delta N^\mu, \quad (2.5a)$$

$$T^{\mu\nu} = T_{eq}^{\mu\nu} + \delta T^{\mu\nu}, \quad (2.5b)$$

where the dissipative flows δN^μ and $\delta T^{\mu\nu}$ are generated by the non-equilibrium contribution δf . By imposing the ‘‘Landau matching conditions’’ [200] for an arbitrary frame u^μ : $u_\mu \delta N^\mu = 0$ and $u_\mu \delta T^{\mu\nu} u_\nu = 0$, one associates N_{eq}^μ and $T_{eq}^{\mu\nu}$ with the equilibrium definitions of net baryon density n and energy density e and pressure p ($n = N^\mu u_\mu$, $e = u_\nu T^{\mu\nu} u_\mu$). In other words, these matching conditions fix the temperature and chemical potential of the equilibrium distribution f_{eq} in (2.4) such that e and n are defined in terms of f_{eq} in the standard way. Then N^μ , $T^{\mu\nu}$ can be fully decomposed as [209]:

$$N^\mu = nu^\mu + V^\mu, \quad (2.6a)$$

$$T^{\mu\nu} = eu^\mu u^\nu - p\Delta^{\mu\nu} - \Pi\Delta^{\mu\nu} + \pi^{\mu\nu} + W^\mu u^\nu + W^\nu u^\mu, \quad (2.6b)$$

where V^μ , Π , $\pi^{\mu\nu}$ and W^μ are called dissipative or viscous flows. More specifically, $V^\mu = \Delta^{\mu\nu} N_\nu$ describes a baryon flow in the local rest frame, and $W^\mu = \Delta^{\mu\nu} T_{\nu\alpha} u^\alpha \equiv \frac{e+p}{n} V^\mu + q^\mu$ (where q^μ is the ‘‘heat flow vector’’) describes an energy flow in the local rest frame. W^μ , V^μ and q^μ are all transverse to the frame u^μ : $W^\mu u_\mu = 0$, $V^\mu u_\mu = 0$ and $q^\mu u_\mu = 0$, so each of them has 3 independent components. Since q^μ is defined through V^μ and W^μ , the 3 vectors leave 6 independent components altogether. $\Pi = -\frac{1}{3}\Delta_{\mu\nu} T^{\mu\nu} - p$ is the viscous bulk pressure, which contributes to the trace of energy momentum tensor. $\pi^{\mu\nu} = T^{\langle\mu\nu\rangle} \equiv [\frac{1}{2}(\Delta^{\mu\sigma}\Delta^{\nu\tau} + \Delta^{\nu\sigma}\Delta^{\mu\tau}) - \frac{1}{3}\Delta^{\mu\nu}\Delta^{\sigma\tau}]T_{\tau\sigma}$ (where the expression $\langle\mu\nu\rangle$ is the shorthand for traceless and transverse to u_μ and u_ν as defined by the projector in square brackets) is called the shear stress tensor. $\pi^{\mu\nu}$ is traceless

and transverse to u^ν , $\pi_\mu^\mu = 0$ and $\pi^{\mu\nu}u_\nu = 0$, and it is symmetric (like $T^{\mu\nu}$); it thus has 5 independent components.

The Landau matching conditions, however, leave the choice of frame u^μ unconstrained. Two commonly used frames are the Eckart frame [199] and the Landau frame [200]. The Eckart frame sets u^μ parallel to the charge flow N^μ . As a consequence, V^μ disappears and the energy flow vector reduces to the heat flow vector $W^\mu = q^\mu$. However, for a system with very small or vanishing net baryon number, which is approximately realized in nuclear collisions at top RHIC energy, this frame is ill defined [211]. Therefore, this thesis and other theoretical viscous hydrodynamics frameworks aimed at RHIC physics [195, 196, 197, 124, 212, 213] adopt the second choice – the Landau frame. In the Landau frame, u^μ is taken parallel to the 4-velocity of energy flow ($\propto T^{\mu\nu}u_\nu$), which leads to a zero value for W^μ . Then the tensor decomposition shown in eq. (2.6) simplifies as follows:

$$N^\mu = nu^\mu - \frac{n}{e+p}q^\mu, \quad (2.7a)$$

$$T^{\mu\nu} = eu^\mu u^\nu - (p + \Pi)\Delta^{\mu\nu} + \pi^{\mu\nu}. \quad (2.7b)$$

For the full evolution of all components of $T^{\mu\nu}$ and N^μ , we need in addition to the 5 conservation law equations (2.1) additional equations for q^μ , Π and $\pi^{\mu\nu}$.

2.2 Navier-Stokes formalism

The Navier-Stokes (N-S) formalism comes from the relativistic generalization of the non-relativistic N-S equations, which impose linear relationships between the dissipative flows and the corresponding thermodynamic forces [199, 200]:

$$q^\nu = -\lambda \frac{nT^2}{e+p} \nabla^\nu \left(\frac{\nu}{T} \right) \equiv \lambda X^\nu, \quad (2.8a)$$

$$\Pi = -\zeta\theta \equiv \zeta X, \quad (2.8b)$$

$$\pi^{\mu\nu} = 2\eta \nabla^{\langle\mu} u^{\nu\rangle} \equiv 2\eta X^{\mu\nu}. \quad (2.8c)$$

The (positive) “transport” coefficients ζ , λ and η are the bulk viscosity, heat conductivity and shear viscosity, respectively. The scalar, vector and tensor thermodynamical forces on the right hand side are explicitly given by $X \equiv -\theta = -\partial \cdot u$, $X^\nu \equiv \frac{\nabla^\nu}{T} - \dot{u}^\nu = -\frac{nT}{e+p} \nabla^\nu \frac{\mu}{T}$ and $X^{\mu\nu} \equiv \nabla^{\langle\mu} u^{\nu\rangle} = \sigma^{\mu\nu} = \frac{1}{2}(\nabla^\mu u^\nu + \nabla^\nu u^\mu) - \frac{1}{3}\Delta^{\mu\nu} \partial_\alpha u^\alpha$.

Unfortunately the N-S equations violate causality [214, 215, 216] and lead to infinite speed of signal propagation: if the thermodynamic forces turn off suddenly, the dissipative flows will also disappear instantaneously. This conflicts with the fact that a macroscopic process caused by microscopic scattering is delayed by a relaxation time comparable to the kinetic scattering time scale. Connected with the acausality problem in the N-S formalism are numerical instabilities [214, 215, 216], which render it useless for numerical simulations. Both of these two problems are avoided in the 2nd order formalism which is introduced in the following sections.

2.3 Israel-Stewart formalism from the 2nd law of thermodynamics

The 2nd order formalism for relativistic dissipative fluids was first obtained by Israel and Stewart in the late 1970’s, generalizing earlier non-relativistic work by I. Müller [217]. They gave two derivations, a macroscopic one based on the 2nd law of thermodynamics, derived by expanding the entropy current up to the 2nd order in deviations from local equilibrium, and a microscopic one based on a near-equilibrium expansion of the Boltzmann equation. Detailed presentations can be found in the original articles of Israel

and Stewart [201, 202] and in recent articles by Muronga [195, 196, 197, 212, 213], who first brought this work to the attention of the RHIC community.

In a relativistic equilibrium system, the entropy current is written as:

$$S_{eq}^\mu = p(\alpha, \beta)\beta^\mu - \alpha N_{eq}^\mu + \beta_\nu T_{eq}^{\mu\nu}, \quad (2.9)$$

where α and β are related to the local temperature T and chemical potential μ by $\alpha = \frac{\mu}{T}$, $\beta = \frac{1}{T}$. For a near-equilibrium system, one can generalize the entropy current by the following off-equilibrium expansion:

$$S^\mu = p(\alpha, \beta)\beta^\mu - \alpha(N_{eq}^\mu + \delta N^\mu) + \beta_\nu(T_{eq}^{\mu\nu} + \delta T^{\mu\nu}) + Q^\mu(\delta N^\mu, \delta T^{\mu\nu}), \quad (2.10)$$

where, in addition to the first order corrections δN^μ and $\delta T^{\mu\nu}$ appearing in the middle terms, the last term Q^μ includes second and higher order corrections in terms of δN^μ and $\delta T^{\mu\nu}$. After some algebra, the entropy production rate can be written as:

$$\partial_\mu S^\mu = \delta N^\mu \partial_\mu \alpha + \delta T^{\mu\nu} \partial_\mu \beta_\nu + \partial_\mu Q^\mu. \quad (2.11)$$

After rewriting δN^μ and $\delta T^{\mu\nu}$ in terms of the corresponding dissipative flows Π , q^μ and $\pi^{\mu\nu}$, expressing $\partial_\mu \alpha$ and $\partial_\mu \beta_\nu$ through the thermodynamics forces X^μ and $X^{\mu\nu}$ defined in eq. (2.8), this can be further recast into:

$$T \partial_\mu S^\mu = \Pi X - q^\mu X_\mu + \pi^{\mu\nu} X_{\mu\nu} + T \partial_\mu Q^\mu \geq 0. \quad (2.12)$$

The inequality on the right implements the 2nd law of thermodynamics $\partial \cdot S \geq 0$. Note that the first three terms on the r.h.s. are first order, while the last term is higher order in the dissipative flows.

The first order theory [199, 200] neglects the second order and higher order contributions and sets $Q^\mu = 0$. By postulating linear relationships between the dissipative flows and the thermodynamic forces with non-negative coefficients described by the N-S equations (2.8), the inequality $\partial \cdot S \geq 0$ is automatically satisfied:

$$T \partial_\mu S^\mu = \frac{\Pi^2}{\zeta} - \frac{q_\mu q^\mu}{2\lambda T} + \frac{\pi_{\mu\nu} \pi^{\mu\nu}}{2\eta} \geq 0. \quad (2.13)$$

Note that, since $u^\mu q_\mu = 0$, q_μ is space-like, $q^\mu q_\mu < 0$. The N-S equations thus corresponds to a 1st order expansion of the entropy current, which is why the Navier-Stokes formalism is known as 1st order viscous hydrodynamics.

The 2nd order theory of Israel and Stewart [201, 202, 195, 196] keeps Q^μ , more precisely, it keeps all terms that are second order in the dissipative flows:

$$Q^\mu = -(\beta_0 \Pi^2 - \beta_1 q^\mu q_\mu + \beta_2 \pi_{\mu\nu} \pi^{\mu\nu}) \frac{u^\mu}{2T} - \frac{\alpha_0 \Pi q^\mu}{T} + \frac{\alpha_1 \pi^{\mu\nu} q_\nu}{T}, \quad (2.14)$$

where $\beta_0, \beta_1, \beta_2$ and α_0, α_1 are phenomenological expansion coefficients. After a bit of algebra, the entropy production rate $T \partial \cdot S$ is now written as [196, 197]

$$\begin{aligned} T \partial_\mu S^\mu &= -\Pi \left[\theta + \beta_0 \dot{\Pi} + \frac{1}{2} T \partial_\mu \left(\frac{\beta_0}{T} u^\mu \right) \Pi - \alpha_0 \nabla_\mu q^\mu \right] \\ &\quad - q^\mu \left[\nabla_\mu \ln T - \dot{u}_\mu - \beta_1 \dot{q}_\mu - \frac{1}{2} T \partial_\nu \left(\frac{\beta_1}{T} u^\nu \right) q_\mu - \alpha_0 \nabla_\nu \pi_\mu^\nu - \alpha_1 \nabla_\mu \Pi \right] \\ &\quad + \pi^{\mu\nu} \left[\sigma_{\mu\nu} - \beta_2 \dot{\pi}_{\mu\nu} + \frac{1}{2} T \partial_\lambda \left(\frac{\beta_2}{T} u^\lambda \right) \pi_{\mu\nu} + \alpha_1 \nabla_{\langle \nu} q_{\mu \rangle} \right]. \end{aligned} \quad (2.15)$$

Again, one can ensure the second law of thermodynamics by writing $T\partial_\mu S^\mu$ in the form of eq. (2.13). This leads to the following 2nd order viscous equations for the dissipative flows:

$$\dot{\Pi} = -\frac{1}{\tau_\Pi} \left[\Pi + \zeta\theta - l_{\Pi q} \nabla_\mu q^\mu + \Pi \zeta T \partial_\mu \left(\frac{\tau_\Pi u^\mu}{2\zeta T} \right) \right], \quad (2.16a)$$

$$\Delta_\nu^\mu \dot{q}^\nu = -\frac{1}{\tau_q} \left[q_\mu + \lambda \frac{nT^2}{e+p} \nabla^\mu \frac{\nu}{T} + l_{q\pi} \nabla_\nu \pi^{\mu\nu} + l_{q\Pi} \nabla^\mu \Pi - \lambda T^2 q^\mu \partial_\mu \left(\frac{\tau_q u^\mu}{2\lambda T^2} \right) \right], \quad (2.16b)$$

$$\Delta^{\mu\alpha} \Delta^{\nu\beta} \dot{\pi}_{\alpha\beta} = -\frac{1}{\tau_\pi} \left[\pi^{\mu\nu} - 2\eta \nabla^{\langle\mu} u^{\nu\rangle} - l_{\pi q} \nabla^{\langle\mu} q^{\nu\rangle} + \pi_{\mu\nu} \eta T \partial_\alpha \left(\frac{\tau_\pi u^\alpha}{2\eta T} \right) \right], \quad (2.16c)$$

where β_0 , β_1 and β_2 have been replaced by the relaxation times $\tau_\Pi \equiv \zeta\beta_0$, $\tau_q \equiv \lambda T\beta_1$ and $\tau_\pi \equiv 2\eta\beta_2$, respectively, and the mixing coefficients α_0 , α_1 have also been rewritten into $l_{\Pi q} = \zeta\alpha_0$, $l_{q\Pi} = \lambda T\alpha_0$, $l_{q\pi} = \lambda T\alpha_1$ and $l_{\pi q} = 2\eta\alpha_1$. The relaxation times replace the instantaneous identification between dissipative flows and thermodynamics forces in the N-S equations. They ensure the causality of the theory and the numerical stability [214, 218] as long as they are not too small [218]. The viscous hydrodynamics based on the I-S formalism is thus also known as *causal viscous hydrodynamics*¹⁶.

In this phenomenological approach, both the viscous coefficients and the corresponding relaxation times are arbitrary free parameters, which must be determined from other theoretical consideration or extracted from experimental data.

2.4 Israel-Stewart formalism from kinetic theory

The kinetic theory approach starts from a Taylor expansion of the distribution function f around its local equilibrium form:

$$f = f_0 [1 + (1 \pm f_0)\delta f], \quad \delta f \ll 1, \quad (2.17)$$

$$\text{with,} \quad \delta f(\mathbf{x}, t, \mathbf{p}) = \epsilon(\mathbf{x}, t) + \epsilon_\lambda(\mathbf{x}, t)p^\lambda + \epsilon_{\lambda\nu}(\mathbf{x}, t)p^\lambda p^\nu + O(p^3).$$

Note that the scalar, vector and tensor coefficients ϵ , ϵ_λ , $\epsilon_{\lambda\nu}$ are functions of space-time, which, through kinetic theory, can be related to the dissipative flows. After putting eq. (2.17) into the kinetic definition (2.3) of $T^{\mu\nu}$ and integrating out the momentum degrees of freedoms, one finds that specific combinations of ϵ , ϵ_λ , $\epsilon_{\lambda\nu}$ correspond to bulk pressure Π , heat flow q_λ and shear stress tensor $\pi_{\lambda\nu}$. For simplicity, we consider a fluid with only shear viscosity, neglecting bulk viscosity and heat conductivity, which simplifies the expansion of δf as

$$\delta f(\mathbf{x}, t, \mathbf{p}) = \epsilon_{\lambda\nu}(\mathbf{x}, t)p^\lambda p^\nu, \quad (2.18)$$

with $\epsilon_{\lambda\nu}$ being traceless. Then, the shear stress tensor $\pi^{\mu\nu}$ is directly related to $\epsilon^{\mu\nu}$ after integrating out the momentum degrees of freedom in eq. (2.3). For a massless Boltzmann gas $f_0 = \exp(-p_\mu u^\mu/T)$, one finds [131]

$$\epsilon^{\mu\nu} = \frac{1}{2T^2(e+p)} \pi^{\mu\nu}, \quad (2.19)$$

with small quantum statistical corrections for fermions or bosons [137].

In the kinetic theory approach, the macroscopic conservation laws $\partial_\mu N^\mu = 0$ and $\partial_\mu T^{\mu\nu} = 0$ and the 2nd order I-S equations can be obtained from the Boltzmann equation $p^\mu d_\mu f(\mathbf{x}, t, \mathbf{p}) = \mathcal{C}(x)$ after integrating

¹⁶The projectors $\Delta^{\mu\nu}$ on the r.h.s. of (2.16 b, c) ensure that the transversality to the flow u^μ of q_μ and $\pi_{\mu\nu}$ is preserved during the time evolution.

out the momentum degrees of freedom, $\int d\omega \equiv \int \frac{d^3 p}{(2\pi)^3 p_0}$, with different combinations of momentum p^μ as weighting:

$$\int d\omega p^\mu \partial_\mu f = \int d\omega \mathcal{C}, \quad (2.20)$$

$$\int d\omega p^\mu p^\alpha \partial_\mu f = \int d\omega p^\alpha \mathcal{C}, \quad (2.21)$$

$$\int d\omega p^\mu p^\alpha p^\beta \partial_\mu f = \int d\omega p^\alpha p^\beta \mathcal{C}. \quad (2.22)$$

Here $\mathcal{C}(x)$ is the collision term whose precise form is related to the interaction matrix elements between particles. For a theory with conserved charges and with interactions that conserve energy and momentum: $\int d\omega \mathcal{C} = 0$ and $\int d\omega p^\alpha \mathcal{C} = 0$. Eqs. (2.20, 2.21) then lead to $\partial_\mu N^\mu = 0$ and $\partial_\mu T^{\mu\nu} = 0$, respectively. After employing the relaxation time approximation for the collision term:

$$\mathcal{C} = -p_\mu u^\mu \frac{f - f_0}{\tau_\pi}. \quad (2.23)$$

and integrating out $\int d\omega$ in eq. (2.22) one finds the 2nd order I-S equations [131, 204]:

$$\pi^{\mu\nu} + \tau_\pi \left[\Delta_\alpha^\mu \Delta_\beta^\nu D\pi^{\alpha\beta} + \frac{4}{3} \pi^{\mu\nu} \nabla_\alpha u^\alpha - 2\pi^{\phi(\mu} \Omega^{\nu)}_\phi + \frac{\pi^{\phi(\mu} \pi^{\nu)}}{2\eta} \right] = \eta \nabla^{\langle\mu} u^{\nu\rangle}, \quad (2.24)$$

where $\Omega_{\mu\nu}$ is the vorticity tensor, $\Omega_{\mu\nu} = \Delta_\mu^\alpha \Delta_\nu^\beta \partial_{[\beta} u_{\alpha]}$. In contrast to the macroscopic approach of Chap. 2.3, the relaxation time τ_π and shear viscosity η here are no longer independent from each other. One finds $\tau_\pi = \frac{6\eta}{sT}$ for a massless Boltzmann gas, $\tau_\pi = \frac{6\eta}{4p} = \frac{(3+\frac{T}{s})\frac{4\eta}{sT}}{sT}\eta$ for a massive Boltzmann gas, and $\tau_\pi \simeq 1.024 \frac{6\eta}{sT}$ for a massless Bose-Einstein gas [131]. Actually, the shear viscosity η can also be self-consistently calculated in the kinetic theory approach, after explicitly writing out the collision term. For purely gluonic matter, where interactions are dominated by $2 \rightarrow 2$ scattering processes with HTL cross sections, one finds: $\eta = \frac{960}{\pi^7} \zeta^2(5) T^3 \frac{(4\pi)^2}{g^4 \ln(4\pi/g^2)}$ [131].

Based on consistent expansions to the 2nd order in Knudsen number¹⁷, Betz, Henkel and Rischke [203] deduced the complete set of I-S equations from the Boltzmann equation for the bulk pressure Π , shear stress tensor $\pi^{\mu\nu}$ and heat flow vector q^μ via Grad's 14-Momentum method [219]:

$$\begin{aligned} \Pi &= \Pi_{\text{NS}} - \tau_\Pi \dot{\Pi} \\ &+ \tau_{\Pi q} q \cdot \dot{u} - \ell_{\Pi q} \partial \cdot q - \zeta \hat{\delta}_0 \Pi \theta \\ &+ \lambda_{\Pi q} q \cdot \nabla \alpha + \lambda_{\Pi\pi} \pi^{\mu\nu} \sigma_{\mu\nu}, \end{aligned} \quad (2.25a)$$

$$\begin{aligned} q^\mu &= q_{\text{NS}}^\mu - \tau_q \Delta^{\mu\nu} \dot{q}_\nu \\ &- \tau_{q\Pi} \Pi \dot{u}^\mu - \tau_{q\pi} \pi^{\mu\nu} \dot{u}_\nu + \ell_{q\Pi} \nabla^\mu \Pi - \ell_{q\pi} \Delta^{\mu\nu} \partial^\lambda \pi_{\nu\lambda} + \tau_q \Omega^{\mu\nu} q_\nu - \frac{\kappa}{\beta} \hat{\delta}_1 q^\mu \theta \\ &- \lambda_{qq} \sigma^{\mu\nu} q_\nu + \lambda_{q\Pi} \Pi \nabla^\mu \alpha + \lambda_{q\pi} \pi^{\mu\nu} \nabla_\nu \alpha, \end{aligned} \quad (2.25b)$$

$$\begin{aligned} \pi^{\mu\nu} &= \pi_{\text{NS}}^{\mu\nu} - \tau_\pi \dot{\pi}^{\langle\mu\nu\rangle} \\ &+ 2\tau_{\pi q} q^{\langle\mu} \dot{u}^{\nu\rangle} + 2\ell_{\pi q} \nabla^{\langle\mu} q^{\nu\rangle} + 2\tau_\pi \pi_\lambda^{\langle\mu} \Omega^{\nu\rangle\lambda} - 2\eta \hat{\delta}_2 \pi^{\mu\nu} \theta \\ &- 2\tau_\pi \pi_\lambda^{\langle\mu} \sigma^{\nu\rangle\lambda} - 2\lambda_{\pi q} q^{\langle\mu} \nabla^{\nu\rangle} \alpha + 2\lambda_{\pi\Pi} \Pi \sigma^{\mu\nu}. \end{aligned} \quad (2.25c)$$

They found that the form of the I-S equations is independent of the choice of frame (Eckart frame vs. Landau frame), whereas the coefficients τ_Π , τ_q , τ_π , $\tau_{\Pi q}$, $\tau_{q\Pi}$, $\tau_{q\pi}$ etc. are frame dependent and are complicated

¹⁷Knudsen number is defined as microscopic mean free path over macroscopic scale of hydrodynamics, $K \equiv l_{mf}/L_{hydro}$.

functions of temperature and chemical potential. The first terms on r.h.s of each equation, corresponding to the Navier-Stokes first order approximation in Chap.2.2, are of first order in the Knudsen number. All other term on r.h.s are of second order in the Knudsen number. Compared with eq. (2.16) from the macroscopic approach, the Knudsen number expansion yields more terms for the 2nd order viscous equations. Some of these terms do not contribute to entropy production and thus can not manifest themselves in the 2nd law of thermodynamics; some others are suspected to correspond to higher order corrections in the entropy expansion approach [203].

2.5 Israel-Stewart formalism from conformal symmetry constraints

For conformally invariant theories, the action $S[\phi, g^{\mu\nu}]$, as a functional of the external metric $g^{\mu\nu}$, is invariant under Weyl transformations: $g_{\mu\nu} \rightarrow e^{-2\omega} g_{\mu\nu}$. As a consequence, the energy momentum tensor $T^{\mu\nu}$ is traceless and transforms as $T^{\mu\nu} \rightarrow e^{6\omega} T^{\mu\nu}$ under Weyl rescaling in 4 dimensions. Correspondingly, the shear stress tensor also transforms as

$$\pi^{\mu\nu} \rightarrow e^{6\omega} \pi^{\mu\nu}. \quad (2.26)$$

The above Weyl rescaling for the shear stress tensor $\pi^{\mu\nu}$ gives a constraint for the possible form of the viscous equations for $\pi^{\mu\nu}$, if one assumes that the conformal invariance is preserved throughout the evolution of the system [204]. It is easy to prove that the 1st order N-S equation $\pi^{\mu\nu} = 2\eta \nabla^{\langle\mu} u^{\nu\rangle}$ naturally satisfies this constraint, since the shear viscosity and velocity tensor transform as $\eta \rightarrow e^{3\omega} \eta$ and $\nabla^{\langle\mu} u^{\nu\rangle} \rightarrow e^{3\omega} \nabla^{\langle\mu} u^{\nu\rangle}$, respectively.

The 2nd order viscous equations can be generalized from the 1st order one by adding 2nd order corrections: $\pi^{\mu\nu} = 2\eta \nabla^{\langle\mu} u^{\nu\rangle} + (2\text{nd order corrections})$, satisfying the conformal constraint (2.26) and the transversality and tracelessness properties: $\pi^{\mu\nu} u_\mu = 0$ and $\pi^\mu_\mu = 0$ [204]. The last two constraints allow for 8 possible 2nd order corrections [204]:

$$\begin{aligned} & D^{\langle\mu} \ln \epsilon D^{\nu\rangle} \ln \epsilon, \quad D^{\langle\mu} D^{\nu\rangle} \ln \epsilon, \quad \nabla^{\langle\mu} u^{\nu\rangle} (\nabla_\alpha u^\alpha), \quad P^{\mu\nu}_{\alpha\beta} \nabla^{\langle\alpha} u^{\gamma\rangle} g_{\gamma\delta} \nabla^{\delta} u^{\beta\rangle} \\ & P^{\mu\nu}_{\alpha\beta} \nabla^{\langle\alpha} u^{\gamma\rangle} g_{\gamma\delta} \Omega^{\beta\delta}, \quad P^{\mu\nu}_{\alpha\beta} \Omega^{\alpha\gamma} g_{\gamma\delta} \Omega^{\beta\delta}, \quad u_\gamma R^{\gamma\langle\mu\nu\rangle\delta} u_\delta, \quad R^{\langle\mu\nu\rangle}, \end{aligned} \quad (2.27)$$

where $R^{\alpha\mu\nu\beta}$ is the Riemann tensor and $R^{\mu\nu}$ is the Ricci tensor. However, only 5 combinations of the above terms transform homogeneously under Weyl transformation. This determines the form of the 2nd order viscous equations, leaving 5 independent coefficients [204]:

$$\begin{aligned} \pi^{\mu\nu} = & 2\eta \nabla^{\langle\mu} u^{\nu\rangle} - \tau_\pi \left[\Delta_\alpha^\mu \Delta_\beta^\nu D \pi^{\alpha\beta} + \frac{4}{3} \pi^{\mu\nu} (\nabla_\alpha u^\alpha) \right] \\ & + \frac{\kappa}{2} \left[R^{\langle\mu\nu\rangle} + 2u_\alpha R^{\alpha\langle\mu\nu\rangle\beta} u_\beta \right] \\ & - \frac{\lambda_1}{2\eta^2} \pi^{\langle\mu}{}_\lambda \pi^{\nu\rangle\lambda} - \frac{\lambda_2}{2\eta} \pi^{\langle\mu}{}_\lambda \Omega^{\nu\rangle\lambda} - \frac{\lambda_3}{2} \Omega^{\langle\mu}{}_\lambda \Omega^{\nu\rangle\lambda}. \end{aligned} \quad (2.28)$$

Note that the κ term is related to curved spaces and vanishes in flat space. The conformal symmetry constraint requires that $\Delta_\alpha^\mu \Delta_\beta^\nu D \pi^{\alpha\beta}$ must combine with the term $\frac{4}{3} \pi^{\mu\nu} (\nabla_\alpha u^\alpha)$ such that the additional derivatives of the function $\omega(x)$ in the Weyl transformation cancel between the two terms. The term $\frac{4}{3} \pi^{\mu\nu} (\nabla_\alpha u^\alpha)$ term can be written in different ways as discussed in Chap. 2.7 below.

While the conformal symmetry constraint approach provides the general form of the 2nd order viscous equations, it does not give the 2nd order coefficients τ_π , κ , λ_1 , λ_2 and λ_3 . They must be determined through explicit calculation. Such calculations were performed for weakly coupled QCD by York and Moore [159] and for strongly coupled N=4 SYM theory in [204]. Table 2.1 summarizes the results. It is reasonable to assume that the strong and weak coupling results bracket the value for these coefficients in QCD at realistic values for the coupling strength.

Approaches	τ_π	λ_1	λ_2	λ_3	κ
1) N=4 SYM	$\frac{2-\ln 2}{2\pi T}$	$\frac{\eta}{2\pi T}$	$-\ln 2\frac{\eta}{\pi T}$	0	$\frac{\eta}{\pi T}$
2) Kinetic theory	$\frac{5.0\dots 5.9}{T} \frac{\eta}{s}$	$\frac{4.1\dots 5.2}{T} \frac{\eta^2}{s}$	$-2\eta\tau_\pi$	0	$\mathcal{O}(g^{-4})T^2$

Table 2.1: 2nd order Israel-Stewart Coefficients in the strong coupling [204] and weakly coupling [159] limits.

2.6 Öttinger-Grmela formalism

The I-S formalism discussed in Chap 2.3-2.5 directly deals with the dissipative flows ($\pi^{\mu\nu}$, Π and q^μ) and their viscous equations. In contrast, the Öttinger-Grmela formalism starts with an auxiliary field $c^{\mu\nu}$ and its evolution equation (O-G equation). The details for the Öttinger-Grmela formalism can be found in [205, 206, 207]. In numerical implementation, one solves the O-G equation first and then relates the auxiliary field $c_{\mu\nu}$ to the commonly used dissipative flows in the subsequent spectra calculations [137].

If taking the O-G equation and directly replacing the auxiliary field $c^{\mu\nu}$ by the dissipative flows, one obtains an effective I-S equation in the Öttinger-Grmela approach. For vanishing bulk viscosity and heat conductivity, the effective I-S equations for shear stress tensor $\pi^{\mu\nu}$ was deduced by Dusling and Teaney, and has the following form [208, 220, 221]:

$$\begin{aligned} \pi^{\mu\nu} = & 2\eta\nabla^{\langle\mu}u^{\nu\rangle} - \tau_\pi \left[\Delta_\alpha^\mu \Delta_\beta^\nu D\pi^{\alpha\beta} + \left[\frac{4}{3} + \frac{2}{3} - \frac{2\beta}{\alpha} \right] \pi^{\mu\nu} (\nabla_\alpha u^\alpha) \right] \\ & - \frac{\tau_\pi}{\eta} \pi^{\langle\mu}{}_\lambda \pi^{\nu\rangle\lambda} - \tau_\pi \pi^{\langle\mu}{}_\lambda \Omega^{\nu\rangle\lambda}, \end{aligned} \quad (2.29)$$

Where, the third order and higher order terms have been dropped. α and β are free parameters here. Generally, one uses α to fix the relaxation time $\tau_\pi = \eta/p\alpha$ and sets $\beta = \alpha/3$ to ensure conformal invariance (see eq. (2.28)).

2.7 Final comments on the state of the formalism

Comparing the 2nd order equations (2.16c), (2.24), (2.25c), (2.28) and (2.29) superficially, one finds as the common terms that are obtained in all of the different approaches only the following:

$$\Delta^{\mu\alpha} \Delta^{\nu\beta} D\pi_{\alpha\beta} = -\frac{1}{\tau_\pi} \left[\pi^{\mu\nu} - 2\eta\nabla^{\langle\mu}u^{\nu\rangle} \right]. \quad (2.30)$$

This so-called *simplified I-S equation*, was used in our early calculations [125, 126] and in Chaudhuri's work [142, 143, 144]. However this equation does not preserve the conformal symmetry for a conformal fluid (i.e. a fluid that consists of massless degrees of freedom). To fix this problem one needs to add an additional term $\frac{4}{3}\tau_\pi\pi^{\mu\nu}(\nabla_\alpha u^\alpha)$ as pointed out in Ref [204]:

$$\Delta^{\mu\alpha} \Delta^{\nu\beta} D\pi_{\alpha\beta} = -\frac{1}{\tau_\pi} \left[\pi^{\mu\nu} - 2\eta\nabla^{\langle\mu}u^{\nu\rangle} + \frac{4}{3}\tau_\pi\pi^{\mu\nu}(\nabla_\alpha u^\alpha) \right]. \quad (2.31)$$

In Ref. [127] we called this equation the *full I-S equation*. The last term in eq. (2.31) is clearly illustrated in Eqs. (2.24), (2.28) and (2.29)¹⁸. At first sight, eq.(2.16c) seems to miss this term, but this naive impression is incorrect. For a conformally symmetric fluid, the temperature T is the only scale in the problem and

¹⁸Eq.(2.25) also contains a term of $\pi^{\mu\nu}\theta = \pi^{\mu\nu}(\nabla_\alpha u^\alpha)$, but leaves an undetermined coefficient in front of it.

therefore $\eta \sim s \sim T^3$ and $\tau_\pi \sim 1/T$, hence $\eta T/\tau_\pi \sim T^5$. In this limit, The last term in eq. (2.16c) can then be rewritten as:

$$-\frac{1}{2}\pi^{\mu\nu}\frac{\eta T}{\tau_\pi}d_\lambda\left(\frac{\tau_\pi}{\eta T}u^\lambda\right)=\frac{1}{2}\pi^{\mu\nu}(5D(\ln T)-\theta)=-\frac{4}{3}\pi^{\mu\nu}(\nabla_\alpha u^\alpha). \quad (2.32)$$

The last equality follows from the 2nd order hydrodynamic equation [134], showing that, up to terms of sub-leading order, the last terms in eq. (2.16c) and eq. (2.31) agree.

The “full I-S” equation, with slight variations, such as using the replacement eq. (2.32), has been established as the standard viscous equation for numerical implementations [127, 130, 134, 135, 136, 141]. It has received additional support by the observation made in [127] that it appears to minimize the dependence of the hydrodynamic evolution on the value of the microscopic relaxation time τ_π . While the variations related to the use of eq. (2.32) are equivalent for conformal systems, they differ in principle for systems with an EOS that breaks conformal invariance, e.g. through a phase transition. These differences turn out to be negligible in practice [127]. For a conformal theory with vanishing chemical potentials, 4 other terms can be added to the right hand side of the “full I-S” equation, with additional coefficients λ_1 , λ_2 , λ_3 , and κ ($\kappa = 0$ in Minkowski space), as shown in eq. (2.28) [204]. These terms include couplings to the vorticity tensor [204] which turns out to be small in heavy-ion collisions if the initial longitudinal velocity profile is boost invariant [134]. Even more terms arise in a kinetic theory derivation that does not assume conformal symmetry and includes the effects from bulk viscosity and heat conductivity, as shown by Eqs. (2.16c, 2.25). Their coefficients can be obtained from kinetic theory [203, 159] at weak coupling or from the AdS/CFT correspondence at strong coupling [204](see Table.2.1). The so far accumulated numerical evidence [127, 135] (see Chap. 7.3 and 7.4) suggests that, except for the last terms in Eqs. (2.31), all other second order terms are unimportant in practice, but a systematic study that confirms this beyond doubt remains outstanding.

Chapter 3: Causal Viscous Hydrodynamics in 2+1 Dimensions

Although the Israel-Stewart 2nd order formalism for relativistic dissipative fluid dynamics was established thirty years ago, its numerical implementations for describing relativistic heavy ion collisions started only quite recently [195, 196, 197, 124, 212, 213]. Currently all of the available viscous hydrodynamics codes are restricted to either 1+1 dimensions [131, 132, 133] or 2+1 dimensions [125, 126, 127, 130, 134, 135, 136, 137, 140, 142, 143, 144]. Here the first number indicates the number of spatial dimensions in which the code solves numerically for the evolution of the hydrodynamic fields, and the “+1” stand for time. All existing codes assume longitudinal boost invariance, which allows to treat the longitudinal expansion along the beam direction analytically. This is a good approximation at RHIC and LHC energies for particle production near midrapidity. (1+1)-d codes assume additionally azimuthal symmetry around the beam axis, allowing spatial expansion in the radial direction. With them, we can only simulate heavy ion collisions with zero impact parameter. To describe non-central collisions, and in particular anisotropic (elliptic) flow, requires a (2+1)-d code, which allows for anisotropic expansion in the two dimensions transverse to the beam.

During the past years, the OSU group developed a (2+1)-dimensional viscous hydrodynamic code to describe the space-time evolution of the QGP and subsequent hadronic matter in the two dimensional transverse plane – VISH2+1 (Viscous Israel-Stewart Hydrodynamics in 2+1 dimensions) [125, 126, 127, 130]. In this chapter, we will summarize the crucial ingredients for the numerical calculations. These include the explicit form of the viscous hydrodynamic equations in 2+1 dimensions (Chap. 3.1), the initial conditions (Chap. 3.2), the equation of state (Chap. 3.3) and the freeze-out condition, including the freeze-out procedure and the calculation of spectra (Chap. 3.4). We also discuss the inputs for shear viscosity, bulk viscosity and the relaxation times (Chap. 3.5).

3.1 Viscous hydrodynamic equations in 2+1 dimensions

For ease of numerical implementation, the current viscous hydrodynamic calculations focus on boost-invariant systems, realized by assuming a specific “scaling” velocity profile $v_z = z/t$ along the beam direction. As shown by Bjorken [222], this profile is a solution of the hydrodynamic equations (ideal or viscous) if the initial conditions are independent of the longitudinal reference frame (boost invariance), i.e. do not depend on space-time rapidity η . After implementing the Bjorken approximation, the (3+1)-d viscous hydrodynamics reduces to (2+1)-d viscous hydrodynamics with boost invariance. Currently, all of the existing (2+1)-d viscous hydrodynamic codes [125, 126, 127, 135, 136, 137] also assume zero net baryon density and zero heat conductivity. These conditions are approximately realized in experiments at top RHIC and LHC energies and simplify the implementation further by eliminating the need to solve for the flows of baryon number and heat.

Longitudinally boost-invariant systems are conveniently described in curvilinear coordinates $x^m = (\tau, x, y, \eta)$, where $\tau = \sqrt{t^2 - z^2}$ is the longitudinal proper time, $\eta = \frac{1}{2} \ln\left(\frac{t+z}{t-z}\right)$ is the space-time rapidity, and (x, y) are the usual Cartesian coordinates in the plane transverse to the beam direction z . In this coordinate system, the transport equations for the full energy momentum tensor $T^{\mu\nu}$ are written as [124, 126]:

$$\partial_\tau \tilde{T}^{\tau\tau} + \partial_x (v_x \tilde{T}^{\tau\tau}) + \partial_y (v_y \tilde{T}^{\tau\tau}) = \mathcal{S}^{\tau\tau}, \quad (3.1a)$$

$$\partial_\tau \tilde{T}^{\tau x} + \partial_x (v_x \tilde{T}^{\tau x}) + \partial_y (v_y \tilde{T}^{\tau x}) = \mathcal{S}^{\tau x}, \quad (3.1b)$$

$$\partial_\tau \tilde{T}^{\tau y} + \partial_x (v_x \tilde{T}^{\tau y}) + \partial_y (v_y \tilde{T}^{\tau y}) = \mathcal{S}^{\tau y}. \quad (3.1c)$$

Here $\tilde{T}^{mn} \equiv \tau(T_0^{mn} + \pi^{mn} - \Pi\Delta^{mn})$, $T_0^{mn} = \epsilon u^m u^n - p\Delta^{mn}$ being the ideal fluid contribution, $u^m = (u^\tau, u^x, u^y, 0) = \gamma_\perp(1, v_x, v_y, 0)$ is the flow profile (with $\gamma_\perp = \frac{1}{\sqrt{1-v_x^2-v_y^2}}$), and $g^{mn} = \text{diag}(1, -1, -1, -1/\tau^2)$ is the metric tensor for our coordinate system. The source terms \mathcal{S}^{mn} on the right hand side of Eqs. (3.1) are given explicitly as

$$\begin{aligned} \mathcal{S}^{\tau\tau} = & -(p + \Pi) - \tau^2 \pi^{\eta\eta} - \tau \partial_x (p v_x + \Pi v_x + \pi^{x\tau} - v_x \pi^{\tau\tau}) \\ & - \tau \partial_y (p v_y + \Pi v_y + \pi^{y\tau} - v_y \pi^{\tau\tau}), \end{aligned} \quad (3.2a)$$

$$\mathcal{S}^{\tau x} = -\tau \partial_x (p + \Pi + \pi^{xx} - v_x \pi^{\tau x}) - \tau \partial_y (\pi^{xy} - v_y \pi^{\tau x}), \quad (3.2b)$$

$$\mathcal{S}^{\tau y} = -\tau \partial_x (\pi^{xy} - v_x \pi^{\tau y}) - \tau \partial_y (p + \Pi + \pi^{yy} - v_y \pi^{\tau y}). \quad (3.2c)$$

The transport equations for the shear pressure tensor and bulk pressure in 2+1 dimensions are written as [126, 127]:

$$D\tilde{\pi}^{mn} = -\frac{1}{\tau_\pi}(\tilde{\pi}^{mn} - 2\eta\tilde{\sigma}^{mn}) - (u^m \tilde{\pi}^{nk} + u^n \tilde{\pi}^{mk})Du_k - \frac{1}{2}\tilde{\pi}^{mn}\frac{\eta T}{\tau_\pi}d_k\left(\frac{\tau_\pi}{\eta T}u^k\right), \quad (3.3a)$$

$$D\Pi = -\frac{1}{\tau_\Pi}(\Pi - \zeta\theta) - \frac{1}{2}\Pi\frac{\eta T}{\tau_\Pi}d_k\left(\frac{\tau_\Pi}{\eta T}u^k\right), \quad (3.3b)$$

Here, we have written out the explicit (2+1)-d form for the full ‘‘I-S equations’’ described in Chap. 2.7. The expressions for $\tilde{\sigma}^{mn}$ and $\tilde{\pi}^{mn}$ are found in Eqs. (A.2, A.3) in Appendix A.2.1; they differ from π^{mn} in Eqs. (3.2a-3.2c) and σ^{mn} given in Ref. [124] by a Jacobian τ^2 factor in the $(\eta\eta)$ -component: $\tilde{\pi}^{\eta\eta} = \tau^2 \pi^{\eta\eta}$, $\tilde{\sigma}^{\eta\eta} = \tau^2 \sigma^{\eta\eta}$. This factor arises from the curved metric where the local time derivative $D = u^m d_m$ must be evaluated using covariant derivatives d_m . Since $u^\eta = 0$, no such extra Jacobian terms arise in the derivative Du_k in the first line of Eq. (3.3). In more detail, $D = u^\tau \partial_\tau + u^x \partial_x + u^y \partial_y$, $\theta = \partial \cdot u = \partial_\tau u^\tau + \partial_x u^x + \partial_y u^y + \frac{u^\tau}{\tau}$ and $\sigma^{mn} = \nabla^{(m} u^{n)} = \frac{1}{2}(\nabla^m u^n + \nabla^n u^m) - \frac{1}{3}\Delta^{mn}\theta$ (with $\nabla^m = \Delta^{ml}d_l$).

Even though several components of the symmetric shear pressure tensor π^{mn} are redundant [124] on account of its tracelessness and transversality to the flow velocity u^m , VISH2+1 propagates all 7 non-zero components and uses the tracelessness and transversality conditions as checks of the numerical accuracy [125]. We find them to be satisfied with an accuracy of better than 1 – 2% everywhere except for the fireball edge where the π^{mn} are very small and the error on the transversality and tracelessness constraints can become as large as 5%.

3.2 Initial conditions

The initialization of a hydrodynamic simulation requires a starting time τ_0 and initial profiles for the energy momentum tensor $T^{\tau\tau}$, $T^{\tau x}$ and $T^{\tau y}$, which are given by the initializations for the energy density, velocity and stress stress tensor π^{mn} . Through all of this thesis, we set $\tau_0 = 0.6$ fm/c, following the ‘‘standard’’ thermalization time used in most ideal hydrodynamic simulations [26], and we use zero initial transverse flow velocity. We have not explored the need for rescaling τ_0 when including viscosity; this awaits a careful comparison with the experimental data. The initializations for energy density and π^{mn} profiles are described below.

3.2.1 Initializations for the energy density

Glauber model initialization

A simple Glauber model initialization assumes that the initial energy density in the transverse plane is proportional to the wounded nucleon density [223, 126]:

$$\begin{aligned}
e_0(x, y; b) &= Kn_{\text{WN}}(x, y; b) \\
&= K \left\{ T_A(x + \frac{b}{2}, y) \left[1 - \left(1 - \frac{1 - \sigma T_B(x - \frac{b}{2}, y)}{B} \right)^B \right] \right. \\
&\quad \left. + T_B(x - \frac{b}{2}, y) \left[1 - \left(1 - \frac{1 - \sigma T_A(x + \frac{b}{2}, y)}{A} \right)^A \right] \right\}.
\end{aligned} \tag{3.4}$$

Here σ is the total inelastic nucleon-nucleon cross section for which we take $\sigma = 40$ mb. $T_{A,B}$ is the nuclear thickness function of the incoming nucleus A or B , defined as $T_A(x, y) = \int_{-\infty}^{\infty} dz \rho_A(x, y, z)$; $\rho_A(x, y, z)$ is the nuclear density given by a Woods-Saxon profile: $\rho_A(\mathbf{r}) = \frac{\rho_0}{1 + \exp[(r - R_A)/\xi]}$. We take $R_{\text{Cu}} = 4.2$ fm, $\xi = 0.596$ fm for Cu+Cu collisions and $R_{\text{Au}} = 6.37$ fm, $\xi = 0.56$ fm for Au+Au collisions (these two parameter sets for Au and Cu nuclei correspond to a nuclear density $\rho_0 = 0.17 \text{ fm}^{-3}$). The proportionality constant K does not depend on collision centrality but on collision energy; it fixes the overall scale of the initial energy density and, via the associated entropy, the final hadron multiplicity to which it must be fitted as a function of collision energy. The energy density profile for specific collision energy is therefore normalized by a parameter $e_0(\tau = \tau_0, r = b = 0)$ giving the peak energy density in the center of the fireball for central collisions (impact parameter $b = 0$). For central Au+Au collisions at top RHIC energies, one sets $e_0 \equiv e(0, 0; b=0) = 30 \text{ GeV/fm}^3$ and $\tau_0 = 0.6 \text{ fm/c}$ to reproduce the final multiplicity in ideal hydrodynamic calculations. In the viscous hydrodynamics comparison runs, we use the same initialization as for ideal hydrodynamics. Viscous entropy production then leads to slightly larger final multiplicities than in ideal hydrodynamics. Again, we leave a corresponding retuning of initial conditions to a careful comparison study with experimental data. The Glauber initialization (3.4) does not correctly reproduce the measured centrality dependence of dN_{ch}/dy [224]. To fix this problem, more sophisticated initialization schemes have been developed [224], where one uses a superposition of wounded nucleon and binary collision densities. We also leave this for future data comparisons.

Color glass condensate (CGC) initialization

The CGC initialization based on the Kharzeev-Levin-Nardi (KLN) approach [225, 226] and its more recent fKLN improvement [227] has been applied in earlier ideal hydrodynamic calculations [228, 229, 230] and recently also in viscous hydrodynamic calculations [135, 136]. Details of the CGC initialization can be found in Ref. [227, 228].

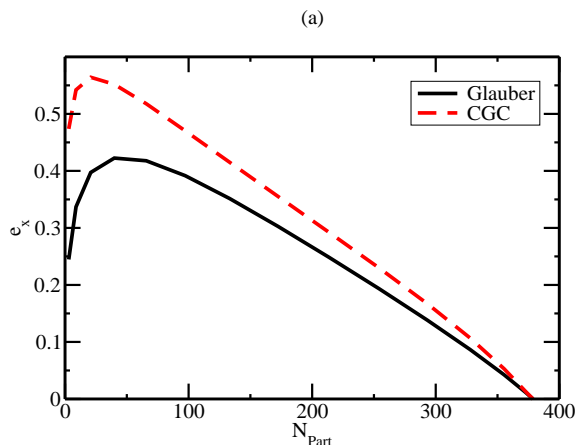


Figure 3.1: The initial eccentricity ε_x from Glauber and CGC initializations, for Au+Au collisions at different centrality [135].

Compared with the Glauber initialization, the CGC initialization gives a more “plateau-like” initial profile for the energy density [230], which leads to larger initial eccentricity $\varepsilon_x = \frac{\langle y^2 - x^2 \rangle}{\langle x^2 + y^2 \rangle}$ than for the Glauber model. Fig.3.1 shows the initial eccentricity ε_x from the Glauber and fKLN initializations [135]. One finds that the CGC initialization predicts 20 – 50% larger initial eccentricity than the Glauber one, especially at small impact parameters, where the eccentricity is small but the discrepancy between models is large [231].

3.2.2 Initializations for π^{mn} and Π

Lacking a microscopic dynamical theory for the early pre-equilibrium stage, initializing the viscous pressure tensor π^{mn} requires some guess-work. We here explore two options: (i) zero initialization, which sets $\pi_0^{mn} = 0$ at initial time τ_0 [134, 125, 126]. (ii)(Navier- Stokes) N-S initialization: $\pi_0^{mn} = 2\eta\sigma_0^{mn}$, where the shear tensor σ_0^{mn} is calculated from the initial velocity profile $u^m = (1, 0, 0, 0)$ [125, 126, 127, 135, 136, 137]. The second option is the default choice for most of the results shown in this thesis. It gives $\tau^2\pi_0^{\eta\eta} = -2\pi_0^{xx} = -2\pi_0^{yy} = -\frac{4\eta}{3\tau_0}$, i.e. a negative contribution to the longitudinal pressure and a positive contribution to the transverse pressure.

3.3 The equation of state (EOS)

The equation of state (EoS), which relates the pressure p to energy density e and net baryon density n_B : $p = p(n_B, e)$ (or equivalently relates it to temperature T and net baryon chemical potential μ_B , $p = p(T, \mu_B)$) is a necessary input for both ideal and viscous hydrodynamic simulations. In this section, we will describe the different EoS used in this thesis [126, 127]. Currently, all of the existing viscous hydrodynamics calculation neglect net baryon density and set $n_B = 0$. The EoS described below thus reduces to a simple one dimensional EOS: $p = p(e)$.

EOS I:

EOS I models a non-interacting gas of massless quarks and gluons, with $p = \frac{1}{3}e$. It has no phase transition. Where needed, the temperature is extracted from the energy density via the relation $e = (16 + \frac{21}{2}N_f) \frac{\pi^2}{30} \frac{T^4}{(\hbar c)^3}$, corresponding to a chemically equilibrated QGP with $N_f = 2.5$ effective massless quark flavors [223].

EOS Q:

EOS Q [223] connects a noninteracting massless QGP gas to a chemically equilibrated hadron resonance gas through a first order phase transition. The EOS in the QGP phase is defined by $p = \frac{1}{3}e - \frac{4}{3}B$ (i.e. $c_s^2 = \frac{\partial p}{\partial e} = \frac{1}{3}$). The vacuum energy (bag constant) $B^{1/4} = 230$ MeV is a parameter that is adjusted to yield a critical temperature $T_c = 164$ MeV. The hadron resonance gas below T_c can be approximately characterized by the relation $p = 0.15 e$ (i.e. $c_s^2 = 0.15$) [223]. The two sides are matched through a Maxwell construction, yielding a relatively large latent heat $\Delta e_{\text{lat}} = 1.15$ GeV/fm³. For energy densities between $e_H = 0.45$ GeV/fm³ and $e_Q = 1.6$ GeV/fm³ one has a mixed phase with constant pressure (i.e. $c_s^2 = 0$).

SM-EOS Q:

SM-EOS Q is a smoothed version of EOS Q [126]. The discontinuous jumps of c_s^2 in EOS Q from a value of 1/3 to 0 at e_Q and back from 0 to 0.15 at e_H generate propagating numerical errors in VISH2+1 which grow with time and cause problems. We avoid these by smoothing the function $c_s^2(e)$ with a Fermi distribution of width $\delta e = 0.1$ GeV/fm³ centered at $e = e_Q$ and another one of width $\delta e = 0.02$ GeV/fm³ centered at $e = e_H$. Both the original EOS Q and our smoothed version SM-EOS Q are shown in Figure 3.2. A comparison of simulations using ideal hydrodynamics with EOS Q and SM-EOS Q is given in Appendix A.3.1. It gives an idea of the magnitude of smoothing effects on the ideal fluid evolution of elliptic flow.

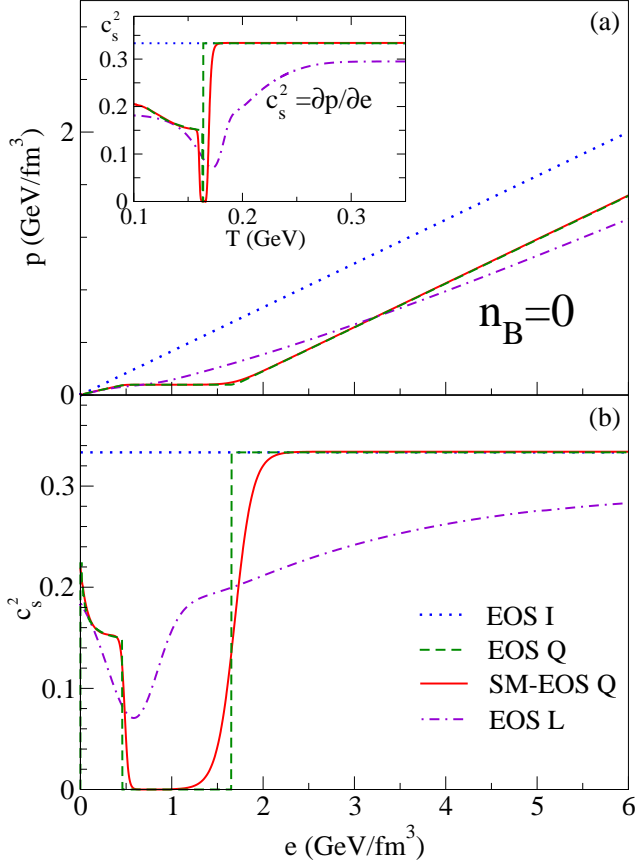


Figure 3.2: The equation of state. Panel (a) shows the pressure p as a function of energy density e and (in the inset) the squared speed of sound $c_s^2 = \frac{\partial p}{\partial e}$ as a function of temperature T , for EOS I, EOS Q, SM-EOS Q and EOS L. Panel (b) shows c_s^2 as a function of energy density e for different EOS.

EOS L:

EOS L [127] matches the hadron resonance gas below T_c smoothly in a rapid cross-over transition to lattice QCD data [232] above T_c . For the fit, the lattice data were plotted in the form $p(e)$, interpolated and then smoothly joined to the $p(e)$ curve of the HRG with a cross-over transition near $T_c \sim 175 \text{ MeV}$. As can be seen in the upper panel of Fig. 3.2 in the inset, our procedure is not fully thermodynamically consistent and leads to a somewhat different temperature dependence of c_s^2 below T_c than for EOS Q and SM-EOS Q. Since this only affects the flow dynamics below our decoupling temperature of $T_{dec} = 130 \text{ MeV}$, we have not put any effort into correcting this¹⁹.

PCE-EOS for the HRG phase:

EOS Q assumes that chemical and thermal freeze-out happen at the same temperature $T_{th} \sim 130 \text{ MeV}$ [93, 234]. However, the experimental data indicate that chemical freeze-out happens earlier near $T_c \sim 165 \text{ MeV}$ [98, 99]. The unrealistic implementation of chemical freeze-out in EOS Q leads to wrong predictions for the particle ratios which need to be fixed by hand using normalization factors.

Microscopically, chemical and thermal freeze-out are related to inelastic and total (elastic + quasi-elastic + inelastic) scattering rates between particles, respectively. The cross sections of the inelastic, particle number changing processes, are smaller than the elastic and quasi-elastic ones, which leads to an earlier chemical than thermal freeze-out [32]. A complete chemical freeze-out corresponds to a picture where all hadron numbers are fixed below T_{ch} . However, quasi-elastic resonant scatterings constantly change

¹⁹The EOS L here is different from the cross-over EOS used in Ref [134], which was constructed by connecting a hadron resonance gas EOS with the QGP EOS from a high-order weak-coupling QCD calculation [233].

resonances and their daughter particles (e.g. $\pi\pi \rightarrow \rho \rightarrow \pi\pi$, $\pi N \rightarrow \Delta \rightarrow \pi N$, $\pi K \rightarrow K^* \rightarrow \pi K$, etc.), such that the resonances are in relative chemical equilibrium with their decay products and their abundances only freeze out at thermal decoupling. This partial chemical equilibrium picture is naturally incorporated in any hadron cascade model, that solves the Boltzmann equations with elastic, quasi-elastic and inelastic cross sections for different hadron species [47, 38, 37]. In pure hydrodynamic simulations it is realized by introducing an EOS describing partially chemical equilibrium (PCE-EOS) with effective chemical potentials adjusted to conserve the relative hadron abundances after resonance decays in the HRG phase [235, 236, 237, 238]. Although the effective chemical potentials only slightly change the equation of state $p(e)$, they affect significantly the relation between temperature and energy density $T(e)$ in the HRG phase, since a larger portion of the energy density is stored in particle rest masses, reducing the thermal energy and temperature. As a result, the typical freeze-out temperature drops from 130 MeV (EOS Q) to 100 MeV (PCE-EOS) for the same freeze-out energy density $e_{dec} = 0.085 \text{ GeV}/\text{fm}^3$.

Currently, the PCE-EOS has been well studied and implemented in ideal hydrodynamic simulations, but has not been applied to any viscous hydrodynamic simulations. However, the chemical content in the HRG phase at freeze-out will affect the extracted value of the QGP shear viscosity. This will be further discussed in Chap. 8.

3.4 Freeze-out procedure and calculation of spectra

The hadron spectra are computed from the hydrodynamic output via a modified Cooper-Frye procedure [239]. We here compute spectra only for directly emitted particles and do not include feeddown from resonance decays after freeze-out. We first determine the freeze-out surface $\Sigma(x)$, by postulating (as common in hydrodynamic studies) that freeze-out from a thermalized fluid to free-streaming, non-interacting particles happens suddenly when the temperature drops below a critical value. As in the ideal fluid case with EOS Q [223] we choose $T_{dec} = 130 \text{ MeV}$. The particle spectrum is then computed as an integral over this surface [239],

$$\begin{aligned} E \frac{d^3 N_i}{d^3 p} &= \frac{g_i}{(2\pi)^3} \int_{\Sigma} p \cdot d^3 \sigma(x) f_i(x, p) \\ &= \frac{g_i}{(2\pi)^3} \int_{\Sigma} p \cdot d^3 \sigma(x) [f_{eq,i}(x, p) + \delta f_i(x, p)], \end{aligned} \quad (3.5)$$

where g_i is the spin-isospin degeneracy factor for particle species i , $d^3 \sigma^\mu(x)$ is the outward-pointing surface normal vector on the decoupling surface $\Sigma(x)$ at point x , which for boost-invariant freeze-out at longitudinal proper time $\tau_f(\mathbf{r})$ reads

$$p \cdot d^3 \sigma(x) = [m_T \cosh(y-\eta) - \mathbf{p}_\perp \cdot \nabla_\perp \tau_f(\mathbf{r})] \times \tau_f(\mathbf{r}) r dr d\phi d\eta, \quad (3.6)$$

(with $\mathbf{r} = (x, y) = (r \cos \phi, r \sin \phi)$ denoting the transverse position vector), and $f_i(x, p)$ is the local distribution function for particle species i , computed from the hydrodynamic output. Equation (3.5) generalizes the usual Cooper-Frye prescription for ideal fluid dynamics [239] by accounting for the fact that in a viscous fluid the local distribution function is never exactly in local equilibrium, but deviates from its local equilibrium form by small terms proportional to the non-equilibrium viscous flows [240, 126, 131]. Both contributions can be extracted from hydrodynamic output along the freeze-out surface. The equilibrium contribution is

$$f_{eq,i}(p, x) = f_{eq,i} \left(\frac{p \cdot u(x)}{T(x)} \right) = \frac{1}{e^{p \cdot u(x)/T(x)} \pm 1}, \quad (3.7)$$

where the exponent is computed from the temperature $T(x)$ and hydrodynamic flow velocity $u^\mu = \gamma_\perp (\cosh \eta, v_x, v_y, \sinh \eta)$ along the surface $\Sigma(x)$:

$$p \cdot u(x) = \gamma_\perp [m_T \cosh(y-\eta) - p_x v_x - p_y v_y]. \quad (3.8)$$

Here $m_T = \sqrt{p_T^2 + m_i^2}$ is the particle's transverse mass.

As long as only shear viscosity is implemented²⁰, the viscous deviation from local equilibrium is given by [240, 131]

$$\delta f_i(x, p) = f_{\text{eq},i}(p, x) (1 \mp f_{\text{eq},i}(p, x)) \frac{p^\mu p^\nu \pi_{\mu\nu}(x)}{2T^2(x) (e(x) + p(x))}. \quad (3.9)$$

The viscous correction is proportional to $\pi^{\mu\nu}(x)$ on the freeze-out surface (normalized by the equilibrium enthalpy $e+p$) and increases quadratically with the particle's momentum (normalized by the temperature T). At large p_T , the viscous correction can exceed the equilibrium contribution, indicating a breakdown of viscous hydrodynamics. In that domain, particle spectra can not be reliably computed with viscous fluid dynamics. The limit of applicability depends on the actual value of $\pi^{\mu\nu}/(e+p)$ and thus on the specific dynamical conditions encountered in the heavy-ion collision.

In Eq. (3.9), the final expression for viscous correction to the spectrum are written explicitly as:

$$\begin{aligned} p_\mu p_\nu \pi^{\mu\nu} &= m_T^2 (\cosh^2(y-\eta) \pi^{\tau\tau} + \sinh^2(y-\eta) \tau^2 \pi^{\eta\eta}) \\ &- 2m_T \cosh(y-\eta) (p_x \pi^{\tau x} + p_y \pi^{\tau y}) \\ &+ (p_x^2 \pi^{xx} + 2p_x p_y \pi^{xy} + p_y^2 \pi^{yy}). \end{aligned} \quad (3.10)$$

Due to longitudinal boost-invariance, the integration over space-time rapidity η in Eq. (3.5) can be done analytically, resulting in a series of contributions involving modified Bessel functions [32, 132]. VISH2+1 does not exploit this possibility and instead performs this and all other integrations for the spectra numerically [126].

Once the spectrum (3.5) has been computed, a Fourier decomposition with respect to the azimuthal angle ϕ_p yields the anisotropic flow coefficients. For collisions between equal spherical nuclei followed by longitudinally boost-invariant expansion of the collision fireball, only even-numbered coefficients contribute, the “elliptic flow” v_2 being the largest and most important one:

$$E \frac{d^3 N_i}{d^3 p}(b) = \frac{dN_i}{dy p_T dp_T d\phi_p}(b) = \frac{1}{2\pi} \frac{dN_i}{dy p_T dp_T} [1 + 2v_2(p_T; b) \cos(2\phi_p) + \dots]. \quad (3.11)$$

In practice it is evaluated as the $\cos(2\phi_p)$ -moment of the final particle spectrum,

$$v_2(p_T) = \langle \cos(2\phi_p) \rangle \equiv \frac{\int d\phi_p \cos(2\phi_p) \frac{dN}{dy p_T dp_T d\phi_p}}{\int d\phi_p \frac{dN}{dy p_T dp_T d\phi_p}}, \quad (3.12)$$

where, according to Eq. (3.5), the particle spectrum is a sum of a local equilibrium and a non-equilibrium contribution (to be indicated symbolically as $N = N_{\text{eq}} + \delta N$).

3.5 Additional viscous inputs: shear viscosity, bulk viscosity and relaxation times

The shear viscosity η , bulk viscosity ζ and their relaxation times τ_π and τ_Π are free inputs in viscous hydrodynamic calculations.

Although the future trend for viscous hydrodynamic calculations will be to input a temperature dependent η/s to consider the fact that η/s is small in the QGP phase, reaches a minimum during the phase transition and rises again to much larger values in the hadronic phase (see Chap. 1.4 for details), all of the presently existing viscous hydrodynamic calculations [125, 126, 127, 135, 136, 137] (including those presented here) use a

²⁰For the case with both shear and bulk viscosity, the expression for δf can be found in Ref. [241].

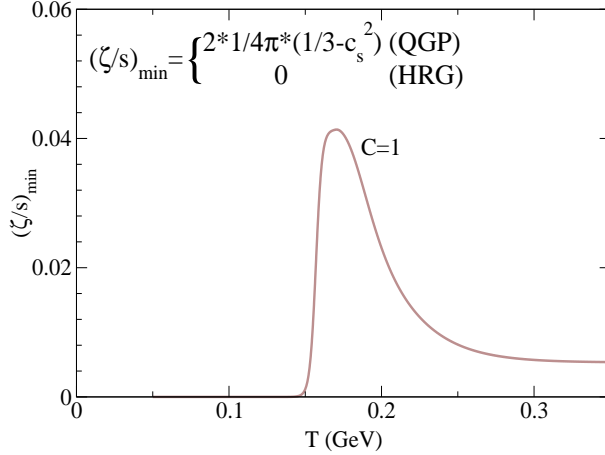


Figure 3.3: Minimally constructed bulk viscosity to entropy ratio, ζ/s , as a function of temperature.

constant η/s as input: $\eta/s = C \times \frac{1}{4\pi}$, with $C = 0, 1, 2, 3 \dots$ ($\frac{1}{4\pi}$ is the minimal KSS bound from AdS/CFT [146]). Typically, we set $\tau_\pi = \frac{3\eta}{sT}$, except where mentioned otherwise. This expression is very close to the AdS/CFT prediction $\tau_\pi = \frac{2 - \ln 2}{2\pi T}$ [242, 243], and is half of the kinetic theory prediction for massless Boltzmann particles [201, 131].

The bulk viscosity of the QCD matter is still under theoretical development (see Chap. 1.4, 1.5 for details). It is generally believed that ζ/s peaks near the phase transition [176, 178]. However, one finds that the minimal peak value from AdS/CFT predictions [180, 179] is more than 10 times smaller than the one extracted from lattice QCD data [164, 177, 178]²¹. Things become even more complicated for the bulk viscosity in the hadronic phase [153]. When neglecting hadron masses, chiral perturbation theory predicts a rising $(\zeta/s)(T)$ below T_c [244]. In contrast, a theory with non-zero hadron masses shows a decreasing $(\zeta/s)(T)$ below T_c [170, 171]. Considering these theoretical uncertainties, ζ/s here is treated as a free input. We concentrate on the bulk viscosity effects near the phase transition, but totally neglect bulk viscosity effects in the hadronic matter. Fig. 3.3 shows the minimally constructed $(\zeta/s)_{min}$, which is obtained by connecting the minimal strong coupling AdS/CFT result $\zeta/s = 2(\eta/s)(1/3 - c_s^2)$ [194] above T_c through a Gaussian function peaked at T_c with a zero value in the hadronic phase (the speed of sound, $c_s^2(T)$, is evaluated from the same lattice QCD data [232] that are used in our EOS L). To simulate effects from larger bulk viscosity, we multiply the entire function $(\zeta/s)_{min}(T_c)$ by a constant $C > 1$. For the bulk relaxation time τ_Π , there are no standard theoretical results (see, however, the recent work [245]). In Chap. 6.2, we set $\tau_\Pi = \tau_\pi = \frac{3}{4\pi T}$ just for the purpose of a qualitative comparison of shear and bulk viscous effects without claim of quantitative accuracy. In Chap. 6.3 and Chap. 6.4, we will investigate the effects of critical slowing down during the phase transition and corresponding bulk viscosity effects. There we will set τ_Π to be **a**) a temperature-independent constant that we change it from 0.1 fm/c to 10 fm/c; **b**) a temperature dependent function $\tau_\Pi(T) = \max[\tilde{\tau} \cdot \frac{\zeta}{s}(T), 0.1 \text{ fm/c}]$ with $\tilde{\tau} = 120 \text{ fm/c}$. This choice implements phenomenologically the concept of critical slowing down; it yields $\tau_\Pi \approx 0.6 \text{ fm/c}$ at $T = 350 \text{ MeV}$ and $\tau_\Pi \approx 5 \text{ fm/c}$ at T_c .

²¹ Refer to Ref. [181] for a critical discussion of the lattice QCD approach.

Chapter 4: Generic Viscous Effects

– Shear Viscosity

4.1 Introduction

In this chapter, we will study generic shear viscous effects by comparing ideal and viscous hydrodynamic runs. The results shown here are for Au+Au collisions and complement those from our two early viscous hydrodynamics papers [125, 126] where we presented results for the smaller Cu+Cu systems. The choice of the Cu+Cu system was purely technical since the numerical grid in early VISH2+1 could not accommodate the larger Au+Au collision fireballs. This problem was solved in an up dated version of VISH2+1 with a new treatment of the boundary. However, since a similar detailed and systematic investigation for the shear viscous effects for Au+Au collisions have not been documented anywhere else, I decided to redo the graphs from [126] for Au+Au collisions and include them in this thesis, instead of using the old Cu+Cu graphs.

As discussed in Ref. [127], the shear viscous effects are qualitatively similar in Cu+Cu collisions and Au+Au collisions. However, on a quantitative level, the smaller Cu+Cu system shows larger viscous effects [127]. This manifests itself through a much larger viscous v_2 suppression for non-central Cu+Cu collisions than for non-central Au+Au collisions. The new Au+Au results were calculated with the updated VISH2+1, which solves the “full I-S equation” rather than the simplified I-S equation used in our early papers [125, 126], and organized along lines similar to Ref. [127] for comparison and later reference. As briefly mentioned in Chap. 2.7, the “full” I-S equation is preferred since it preserves conformal symmetry for a conformal fluid and reduces the dependence on the relaxation time τ_π . Systematic numerical comparisons between the “full” and “simplified” I-S equations were presented in Ref. [127], and will be discussed later in Chap. 7.

Let me begin with a description of the default settings for the free parameters (see Chap. 3) used in the calculations for this chapter.

For ideal and viscous hydrodynamic comparison runs, we use identical initial and final conditions, with the same standard parameters previously used in early ideal hydrodynamic simulations. Following Refs. [223, 234], we use a Glauber initialization for the energy density and set $e_0(\tau_0, b = 0, r = 0) = 30 \text{ GeV/fm}^3$ at $\tau_0 = 0.6 \text{ fm/c}$ for central Au+Au collisions. The freeze-out surface is extracted using the AZHYDRO decoupling algorithm [246] with a constant decoupling temperature $T_{dec} = 130 \text{ MeV}$, and the final particle spectra are calculated with the modified Cooper-Fye formula, given by eqs. (3.5-3.10) in Chap 3.4. In the viscous hydrodynamic calculations, we use the KSS value for the shear viscosity $\eta/s = 1/4\pi$ [146], and set bulk viscosity to zero: $\zeta/s = 0$. For the relaxation time, we use $\tau_\pi = 3\eta/sT$, and the shear stress tensor is initialized by the N-S initialization $\pi^{mn}(\tau_0) = 2\eta\sigma^{mn}$, unless otherwise noted (e.g. in Chap. 4.4, where we explore the effects from varying the relaxation time and for shear stress tensor initialization).

To isolate effects introduced by the phase transition from generic shear viscous effects, we perform calculations with two different EOS, using EOS I for a pure massless quark-gluon gas without phase transition and SM-EOS Q for a more realistic EOS that includes a phase transition between QGP and hadron gas. Results from the lattice-QCD based EOS (EOS L), can be found in Chap. 6, where we also study the the bulk viscous effects.

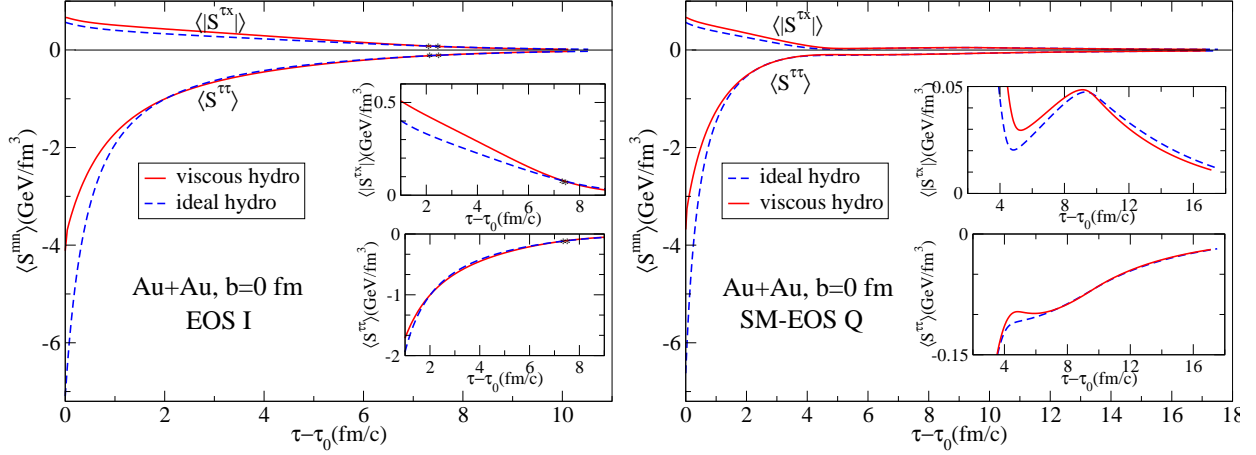


Figure 4.1: Time evolution of the hydrodynamic source terms (3.2a-3.2c), averaged over the transverse plane, for central Au+Au collisions, calculated with EOS I in the left panel and with SM-EOS Q in the right panel. The smaller insets blow up the vertical scale to show more detail. The dashed blue lines are for ideal hydrodynamics with $e_0 = 30 \text{ GeV/fm}^3$ and $\tau_0 = 0.6 \text{ fm/c}$. Solid red lines show results from viscous hydrodynamics with identical initial conditions and $\frac{\eta}{s} = \frac{1}{4\pi} \approx 0.08$, $\tau_\pi = \frac{3\eta}{sT} \approx 0.24 \left(\frac{200 \text{ MeV}}{T}\right) \text{ fm/c}$. The stars in left panel indicate the freeze-out times at $T_c = 130 \text{ MeV}$. The positive source terms drive the transverse expansion while the negative ones affect the longitudinal expansion.

4.2 Hydrodynamic evolution

Central collisions:

Even without initial transverse flow, the N-S initialization $\pi^{mn} = 2\eta\sigma^{mn}$ generates three non-zero values for the components of the shear viscous pressure tensor: $\tau^2\pi^{\eta\eta} = \frac{-4\eta}{3\tau_0}$, $\pi^{xx} = \pi^{yy} = \frac{2\eta}{3\tau_0}$, due to the boost-invariant longitudinal expansion. Inspection of the source terms in Eqs. (3.2a-3.2c) reveals that the initially negative $\tau^2\pi^{\eta\eta}$ effectively reduces the longitudinal pressure, thus reducing the cooling rate, while the initially positive values of π^{xx} and π^{yy} effectively increase the transverse pressure and accelerate the development of transverse flow in x and y directions. As the fireball evolves, the shear viscous pressure tensor deviates from its N-S value (although for small relaxation time τ_π , the deviation remains small²²), and the stress tensor σ^{mn} receives additional contributions involving the transverse flow velocity and its derivatives (see Eq. (A.3)), which renders an analytic discussion of its effects on dynamics impractical.

Figure 4.1 shows what one gets numerically. Plotted are the source terms (3.2a) and (3.2b), averaged over the transverse plane with the energy density as weight function, as a function of time, for evolution of central Au+Au collisions with two different equations of state, EOS I and SM-EOS Q. (In central collisions $\langle |S^{\tau x}| \rangle = \langle |S^{\tau y}| \rangle$.) One sees that the initially strong viscous reduction of the (negative) source term $S^{\tau\tau}$, which controls the cooling by longitudinal expansion, quickly disappears. This is due to a combination of effects: while the magnitude of $\tau^2\pi^{\eta\eta}$ decreases with time, its negative effects are further compensated by a growing positive contribution $\tau(\partial_x(pv_x) + \partial_y(pv_y))$ arising from the increasing transverse flow gradients. In contrast, the viscous increase of the (positive) transverse source term $S^{\tau x}$ persists much longer, until about 6 fm/c. After that time, however, the viscous correction switches sign (clearly visible in the upper inset in the right panel of Fig. 4.1b) and turns negative, thus reducing the transverse acceleration at late times relative to the ideal fluid case. We can summarize these findings by stating that shear viscosity reduces longitudinal cooling mostly at early times while causing initially increased but later reduced acceleration

²² These deviations from the N-S limit are investigated in Sec. 7.3.1.

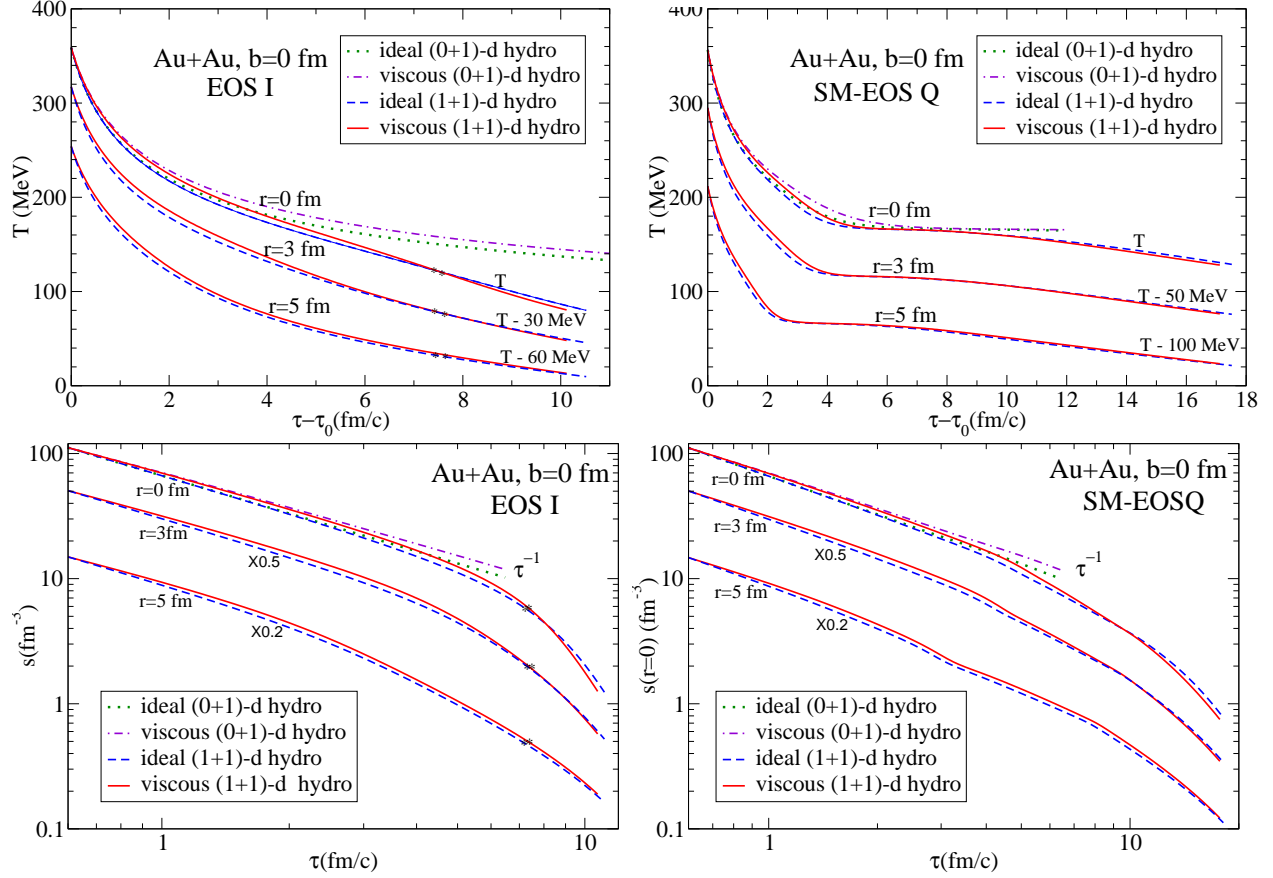


Figure 4.2: Time evolution of the local temperature and local entropy density (down) in central Au+Au collisions, calculated with EOS I and SM-EOS Q (right), for the center of the fireball ($r=0$, upper set of curves) and points at $r=3$ fm and $r=5$ fm (middle and lower set of curves). For clarity, the temperature curve for $r=3$ fm and $r=5$ fm have been lowered by constant offsets, as indicated. Same parameters as in Fig. 4.1. See text for discussion.

in the transverse direction. Due to the general smallness of the viscous pressure tensor components at late times, the last-mentioned effect (reduced acceleration) is not very strong.

The phase transition in SM-EOS Q is seen to cause an interesting non-monotonic behaviour of the time evolution of the source terms (right panel in Fig. 4.1), leading to a transient increase of the viscous effects on the longitudinal source term while the system passes through the mixed phase.

The viscous slowing of the cooling process at early times and the increased rate of cooling at later times due to accelerated transverse expansion are shown in Figure 4.2 by the time evolution of local temperatures. For comparison we also show curves for boost-invariant longitudinal Bjorken expansion without transverse flow, labeled “(0+1)-d hydro”. These are obtained with flat initial density profiles for the same value e_0 (no transverse gradients). The dotted green line in the left panel shows the well-known $T \sim \tau^{-1/3}$ behaviour of the Bjorken solution of ideal fluid dynamics [222], modified in the right panel by the quark-hadron phase transition where the temperature stays constant in the mixed phase.

The dash-dotted purple line shows the slower cooling in the viscous (0+1)-dimensional case [211], due to reduced work done by the longitudinal pressure. The expansion is still boost-invariant a la Bjorken [222] (as it is for all other cases discussed in this thesis), but viscous effects generate entropy, thereby keeping the temperature at all times higher than for the adiabatic case. The dashed blue (ideal) and solid red (viscous)

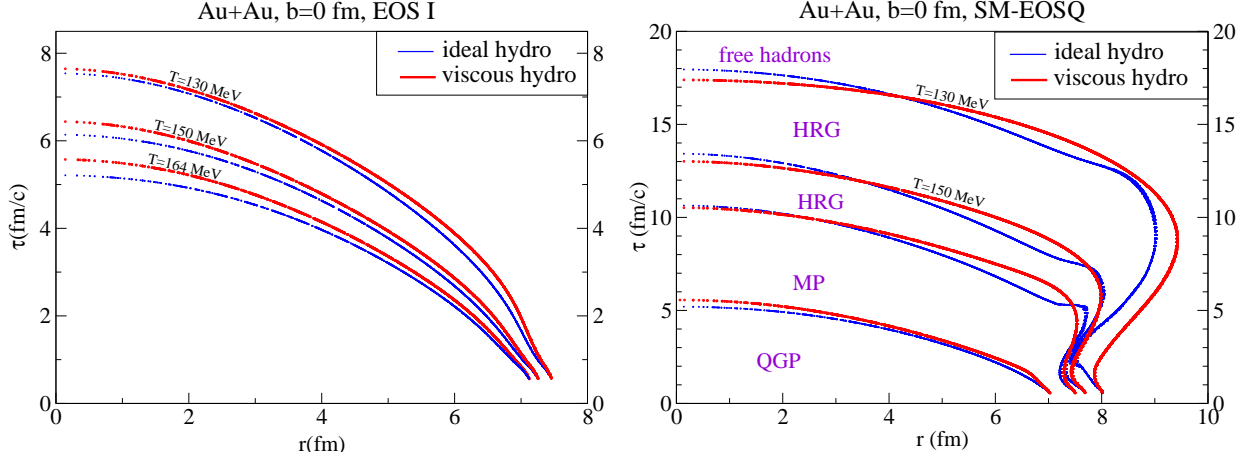


Figure 4.3: Surfaces of constant temperature T for central Au+Au collisions, evolved with EOS I (left panel) and SM-EOS Q (right panel). In each panel, results from viscous hydrodynamics (red lines) are directly compared with the corresponding ideal fluid evolution (blue lines). The right panel contains two isotherms for $T_c = 164$ MeV, one separating the mixed phase (MP) from the QGP at energy density $e_Q = 1.6$ GeV/fm³, the other separating it from the hadron resonance gas (HRG) at energy density $e_H = 0.45$ GeV/fm³. See text for discussion.

lines for the azimuthally symmetric (1+1)-dimensional case show the additional cooling caused by transverse expansion. Again the cooling is initially slower in the viscous case (solid red), but at later times, due to faster build-up of transverse flow by the viscously increased transverse pressure, the viscous expansion is seen to cool the fireball center *faster* than ideal hydrodynamics. (Note also the drastic reduction of the lifetime of the mixed phase by transverse expansion; due to increased transverse flow and continued acceleration in the mixed phase from viscous pressure gradients, it is even more dramatic in the viscous than the ideal case.)

The lower panels of Fig. 4.2 show the evolution of the entropy density. (In the QGP phase $s \sim T^3$.) The double-logarithmic presentation emphasizes the effects of viscosity and transverse expansion on the power law $s(\tau) \sim \tau^{-\alpha}$: One sees that the τ^{-1} scaling of the ideal Bjorken solution is flattened by viscous effects, but steepened by transverse expansion. As is well-known, it takes a while (here about 6-8 fm/c, depending on the EOS) until the transverse rarefaction wave reaches the fireball center and turns the initially 1-dimensional longitudinal expansion into a genuinely 3-dimensional one. When this happens, the power law $s(\tau) \sim \tau^{-\alpha}$ changes from $\alpha = 1$ in the ideal fluid case to $\alpha > 3$ [26]. Here 3 is the dimensionality of space, and the fact that α becomes larger than 3 reflects relativistic Lorentz-contraction effects through the transverse-flow-related γ_{\perp} -factor that keeps increasing even at late times. In the viscous case, α changes from 1 to 3 sooner than for the ideal fluid, due to the faster growth of transverse flow. At very late times (not shown in Fig. ??) the $s(\tau)$ curves for ideal and viscous hydrodynamics are almost perfectly parallel [126], indicating that very little entropy is produced during this late stage.

In Fig. 4.3 we plot the evolution of temperature in $r-\tau$ space, in the form of constant- T surfaces, obtained from ideal hydrodynamics (blue lines) and viscous hydrodynamics (red lines), respectively. Again the two panels compare the evolution with EOS I (left) to the one with SM-EOS Q (right). As already noted, at $r = 0$ the viscous fluid cools initially more slowly (thereby giving somewhat longer life to the QGP phase) but later more rapidly (thereby freezing out earlier for SM-EOS Q). Comparing the two sets of temperature contours shown in the right panel of Fig. 4.3, one sees that viscous effects tend to smoothen any structures related to the (first order) phase transition in SM-EOS Q. The reason for this is that, with the rapid change of the speed of sound at either end of the mixed phase, the radial flow velocity profile develops dramatic structures at the QGP-MP and MP-HRG interfaces [126, 223]. This leads to large velocity gradients across these interfaces,

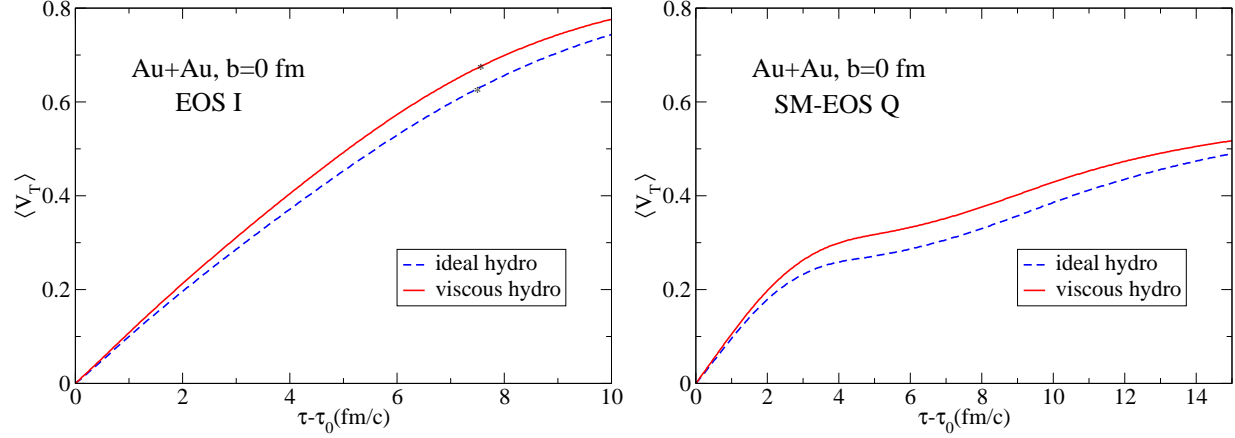


Figure 4.4: Time evolution of the average radial flow velocity $\langle v_T \rangle \equiv \langle v_\perp \rangle$ in central Au+Au collisions, calculated with EOS I (left panel) and SM-EOS Q (right panel). Solid (dashed) lines show results from ideal (viscous) fluid dynamics. The initially faster rate of increase reflects large positive shear viscous pressure in the transverse direction at early times. The similar rates of increase at late times indicate the gradual disappearance of shear viscous effects. In the right panel, the curves exhibit a plateau from 2 to 4 fm/c, reflecting the softening of the EOS in the mixed phase.

inducing large viscous pressures which work to reduce these gradients. In effect, shear viscosity softens the first-order phase transition into a smooth but rapid cross-over transition. These same viscous pressure gradients cause the fluid to accelerate even in the mixed phase where all thermodynamic pressure gradients vanish (and where the ideal fluid therefore does not generate additional flow). As a result, the lifetime of the mixed phase is shorter in viscous hydrodynamics, as also seen in the right panel of Figure 4.3.

Fig. 4.4 plots the time evolution of radial velocity $\langle v_T \rangle$ (radial flow), calculated as an average over the transverse plane with the Lorentz contracted energy density $\gamma_\perp e$ as weight function, for ideal and viscous fluids. One finds that radial flow builds up more quickly in the viscous fluid. The shear viscosity driven acceleration is strongest in the early and middle stages, but almost negligible in the later hadronic stage, where the ideal and viscous fluid lines are almost parallel with each other. Compared with the old radial flow figure for central Cu+Cu collisions in Ref. [126] (see Fig. 6 there), one finds a slightly larger increase in radial flow for the smaller Cu+Cu system, which can be interpreted as larger viscous effects for smaller systems. Such system size effects are more significant for non-central collisions, which will be discussed below.

Non-central collisions:

We now turn to non-central collisions and take full advantage of the ability of VISH2+1 to solve the transverse expansion in 2 spatial dimensions. To evaluate the anisotropic evolution of the fireball, we will study the time evolution of flow anisotropy $\langle |v_x| - |v_y| \rangle$ (Fig 4.5) and the time evolution of “spatial eccentricity” and “momentum anisotropy” (Fig.4.6). The spatial eccentricity [72,93] characterizes the spatial deformation of the fireball in the transverse plane; it is defined as $\epsilon_x = \frac{\langle x^2 - y^2 \rangle}{\langle x^2 + y^2 \rangle}$ (here $\langle \dots \rangle$ means averaging over the transverse plane with the energy density $e(x)$ as weight function). The momentum anisotropy $\epsilon_p = \frac{\langle T_0^{xx} - T_0^{yy} \rangle}{\langle T_0^{xx} + T_0^{yy} \rangle}$ (where $\langle \dots \rangle$ means average over the transverse plane) [72,93] measures the anisotropy of the transverse momentum density due to anisotropies in the collective flow pattern, which includes only the ideal fluid part of the energy momentum tensor. In viscous hydrodynamics, we also define the *total momentum anisotropy* $\epsilon'_p = \frac{\langle T^{xx} - T^{yy} \rangle}{\langle T^{xx} + T^{yy} \rangle}$, similarly defined in terms of the total energy momentum tensor $T^{\mu\nu} = T_0^{\mu\nu} + \pi^{\mu\nu}$, which additionally counts anisotropic momentum contributions arising from the viscous pressure tensor. Since the latter quantity includes effects arising from the deviation δf of the local distribution function from

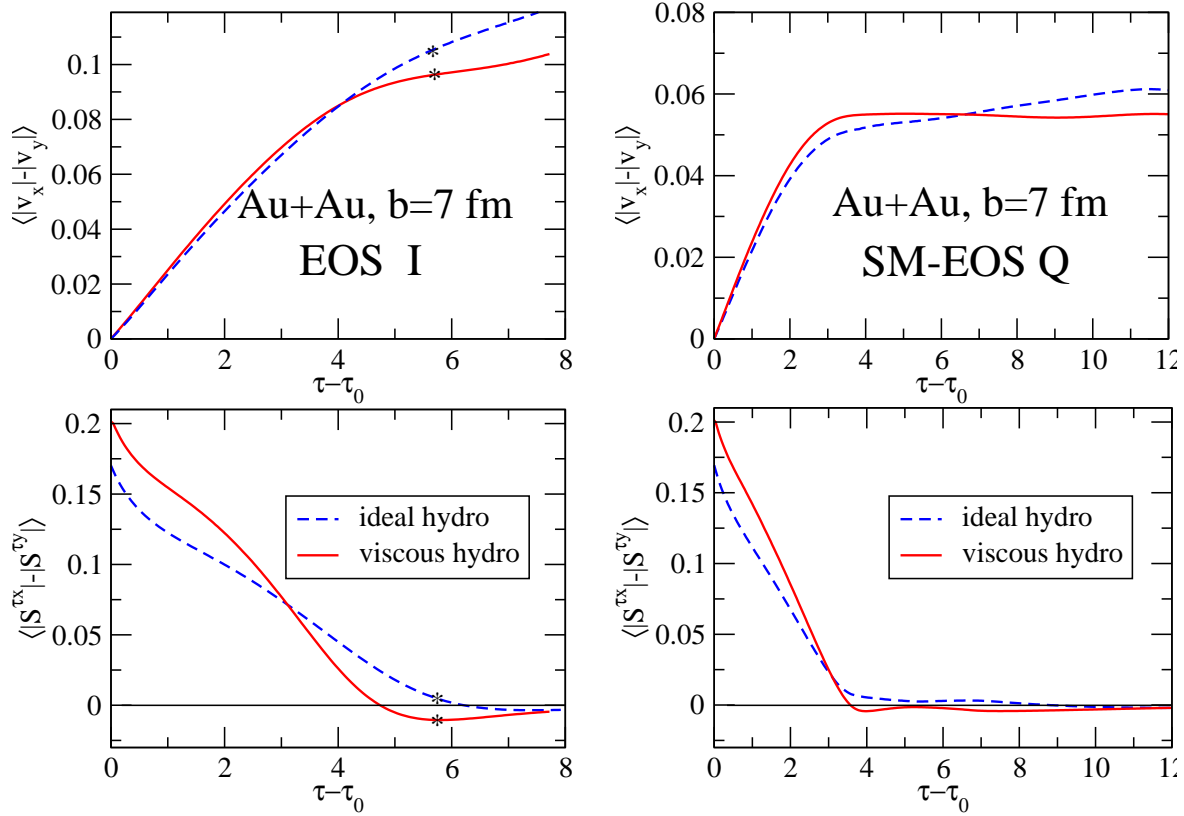


Figure 4.5: Time evolution of the transverse flow anisotropy $\langle |v_x| - |v_y| \rangle$ (top row) and of the anisotropy in the transverse source term $\langle |\mathcal{S}^{\tau x}| - |\mathcal{S}^{\tau y}| \rangle$ (bottom row). Both quantities are averaged over the transverse plane, with the Lorentz-contracted energy density $\gamma_{\perp} e$ as weight function. The left (right) column shows results for EOS I (SM-EOS Q), with solid (dashed) lines representing ideal (viscous) fluid dynamical evolution.

its thermal equilibrium form which, according to Eq. (3.5), also affects the final hadron momentum spectrum and elliptic flow, it is this *total momentum anisotropy* that should be studied in viscous hydrodynamics if one wants to understand the evolution of hadron elliptic flow. In other words, in viscous hydrodynamics hadron elliptic flow is not simply a measure for anisotropies in the collective flow velocity pattern, but additionally reflects anisotropies in the local rest frame momentum distributions, arising from deviations of the local momentum distribution from thermal equilibrium and thus being related to the viscous pressure.

Fig. 4.5 shows the time evolutions of the flow anisotropy $\langle |v_x| - |v_y| \rangle$ and source term anisotropy $\langle |\mathcal{S}^{\tau x}| - |\mathcal{S}^{\tau y}| \rangle$. In central collisions these quantities vanish. In ideal hydrodynamics, the flow anisotropy is driven by the anisotropic gradients of the thermodynamic pressure. In viscous fluid dynamics, the source terms (3.2b,3.2c), whose difference is shown in the bottom row of Fig. 4.5, receive additional contributions from gradients of the viscous pressure tensor which contribute their own anisotropies. Fig. 4.5 demonstrates that these additional anisotropies *increase* the driving force for anisotropic flow at very early times ($\tau - \tau_0 < 3 \text{ fm}/c$), but *reduce* this driving force throughout the later evolution. At times $\tau - \tau_0 > 5 \text{ fm}/c$ the anisotropy of the effective transverse pressure even changes sign and turns negative, working to *decrease* the flow anisotropy. As a consequence of this, the buildup of the flow anisotropy stalls around $\tau - \tau_0 \approx 4 \text{ fm}/c$ (even earlier for SM-EOS Q where the flow buildup stops as soon as the fireball medium enters the mixed phase) and proceeds to slightly decrease thereafter. This happens during the crucial period where ideal fluid dynamics still

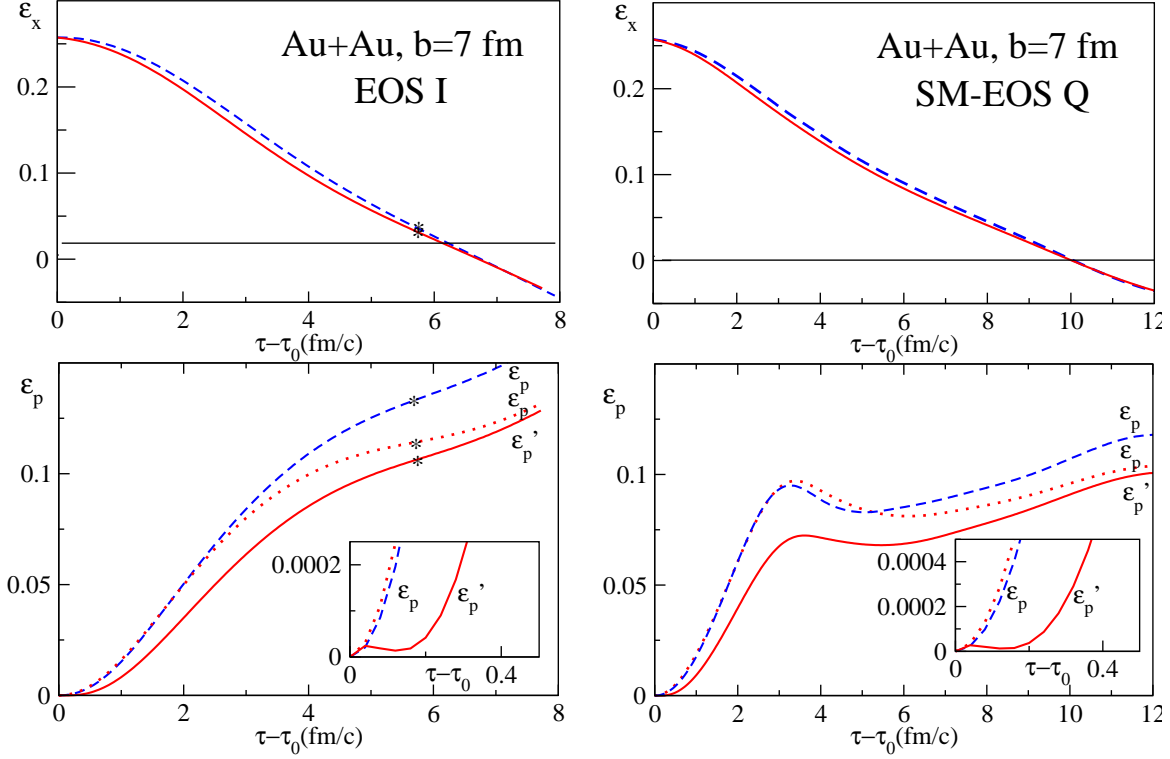


Figure 4.6: Time evolution for the spatial eccentricity ϵ_x , momentum anisotropy ϵ_p and total momentum anisotropy ϵ'_p (see text for definitions), calculated for $b=7$ fm Au+Au collisions with EOS I (left column) and SM-EOS Q (right column). Dashed lines are for ideal hydrodynamics while the solid and dotted lines show results from viscous hydrodynamics. See text for discussion.

shows strong growth of the flow anisotropy. By the time the fireball matter decouples, the average flow velocity anisotropy of viscous hydro lags about 10-15% behind the value reached during ideal fluid dynamical evolution.

Figure 4.6 correlates the decrease in time of the spatial eccentricity ϵ_x with the buildup of the momentum anisotropies ϵ_p and ϵ'_p . In viscous dynamics the spatial eccentricity is seen to decrease initially faster than for ideal fluids, due to the faster radial expansion shown in Fig. 4.4. The effects of early pressure gradient anisotropies are reflected in the initial growth rate of the flow anisotropy (Fig. 4.5) and the momentum anisotropy ϵ_p (bottom panels in Fig. 4.6) which are seen to slightly exceed that observed in the ideal fluid at times up to about 3 fm/c after the beginning of the transverse expansion. Figure 4.5 also shows that in the viscous fluid the flow velocity anisotropy stalls about 2 fm/c (for SM-EOS Q) after start and remains about 10% below the final value reached in ideal fluid dynamics. This causes the spatial eccentricity of the viscous fireball to decrease more slowly at later times than that of the ideal fluid (top panels in Fig. 4.6) which, at late times, features a significantly larger difference between the horizontal (x) and vertical (y) expansion velocities. We note that the differences between ideal and viscous evolution were found to be significantly larger in the smaller Cu+Cu systems studied in Ref. [126].

It is very instructive to compare the behaviour of the flow-induced ideal-fluid contribution to the momentum anisotropy, ϵ_p , with that of the total momentum anisotropy ϵ'_p . At early times they are very different, with ϵ'_p being much smaller than ϵ_p (see insets in the lower panels of Fig. 4.6). This reflects very large *negative* contributions to the anisotropy of the total energy momentum tensor from the shear viscous pressure whose gradients along the out-of-plane direction y strongly exceed those within the reaction plane along the

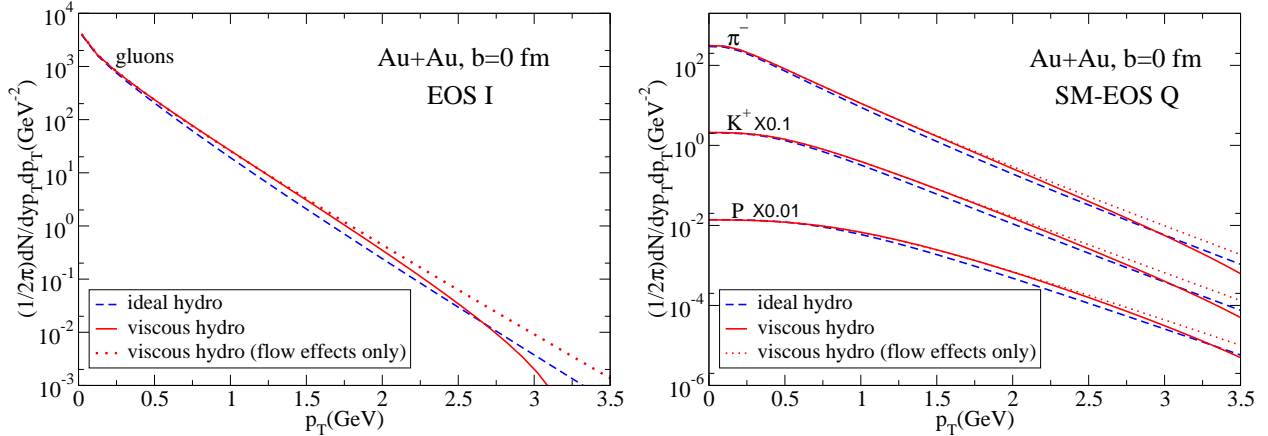


Figure 4.7: Mid-rapidity particle spectra for central Au+Au collisions, calculated with EOS I (left, gluons) and with SM-EOS Q (right, π^- , K^+ and p). The solid blue (red dashed) lines are from ideal (viscous) hydrodynamics. The purple dotted lines show viscous hydrodynamic spectra that neglect the viscous correction δf_i to the distribution function in Eq. (3.5), i.e. include only the effects from the larger radial flow generated in viscous hydrodynamics.

x direction. At early times this effect almost compensates for the larger in-plane gradient of the thermal pressure. The *negative* viscous pressure gradient anisotropy (which is even larger in the smaller Cu+Cu systems studied in [126]) is responsible for reducing the growth of flow anisotropies, thereby causing the flow-induced momentum anisotropy ϵ_p to significantly lag behind its ideal fluid value at later times. The negative viscous pressure anisotropies responsible for the difference between ϵ_p and ϵ'_p slowly disappear at later times, since all viscous pressure components then become very small (see Fig. 4.10 below).

The net result of this interplay is a total momentum anisotropy in Au+Au collisions (i.e. a source of elliptic flow v_2) that for a “minimally” viscous fluid with $\frac{\eta}{s} = \frac{1}{4\pi}$ is 20-25% lower than for an ideal fluid, at all except the earliest times (where it is even smaller). The origin of this reduction changes with time: Initially it is dominated by strong momentum anisotropies in the local rest frame, with momenta pointing preferentially out-of-plane, induced by deviations from local thermal equilibrium and associated with large shear viscous pressure. At later times, the action of these anisotropic viscous pressure gradients integrates to an overall reduction in collective flow anisotropy, while the viscous pressure itself becomes small; at this stage, the reduction of the total momentum anisotropy is indeed mostly due to a reduced anisotropy in the collective flow pattern while momentum isotropy in the local fluid rest frame is approximately restored.

4.3 Final particle spectra and elliptic flow v_2

Spectra for central collisions:

After obtaining the freeze-out surface, we calculate the particle spectra from the generalized Cooper-Frye formula (3.5), using the AZHYDRO algorithm [246] for the integration over the freeze-out surface Σ . For calculations with EOS I which lacks the transition from massless partons to hadrons, we cannot compute any hadron spectra. For illustration we instead compute the spectra of hypothetical massless bosons (“gluons”). They can be compared with the pion spectra from SM-EOS Q which can also, to good approximation, be considered as massless bosons.

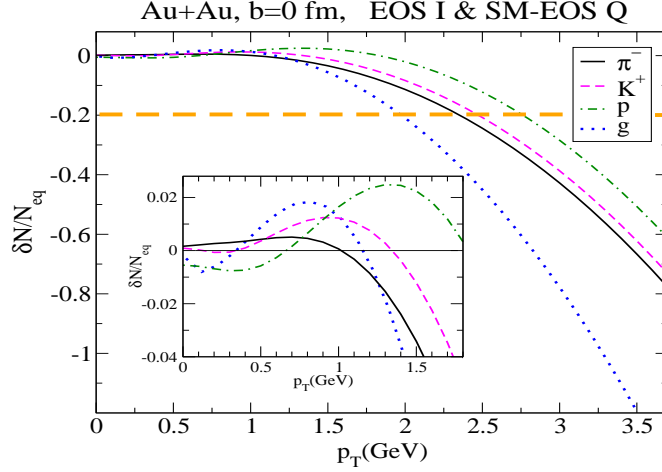


Figure 4.8: Ratio of the viscous correction δN , resulting from the non-equilibrium correction δf , Eq. (3.9), to the distribution function at freeze-out, to the equilibrium spectrum $N_{\text{eq}} \equiv dN_{\text{eq}}/(dyd^2p_T)$ calculated from Eq. (3.5) by setting $\delta f = 0$. The gluon curves are for evolution with EOS I, the curves for π^- , K^+ and p are from calculations with SM-EOS Q. The horizontal dashed line at 0.2 indicates breakdown of the viscous hydrodynamic approach.

The larger radial flow generated in viscous hydrodynamics, for a fixed set of initial conditions (shown in Fig. 4.4), leads to flatter transverse momentum spectra [247, 132, 248] (at least at low p_T where the viscous correction δf_i to the distribution function can be neglected in (3.5)). This is seen in Figure 4.7, by comparing the dotted and dashed lines. This comparison also shows that the viscous spectra lie systematically above the ideal ones, indicating larger final total multiplicity. This reflects the creation of entropy during the viscous hydrodynamic evolution. As pointed out in [247, 132], this requires a retuning of initial conditions (starting the hydrodynamic evolution later with smaller initial energy density) if one desires to fit a given set of experimental p_T -spectra. Since we here concentrate on investigating the origins and detailed mechanics of viscous effects in relativistic hydrodynamics, we will not explore any variations of initial conditions. All comparisons between ideal and viscous hydrodynamics presented here will use identical starting times τ_0 and initial peak energy densities e_0 . The solid lines in Figure 4.7 show that in our calculations for $p_T \gtrsim 2 \text{ GeV}/c$ the effects from δf_i have an overall negative sign, leading to a reduction of the p_T -spectra at large p_T relative to both the viscous spectra without δf_i and the ideal hydrodynamic spectra. This is true for all particle species, irrespective of the EOS used to evolve the fluid.

However, the earlier blast-wave model estimate from Teaney [240] found that the correction is positive, growing quadratically with p_T . A later calculation by Dusling and Teaney, using causal viscous hydrodynamics in the O-G formalism and a different (kinetic) freeze-out criterium to determine the decoupling surface, also found a (small) positive effect from δf_i on the final pion spectra, at least up to $p_T = 2 \text{ GeV}/c$, for freeze-out around $T_{\text{dec}} \sim 130 \text{ MeV}$, turning weakly negative when their effective freeze-out temperature was lowered to below 100 MeV [137]. Inspecting Eqs. (3.5, 3.10) reveals that the viscous correction δf_i in Eqs. (3.5, 3.9) depends on the signs and magnitudes of the various viscous pressure tensor components along the freeze-out surface, weighted by the equilibrium part $f_{\text{eq},i}$ of the distribution function. Its effect on the final p_T -spectra (even its sign!) is not *a priori* obvious. In Appendix A.4, we will explore the origin of the discrepancy of the sign of δf between the different groups by investigating the effects of different freeze-out surfaces in hydrodynamics and in the simple blast wave model.

In Figure 4.8 we show the non-equilibrium contribution to the final hadron spectra in greater detail. The figure shows that the non-equilibrium effects from δf_i are largest for massless particles and, at high p_T , decrease in magnitude with increasing particle mass. The assumption $|\delta f| \ll f_{\text{eq}}$, which underlies the viscous

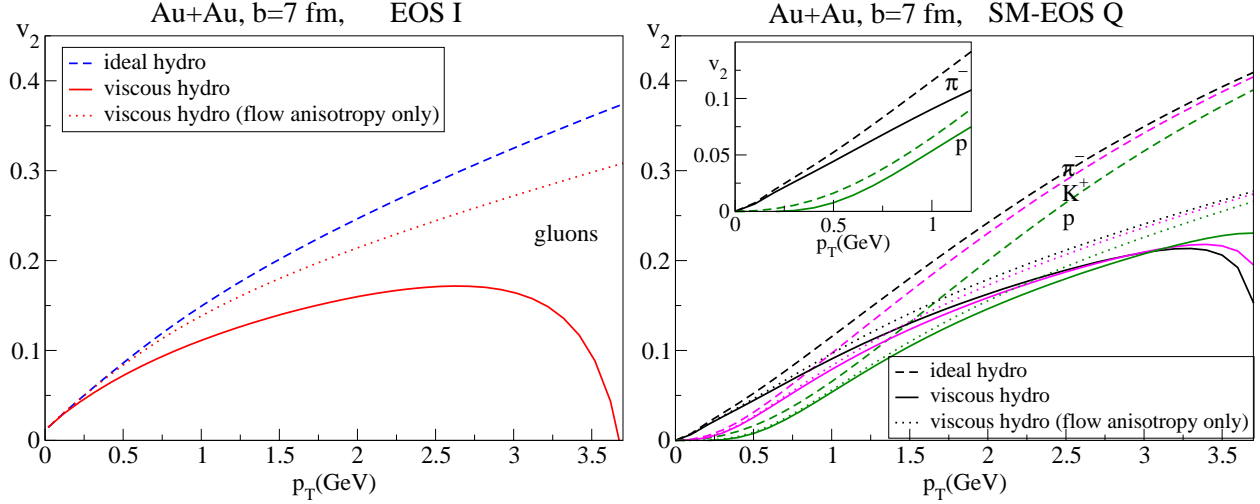


Figure 4.9: Differential elliptic flow $v_2(p_T)$ for Au+Au collisions at $b=7$ fm. *Left panel:* Gluons from evolution with EOS I. *Right panel:* π^- , K^+ , and p from evolution with SM-EOS Q. Dashed lines: ideal hydrodynamics. Solid lines: viscous hydrodynamics. Dotted lines: viscous hydrodynamics without non-equilibrium distortion δf of distribution function at freeze-out.

hydrodynamic formalism, is seen to break down at high p_T , but to do so later for heavier hadrons than for lighter ones. Once the correction exceeds $\mathcal{O}(20\%)$ (indicated by the horizontal dashed line in Fig. 4.8), the calculated spectra can no longer be trusted.

In contrast to viscous hydrodynamics, ideal fluid dynamics has no intrinsic characteristic that will tell us when it starts to break down. Comparison of the calculated elliptic flow v_2 from ideal fluid dynamics with the experimental data from RHIC [26] suggests that the ideal fluid picture begins to break down above $p_T \simeq 2.5$ GeV/ c for pions and above $p_T \simeq 3$ GeV/ c for protons. This phenomenological hierarchy of thresholds where viscous effects appear to become essential is qualitatively consistent with the mass hierarchy from viscous hydrodynamics shown in Fig. 4.8.

In the region $0 < p_T \lesssim 1.5$ GeV/ c , the interplay between m_T - and p_T -dependent terms in Eq. (3.10) is subtle, causing sign changes of the viscous spectral correction depending on hadron mass and p_T (see inset in Fig. 4.8). The fragility of the sign of the effect is also obvious from Fig. 8 in the work by Dusling and Teaney [137] where it is shown that in this p_T region the viscous correction changes sign from positive to negative when freeze-out is shifted from earlier to later times (higher to lower freeze-out temperature). Overall, we agree with them that the viscous correction effects on the p_T -spectra are weak in this region [137]. We will see below that a similar statement does not hold for the elliptic flow.

Elliptic flow for non-central collisions

The shear viscous effects on the suppression of the total momentum anisotropy ϵ'_p discussed in the last section also reflect themselves in a suppression of the final particle elliptic flow v_2 , which is shown in Figure 4.9. Even for the “minimal” viscosity $\frac{\eta}{s} = \frac{1}{4\pi}$ considered here one sees a very strong suppression of the differential elliptic flow $v_2(p_T)$ from a viscous fluid (solid lines) compared to the ideal fluid (dashed lines). Both the viscous reduction of the collective flow anisotropy (whose effect on v_2 is shown as the dotted lines) and the viscous contributions to the anisotropy of the local momentum distribution (embodied in the term δf in Eq. (3.5)) play big parts in this reduction. The runs with EOS I (which is a very hard EOS) decouple more quickly than those with SM-EOS Q; correspondingly, the viscous pressure components are still large at

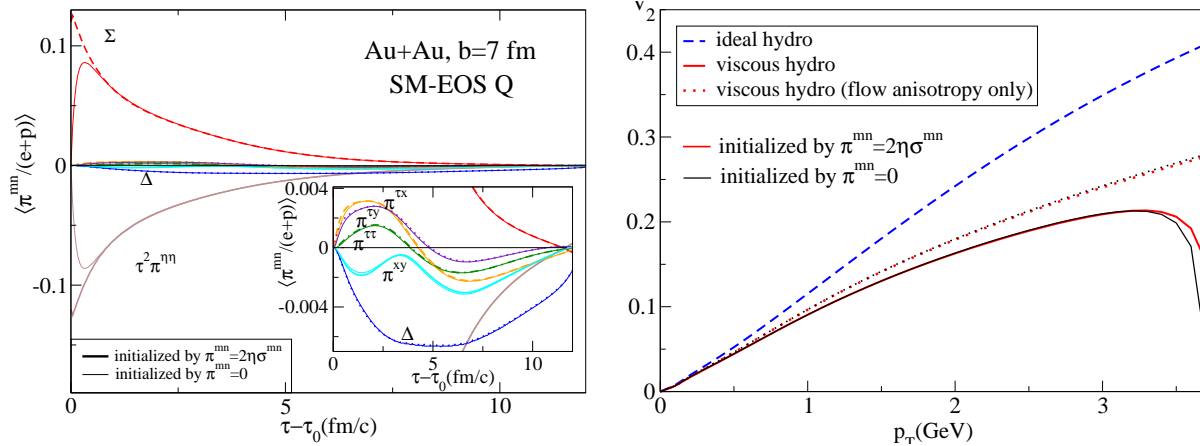


Figure 4.10: Left: Time evolution of the various components of the shear viscous pressure tensor, normalized by the enthalpy and averaged in the transverse plane over the thermalized region inside the freeze-out surface (note that the normalizing factor $e+p \sim T^4$ decreases rapidly with time), compared with different π^{mn} initial conditions. Right: Differential elliptic flow $v_2(p_T)$ for pions from $b = 7$ fm Cu+Cu collisions with SM-EOS Q, compared with different π^{mn} initial conditions. The thick lines in both figures are for N-S initialization: $\pi^{mn}(\tau_0) = 2\eta\sigma^{mn}$, while thin lines are for zero initialization: $\pi^{mn}(\tau_0) = 0$.

freeze-out, and the viscous correction δf to the distribution function plays a bigger role. With SM-EOS Q the fireball doesn't freeze out until π^{mn} has become very small (see Fig. 4.10 below), resulting in much smaller corrections from δf (difference between dashed and dotted lines in Fig. 4.9). On the other hand, due to the longer fireball lifetime the negatively anisotropic viscous pressure has more time to decelerate the buildup of anisotropic flow, so v_2 is strongly reduced because of the much smaller flow-induced momentum anisotropy ϵ_p .

The net effect of all this is that, for Au+Au collisions and in the soft momentum region $p_T < 1.5$ GeV/c, the viscous evolution with $\frac{\eta}{s} = \frac{1}{4\pi}$ leads to a $\sim 30\%$ suppression of v_2 for pions, in both the slope of its p_T -dependence and its p_T -integrated value. (Due to the flatter p_T -spectra from the viscous dynamics, the effect in the p_T -integrated v_2 is not quite as large as for $v_2(p_T)$ at fixed p_T .) For protons, the larger radial flow generated in the viscous evolution also pushes the proton elliptic flow out towards larger p_T (see inserts in the right panel of Fig.4.9), causing an additional suppression of $v_2^p(p_T)$ at fixed p_T . This effect is much weaker in Cu+Cu collisions in [126] where, due to the small fireball size, the radial flow effects are less pronounced.

4.4 Sensitivity to relaxation time and π^{mn} initialization

Initialization of π^{mn} :

Lacking input from a microscopic model of the pre-equilibrium stage preceding the (viscous) hydrodynamic one, one must supply initial conditions for the energy momentum tensor, including the viscous pressure π^{mn} . The most popular choice has been to initialize π^{mn} with its Navier-Stokes value, i.e. to set initially $\pi^{mn} = 2\eta\sigma^{mn}$. Up to this point, this has also been our choice in Chapters 4.2 and 4.3. Ref. [134] advocated the choice $\pi^{mn} = 0$ at time τ_0 in order to minimize viscous effects and thus obtain an upper limit on η/s in a comparison with experimental data. In the present subsection we explore the sensitivity of the final spectra and elliptic flow to these different choices of initialization, keeping all other model parameters unchanged.

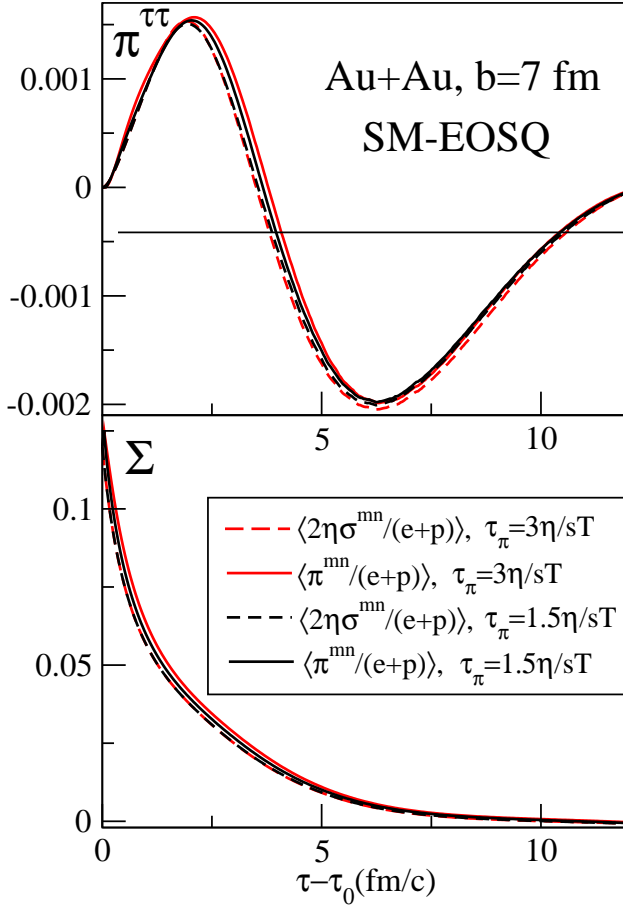


Figure 4.11: Time evolution of the two independent viscous pressure tensor components $\pi^{\tau\tau}$ and $\Sigma = \pi^{xx} + \pi^{yy}$, for central Au+Au collisions (solid lines), compared with their Navier-Stokes limits $2\eta\sigma^{\tau\tau}$ and $2\eta(\sigma^{xx} + \sigma^{yy})$ (dashed lines), for two values of the relaxation time, $\tau_\pi = 3\eta/sT$ (thick red lines) and $\tau_\pi = 1.5\eta/sT$ (thin black lines). All quantities are scaled by the thermal equilibrium enthalpy $e+p$ and transversally averaged over the thermalized region inside the decoupling surface.

Figure 4.10 left shows the time evolution of the viscous pressure tensor, comparing the two different initializations $\pi^{mn}(\tau_0) = 2\eta\sigma^{mn}$ and $\pi^{mn}(\tau_0) = 0$. Differences are visible only at early times $\tau - \tau_0 \lesssim 5\tau_\pi \approx 1 \text{ fm}/c$. After $\tau_\pi \sim 0.2 \text{ fm}/c$, the initial differences have decreased by roughly a factor $1/e$, and after several kinetic scattering times τ_π the hydrodynamic evolution has apparently lost all memory how the viscous terms were initialized.

Correspondingly, the final spectra and elliptic flow show very little sensitivity to the initialization of π^{mn} , as seen in Fig. 4.10 right. With vanishing initial viscous pressure, viscous effects on the final flow anisotropy are a little weaker (dotted lines in Fig. 4.10 right), but this difference is overcompensated in the total elliptic flow by slightly stronger anisotropies of the local rest frame momentum distributions at freeze-out (solid lines in Fig. 4.10 right). For shorter kinetic relaxation times τ_π , the differences resulted from different initializations of π^{mn} would be even smaller.

Relaxation time τ_π :

While the finite relaxation time τ_π for the viscous pressure tensor in the Israel-Stewart formalism eliminates problems with superluminal signal propagation in the relativistic Navier-Stokes theory, it also keeps the viscous pressure from ever fully approaching its Navier-Stokes limit $\pi^{mn} = 2\eta\sigma^{mn}$. In this subsection we explore how far, on average, the viscous pressure evolved by VISH2+1 deviates from its Navier-Stokes limit,

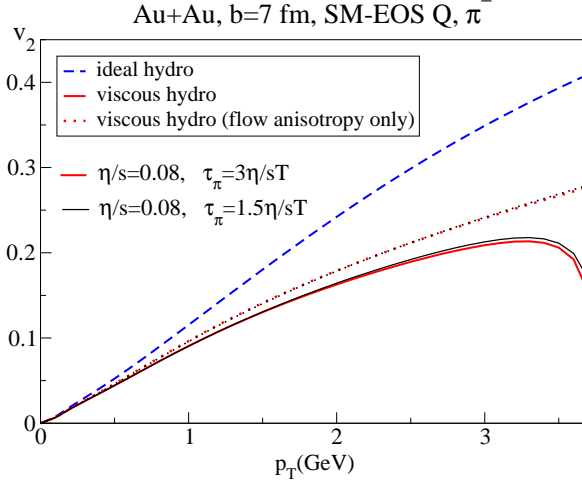


Figure 4.12: Differential elliptic flow $v_2(p_T)$ for π^- from $b=7$ fm Au+Au collisions with SM-EOS Q, calculated from viscous hydrodynamics with two different values for the relaxation time τ_π .

and how this changes if we reduce the relaxation time τ_π by a factor 2. (Another investigation of relaxation time effects and the approach towards the N-S limit can be found in Sec. 7.3.1, where we compare the “full” and “simplified” I-S equations.)

In Figure 4.11 we compare, for non-central Au+Au collisions, the time evolution of the scaled viscous pressure tensor, averaged in the transverse plane over the thermalized region inside the freeze-out surface, with its Navier-Stokes limit, for two values of τ_π , $\tau_\pi = 3\eta/sT = \tau_\pi^{\text{class}}/2$ and $\tau_\pi = \tau_\pi^{\text{class}}/4$. For the larger relaxation time, the deviation from the Navier-Stokes limit is always less than 10%, and this fraction greatly decreases at later times. For the twice shorter relaxation time, the fractional deviation from Navier-Stokes decreases by somewhat more than a factor 2 and never exceeds a value of about 5%.

Figure 4.12 shows the corresponding elliptic flow v_2 . For the viscous fluid curves (both the flow anisotropy only and the full viscous hydrodynamics curves), one finds only very slight dependencies on relaxation times τ_π . This result is in sharp contrast to what we found in [126] for Cu+Cu collisions at $b=7$ fm, where we saw a much stronger dependence on the relaxation time. As already pointed out in [127], the main reason behind this is that the calculations presented here and in [126] use different versions of the I-S equations. The “full” I-S equation used here greatly reduces the dependence on τ_π for final observables compared to the “simplified” I-S equation used in the early calculations in [126], which lead to a much stronger sensitivity to τ_π . This will be further investigated in Chap.7.3.1.

4.5 Shear viscosity effects: dependence on system size and collision energies

In Ref. [127], we showed qualitatively that shear viscosity effects are larger for smaller systems, by comparing the viscous v_2 suppression for Au+Au collisions at $b=7$ fm and Cu+Cu collisions at $b=7$ fm. Although the two systems have similar initial eccentricity ε_x , the latter system is not a scaled transformation of the former one due to the Woods-Saxon parametrization in the Glauber initialization (see Chap. 3.2). To quantitatively study the dependence of shear viscosity effects on system size and collision energies, we here set the initial energy density to a simple Gaussian function, $e(x, y, \tau_0) = e_0 \cdot \exp(-\frac{x^2}{(R/2)^2} - \frac{y^2}{R^2})$. This construction creates an initially elliptic fireball with eccentricity $\varepsilon_x(\tau_0) = 0.6$, independent of the parameter R . To study system size effects, we do comparison runs with $R = 4$ fm, $\tau_0 = 0.4$ fm/c and $R = 6$ fm, $\tau_0 = 0.6$ fm/c; the second system is an exact scale transformation of the first one in both space and time, by

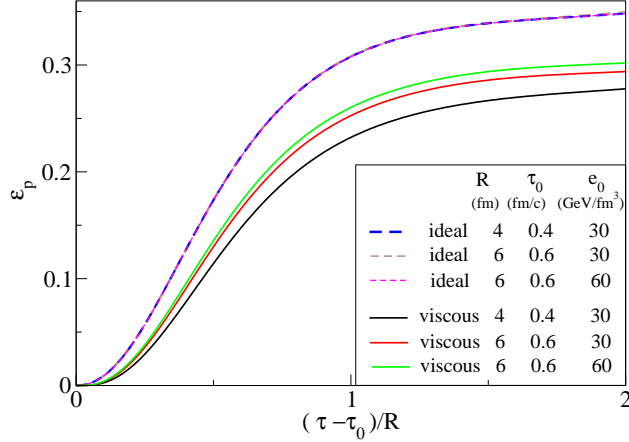


Figure 4.13: Time evolution of total momentum anisotropy ε'_p from ideal and viscous hydrodynamics with different initial conditions. For viscous hydrodynamics: $\eta/s = 0.08$ and $\tau_\pi = \frac{3\eta}{sT}$.

a factor 1.5. To study collision energy effects, we compare hydrodynamic evolutions starting with an initial energy density $e_0 = 30 \text{ GeV/fm}^3$ and with $e_0 = 60 \text{ GeV/fm}^3$.

Fig. 4.13 shows the time evolution of total momentum anisotropy ε'_p for different initial conditions (with ideal EOS: EOS I). Instead of using the proper time τ for the horizontal axis, we change it to the normalized unitless “time” $(\tau - \tau_0)/R$. For ideal fluid evolution, one observes exact scale invariance, independent of system size or collision energy, due to the scale invariance of the ideal hydrodynamic equations. However, realistic simulations for relativistic heavy ion collisions requires a freeze-out condition, a realistic EOS with a phase transition, and using more complicated initial conditions (e.g. the Glauber model). All of these introduce additional external scales (an external time scale through the freeze-out condition, an external energy scale through T_c in the EOS, the surface thickness in the Wood-Saxon density profile), which break the scale invariance of ideal hydrodynamics. This will be discussed in more detail in Chap. 5.

Microscopically, a finite shear viscosity corresponds to a finite mean free path, which introduces an additional length scale, again breaking the scale invariance of the hydrodynamic system. If one examines the analytical solution (A.9) for the relativistic Navier-Stokes equations for a (0+1)-d longitudinally boost invariant system (see Appendix A.3.2), one finds a scale-breaking term proportional to $\frac{\eta}{s\tau_0 T_0}$. This term shows that, for a constant η/s , the scale breaking effect is smaller for larger systems or higher collision energies (corresponding to larger τ_0 or T_0 , respectively). For (2+1)-d viscous hydrodynamics, there is no analytical solution. The numerical results in Fig. 4.13 clearly show scale breaking effects caused by shear viscosity in the viscous ε'_p suppression, relatively to the (universal) ideal fluid lines. For identical collision energy, one finds stronger suppression (i.e. larger scale breaking effects) in the smaller system (comparing red and black solid lines); for identical system size, one finds smaller viscous ε'_p suppression for higher collision energies (comparing red and green solid lines). Both tendencies agree with qualitative expectations based on the analytical results for the (1+1)-d case. The system size and collision energy dependence of the viscous ε'_p suppression translates into a corresponding dependence of the viscous v_2 suppression, which will be further studied in Chap. 5.

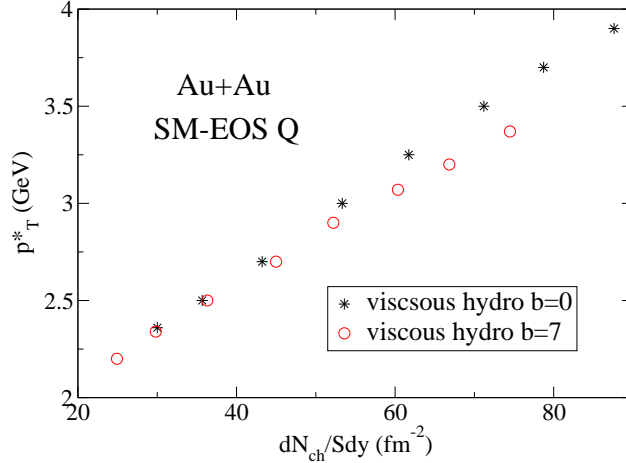


Figure 4.14: Characteristic transverse momentum p_T^* where the viscous corrections to the final pion spectrum become so large ($> 20\%$) that the spectrum becomes unreliable, as a function $(1/S)dN_{ch}/dy$. Stars are for central Au+Au collisions, open circles for semi-central Au+Au collisions at $b = 7$ fm.

4.6 Breakdown of viscous hydrodynamics at high p_T

As indicated by the horizontal dashed lines in Figs. 4.8, the assumption $|\delta f| \ll |f_{eq}|$ under which the viscous hydrodynamic framework is valid breaks down at sufficiently large transverse momenta. For a quantitative assessment we assume conservatively that viscous hydrodynamic predictions are no longer reliable when the viscous corrections to the particle spectra exceed 20%. Fig. 4.8 shows that the characteristic transverse momentum p_T^* where this occurs depends on the particle species and increases with particle mass. To be specific, we here consider p_T^* for pions — the values for protons would be about 15% higher.

In Fig. 4.14 we show the breakdown momentum p_T^* for pions as a function of $(1/S)dN_{ch}/dy$ (final multiplicity dN_{ch}/dy per overlap area S , the details for calculating $(1/S)dN_{ch}/dy$ can be found in Chap. 5.2), for both central and semi-central Au+Au collisions. (Larger $(1/S)dN_{ch}/dy$ corresponds larger collision energies. The initial time was fixed by taking the relation $\tau_0 T_0 = \text{const.}$, following Ref. [249].) One finds that p_T^* rises with collision energy for both central and non-central Au+Au collisions. The rise of p_T^* with increasing $e(r=0)$ reflects the growing fireball lifetime which leads to smaller viscous pressure components at freeze-out. This lifetime effect is obviously stronger for central than for non-central collisions, leading to the faster rise of the stars than the open circles in Fig. 4.14. For fixed $(1/S)dN_{ch}/dy$ (which corresponds to similar initial entropy densities in the fireball center), we find that in central collisions ($b = 0$) the validity of viscous hydrodynamics extends to *larger* values of p_T than in non-central collisions ($b = 7$ fm): Viscous effects are more serious in non-central than in central collisions.

4.7 Conclusions

In this chapter, we numerically studied the shear viscous effects on the hydrodynamic evolution, final hadron spectra, and elliptic flow v_2 . Complementary to our early paper [125, 126], which concentrated on Cu+Cu collisions and used the “simplified I-S equation”, we studied Au+Au collisions, using an updated version of VISH2+1 that solves the “full I-S equation”.

By comparing ideal and viscous hydrodynamic runs, we explored the effects of shear viscosity for a “minimally” [146] viscous fluid with $\frac{\eta}{s} = \frac{1}{4\pi}$ in central and non-central Au+Au collisions, comparing the

evolution for two different equations of state – an ideal massless parton gas (EOS I) and an EOS with a semirealistic parametrization of the quark-hadron phase transition (SM-EOS Q).

We found that shear viscosity decelerates longitudinal expansion, but accelerates the build-up of transverse flow. This slows the cooling process initially, leading to a longer lifetime for the QGP phase, but causes accelerated cooling at later stages by faster transverse expansion. For SM-EOS Q, we saw that viscous pressure gradients during the mixed phase increase the acceleration during this stage and slightly reduce its lifetime. They counteract large gradients of the radial velocity profile that appear in ideal fluid dynamics as a result of the softness of the EOS in the mixed phase, thereby *de facto* smoothing the assumed first-order phase transition of SM-EOS Q into a rapid cross-over transition. In the end the larger radial flow developing in viscous hydrodynamics leads to flatter transverse momentum spectra of the finally emitted particles, while their azimuthal anisotropy and the final elliptic flow v_2 in non-central heavy-ion collisions is found to be strongly reduced. These generic shear viscous effects are qualitatively similar for different systems at different collision energies, as seen by comparing the results for Au+Au collision shown in this chapter with our early results for Cu+Cu collision presented in Ref. [126]. On a more quantitative level, one finds that smaller systems and lower collision energies lead to larger viscous effects, as shown in Chap. 4.5.

Our studies show that shear viscous effects are strongest during the early stage of the expansion phase when the longitudinal expansion rate is largest. The discussion in Chap. 4.5 suggests that $\Gamma_s \theta = \frac{\eta}{sT} (\partial \cdot u)$ is the parameter that controls the strength of viscous effects. At later times the viscous corrections become small, although non-negligible. Small non-zero viscous pressure components along the hadronic decoupling surface have significant effects on the final hadron spectra that grow quadratically with transverse momentum and thus limit the applicability of the viscous hydrodynamic calculation to transverse momenta below 2-3 GeV/ c , depending on impact parameter, collision energy, and particle mass. Viscous effects are more important in peripheral than in central collisions, and larger for light than for heavy particles. Since the breakdown of viscous hydrodynamics is signalled by the theory itself, through the relative magnitude of the viscous pressure, the applicability of the theory can be checked quantitatively case by case and during each stage of the expansion.

For the kinetic relaxation times τ_π considered in the present work, sensitivities to the initial value of the viscous pressure tensor were found to be small and practically negligible. Sensitivity of the elliptic flow to the value of τ_π was also found to be weak if the full I-S equation is used when solving viscous hydrodynamics.

The most important finding here is the large v_2 suppression caused by shear viscosity. While the viscous hardening of the hadron p_T -spectra can be largely absorbed by retuning the initial conditions, starting the transverse expansion later and with lower initial entropy density [131, 132], this only acerbates the viscous effects on the elliptic flow v_2 which is further reduced by the decreased fireball lifetime following the retuning. The reduction of the elliptic flow v_2 by shear viscous effects is therefore a sensitive and robust diagnostic tool for shear viscosity of a fluid. This exciting finding can be used to extract the shear viscosity from experimental data. Similar conclusions have been obtained by several groups in the past three years, using independently developed viscous hydrodynamic codes, with different initial and final conditions and different EOS input [125, 126, 134, 135, 137]. The extraction of the QGP viscosity from experimental data, together with an uncertainty analysis based on currently available viscous hydrodynamic studies, will be discussed in Chap. 8.

Chapter 5: Multiplicity Scaling of v_2/ε and Shear Viscosity Effects

5.1 Introduction

This chapter will continue to investigate shear viscosity effects by studying the multiplicity scaling of the normalized elliptic flow v_2/ε within ideal and viscous hydrodynamics. The results compiled in this thesis are based on our paper [127]. The motivation for this research is provided by the well-known systematic comparison of Voloshin *et al.* [250, 251, 252] of elliptic flow data with ideal fluid dynamical predictions which suggests that the elliptic flow parameter v_2 scaled by the initial source eccentricity ε , v_2/ε , while strongly deviating from ideal hydrodynamics at low multiplicities, still scales with the final multiplicity dN_{ch}/dy per unit overlap area S :

$$\frac{v_2}{\varepsilon} \propto \frac{1}{S} \frac{dN_{ch}}{dy}. \quad (5.1)$$

For ideal fluids the right hand side is a direct measure of the initial entropy density [253]. The scaling (5.1) implies that all dependence on impact parameter, collision energy and system size can be, to good approximation, absorbed by simply taking into account how these control parameters change the final hadron multiplicity density. We will call this observation simply “multiplicity scaling of the elliptic flow”, where “elliptic flow” is a shorthand for the eccentricity-scaled elliptic flow v_2/ε and “multiplicity” stands for $(1/S)dN_{ch}/dy$.

Such a scaling is expected for ideal fluid dynamics whose equations of motion are scale invariant and where the eccentricity-scaled elliptic flow is therefore predicted [72, 254] to depend only on the squared speed of sound, $c_s^2 = \frac{\partial p}{\partial e}$, which describes the stiffness of the equation of state (EOS) or “pushing power” of the hydrodynamically expanding matter. It has been known, however, for many years [223] that this ideal-fluid scaling is broken by the final freeze-out of the matter: if hadron freeze-out is controlled by hadronic cross sections (mean free paths) or simply parametrized by a critical decoupling energy density e_{dec} or temperature T_{dec} , this introduces an additional scale into the problem that is independent of (or at least not directly related to) the initial geometry of the fireball. This breaks the above argument based on scale invariance of the ideal fluid equations of motion. We will show here that this also leads to a breaking of the multiplicity scaling of v_2/ε not only in the most peripheral or lowest energy collisions, where freeze-out obviously cuts the hydrodynamic evolution short since the freeze-out density is reached before the flow anisotropy can fully build up [223], but even in the most central collisions at RHIC where freeze-out still terminates the hydrodynamic evolution before the elliptic flow can fully saturate (see also [128, 229]).

The more interesting aspect of the experimentally observed scaling is, however, its apparent validity in regions where ideal fluid dynamics does not work (these encompass most of the available data [250]). Many years ago, simple scaling laws for the centrality dependence of elliptic flow were derived from kinetic theory in the dilute gas limit, where the particles in the medium suffer at most one rescattering before decoupling [255, 256]; these can be reinterpreted in terms of multiplicity scaling for v_2/ε . The dilute gas limit is expected to hold for very small collision systems, very large impact parameters or very low collision energies. More recently, a successful attempt was made to phenomenologically connect the dilute gas and hydrodynamic limits with a 1-parameter fit involving the Knudsen number [257]. This fit works very well for Au+Au and Cu+Cu data from RHIC, but predicts that even in the most central Au+Au collisions at RHIC the ideal fluid dynamical limit has not yet been reached and is missed by at least 25% [257]. In this chapter, we use viscous

relativistic hydrodynamics to explore the multiplicity scaling of v_2/ε in the phenomenologically relevant region. We conclude (not surprisingly since much of the available data is from regions where the viscous hadronic phase plays a large role [229]) that the multiplicity scaling data [250, 251, 252] require significant shear viscosity for the medium, especially during its hadronic stage, but also that viscous hydrodynamics predicts subtle scaling violations which seem to be qualitatively consistent with trends seen in the data (even if the experimental evidence for scaling violations is presently not statistically robust) and whose magnitude is sensitive to the specific shear viscosity η/s . This gives hope that future, more precise data can help constrain the QGP shear viscosity through exactly such scaling violations.

We should caution the reader that, similar to Ref. [257] which used a constant (time-independent) cross section for the Knudsen number, our viscous hydrodynamic calculations are done with a constant (temperature-independent) specific shear viscosity η/s . Neither assumption is realistic, and we expect η/s in particular to show strong temperature dependence near T_c (the critical temperature for the quark-hadron phase transition, see Chap. 1.4 for details) and emerge from the phase transition with much larger values than in the QGP phase. Comparisons between the results presented here and experimental data are therefore, at best, indicative of qualitative trends, and improved calculations, which in particular match viscous hydrodynamics to a realistic hadron cascade below T_c , are required before quantitative extraction of η/s from experimental data can be attempted.

5.2 Multiplicity scaling of v_2/ε in ideal and viscous hydrodynamics

In this section we explore the multiplicity scaling (as defined in the introduction) of the eccentricity-scaled elliptic flow v_2/ε , comparing ideal fluid dynamics with that of near-minimally viscous fluids with specific shear viscosity $\frac{\eta}{s} = \mathcal{O}\left(\frac{1}{4\pi}\right)$ with three different EOS: EOS I, SM-EOS Q and EOS L (see Fig.3.2 and explanation there.). Here we consider both Au+Au collisions and Cu+Cu collisions. The initial conditions, final conditions and other free inputs are described in Chap. 3. In the spectra calculation, we neglect resonance decays and only show the elliptic flow of directly emitted pions. To estimate the total charged hadron multiplicity, we take the directly emitted positive pions, multiply by 1.5 to roughly account for multiplication by resonance decays at T_{dec} , then multiply by another factor $2 \times 1.2 = 2.4$ to account for the negatives and roughly 20% of final charged hadrons that are not pions. A proper calculation of the resonance decay chain is computationally expensive and, for a systematic study like the one presented here that requires hundreds of runs of VISH2+1, beyond our presently available resources.

5.2.1 EOS I: conformal fluids with $e = 3p$

We begin with the simple case of a conformal fluid with the equation of state $e = 3p$ (EOS I), without phase transition. In this case the speed of sound is a constant, independent of temperature T , $c_s^2 = \frac{1}{3}$. For the ideal fluid case, naive scaling arguments based on the scale invariance of the ideal fluid equations of motion would thus predict a constant v_2/ε , independent of multiplicity density $(1/S)dN_{\text{ch}}/dy$. (The nuclear overlap area S is computed as $S = \pi\sqrt{\langle x^2 \rangle \langle y^2 \rangle}$ where $\langle \dots \rangle$ denotes the energy density weighted average over the transverse plane, and we here use the standard the eccentricity $\varepsilon = \frac{\langle y^2 - x^2 \rangle}{\langle y^2 + x^2 \rangle}$, which is slightly different from the one we used in [127]. The left panel in Fig. 5.1 clearly contradicts this expectation. Freeze-out at $T_{\text{dec}} = 130$ MeV cuts the hydrodynamic evolution of the momentum anisotropy ε_p short before the elliptic flow has fully saturated. As the left panel of the figure shows, this not only causes a strong suppression of v_2/ε at low multiplicity densities, where the time between beginning of the hydrodynamic expansion and freeze-out becomes very short, but it also breaks the multiplicity scaling at high multiplicity density, albeit more weakly. At a fixed value of $(1/S)dN_{\text{ch}}/dy$, one sees larger v_2/ε for more central collisions initiated at lower collision energies (corresponding to smaller e_0 parameters) than for more peripheral collisions between

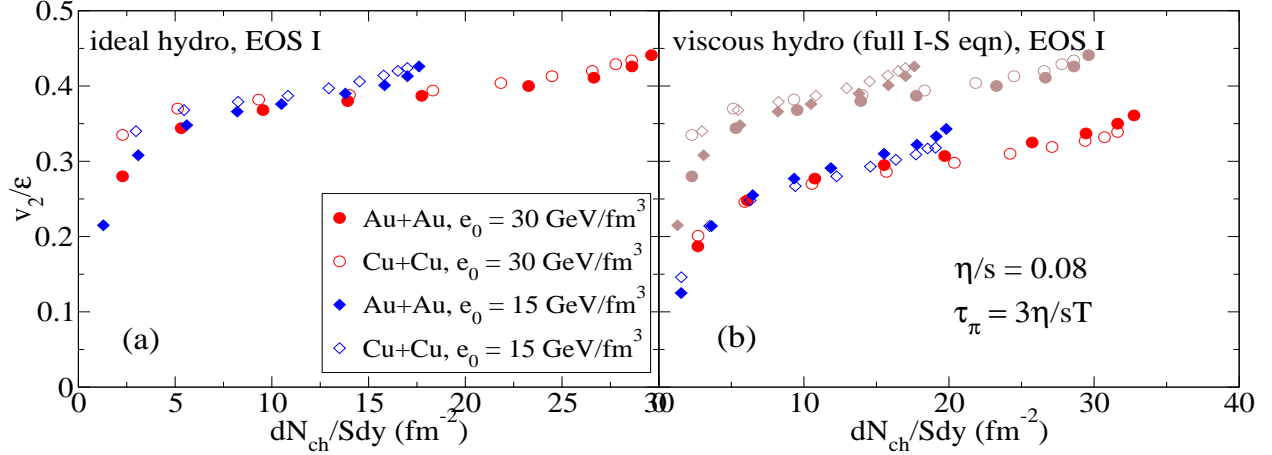


Figure 5.1: The eccentricity-scaled elliptic flow v_2/ε as a function of charged multiplicity density, $(1/S)dN_{\text{ch}}/dy$, for a conformal fluid with EOS I. Results for Cu+Cu and Au+Au collisions with two different initial energy densities at a variety of impact parameters, as indicated in the legend, are superimposed. Results from ideal fluid dynamics (a) are compared with those from viscous hydrodynamics, using the full Israel-Stewart equations (b). In all cases approximate, but not perfect multiplicity scaling is observed (see text for discussion). In panels (b), the ideal fluid results from the left panel are reproduced as brown symbols for comparison.

the same nuclei at higher beam energies, and also for more central Cu+Cu collisions (with a rounder shape) than for more peripheral Au+Au collisions (with a more deformed initial shape). We find that the larger v_2/ε values in central compared to peripheral collisions can be traced directly to somewhat longer lifetimes of the corresponding fireballs, i.e. to the availability of more time to approach the saturation values of the momentum anisotropy and elliptic flow before reaching freeze-out [128] (see Fig. A.5 in Appendix A.5). These freeze-out induced scaling violations in ideal fluid dynamics disappear at sufficiently high collision energies (i.e. large e_0) where the momentum anisotropy has time to fully saturate in *all* collision systems and at *all* impact parameters, before freezing out (see Fig. 5.2 below).

The right panels in Fig. 5.1 show the analogous results for a minimally viscous fluid with $\frac{\eta}{s} = \frac{1}{4\pi}$ and kinetic relaxation time $\tau_\pi = \frac{3\eta}{sT}$. Along with the suppression of v_2/ε by shear viscosity, we see the appearance of additional scale-breaking effects. Shear viscosity breaks the multiplicity scaling of v_2/ε because (as shown in the preceding section) viscous effects are larger in smaller collision fireballs. Consequently, if we compare different collision systems that produce the same charged multiplicity density $(1/S)dN_{\text{ch}}/dy$, we find smaller v_2/ε for Cu+Cu than for Au+Au collisions, and for peripheral Au+Au collisions at higher collision energy than for more central Au+Au collisions at lower collision energy. Again, the amount of elliptic flow v_2/ε generated for given $(1/S)dN_{\text{ch}}/dy$ correlates directly with the time before freeze-out, as shown in the right panel of Fig. A.5 in Appendix A.5.

Viscous effects also generates entropy, which increase the final charged multiplicity dN_{ch}/dy . Comparing in the right panels of Fig. 5.1 the brown (shaded) symbols from ideal fluid dynamics with the colored (solid) symbols for viscous hydrodynamics, points corresponding to the same collision system and impact parameter are seen to be shifted to the right. This enhances the scaling violations: for a given collision system, impact parameter and collision energy, viscosity decreases the eccentricity scaled elliptic flow v_2/ε , pushing the corresponding point downward in the diagram, and simultaneously increases the entropy, pushing the corresponding point horizontally to the right. The combination of these two effects separates the curves for different collision systems and energies farther in viscous hydrodynamics than in ideal fluid dynamics.

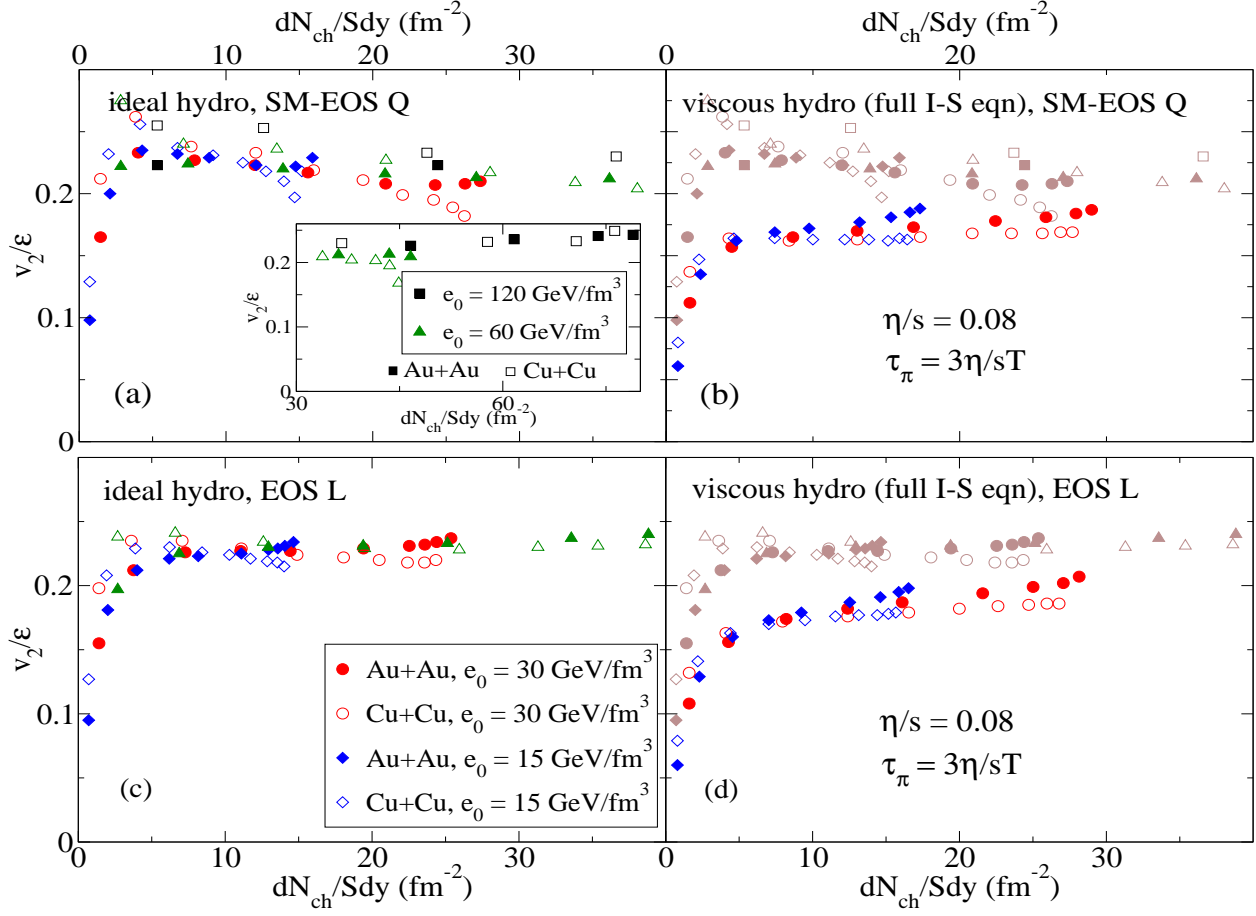


Figure 5.2: Same as Fig. 5.1, but for SM-EOS Q (top row) and EOS L (bottom row). For the ideal fluid case (a,c) an extended range of e_0 values up to $e_0 = 120 \text{ GeV/fm}^3$ was studied, in order to show that v_2/ϵ eventually increases again at higher collision energies [223].

5.2.2 Phase transition effects: EOS Q vs. EOS L

Figure 5.2 shows the analogous results if the fluid evolves under the influence of an equation of state with a quark-hadron phase transition, EOS Q (top row) or EOS L (bottom row). Again approximate multiplicity scaling of v_2/ϵ is observed, but some scale-breaking effects are visible in both ideal and viscous hydrodynamics. For the equations of state with a phase transition, the scale-breaking effects are actually larger in the ideal than in the viscous case, i.e. *in viscous hydrodynamics v_2/ϵ shows better multiplicity scaling than in ideal fluid dynamics!* We interpret the large scale-breaking effects in the ideal fluid case as a complication arising from interference between the freeze-out process and the weak acceleration of matter in the phase transition region. This interpretation is supported by a comparison between SM-EOS Q with its first-order phase transition (upper left panel in Fig. 5.2) and the smooth crossover transition in EOS L (lower left panel): for ideal fluids, the scale-breaking effects are obviously larger for SM-EOS Q than for EOS L. As already observed in [125] and in Chap. 4.2, shear viscosity effectively smears out the phase transition and reduces its effect on the dynamics. In Fig. 5.2 this is clearly seen on the left side of each panel (i.e. at small values of $\frac{1}{S} \frac{dN_{ch}}{dy}$) where for the ideal fluid v_2/ϵ shows a non-monotonic peak structure [223] that is completely gone in the viscous case.

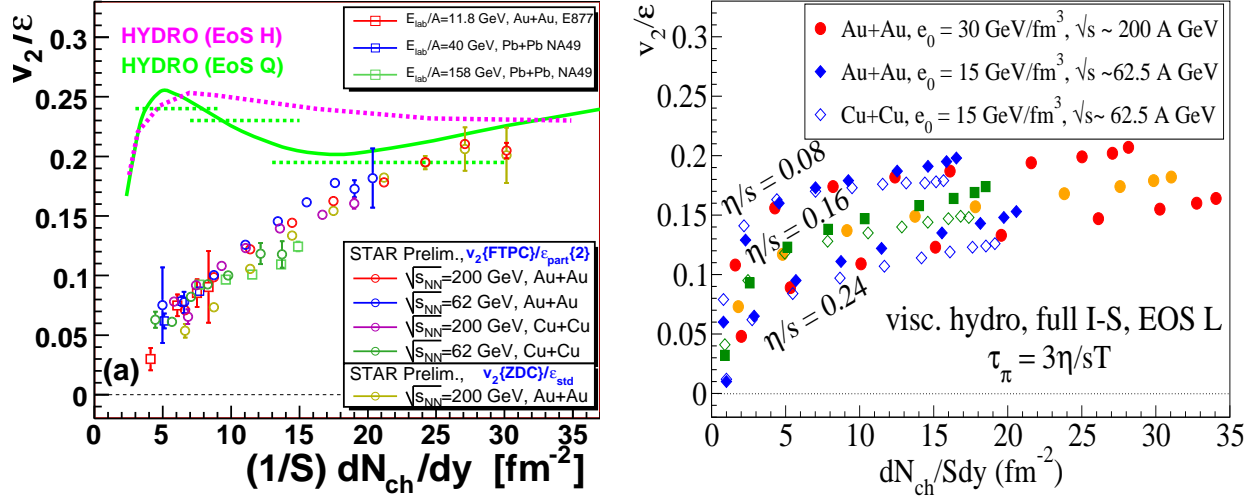


Figure 5.3: (a) The experimental observation of multiplicity scaling for v_2/ϵ , with data from Au+Au, Pb+Pb, and Cu+Cu collisions at RHIC, SPS and AGS [251,252]. (b) Theoretical prediction of approximate multiplicity scaling from viscous hydrodynamics using the full I-S equations, for three different (constant) specific entropy values $\eta/s = 0.08, 0.16, 0.24$.

It is interesting to observe that, for ideal fluids, EOS L leads to about 10% more elliptic flow under RHIC conditions than SM-EoS Q. The reason is that in the phase transition region EOS L is stiffer than SM-EoS Q. This plays an important role at RHIC because the softness of the EOS near T_c inhibits the buildup of elliptic flow exactly under RHIC conditions [223]. As a corollary we note that, if RHIC elliptic flow data exhaust ideal fluid predictions made with SM-EoS Q [26], they will not exhaust ideal fluid predictions based on EOS L, thus leaving some room for shear viscous effects.

5.2.3 A look at the experimental data

Figure 5.3(a) shows the famous experimental plot by Voloshin [251,252] which provides empirical evidence for multiplicity scaling of v_2/ϵ . The lines labelled “HYDRO” are sketches for expectations from rough ideal fluid dynamics, based on early calculations presented in [223] for v_2 in Au+Au collisions at fixed impact parameter $b = 7$ fm as a function of multiplicity (parametrized by e_0). They should be replaced by the curves shown in the left panels of Fig. 5.2.

In Fig. 5.3(b) we present multiplicity scaling curves for v_2/ϵ obtained from viscous hydrodynamics with the full I-S equations. On a superficial level, the theoretical curves show qualitative similarity with the experimental data, giving correct ball-park numbers if one assumes $\eta/s \sim 0.24 \sim 3/4\pi$. Interestingly, ignoring experimental error bars, one can see evidence for small scaling violations in the experimental data whose pattern agrees with the theoretical predictions from viscous hydrodynamics (see discussion at the end of Sec. 5.2.1): the 62.5 A GeV Au+Au data lie slightly above the 200 A GeV Au+Au points, and the 200 A GeV Cu+Cu points fall slightly below the 62.5 A GeV Au+Au data. Of course, these fine features of the experimental data are presently not statistically robust (significant); much more precise data are needed to confirm or disprove the theoretical predictions, but upcoming high-statistic runs at RHIC should be able to deliver them.

Closer inspection of the two panels in Fig. 5.3 shows, however, that the theoretical scaling curves have the wrong slope: on the left side of the plot, i.e. for small multiplicity densities, the data seem to point

towards larger specific shear viscosities $\frac{\eta}{s} > 3 \times \frac{1}{4\pi}$ whereas on the right side of the plot, for $\frac{1}{S} \frac{dN_{\text{ch}}}{dy} > 20 \text{ fm}^{-2}$, the experimental data require smaller shear viscosities, $\frac{\eta}{s} \lesssim (1-2) \times \frac{1}{4\pi}$. But this is not at all unexpected: Collisions represented by points in the right half of the plot correspond to high collision energies and large initial energy densities whose expanding fireballs spend the largest fraction of their life in the QGP phase. Fireballs created in collisions represented by points in the left part of the diagram have smaller initial energy densities and thus spend most of their time in the much more viscous hadronic phase [229]. A meaningful comparison between theory and experiment thus must necessarily account for the temperature dependence of η/s and its dramatic increase during the quark-hadron phase transition [37]. This would lead to scaling curves in Fig. 5.3(b) with a larger slope that can better reproduce the data. What one can say already now is that the high-energy end of Fig. 5.3 requires very small specific shear viscosity η/s for the QGP, of the same order as the minimal value postulated in [146] (unless, by using the Glauber model eccentricity instead of the fKLN eccentricity, the initial source eccentricity ε was strongly underestimated in the experimental data, see discussion in Chap. 8).

5.3 Multiplicity scaling of entropy production in viscous hydrodynamics

In this section, we investigate the entropy production in viscous hydrodynamics for Au+Au and Cu+Cu systems at a variety of collision energies and impact parameters. Similar to Ref. [132], we compute entropy production by exploiting the proportionality of final entropy to final charged multiplicity. We compute the final multiplicity dN_{ch}/dy for both ideal and viscous hydrodynamics and then equate the fractional increase in dN_{ch}/dy with the fractional increase in dS/dy . This ignores a small negative correction due to the viscous deviation of the distribution function on the freeze-out hypersurface from local equilibrium [201, 212] which slightly reduces the entropy per finally observed particle in the viscous case. The real entropy production is thus slightly smaller than calculated with our prescription. However, since on the freeze-out surface the viscous pressure components are small [125], this correction should be negligible.

We checked the above procedure by also directly integrating the viscous entropy production rate $\partial \cdot s = \pi^{\mu\nu} \pi_{\mu\nu} / 2\eta$ over the space-time volume enclosed between the initial condition Cauchy surface and the final freeze-out surface. This method results in slightly larger entropy production, the relative difference amounting to about 0.7% (or about 0.07% in the absolute value of $\Delta S/S_0$) for central Au+Au collisions. Since the estimate from the final multiplicity gives a lower entropy production value even without accounting for the somewhat smaller entropy per particle in the viscous case, we conclude that entropy production due to *numerical* viscosity must be a bit smaller in the viscous fluid than in the ideal one. This is not unreasonable, given the observation in [125] that, compared to the ideal fluid case, the physical viscosity smoothens the strong velocity gradients near the quark-hadron phase transition, thereby presumably also reducing the effects of numerical viscosity.²³

Figure 5.4 shows the viscous entropy production ΔS , as a fraction of the initial entropy S_0 , for Cu+Cu and Au+Au collisions at various impact parameters and collision energies, as a function of multiplicity density. One observes approximate multiplicity scaling of the fractional entropy production, with scaling functions that depend on the equation of state. As for v_2/ε , we see small scale-breaking effects, but generally the produced entropy fraction shows better multiplicity scaling than elliptic flow. The scale breaking effects for the viscous entropy production rate go in the same direction as with elliptic flow insofar as, at the same value of $\frac{1}{S} \frac{dN_{\text{ch}}}{dy}$, larger collision systems and more central collisions produce fractionally more entropy than smaller or more peripheral collisions, due to their longer lifetimes before freeze-out (see Fig. A.5). Figure 5.4

²³ We note that our viscous evolution starts earlier (at $\tau_0 = 0.6 \text{ fm}/c$) than that of Ref. [132] (who use $\tau_0 = 1 \text{ fm}/c$). This earlier start results in larger entropy production fractions. As the inset in Fig. 5.4(b) shows, most of the entropy is produced during the early stage of the expansion. We have confirmed that the difference between Ref. [132] and the work here is quantitatively reproduced by the entropy generated during the time interval from 0.6 to 1.0 fm/c, which can be calculated to excellent approximation analytically [211] (using Eq. (D3) in Ref. [125]) by assuming boost-invariant longitudinal expansion without transverse flow during this period.

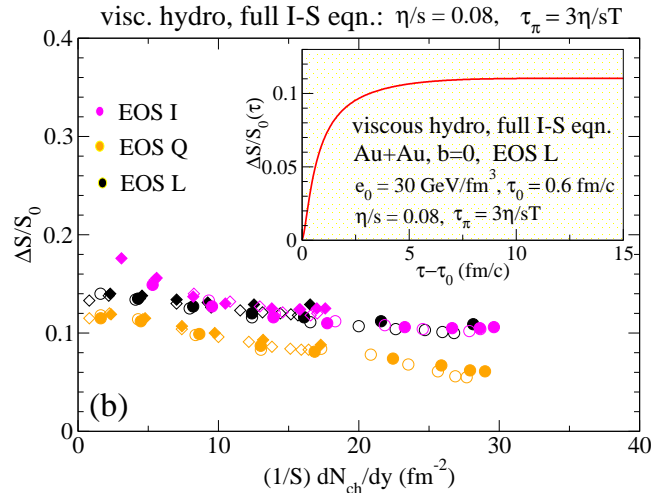


Figure 5.4: Entropy production ΔS , normalized by the initial entropy S_0 , as a function of charged multiplicity density $\frac{1}{S} \frac{dN_{\text{ch}}}{dy}$. Calculations with VISH2+1 were performed for Au+Au and Cu+Cu collisions at various impact parameters and collision energies, using $\eta/s = 0.08$, $\tau_\pi = 3\eta/sT$, and three different equations of state (EOS I, SM-EOS Q, and EOS L). The inset in panel (b) shows the entropy production as a function of time, for central Au+Au collisions with parameters as indicated in the legend.

also shows 15–25% differences between the entropy production rates for EOS Q (first order phase transition) and EOS L (rapid crossover transition). The differences are largest for the most central Au+Au and Cu+Cu collisions at top RHIC energies. The somewhat stiffer nature of EOS L near T_c causes the fireball to expand faster and with higher acceleration, leading to larger viscous effects than for EOS Q.

An important comment relates to the negative overall slope of the scaling curves for entropy production shown in Figs. 5.4: Since peripheral collisions produce relatively more entropy than central collisions, and the produced entropy is reflected in the final charged hadron multiplicity, the collision centrality dependence of hadron multiplicities is altered by viscous effects. When viscous effects are accounted for, the charged multiplicity dN_{ch}/dy will rise more slowly as a function of the number of participant nucleons N_{part} than for an ideal fluid with the same set of initial conditions. In a Glauber model parametrization of the initial conditions [26] this tempering effect will have to be compensated for by increasing the “hard” component in the initial entropy production, i.e. the component that scales with the density of binary collisions and is thus responsible for the non-linear increase of dN_{ch}/dy with N_{part} . In the Color Glass Condensate approach [225] this non-linear rise is controlled by the centrality dependence of the saturation momentum scale Q_s , with no free parameters to tune. It remains to be seen whether the success of the CGC model in describing the centrality dependence of dN_{ch}/dy [258] survives the inclusion of entropy (or multiplicity) producing effects resulting from shear viscosity during the evolution from the initial CGC to the finally observed state.

5.4 Concluding Remarks

The main motivation for the work presented in this chapter was provided by the experimentally observed multiplicity scaling of the elliptic flow, shown in Fig. 5.3a, and its deviation at low multiplicities from ideal fluid dynamical predictions. We saw that many of the observed features are qualitatively consistent with viscous hydrodynamic calculations as presented here, and that the same calculations also predict approximate multiplicity scaling for viscous entropy production. Our studies revealed, however, that even for ideal fluid

dynamics the multiplicity scaling of the elliptic flow is not perfect, with small scaling violations introduced by the initial density profiles and by the freeze-out process which cuts the evolution of elliptic flow short. Even at RHIC energies, where the elliptic flow almost saturates before freeze-out, kinetic decoupling truncates the momentum anisotropy at values slightly below their asymptotic saturation value, and the deviations depend on the size of the colliding nuclei and the deformation of the fireball created in the collision through the time available for building elliptic flow before freeze-out.

Shear viscosity strongly suppresses the build-up of momentum anisotropy and elliptic flow, especially for low multiplicity densities, i.e. at large impact parameters, low collision energies or for small sizes of the colliding nuclei. This changes the slope of the multiplicity scaling curve for v_2/ε but preserves, to good approximation, its general scaling with $\frac{1}{S} \frac{dN_{ch}}{dy}$. Violations of multiplicity scaling for v_2/ε are somewhat larger for the viscous expansion than for the ideal fluid (especially with EOS I), but remain small enough to be consistent, within statistical errors, with the experimental observation of approximate scaling. The slope of the approximate scaling curve and the spread around this curve caused by scaling violation increase with the value of the specific shear viscosity η/s and can thus be used to constrain it.

Specifically, the observed scaling violations have the following features: At fixed multiplicity density $\frac{1}{S} \frac{dN_{ch}}{dy}$, viscous hydrodynamics predicts slightly larger elliptic flow v_2/ε for larger collision systems or more central collisions than for smaller nuclei colliding at similar energy or more peripheral collisions between similar-size nuclei colliding at higher energy. Larger v_2/ε values are associated with longer lifetimes of the corresponding fireballs before freeze-out and thus also with larger relative entropy production. This correlates the scaling violations for v_2/ε observed in Figs. 5.2 and 5.3 with those for the relative entropy production $\Delta S/S_0$ seen in Fig. 5.4. The pattern of the predicted scaling violations shows qualitative agreement with experiment, although higher quality data are required to render this agreement statistically robust and quantitative.

For a fixed (i.e. temperature independent) ratio η/s , the slope of the multiplicity scaling curve for v_2/ε does not agree with experiment – the curves predicted by viscous hydrodynamics are too flat. The slope can be increased by allowing η/s to increase at lower temperatures: For small multiplicity densities (very peripheral collisions or low collision energies), the data seem to require $\frac{\eta}{s} > 3 \times \frac{1}{4\pi}$, whereas at large multiplicity densities they appear to constrain the specific shear viscosity to values of $\frac{\eta}{s} \lesssim (1-2) \times \frac{1}{4\pi}$. While this is qualitatively consistent with the idea that in high-multiplicity events the dynamics is dominated by the QGP phase (whose viscosity would thus have to be small, of order $1/4\pi$) whereas low-multiplicity events are predominantly controlled by hadron gas dynamics (which is highly viscous [229]), much additional work is needed to turn this observation into quantitative constraints for the function $\frac{\eta}{s}(T)$.

Chapter 6: Generic Viscous Effects

– Bulk Viscosity

6.1 Introduction

In Chap. 4, we studied the generic *shear* viscosity effects and showed that elliptic flow v_2 is very sensitive to the shear viscosity to entropy ratio η/s , and can thus be used to extract the QGP shear viscosity from experimental data [125, 126, 127, 135, 136, 137]. In this chapter, we will investigate the *bulk* viscosity effects and discuss the uncertainties introduced by bulk viscosity when trying to constrain the QGP shear viscosity from experimental data [129, 130].

We will first compare the generic shear and bulk viscosity effects on the hydrodynamic evolution and final particle spectra and elliptic flow, by comparison runs from **a**) ideal hydrodynamics, **b**) viscous hydrodynamics with only shear viscosity and **c**) viscous hydrodynamics with only bulk viscosity. In these comparison runs, identical initial conditions and final conditions are used, which are the same as in Chap. 4 and explained in Chap. 3. For viscous hydrodynamics, the transport coefficient are set as follows: **b**): $\eta/s = 1/4\pi$, $\tau_\pi = 3\eta/sT = 3/4\pi T$ and $\zeta/s = 0$ ($C = 0$); **c**): $\eta/s = 0$, $C = 1$ for ζ/s as shown in Fig. 3.3, $\tau_\Pi = 3/4\pi T$. We here use N-S initializations for both shear stress pressure π^{mn} and bulk pressure Π here. In contrast to Chap. 4, which used EOS I (ideal EOS) and SM-EOS Q (a quasi-first order phase transition EOS), we employ here the lattice-based EOS L, for consistency with the bulk viscosity, which is constructed using the squared speed of sound c_s^2 from EOS L.

Chap. 6.3 concentrates on bulk viscosity effects and studies their sensitivity to the relaxation time and initialization for the bulk pressure. Chap. 6.4 investigates the upper limit of ζ/s , consistent with the validity of 2nd order viscous hydrodynamics. In Chap. 6.5 we will study how much uncertainty bulk viscous effects might contribute to the extracted value of shear viscosity from data.

6.2 Shear viscosity vs. bulk viscosity effects

6.2.1 Hydrodynamic evolution

The left panel of Fig.6.1 shows the time evolution of local temperatures from ideal and viscous hydrodynamics. When compared with the ideal fluid, the shear viscosity slows down the cooling process during the early stage, but speeds it up during the middle and late stages. As discussed in Ref. [125, 126] and Chap. 4.2, this is caused by the competition between decelerated longitudinal expansion and accelerated transverse expansion. During the early stage and before the transverse flow fully builds up, the system experiences quasi one-dimensional expansion, and the reduced work along the longitudinal direction (caused by shear viscosity) slows down the cooling process. In its middle and late stages, the system is in full 3-dimensional expansion, and the faster transverse expansion caused by the additional work done by shear viscous forces in the transverse directions leads to faster cooling. In contrast, bulk viscosity decelerates both the longitudinal and transverse expansion during the entire time evolution, since the negative bulk pressure effectively softens the EoS, especially near the phase transition. As a result the cooling process is slowed down during the whole evolution, with most of the effects concentrated around the phase transition where ζ/s peaks.

The shear-viscosity-accelerated and bulk-viscosity-decelerated transverse expansion also manifests itself in the evolution of the radial flow, shown in the right panel of Fig.6.1. Compared with the ideal fluid, minimal shear viscosity leads to $\sim 5\%$ more radial flow $\langle v_r \rangle$ at the end of the evolution. The increase of $\langle v_r \rangle$

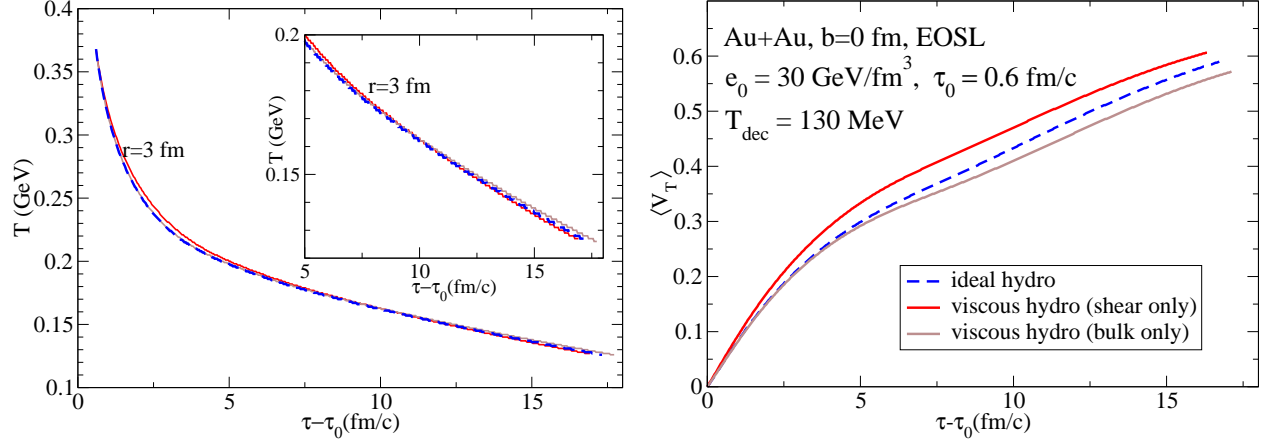


Figure 6.1: Time evolution of local temperature (left) and average radial flow (right), from ideal hydrodynamics, viscous hydrodynamics with only minimal shear or bulk viscosity, calculated with identical initial and final conditions.

mostly happens early, when the shear viscosity effects are largest. In contrast, bulk viscosity counteracts the build-up of radial flow, and minimal bulk viscosity reduces the final radial flow by $\sim 5\%$ relative to the ideal fluid case. Most of the bulk viscous effects occur during the middle stage from 5-10 fm/c, which is when a large portion of the matter passes through the phase transition region where ζ/s is large.

We now turn to non-central collisions. To describe the fireball deformation in configuration and momentum space, we use the spatial eccentricity ϵ_x and the momentum anisotropies ϵ_p , ϵ'_p , following Ref. [223, 126] and our discussions in Chap. 4. Figure 6.2(a) shows the time evolution of the spatial eccentricity ϵ_x for non-central Au+Au collisions at $b=7$ fm. Compared with the ideal fluid, bulk viscosity slows down the decrease of the spatial eccentricity ϵ_x since the negative bulk pressure decelerates both the longitudinal and transverse expansion. In contrast, the spatial eccentricity ϵ_x of the shear viscous fluid without bulk viscosity drops initially faster than that of the ideal fluid due to the faster radial expansion shown in Fig. 6.1 (right), but decreases more slowly than the ideal fluid at later times, due to the smaller flow anisotropy created in the viscous dynamics (see Fig. 4.5 in Chap. 4). This is also reflected in the late-time momentum anisotropy shown in Fig. 6.2(b), as one sees by comparing the dashed blue ideal fluid line with the dash-dotted red shear viscous fluid line.

It is worth discussing the time evolution of the momentum anisotropies ϵ_p and ϵ'_p in more detail. In viscous hydrodynamics, the difference between the total momentum anisotropy ϵ'_p (solid lines) and flow induced momentum anisotropy ϵ_p (dashed dotted lines) reflects the viscous pressure anisotropy. At freeze-out, this difference generates additional viscous effects on the v_2 suppression, arising from the non-equilibrium part of the distribution function δf along the freeze-out surface, which adds to or subtracts from that caused by the viscous suppression of the flow anisotropy. Shear viscous effects are mostly concentrated at earlier times, where they greatly reduce ϵ'_p in comparison with ϵ_p . The negative momentum anisotropy from the shear stress pressure slows down the growth of the flow anisotropy and causes the total momentum anisotropy ϵ_p (solid red line) to fall behind that of the ideal fluid (dashed blue line) at late times. Similarly bulk viscosity also suppresses the development flow anisotropy, since the gradients of the effective pressure $p+\Pi$ are reduced by the negative bulk pressure contribution. As a result, the momentum anisotropy ϵ_p from the bulk viscous fluid (dashed dotted brown line) stays always below the ideal hydro one (dashed blue line). Most of the bulk viscous effects happen during the middle stage where ϵ'_p is seen to significantly deviate from ϵ_p (comparing the solid and dot-dashed brown lines). In contrast to the shear viscous fluid, for the bulk viscous fluid ϵ'_p

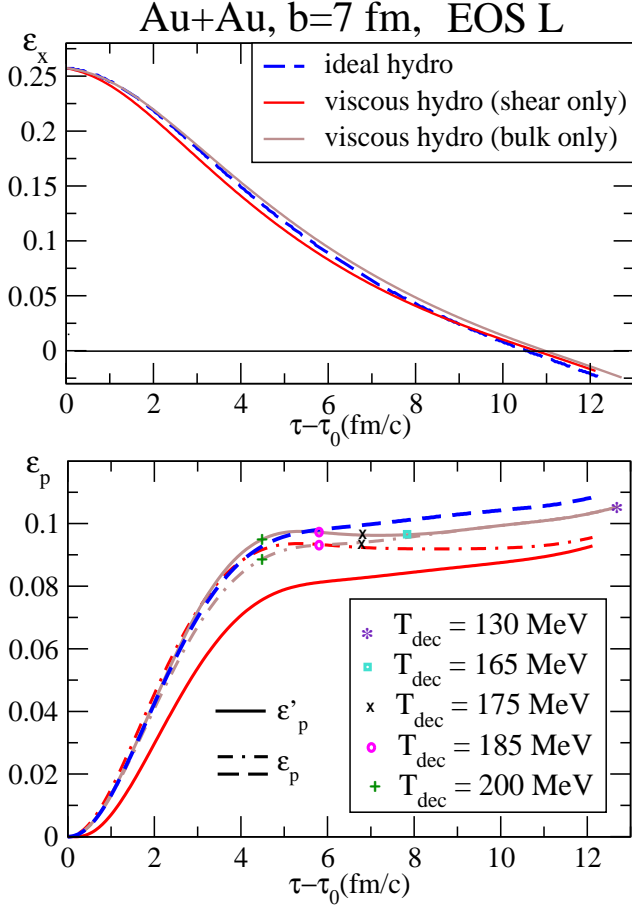


Figure 6.2: Time evolution for spacial anisotropy ϵ_x (upper panel) and momentum anisotropy ϵ_p , ϵ'_p (lower panel), from ideal hydrodynamics, viscous hydrodynamics with only shear viscosity or with only bulk viscosity. The different symbols along the bulk viscous fluid lines indicate freeze-out times for varieties of freeze-out temperatures.

is larger than ϵ_p ; This is mostly due to the negative bulk pressure contribution in the denominator of the expression for ϵ'_p . As a result, ϵ'_p from the bulk viscous fluid is even slightly larger than in the ideal fluid case. But this will not lead to an increase of hadronic v_2 (even if one freezes the system out already at the phase transition), since most of the enhancement happens in the inner core of the QGP phase at temperatures $T > 190$ MeV, as the symbols along the bulk viscous fluid lines indicate. At later times, the total ϵ'_p from the bulk viscous fluid is always below the ideal fluid one, indicating a bulk viscous suppression of hadronic elliptic flow v_2 after freeze-out. For $T_{dec} = 130$ MeV, all of the v_2 suppression comes from flow effects, since in our construction the bulk viscosity ζ is effectively zero below $T < 150$ MeV. If the system freezes-out near the phase transition around $165 - 175$ MeV, the difference between ϵ'_p and ϵ_p along the bulk viscous fluid lines indicates that the viscous corrections δf along the freeze-out surface will increase v_2 ; this was also pointed out by Monnai and Hirano [241], who calculate δf in terms of Π and π^{mn} along the freeze-out surface using Grad's 14-moment method. However, their calculation did not include the flow effects which (according to Fig 6.2) for $T_{dec} = 165 - 175$ MeV are least 2-3 times larger than those from δf , leading to a final overall suppression of v_2 .

6.2.2 Spectra and elliptic flow

The left panel in Fig. 6.3 left shows the pion p_T spectra from central Au+Au collisions, calculated from ideal hydrodynamics, viscous hydrodynamics with only minimal shear viscosity, or viscous hydrodynamics

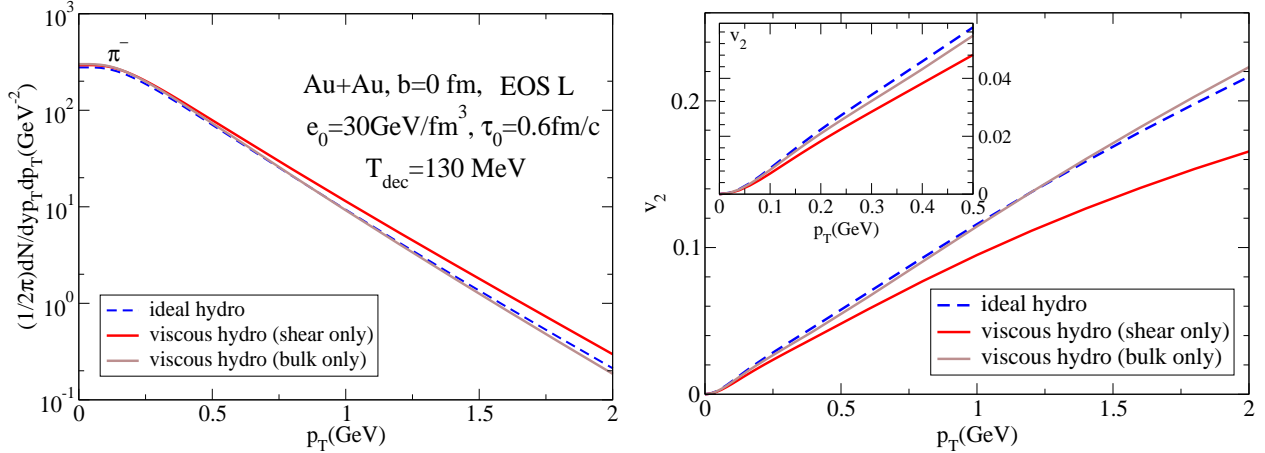


Figure 6.3: p_T spectra and v_2 for directly emitted pions (ie. without resonance decay contribution)

with only minimal bulk viscosity, using identical initial and final conditions. We find that shear viscosity results in flatter spectra due to larger radial flow, as shown in Fig. 6.1 (right). In contrast, bulk viscosity leads to steeper spectra since it decreases radial flow build-up during the fireball expansion. At low p_T , both shear and bulk viscosity lead to a larger yield, when compared with the ones from ideal hydrodynamics. This corresponds to an increase of the final multiplicity caused by viscous entropy production. Even though the shear and bulk viscosity act against each other in the slope of the final spectra, their effects add in the viscous entropy production, and an adjustment of initial conditions from ideal to viscous hydrodynamics can thus not be avoided if one intends to describe a given set of experimental data. In Ref. [133], it was shown that by increasing the thermalization time τ_0 and adjusting the initial energy or entropy density, one can reduce the initial total entropy and reduce the buildup of the radial flow, thereby compensating for the viscous entropy production and allowing for a successful fit of the experimental measured final multiplicities and spectral slopes.

In the right panel of Fig. 6.3, we show the p_T dependent v_2 of pions for non-central Au+Au collisions at $b=7$ fm. The insert enlarges the low- p_T region $p_T < 0.5$ GeV. We find that both shear and bulk viscosity suppress v_2 at low p_T . At higher p_T (~ 2 GeV), shear viscosity further suppresses v_2 due to a negative contribution δf along the freeze-out surface. In contrast, bulk viscosity increases v_2 above 1 GeV, due to its steepening effects on the p_T spectra there. At $p_T = 0.5$ GeV (approximately the mean average transverse momentum for pions) we find that minimal bulk viscosity suppresses v_2 by $\sim 5\%$ and minimal shear viscosity suppresses v_2 by $\sim 20\%$. Using v_2 data to determine η/s , the additional $\sim 5\%$ v_2 suppression from minimal bulk viscosity can thus lead to $\sim 25\%$ uncertainties in the extracted value of η/s . Therefore, we should not neglect bulk viscosity effects when extracting the QGP shear viscosity from experimental data.

6.3 Bulk viscosity effects: sensitivity to relaxation time and bulk pressure initialization

We now concentrate on bulk viscosity and investigate the effects from different relaxation times τ_{Π} and initializations of the bulk pressure Π . For τ_{Π} we here consider three choices: the constant values $\tau_{\Pi} = 0.5$ and 5 fm/c, and the temperature dependent function $\tau_{\Pi}(T) = \max[\tilde{\tau} \cdot \frac{\zeta}{s}(T), 0.1 \text{ fm/c}]$ with $\tilde{\tau} = 120 \text{ fm/c}$. The last choice implements phenomenologically the concept of critical slowing down near a phase transition;

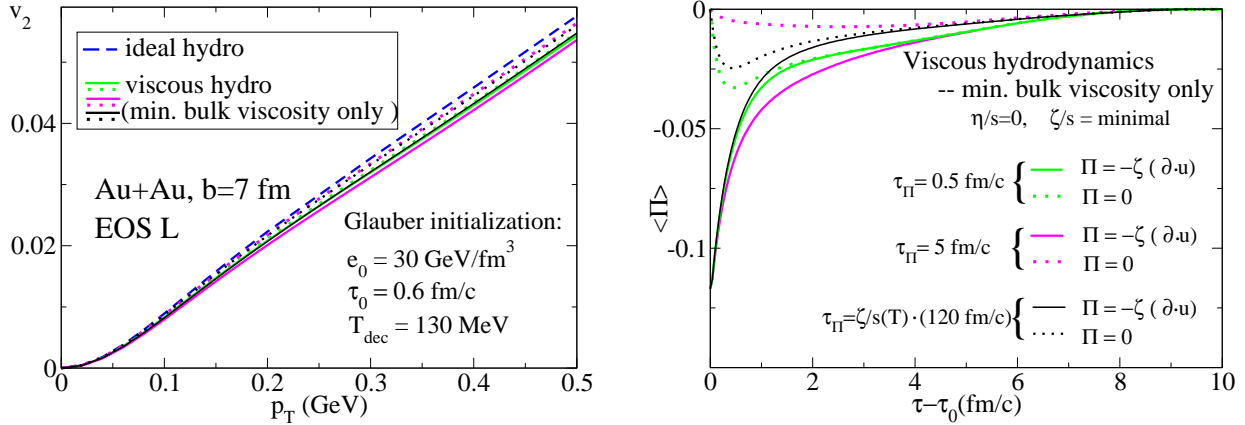


Figure 6.4: *Left*: Differential pion elliptic flow $v_2(p_T)$ from ideal and viscous hydrodynamics, including only bulk viscosity. *Right*: Time evolution of the bulk pressure $\langle \Pi \rangle$ averaged over the transverse plane (weighted by the energy density) from viscous hydrodynamics. Different curves correspond to different initializations and relaxation times, as indicated (see text for discussion).

it yields $\tau_{\Pi} \approx 0.6$ fm/c at $T = 350$ MeV and $\tau_{\Pi} \approx 5$ fm/c at T_c . To study memory effects, we explore two different initializations for the bulk viscous pressure: **(a)** Navier-Stokes (N-S) initialization, $\Pi(\tau_0) = -\zeta \partial \cdot u$, and **(b)** zero initialization, $\Pi(\tau_0) = 0$.

The left panel of Fig. 6.4 shows the differential elliptic flow $v_2(p_T)$ of directly emitted pions (without resonance decays) for non-central Au+Au collisions at $b=7$ fm, calculated from ideal hydrodynamics and minimally bulk viscous hydrodynamics with identical initial and final conditions. The different lines from viscous hydrodynamics correspond to different relaxation times τ_{Π} and different initializations $\Pi(\tau_0)$. One sees that these different inputs can lead to large uncertainties for the bulk viscous v_2 suppression. For minimal bulk viscosity, the v_2 suppression at $p_T = 0.5$ GeV ranges from $\sim 2\%$ to $\sim 10\%$ relative to ideal hydrodynamics (blue dashed line in the left panel).

For the shorter relaxation time, $\tau_{\Pi} = 0.5$ fm/c, the bulk viscous v_2 suppression is insensitive to the initialization of Π , and both N-S and zero initializations show $\sim 8\%$ v_2 suppression relative to ideal fluids. The reason behind this becomes apparent in the right panel showing the time evolution of the average bulk pressure $\langle \Pi \rangle$. For short relaxation times, $\langle \Pi \rangle$ quickly loses all memory of its initial value, relaxing in both cases to the same trajectory after about $1 - 2$ fm/c (i.e. after a few times τ_{Π}). This is similar to what we found for shear viscosity where the microscopic relaxation times are better known and short ($\tau_{\pi}(T_c) \simeq 0.2 - 0.5$ fm/c) and where the shear pressure tensor π^{mn} therefore also loses memory of its initialization after about 1 fm/c [126].

This changes if one accounts for the critical slowing down of the evolution of Π near T_c . If one simply multiplies the constant relaxation time by a factor 10, setting $\tau_{\Pi} = 5$ fm/c, one obtains the dotted and solid magenta lines in Fig. 6.4. Now the bulk viscous v_2 suppression relative to the ideal fluid becomes very sensitive to the initialization of the bulk viscous pressure: For zero initialization $\Pi(\tau_0) = 0$, the viscous v_2 suppression is very small (only $\sim 2\%$ at $p_T = 0.5$ GeV/c). The right panel shows that in this case the magnitude of the (transversally averaged) bulk pressure evolves very slowly and always stays small, leading to almost ideal fluid evolution. On the other hand, if Π is initialized with its Navier-Stokes value, which initially is large due to the strong longitudinal expansion, it decays initially more slowly than for the shorter relaxation time. Its braking effect on the flow evolution is therefore bigger, resulting in much stronger suppression of v_2 than for zero initialization, at $\sim 10\%$ slightly exceeding even the viscous v_2 suppression seen for the tenfold shorter relaxation time.

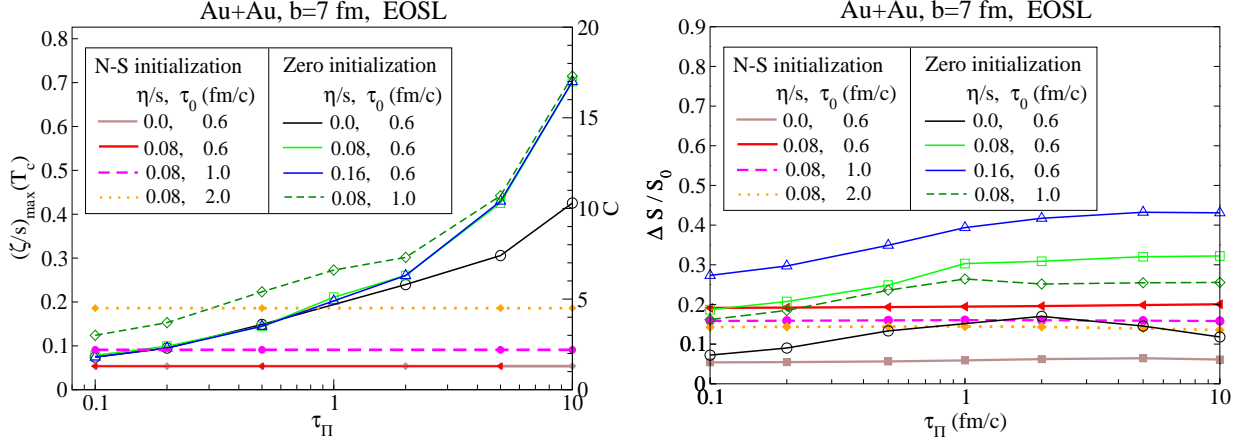


Figure 6.5: Upper limits of ζ/s , and entropy production as a function of relaxation time, for zero initialization $\Pi(\tau_0) = 0$ and N-S initialization $\Pi(\tau_0) = -\zeta\partial \cdot u$, with varieties of conditions.

The “critical slowing down” scenario with temperature-dependent $\tau_{\Pi}(T)$ (black lines) interpolates between the short and long relaxation times. As for the fixed larger value $\tau_{\Pi} = 5$ fm/c, v_2 depends sensitively on the initialization of Π , but for N-S initialization the viscous v_2 suppression is somewhat smaller than for both short and long fixed relaxation times. The reasons for this are subtle since now, at early times, the bulk viscous pressure Π evolves on very different time scales in the dense core and dilute edge regions of the fireball. As a result, for N-S initialization the average value $\langle \Pi \rangle$ is *smaller* in magnitude than for both short and long fixed τ_{Π} , throughout the fireball evolution (right panel, black lines).

6.4 Validity of I-S viscous hydrodynamics and upper limits for ζ/s

Viscous hydrodynamic codes can not run with arbitrarily large bulk viscosity. Physically, a large enough bulk viscosity can lead to a negative value for the total effective pressure $p + \Pi$ (thermal pressure + bulk viscous pressure) if the expansion rate $\partial \cdot u$ is large. When this happens, the fluid becomes mechanically unstable [259] and will tend to break up. In numerical simulations, this corresponds to exponential amplification of local numerical errors, which will eventually stop the code from running. On the other hand, 2nd order viscous hydrodynamics applies only for a near-equilibrium system: $\delta f \ll f_0$. This requires that the dissipative flows are (much) smaller than the equilibrium energy momentum tensor.

In this section, we will investigate upper limits of ζ/s allowed by 2nd order viscous hydrodynamics under dynamical conditions encountered in heavy-ion collisions. If the input ζ/s is small, the condition $p + \Pi(x, y, \tau) > 0$ is stratified everywhere in the transverse (x, y) plane during the entire hydrodynamic evolution. As one increases ζ/s (which corresponds to increasing the coefficient C in our parametrization of $(\zeta/s)(T)$, see Chap. 3.5), the condition $p + \Pi > 0$ will be violated near the phase transition in certain regions of (x, y) and τ . In our calculations we define the upper limit of ζ/s as the critical value of C that can generate negative effective pressure, $p + \Pi < 0$, at some position (x, y) and some time τ , i.e. anywhere inside the freeze-out surface.

Fig. 6.5 shows the upper limit $(\zeta/s)_{\max}(T_c)$ as a function of relaxation time τ_{Π} . The behavior of $(\zeta/s)_{\max}(T_c)$ as a function of τ_{Π} is seen to depend strongly on the initialization of the bulk pressure. For N-S initialization, $\Pi(\tau_0) = -\zeta\partial \cdot u$, $(\zeta/s)_{\max}(T_c)$ is insensitive to the relaxation time τ_{Π} . In this case, the magnitude of the average bulk pressure Π decreases more or less monotonically with time, as shown in the right panel of Fig. 6.4. Violations of the positivity condition $p + \Pi > 0$ always happen at the starting time τ_0

and at transverse positions where the matter is near the phase transition. This leads to a $(\zeta/s)_{max}(T_c)$ that is controlled by initial conditions and independent of the relaxation time. If one includes shear viscosity, $(\zeta/s)_{max}(T_c)$ depends only on the initialization time τ_0 , but not on the value of η/s . The dependence on τ_0 arises from the strong dependence of the initial bulk pressure $\Pi = -\zeta\partial\cdot u$ on τ_0 , through the expansion rate $\partial\cdot u = 1/\tau_0$. Hence the maximal allowed $(\zeta/s)_{max}(T_c)$ increases when the hydrodynamic evolution starts later. This tendency is illustrated by the solid red, dashed magenta and dotted orange lines in Fig. 6.5: as one increase τ_0 from 0.6 fm/c to 1 fm/c and 2 fm/c, the maximal $(\zeta/s)_{max}(T_c)$ lines increases from 0.05 to 0.09 and 0.18.

For zero initialization $\Pi(\tau_0) = 0$, one finds a qualitatively similar dependence of $(\zeta/s)_{max}(T_c)$ on τ_0 : The curves $(\zeta/s)_{max}(T_c)$ move up monotonically as one increases the starting time τ_0 from 0.6 fm/c to 1.0 fm/c (solid green and dashed dark green). In contrast to the N-S initialization, the $(\zeta/s)_{max}(T_c)$ curves now show a strong dependence on relaxation time τ_π , rising monotonically with τ_π . The reason is that it takes some time for the bulk pressure Π to develop large enough magnitudes to violate the positivity condition $p + \Pi > 0$; again this happens typically in regions where the matter is close to the phase transition. Smaller relaxation times allow Π to develop faster, resulting in a monotonic increase of $(\zeta/s)_{max}(T_c)$ with τ_π . For $\tau_\pi < 1$ fm/c, we find "universal" $(\zeta/s)_{max}(T_c) - \tau_\pi$ curves that do not depend on the shear viscosity η/s (solid black, green and blue curves), but move upwards as we increase the starting time τ_0 . This is because the violation of the positivity condition $p + \Pi > 0$ generally happens at early times $\tau < 3$ fm/c when the flow profiles are not yet significantly affected by shear viscous effects. For the two viscous fluid lines with $\eta/s = 0.08$ and 0.16 (solid blue and solid green lines) one see that they continue to overlap each other for $\tau_\pi > 1$ fm/c, where they break away from the $\eta/s = 0$ line. For $\eta/s = 0$, the phase transition generates larger velocity gradients near the phase transition, which cause instability at lower value of ζ/s . Shear viscosity smoothes out these large gradients, as discussed in Chap. 4, allowing the fluid to evolve stably up to larger values of ζ/s . Bulk viscosity ζ alone has no smoothing influence on sharp structures generated by a phase transition; For zero initialization for Π , shear viscosity is thus essential to stabilize the evolution of the viscous fluid against mechanical instabilities caused by strongly negative bulk viscous pressure, especially for large relaxation time τ_π .

6.5 Extracting η/s from experimental data: uncertainties introduced by bulk viscosity

Similar to shear viscosity, bulk viscosity suppresses elliptic flow v_2 , as shown in Fig. 6.3 (right). The bulk viscosity effects, once included, will thus reduce the η/s value needed to account for the suppression of a given measured amount of v_2/ε below the ideal fluid expectation. Current theoretical uncertainties in the relaxation time τ_Π and the initial value of the bulk viscous pressure Π , as well as the unknown value of the bulk viscosity itself, thus introduce a significant uncertainty in the extraction of η/s from elliptic flow data, which can not be reduced without additional theoretical efforts. This is illustrated in Fig. 6.6, where we investigate the additional viscous v_2 suppression from minimal and maximal bulk viscosity. (Here, "maximal bulk viscosity" denotes the largest value compatible with $p + \Pi > 0$ everywhere, as discussed in Chap. 6.4). For N-S initialization (Fig. 6.6, left), the viscous fluid lines with both shear and bulk viscosities ($\eta/s = 1/4\pi$, $C=1.0$ or 1.3) lead to 20-25% more viscous v_2 suppression at $p_T = 0.5$ GeV than a fluid with shear viscosity only. Neglecting the possible need for re-tuning the initial conditions and other hydrodynamic parameters, this additional v_2 suppression will translate into a reduction of the extracted η/s by $O(20\%)$, when fitting the same elliptic flow data. For zero initialization (right panel), the additional bulk viscous v_2 suppression ranges from 2% to 70%. Similarly, this will reduce the the extracted η/s by $O(2-70\%)$. This uncertainty bound covers only the ζ/s range accessible with our viscous hydrodynamics simulations. Larger ζ/s value may be realized in nature but would completely destroy our ability to extract η/s from a comparison of v_2 data with viscous hydrodynamics because the later breaks down. To remove or significantly reduce this uncertainty, it is mandatory to place strict theoretical limits on $(\zeta/s)(T)$ and $\tau_\Pi(T)$ as well as on the initial

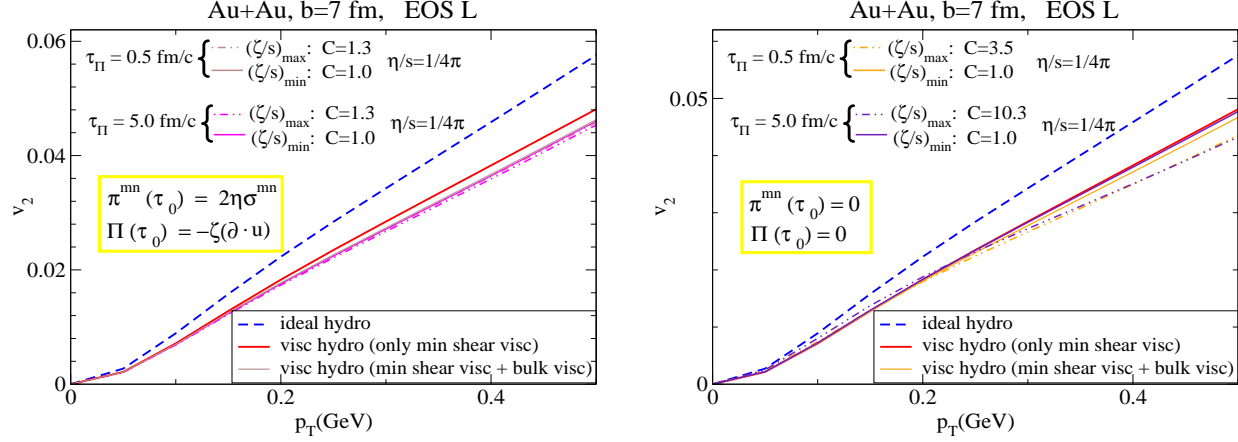


Figure 6.6: $v_2(p_T)$ from ideal hydrodynamics, viscous hydrodynamics with minimal shear viscosity, and viscous hydrodynamics with minimal shear viscosity and minimal or maximal bulk viscosity. Left: N-S initialization, $\pi^{mn}(\tau_0) = 2\eta\sigma^{mn}$, $\Pi(\tau_0) = -\zeta\partial \cdot u$. Right: zero initialization, $\pi^{mn}(\tau_0) = 0$, $\Pi(\tau_0) = 0$.

value for the bulk pressure Π .

6.6 Summary

In this chapter, we first compared shear and bulk viscous effects by studying, for central and non-central Au+Au collisions, simulations based on (a) ideal hydrodynamics, (b) viscous hydrodynamics with only minimal shear viscosity ($\eta/s = 1/4\pi$) and (c) viscous hydrodynamics with only minimal bulk viscosity $(\zeta/s)_{min}$. In all comparisons, we used identical initial and final conditions and the same EOS (EOS L). Similarities and differences between shear and bulk viscous effects are summarized as follows: Shear viscosity decelerates longitudinal expansion, but accelerates transverse expansion. When compared with the ideal fluid case, this leads to an initial slowing down of the cooling process, but to faster cooling during later stages, and more radial flow generation. Bulk viscosity decelerates both longitudinal and transverse expansion, resulting in slower cooling throughout and less creation of radial flow. Both shear viscosity and bulk viscosity generate entropy during the hydrodynamic evolution, and thus lead to larger final multiplicities. The p_T spectra, however, are flatter for a shear viscous fluid, but steeper for a bulk viscous fluid. For non-central Au+Au collisions, we found that both shear and bulk viscosity inhibit the development of momentum anisotropies. Most of the shear viscous effects happen during the early stage, while bulk viscous effects are stronger during the middle stage when most of the matter passes through the phase transition. As a result, both shear and bulk viscosity suppress elliptic flow v_2 at low p_T . At higher p_T , v_2 is further suppressed in a shear viscous fluid due to negative contributions from the non-equilibrium part δf of the freeze-out distribution function. In contrast, v_2 is slightly increased for the bulk viscous fluid above $p_T > 1$ GeV, due to the steeper p_T spectra.

Effects arising from different relaxation times τ_{Π} and different initializations of the bulk pressure Π on the viscous v_2 suppression were studied in Chap. 6.3, in order to assess phenomenological uncertainties arising from limited theoretical knowledge in the bulk viscous sector. The well-known phenomenon of critical slowing down during a phase transition suggests that τ_{Π} may become large near T_c . If one uses larger relaxation times of the order of $\tau_{\pi} = 5$ fm/c (near T_c or at all temperatures), the bulk viscous v_2 suppression becomes sensitive to the initialization of Π , with effects ranging from $\sim 2\%$ (zero initialization for Π) to $\sim 10\%$ (N-S initialization for Π) for minimal bulk viscosity. This strongly suggests a need for more theoretical research

into the relaxation time τ_{Π} and into theories that can provide reliable initializations for the bulk viscous pressure.

The bulk viscosity ζ itself also has theoretical uncertainties: the peak value of ζ/s near the phase transition from lattice QCD estimates is around 10 times larger than the minimal AdS/CFT values, and even less is known for the bulk viscosity of the hadronic phase. Considering these theoretical uncertainties, we investigated the maximal peak value of ζ/s the near phase transition, $(\zeta/s)_{max}(T_c)$, that is allowed by the numerical applicability of 2nd order viscous hydrodynamics with dynamical conditions encountered in heavy ion collisions. For N-S initialization, $(\zeta/s)_{max}(T_c)$ can be as low as 0.05 / 0.09 / 0.18, depending on the starting time τ_0 for hydrodynamic stage, $\tau_0 = 0.6 / 1.0 / 2.0$ fm/c, and this limit is insensitive to the relaxation time τ_{Π} . For zero initialization, $(\zeta/s)_{max}(T_c)$ increases monotonically with the relaxation time τ_{Π} , and can reach values up to 0.7 at $\tau_{\Pi} = 10$ fm/c, for $\tau_0 = 0.6 - 1.0$ fm/c.

The additional bulk viscous effects on the suppression of elliptic flow v_2 (comparing to ideal hydrodynamics) were studied in Chap. 6.5. We concluded that bulk viscous effects can not be ignored when extracting the QGP shear viscosity to entropy ratio η/s from experimental elliptic flow data. Pinning down the bulk viscous effects is important, especially if η/s turns out to be small of order of the KSS bound. It urgently requires to much more tightly constrain the allowed ranges for ζ/s , τ_{π} and $\Pi(\tau_0)$, than presently possible.

Chapter 7: Recent Developments in Viscous Hydrodynamics

7.1 Introduction

During the past couple of years, several groups have independently developed (2+1)-dimensional viscous hydrodynamic codes for relativistic heavy ion collisions and published their first results on shear viscosity effects [125, 126, 127, 134, 135, 137]. In this chapter, I will put my own research results in context with related developments elsewhere, discuss similarities and differences as well as the origin of the latter.

All groups that did viscous hydrodynamics simulations found that the elliptic flow coefficient v_2 is very sensitive to shear viscosity: given the large expansion rates of heavy-ion collision fireballs, even minimal viscosity saturating the KSS bound $\eta/s \geq 1/4\pi$ [146] for the viscosity to entropy density ratio can lead to a strong (and thus easily measurable) suppression of v_2 . Assuming the availability of a well-established ideal fluid dynamical baseline for v_2 as a function of collision energy, centrality and system size, measurements of this suppression could thus be used to constrain the QGP shear viscosity from experimental data.

However, the first results for viscous v_2 suppression published by the different groups seemed to show large quantitative discrepancies, ranging from 20% to 70% even for 'minimal viscosity' $\eta/s = 1/4\pi$. Detailed inspection of the early papers of each group revealed that different initial conditions, final conditions, EOS and different versions of the 2nd order viscous equations were used in these calculations, and that collision systems of different size (Cu+Cu vs. Au+Au collisions) were studied. This motivated us to systematically investigate the physical effects of each of these differences and to collaborate with other groups to carefully verify our numerical codes to eliminate the possibility of numerical error.

In this chapter, we will summarize recent progress in viscous hydrodynamics. We will show how the apparent discrepancies on viscous v_2 suppression are resolved, when one properly accounts for physical effects arising from system size, equation of states (EOS), and different versions of the Israel-Stewart equations (Chap. 7.2). I will also report on the most recent code verification results, obtained within the TECHQM collaboration [260] (Chap. 7.4). In Chap. 7.3, we will numerically compare the different 2nd order I-S equations obtained from the different theoretical approaches described in Chap. 2, which includes a comparison between the "simplified" and "full" I-S equations as well as some effects from other higher order terms. In Chap. 7.4, we will also numerically compare the I-S equation with the O-G equation. Throughout this Chapter, we concentrated on shear viscous effects and set $\zeta = 0$.

7.2 System size, EOS and different I-S equations

In this section, we will briefly discuss the different manifestations of shear viscosity when one varies system size and EOS and uses different versions of the I-S equations [127]. As mentioned in the Introduction, this analysis resolves the initially puzzling differences between the results published by different groups.

Fig. 7.1 shows the differential elliptic flow $v_2(p_T)$ for directly emitted pions from ideal and viscous hydrodynamics. Panels (a) and (b) compare two systems of different size (Cu+Cu and Au+Au, both at $b = 7$ fm), using identical equations of state (SM-EOS Q), I-S equations (simplified, eq. (2.30) in Chap. 2) and other free inputs. Although both systems have similar initial eccentricities, the smaller Cu+Cu system shows a much larger viscous v_2 suppression (by almost 70% below the ideal fluid value at $p_T = 2$ GeV/c [125, 126]) than observed in the larger Au+Au system where the suppression is almost a factor two smaller. Panels (b) and (c) compare the same Au+Au system at $b = 7$ fm for two different EOS and different I-S equations. Changing the EOS from SM-EOS Q to EOS L reduces the viscous suppression of elliptic flow by another

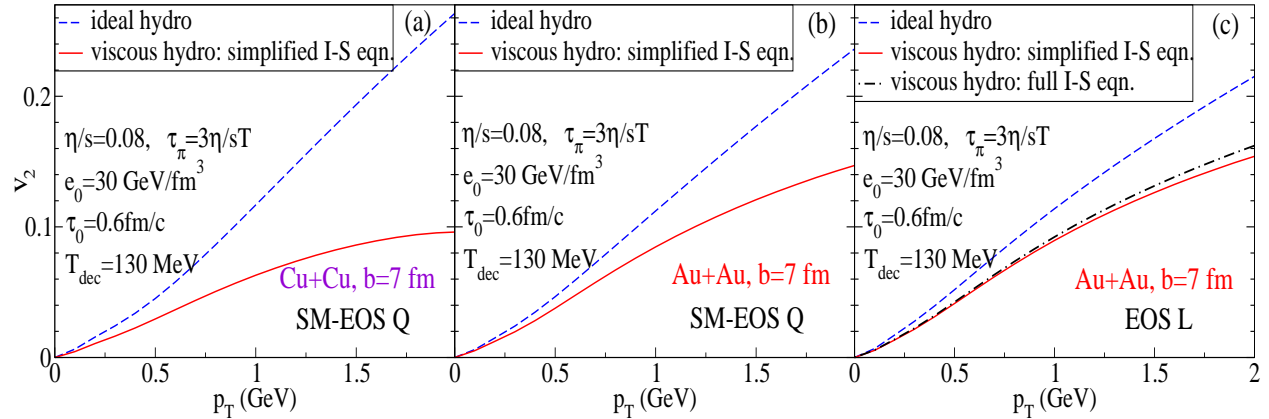


Figure 7.1: Differential elliptic flow $v_2(p_T)$ for directly emitted pions (i.e. without resonance decay contributions), comparing results for different collisions systems and equations of state. (a) Cu+Cu at $b = 7$ fm with SM-EOS Q. (b) Au+Au at $b = 7$ fm with SM-EOS Q. (c) Au+Au at $b = 7$ fm with EOS L. Dashed (solid) lines correspond to ideal (viscous) fluid dynamics, with parameters as indicated.

quarter (from $\sim 40\%$ to $\sim 30\%$ below the ideal fluid value at $p_T = 2$ GeV/ c). Replacing the simplified I-S equations used in [125, 126] by the full I-S equations (eq. (2.31) in Chap. 2) used in [134] further reduces the v_2 suppression from 30% to 25% below the ideal hydrodynamics value at $p_T = 2$ GeV/ c . This final result is consistent with [134]. Although for EOS L the additional terms in the full I-S equations only result in a 5-10% difference in v_2 suppression, its effect is much larger for more rapidly expanding systems, such as Cu+Cu collisions driven by a stiff conformal EOS $e = 3p$ (see Chap. 7.4.1 and Ref. [127] for details).

We conclude that the biggest contribution to the large difference between the results reported in Refs. [125] and [134] arises from the different collision systems studied, with much larger viscous effects seen in the smaller Cu+Cu system than in Au+Au collisions. The next most important sensitivity is to the EOS; for the most realistic EOS studied here, EOS L, the differences between using the full or simplified I-S equations with $\tau_\pi = 3\eta/sT$ are only about 10% on a relative scale, or about 3% on the absolute scale set by the elliptic flow from ideal fluid dynamics. For smaller τ_π , this last difference would shrink even further.

7.3 Detailed comparison of different I-S equations

As discussed in Chap. 2, the I-S formalism can be obtained from different approaches: from the 2nd law of thermodynamics (Chap. 2.3), from kinetic theory (Chap. 2.4) and from the conformal symmetry constraint (Chap. 2.5). The common terms, obtained by all of these approaches, form the so-called “simplified” I-S equation shown in eq. (2.30). The “full” I-S equation used here and in Ref. [127] is defined as the simplified I-S equation plus a term that helps to maintain the conformal symmetry for a conformal fluid, shown in eq. (2.31). With the identity (2.32), which holds in the conformal limit, the “full” I-S equation can be written in different forms, and these variations are what one originally obtains from different 2nd order theory approaches. However this “full” I-S equation is still not the most general 2nd order theory, and in a variety of approaches, discussed in Chap. 2, additional 2nd order terms (a vorticity term, a visco-elastic term, and more [203, 204, 221]), each with its own coefficient that takes different values in different theories (see Table 2.1), arise. To find the optimal I-S equations for numerical implementation, one needs systematic comparisons for these different I-S equations from different approaches. In this section, we will give a detailed numerical comparison between the “simplified” and “full” I-S equations [127], and then briefly study the

effects from other higher order terms.

7.3.1 “Simplified” and “full” I-S equations

Evolution of momentum anisotropies

Figure 7.2 shows the temporal evolution of the total momentum anisotropy $\varepsilon_p = \frac{\langle T^{xx} - T^{yy} \rangle}{\langle T^{xx} + T^{yy} \rangle}$ averaged over the transverse plane²⁴ for two collision systems (Cu+Cu at $b = 7$ fm on the left, Au+Au at $b = 7$ fm on the right) and three equations of state (EOS I (top), SM-EOS Q (middle), and EOS L (bottom)). The blue dashed lines at the top indicate the result from ideal fluid dynamics, the black and orange lines below show viscous fluid dynamical results. The black lines show solutions of the “full” I-S equation, the orange ones for the simplified I-S approach; in each case several values of the kinetic relaxation time τ_π are explored. Note that our “full” I-S equation used here is defined by eq. (3.3) (already written in 2+1 dimensions), but not the full I-S equation defined by eq. (2.31) in Chap. 3, which strictly holds only for conformal fluids. We have, however, tested the two expressions on the left and right side of eq. (2.32) against each other also for the other two equations of state (SM-EOS Q and EOS L) which are not conformally invariant, and found no discernible differences. Only for a very long relaxation time $\tau_\pi = 12\eta/sT$ (not shown in Fig. 7.2) did we see for EOS L a difference larger than the line width, with our result for ε_p lying slightly above the one obtained with the conformal approximation eq. (2.32).

Comparison of the black and orange lines in Fig. 7.2 shows that the sensitivity of the momentum anisotropy ε_p to the relaxation time τ_π is significantly larger for the simplified I-S equation (orange) than for the “full” I-S equation (black), and that the τ_π -dependence of ε_p even has the opposite sign for the two sets of equations. With the “full” I-S equations, ε_p moves slowly towards the ideal fluid limit as τ_π increases whereas with the simplified I-S equations ε_p moves away from the ideal fluid limit, at a more rapid rate, resulting in a larger viscous suppression of the momentum anisotropy. In the limit $\tau_\pi \rightarrow 0$, both formulations approach the same Navier-Stokes limit. The difference between “full” and simplified I-S equations is largest for EOS I which is the stiffest of the three studied equations of state, causing the most rapid expansion of the fireball. For this EOS, the simplified I-S equations allow for the largest excursions of π^{mn} away from its Navier-Stokes limit, causing a significant and strongly τ_π -dependent increase of all viscous effects, including the suppression of the momentum anisotropy (Fig. 7.2) and elliptic flow and the amount of viscous entropy production (see below).

For the other two equations of state, SM-EOS Q and EOS L, the difference between “full” and “simplified” I-S dynamics is much smaller, ranging from $\sim 5\%$ for Au+Au to $\sim 15\%$ for Cu+Cu for the largest τ_π value of $6\eta/sT$ studied here. Note that the viscous suppression of ε_p is much stronger for the smaller Cu+Cu collision system than for Au+Au. For SM-EOS Q and EOS L (which yield rather similar results for ε_p , with differences not exceeding $\sim 10\%$), the results from the “full” I-S equations (black lines) are almost completely independent of τ_π , even for the small Cu+Cu system.

The insets in the two upper panels of Fig. 7.2 illustrate the different τ_π -dependences for ε_p in the “full” and “simplified” I-S formulations, by plotting the value of ε_p for EOS I at a fixed time $\tau - \tau_0 = 4$ fm/c as a function of τ_π . One sees that, for the investigated range of relaxation times, the τ_π -dependence is linear, but that the slope has different signs for the “full” and “simplified” I-S equations and is much smaller for the “full” I-S system. Even though VISH2+1 cannot be run for much smaller τ_π values, due to numerical instabilities that develop as the Navier-Stokes limit $\tau_\pi = 0$ is approached, the lines corresponding to the “full” and the “simplified” I-S equations are seen to nicely extrapolate to the same Navier-Stokes point, as they should. For SM-EOS Q and EOS L, the corresponding lines may no longer be linear, due

²⁴Note that ε_p as defined in this section includes the effects from both flow velocity and shear pressure anisotropies [125]. In Ref. [125] and Chap 4 we denoted it by ε'_p in order to distinguish it from the flow-induced momentum anisotropy $\frac{\langle T_0^{xx} - T_0^{yy} \rangle}{\langle T_0^{xx} + T_0^{yy} \rangle}$ which is based only on the ideal fluid part of the energy momentum tensor and neglects anisotropies in the local fluid rest frame caused by the shear pressure tensor π^{mn} . In the present chapter we drop the prime for convenience.

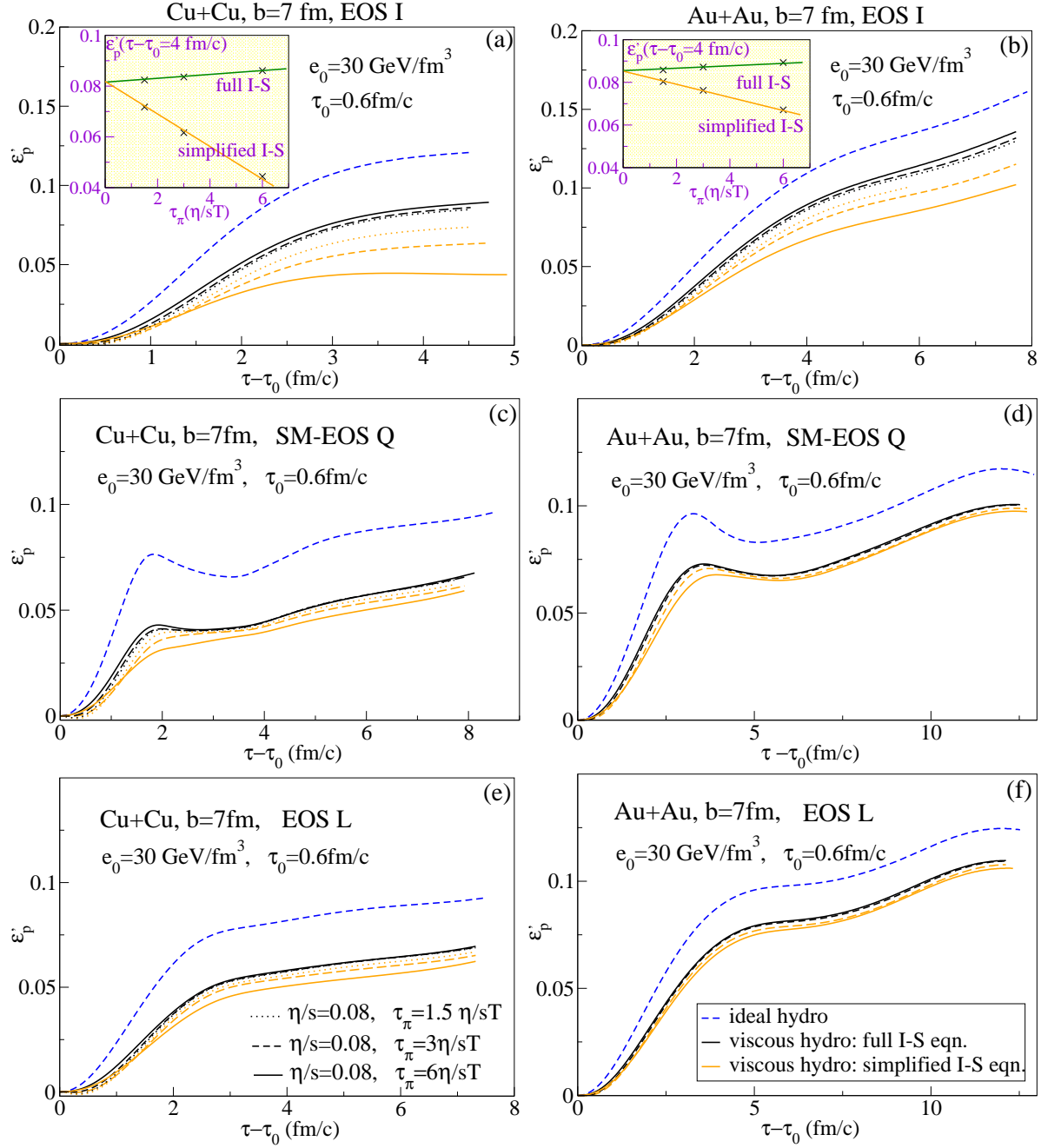


Figure 7.2: Time evolution of the total momentum anisotropy ε'_p for two collision systems (left: Cu+Cu; right: Au+Au), three equations of state (top: EOS I; middle: SM-EOS Q; bottom: EOS L), and three values of the kinetic relaxation time τ_π as indicated (dotted, dashed and solid curves, respectively). The insets in the two top panels show the τ_π -dependence of the momentum anisotropy ε_p at fixed time $\tau - \tau_0 = 4$ fm/c. See text for discussion.

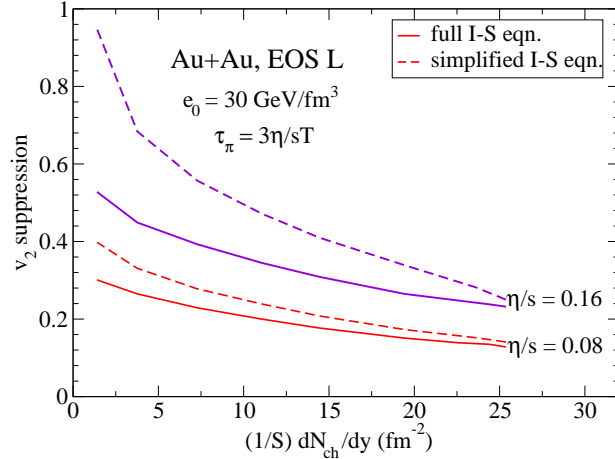


Figure 7.3: Viscous suppression of elliptic flow, $(v_2^{\text{ideal}} - v_2^{\text{viscous}})/v_2^{\text{ideal}}$, as a function of $(1/S)dN_{\text{ch}}/dy$ for Au+Au with EOS L, $\tau_\pi = 3\eta/sT$ and two values of η/s as indicated. Solid (dashed) lines correspond to using the full (simplified) I-S equations, respectively.

to phase transition effects, but are still characterized by opposite slopes for the “simplified” and “full” I-S approaches, with almost vanishing slope in the full I-S case. This agrees with findings reported in [134,135].

Elliptic flow and viscous suppression of v_2 : systematics

In this subsection, we will compare the “simplified” and “full” I-S equations by studying the viscous v_2 suppression with different η/s as inputs. As already shown in Figs. 5.1 and 5.2, the slope of v_2/ε as a function of $\frac{1}{S}\frac{dN_{\text{ch}}}{dy}$ remains positive for viscous hydrodynamics curves even at the highest collision energies (or e_0 values), i.e. v_2/ε continues to increase and evolve in direction of the asymptotic ideal fluid limit. This implies that at higher collision energies the importance of viscous effects decreases. This observation parallels the one made in [125], namely that with increasing collision energy the p_T range increases over which viscous hydrodynamic predictions for the single-particle momentum spectra can be trusted. The reason is in both cases that with increasing collision energy the time until freeze-out grows, and that (at least for constant η/s as assumed here and in [125]) during the later stages of the expansion shear viscous effects are small.

Figure 7.3 shows this more quantitatively. We plot the fractional decrease of the elliptic flow relative to its ideal fluid dynamical value, $(v_2^{\text{ideal}} - v_2^{\text{viscous}})/v_2^{\text{ideal}}$, as a function of multiplicity density $\frac{1}{S}\frac{dN_{\text{ch}}}{dy}$. Larger multiplicity densities lead to smaller viscous suppression effects. Larger viscosity results in stronger suppression of the elliptic flow. The suppression effects are weaker if the “full” I-S equations are used than in the “simplified” approach of Ref. [125] (which also suffers from strong sensitivity to τ_π). For minimal viscosity, $\eta/s = 1/4\pi$, the p_T -integrated elliptic flow v_2 in Au+Au collisions at RHIC is suppressed by about 20%. The suppression is larger at lower energies but will be less at the LHC.

Entropy production:

In this subsection, we compare the entropy production from viscous hydrodynamics using the “simplified” and “full” I-S equations. Figure 7.4 shows that, when the “simplified” I-S equations are used, entropy production depends very sensitively on the kinetic relaxation time τ_π , approaching the much smaller and almost completely τ_π -independent entropy production rates of the “full” I-S framework in the limit $\tau_\pi \rightarrow 0$. The large amount of extra entropy production for non-zero τ_π in the “simplified” I-S approach must thus be considered as unphysical. This is important because this artificial extra entropy production (caused by unphysically large excursions of the viscous shear pressure tensor π^{mn} away from its Navier-Stokes value

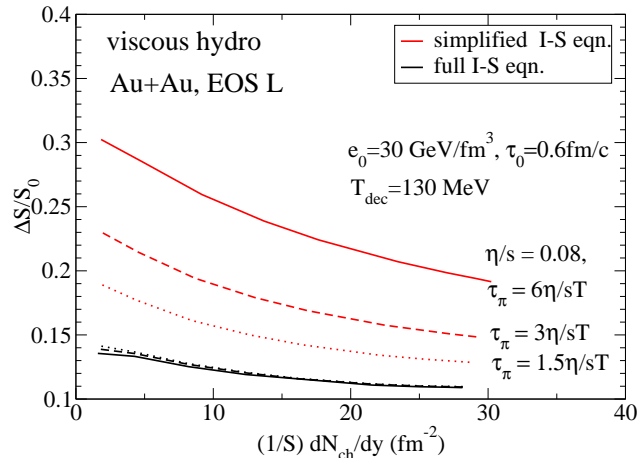


Figure 7.4: Sensitivity of the entropy production ratio $\Delta S/S_0$ shown in Fig. 5.4 to the kinetic relaxation time τ_π , for the Au+Au collision system with $e_0 = 30 \text{ GeV/fm}^3$ (corresponding to a collision energy of $\sqrt{s} \approx 200 \text{ A GeV}$). The three red curves (upper set) are for the simplified Israel-Stewart equations, the three black curves (lower set) for the full I-S equations. Solutions with the full I-S equations produce less entropy and show very little sensitivity to τ_π .

$\pi^{mn} = 2\eta\sigma^{mn}$) manifests itself as additional charged hadron multiplicity in the observed final state. Since the final multiplicity is used to normalize the initial energy density e_0 , this causes a significant distortion of the initial conditions corresponding to a given set of experimental data, affecting their physical interpretation.

We conclude that using the “full” I-S equations is mandatory if one wants to minimize artificial effects of shear viscosity on entropy production and elliptic flow in the realistic situation of non-zero kinetic relaxation times. (We note that, while the value of τ_π for the QGP created at RHIC is not very well known, it can obviously not be zero).

7.4 Code verification and comparison between I-S and O-G equations

Before the code verification process among different groups began, our code VISH2+1 had already passed several tests of its numerical accuracy: (i) in the limit of vanishing viscosity, it accurately reproduces results obtained with the (2+1)-d ideal fluid code AZHYDRO [246]; (ii) for homogeneous transverse density distributions (*i.e.* in the absence of transverse density gradients and transverse flow) and vanishing relaxation time it accurately reproduces the known analytic solution of the relativistic Navier-Stokes equation for boost-invariant 1-dimensional longitudinal expansion [211]; (iii) for very short kinetic relaxation times our Israel-Stewart code accurately reproduces results from a separately coded (2+1)-d relativistic Navier-Stokes code, under restrictive conditions where the latter produces numerically stable solutions; and (iv) for simple analytically parametrized anisotropic velocity profiles the numerical code correctly computes the velocity shear tensor that drives the viscous hydrodynamic effects. The details can be found in Ref [126] and Appendix A.3.

In the rest of this section, we will report on the recent code verification efforts among different groups with independently developed viscous hydrodynamic codes.

Preliminary results of the TECHQM collaboration (please refer to <https://wiki.bnl.gov/TECHQM/index.php/>). I will release the material of this part after the related paper has been made available on-line.

7.5 Conclusions

In this chapter, we first resolved the questions that arose from several recent publications of viscous hydrodynamic calculations (with only shear viscosity) which seemed to yield different results [125, 126, 134, 135]. After accounting for the physical effects arising from different system sizes, different EOS and different versions of the I-S equations, the dramatically different v_2 suppressions, ranging from 70% to 20%, are largely resolved [127]. For a realistic equation of state that implements a quark-hadron transition (here SM-EOS Q and EOS L) it turns out that system size effects play a very important role. At RHIC energies and for a realistic EOS, the viscous suppression effects for v_2/ε in Cu+Cu collisions are almost twice as large as for the larger Au+Au collision system. Non-negligible differences in the amount of viscous v_2 suppression arise also from details in the EOS, with a smooth crossover as implemented in EOS L giving 25-30% less suppression than a first-order transition as in SM-EOS Q. Compared to system size effects and EOS uncertainties, the differences between “simplified” and “full” I-S theory are relatively small, affecting the viscous v_2 suppression at the 10% level relative to each other. The later code verification among different groups eliminated the possibility of significant numerical errors in the independently developed codes. Very good agreement is obtained when testing the hydrodynamic evolution and the calculated spectra.

We also numerically studied the effects of implementing different second order theories for causal relativistic viscous hydrodynamics. We first compared the “simplified Israel-Stewart equations” eq. (2.30) used in our early articles [125, 126] and the “full Israel-Stewart equations” eq. (2.31) used in our later work [127] and in Refs. [134, 135]. For the “simplified” approach, we found a strong sensitivity of physical observables to the presently poorly known kinetic relaxation time τ_π for the viscous shear pressure tensor π^{mn} , in contrast to a much weaker and basically negligible τ_π -dependence in the “full” approach. For non-zero τ_π the “simplified I-S equations” allow for large excursions of π^{mn} away from its Navier-Stokes limit $\pi^{mn} = 2\eta\sigma^{mn}$. These excursions are artificial and disappear in the Navier-Stokes limit $\tau_\pi \rightarrow 0$ which can, however, not be stably simulated numerically. They cause large viscous suppression effects for the elliptic flow and large amounts of extra entropy production (i.e. extra final hadron multiplicity). From our study we conclude that the “simplified I-S approach” should be avoided, and that a reliable extraction of η/s from experimental data mandates the use of the “full Israel-Stewart equations” [134, 135, 127]. We also studied the effects from other higher order terms beyond the full I-S equations, such as the vorticity and visco-elastic terms obtained in other approaches. The numerical evidence from our systematic study in Chap. 7.3.2 as well as the indications from the code verification among different groups suggest that these higher order terms can be neglected in numerical calculations. In short, we recommend to use the “full” Israel-Stewart equation (2.31, 2.32) due to its relatively simple form and its weak dependence on the microscopic relaxation time.

Chapter 8: Extracting Shear Viscosity from Experimental Data – Uncertainty Analysis

8.1 Introduction

With the efforts from different groups [125, 126, 127, 134, 135, 137, 140, 141], the elliptic flow has now been widely accepted as the key observable to constrain the QGP shear viscosity. With the availability of several independently developed causal viscous hydrodynamic codes, we are at the threshold for extracting the QGP shear viscosity from experimental data. However, several issues must be clarified before we can do so. These include: **(1)** establishing quantitative uncertainty estimates for the hydrodynamically predicted elliptic flow related to uncontrolled uncertainties in the initial conditions for the fireball eccentricity and the remaining uncertainties in the QCD equation of state (EOS) near and above T_c ; **(2)** inclusion of non-equilibrium hadronic chemistry into the EOS below T_c (this is known to affect the distribution of the hydrodynamic momentum anisotropy over the various hadron species and thus their v_2 , but has not yet been included in viscous hydrodynamic simulations); **(3)** exploring uncertainties related to the treatment of the final kinetic freeze-out process; and **(4)** including effects from bulk viscosity, especially near T_c . In this chapter, we will try to assess the uncertainties introduced by each of these aspects when extracting the QGP viscosity from experimental elliptic flow data [129]. Resolving these uncertainties will require additional theoretical work that goes beyond this thesis. The analysis laid out in this chapter can serve as a guide for such research.

8.2 Dynamical freeze-out and effects from late hadronic viscosity

In ideal hydrodynamics, one usually imposes “sudden freeze-out”, i.e. a sudden transition from a thermalized fluid to free-streaming particles, on a hypersurface $\Sigma(x)$ of constant temperature or energy density [26]. The same algorithm has also been used in most of the existing viscous hydrodynamic calculations [134, 125, 126, 135, 127, 143]. Since viscous hydrodynamics is based on an expansion in small deviations from local equilibrium, its validity requires the microscopic relaxation time to be much smaller than the inverse macroscopic expansion rate, $\tau_{\text{rel}}\partial\cdot u \ll 1$. This condition (whose long history is discussed in Refs. [261, 262] where it is also applied to ideal hydrodynamics) provides a natural criterium for a dynamical freeze-out algorithm. Dusling and Teaney [137] implemented it into their viscous hydrodynamics. They find that in this case the viscous v_2 suppression is dominated by non-equilibrium corrections to the local thermal distribution function along the freeze-out surface [137]. This is not a collective effect arising from anisotropies of the flow velocity profile, but a reflection of non-equilibrium momentum anisotropies in the local fluid rest frame. In contrast, for isothermal freeze-out we find [126] that the viscous v_2 suppression is dominated by the viscous reduction of the collective flow anisotropy, while local rest frame momentum anisotropies play a much smaller role. This comparison shows that a careful treatment of the hadronic decoupling process will be required for the quantitative extraction of η/s from elliptic flow data. Dusling also found that dynamical freeze-out can increase the slope of the multiplicity dependence of the eccentricity-scaled elliptic flow v_2/ε [208]. This is an improvement over the scaling behavior found in [127] for viscous hydrodynamics with constant η/s and isothermal freeze-out which features a slope that is too small.

There are other reasons why a proper kinetic treatment of the late hadronic phase is important. By matching a realistic hadron rescattering cascade to an ideal fluid description of the QGP and hadronization stages, Hirano *et al.* [229] showed that the HRG phase is highly viscous and strongly suppresses any buildup

of elliptic flow during the hadronic stage. This is consistent with a recent analysis by Demir and Bass [169] who found large shear viscosities for their hadronic UrQMD cascade even close to T_c (between 5-10 times above the KSS bound).

To extract the QGP viscosity from elliptic flow data, one needs a good description of the highly viscous hadronic stage in order to properly include the additional viscous v_2 suppression from the late hadronic stage. However, viscous hydrodynamics with a temperature dependent η/s (using the results from [169]) can not self-consistently describe the highly viscous hadronic stage. The HRG viscosities found in [169] are so large that the viscous hydrodynamics description breaks down even during the early time of the fireball evolution [263] as one reaches the skin of the fireball where the matter is in the HRG phase. This requires the future development of a hybrid approach that connects viscous hydrodynamics (for the QGP phase) with a hadron cascade. Moreover, the correct description of the beam energy and centrality dependence of v_2 is crucially affected by the changing relative weight of QGP and HRG dynamics in building elliptic flow (in central collisions or at higher energies the system spends more time in the QGP phase than in peripheral collisions or at low energies). A realistic kinetic simulation of the hadronic phase and its freeze-out thus appears to be indispensable.

8.3 EoS

Lattice EoS for the QGP phase:

The EOS is a necessary input in hydrodynamic calculations. Early ideal hydrodynamic simulations generally implemented the so-called EOS Q, which connects the QGP phase with chemical equilibrium HRG phase through a first order phase transition [93, 234, 96, 264] (see Sec. 3.3 for details). Lattice QCD with two light quark flavors (u and d) and one heavier quark flavor (s) predicts, however a smooth cross-over transition at small net baryon chemical potential [265]. Using a quasi-particle model, Refs. [266, 267] constructed a lattice inspired EOS (qp-EoS) and applied it to ideal hydrodynamics simulations. From comparison runs with different EOS as inputs (qp-EoS vs. EOS-Q etc.), the order of magnitude of phase transition effects on hadron spectra and elliptic flow were investigated. One found that the differential elliptic flow for heavier particles (such as protons) at low p_T is sensitive to the order of the phase transition. However, whether experimental data favor an EOS with the 1st order phase transition or a cross-over EOS depends on the speed of sound near the phase transition as well as the chemical compositions in the subsequent HRG phase (as can be seen, e.g. from the different conclusions reached in Refs. [266] and [267], respectively). It is thus necessary to construct a more realistic EOS, using the most recent lattice QCD data for the QGP phase followed by a HRG phase in partially chemical equilibrium, and use it as standard input for hydrodynamic calculations in order to eliminate uncertainties associated with inaccurate modeling of the EOS. Recent developments in lattice QCD simulations for the EoS in 2+1 flavor QCD with a physical strange quark mass and almost physical light quark masses [268, 21] make analytical or tabulated constructions of a Lattice QCD inspired, realistic EOS possible, and several groups are working along this direction [269]²⁵.

The other motivation for constructing such a realistic EOS comes from the extraction of the QGP viscosity. As pointed in Ref. [129, 127] (and discussed in Chap. 7.2), this is an $O(25\%)$ effect on viscous v_2 suppression, depending on whether one uses a 1st order or smooth cross-over phase transition EOS. This translates into a $O(25\%)$ effect on the extracted value of the shear viscosity to entropy ratio η/s from experimental data. Considering that elliptic flow at present seems to be the only variable from which η/s can be extracted with some accuracy, it is desirable to eliminate the uncertainties from the EOS using our best available theoretical knowledge based on lattice QCD.

Hadron resonance gas EOS with partial chemical equilibrium:

²⁵The so-called lattice EOS (EOS L) used in this thesis and in Ref. [127] is still a crude one based on old lattice QCD data with unphysical quark masses [232] and without extrapolation to the continuum limit.

Early ideal hydrodynamic calculations [93, 234, 96, 264], assuming simultaneous chemical and kinetic freeze-out, successfully described both the shape of most p_T -spectra and the integrated and differential elliptic flow data from central to semi-central Au+Au collisions at top RHIC energies. However, it failed to reproduce the particle yields (total final multiplicities) and it underpredicted the pion spectra at low p_T . One example is the experimental pion/anti-proton ratio, which could not be reproduced in these ideal hydrodynamics simulation, but had to be fixed by hand by introducing a normalization factor.

Systematic studies of the measured particle yields for large number of hadron species within a statistic model indicates that chemical freeze-out happens right after the phase transition at $T_{ch} = 160 - 175$ MeV [98, 99]. This is much higher than the kinetic freeze-out temperature, $T_{th} = 90 - 130$ MeV, which is obtained from blast-wave model fits to the slope of the p_T spectra [270]. This separation between chemical and kinetic freeze-out motivates the construction an EOS for the HRG phase that implements partial chemical equilibrium among the hadron resonances as discussed in Chap. 3.3 [235, 236, 237, 238]. In this PCE-EOS, effective chemical potentials for different hadron species (that are introduced to maintain the measured particle ratios as the temperature decreases from T_{ch} to T_{th}) change the relation between temperature and energy density, reducing the kinetic freeze-out temperature for the same decoupling energy density. Holding the energy density at the value used in the early ideal hydrodynamic studies [93, 234, 96], this leads to steeper transverse momentum spectra. The experimental spectra can be re-fitted by adding some additional flow (either from the pre-equilibrium stage or introduced by shear viscosity), which flattens the spectra and compensates for the lower freeze-out temperature. However, the non-equilibrium chemical composition of the hadronic fireball also affects the distribution of the total momentum anisotropy among the various hadronic species at freeze-out. Together with the additional radial flow effects, this leads to an almost 25% larger pion elliptic flow [237] compared with early ideal hydrodynamic results and with experimental data, opening room for finite viscosity both in the QGP and hadronic phases. It is clearly necessary to include such a large effect also in the viscous hydrodynamics simulations before a quantitative extraction of η/s from experimental data can be attempted.

As explained in Chap. 3.3, the hadron cascade model [47] naturally incorporates the partial chemical equilibrium through its combination of elastic, quasi-elastic and inelastic cross sections among different hadron species. Since these cross section are finite, it also accounts for kinetic non-equilibrium (or viscous) behavior in the HRG phase, by solving the coupled Boltzmann equations through Monte-Carlo simulations.

Hybrid approaches, constructed by coupling (3+1)-d ideal hydrodynamics to such a hadron cascade model just below T_c , show simultaneously good descriptions of the particle yields, the p_T -spectra and the differential elliptic flow $v_2(p_T)$ for different hadron species from Au+Au collisions at top RHIC energies [38, 37]. Pure ideal hydrodynamic simulations with PCE-EOS give good descriptions of particle yields and spectra, but over-predict the elliptic flow. Viscous suppression of additional elliptic flow buildup in the hadronic phase is necessary to reduce the chemical non-equilibrium enhancement of pion elliptic flow without affecting the hadron yields. These two facts strongly indicate that the chemical non-equilibrium v_2 enhancement and viscous v_2 suppression tend to partially balance each other in the hadronic phase at RHIC energies. This will no longer be true at LHC energies, where the elliptic flow fully saturates in the QGP phase [271] such that viscous v_2 suppression in the hadronic stage is no longer significant, while the v_2 enhancement caused by the non-equilibrium chemistry in the HRG still persists since the latter reshuffles the momentum anisotropy generated in the QGP phase among different hadron species in the HRG phase.

Considering the above factors, viscous hydrodynamics requires implementation of the PCE-EOS for the HRG phase as well as matching to a hadron cascade. Using a partially chemically equilibrated HRG EOS is necessary to ensure approximate insensitivity of the final results to the exact value of the switching temperature T_{ch} , where one switches from viscous hydrodynamics to the cascade model [272]. Such a proper treatment of the HRG phase is necessary before extracting the QGP viscosity from experimental data. A relatively easy procedure is to directly connect viscous hydrodynamics with a hadron cascade right after T_c , where the HRG is still in chemical equilibrium. However, the PCE-EOS helps to generate the correct

hadron chemistry even at lower temperatures, thus enlarging the temperature window where one can switch from hydrodynamics to the hadron cascade description, without changing the hadron yields. This makes the implementation of a more realistic dynamical freeze-out (see Chap. 8.2) possible. Such research is important, but will have to be left for the future.

8.4 Bulk viscosity

Currently, most of the existing viscous hydrodynamic calculations concentrate on shear viscosity effects, but neglect bulk viscosity for simplicity. Bulk viscous effects were investigated in Chap. 6 (see Ref. [130]). We found that the negative bulk pressure ($\Pi = -\zeta\theta$ in the N-S limit) reduces the total pressure (which effectively softens the EOS near T_c), decelerates both longitudinal and transverse expansion, and suppresses the build up of flow. As a result, the hadron spectra become steeper, and the elliptic flow is suppressed in the low- p_T region. Fig. 6.3 in Chap. 6 showed that even the “minimal” bulk viscosity, as constructed there, leads to $\sim 25\%$ additional viscous v_2 suppression if one uses the N-S initialization. This translates into a $\sim 25\%$ uncertainty for the extracted value of QGP shear viscosity η/s when comparing experimental elliptic flow data with viscous hydrodynamics results. However, there are no well-defined theoretical results for the bulk relaxation time τ_Π . Critical slowing down during the phase transition suggests a larger τ_Π near T_c , but the exact analytical form and its maximum value are still unknown. Using a τ_Π with peak value of 5 fm/c near T_c , we found that bulk viscous v_2 suppression is very sensitive to the bulk pressure initialization one inputs, which ranges from 2% (or zero initialization) to $\sim 10\%$ (for N-S initialization), if minimal bulk viscosity as defined in Chap. 3.6 is used.

Considering the current theoretical uncertainties on bulk viscosity itself (the peak value of ζ/s near the phase transition and the bulk viscosity in the hadronic phase) and our poor theoretical control over the initialization for the bulk pressure and the bulk relaxation time (see Chap. 3.5 for details), it is thus unclear how much uncertainty bulk viscosity can bring to the extraction of a shear viscosity value of the QGP. Clearly, bulk viscous effects must be taken into account and additional theoretical research is needed to reduce the uncertainties of its value and relaxation time. Our analysis showed that η/s and ζ/s will always combine in their effects on viscous v_2 suppression. At present, it is not clear how to separate them, possibly by using additional observables.

8.5 Glauber model vs. CGC initialization

We now come to what may turn out to be the most serious road block for precision measurements of the QGP shear viscosity: our insufficient knowledge of the initial source eccentricity ε . It has now been known for a while that the Color Glass Condensate (CGC) model, implemented in the initial entropy or energy density profile via the fKLN parametrizations (see [229,227] and Chap. 3.2 for references), leads to $\sim 30\%$ larger initial source eccentricities than the popular Glauber model. Ideal fluid dynamics transforms this larger source eccentricity into $\sim 30\%$ larger elliptic flow. Since the extraction of η/s is based on the viscous *suppression* of v_2 , obtained by comparing the measured elliptic flow with an ideal (inviscid) fluid dynamical benchmark calculation, a 30% uncertainty in this benchmark can translate into a 100% uncertainty in the extracted value for η/s . This was recently shown by Luzum and Romatschke (see Fig. 8 in [135]). This uncertainty trumps most of the other uncertainties discussed above. Worse, since the initial source eccentricity depends on details of the shape of the fKLN profile near the edge of the distribution where the gluon saturation momentum scale Q_s becomes small and the CGC model reaches its limit of applicability, there is little hope that we can eliminate this uncertainty theoretically from first principles.

Based on their analysis of charged hadron elliptic flow data from the STAR experiment, allowing for a 20% systematic uncertainty of these data, the authors of [135] found an allowed range $0 < \eta/s < 0.1$ for

Glauber and $0.08 < \eta/s < 0.2$ for CGC initial conditions. This amounts to a $O(100\%)$ difference for the extracted η/s between these two initialization models. Since the analysis in [135] did not include a comprehensive investigation of effects caused by permissible variations of the EOS near T_c , by bulk viscosity, or by late hadronic viscosity and non-equilibrium chemical composition at freeze-out (see preceding sections), one should add a significant additional uncertainty band to these ranges. Furthermore, correcting the experimental data for event-by-event fluctuations in the initial source eccentricity [273] may bring down the measured v_2 values even below the range considered in [135]. Still, we agree with Luzum and Romatschke that, even when adding all the above effects in magnitude (ignoring the fact that several of them clearly have opposite signs), viscous hydrodynamics with $\eta/s > 5 \times (1/4\pi)$ would suppress the elliptic flow too much to be incompatible with experiment.

8.6 Numerical viscosity

To study the effects from shear and bulk viscosity one must ensure that numerical viscosity is under control and sufficiently small. Simply speaking, numerical viscosity comes from the discretization of the hydrodynamic equations for numerical calculation. It causes entropy production even in ideal hydrodynamics without shocks and can never be fully avoided. To minimize numerical viscosity, the flux-corrected transport algorithm SHASTA [274] employed by VISH2+1 (and by its ideal fluid ancestor AZHYDRO [246]) implements an “antidiffusion step” involving a parameter Λ called “antidiffusion constant” [274]. For a given grid spacing, numerical viscosity is maximized by setting $\Lambda = 0$. In standard situations, the default value $\Lambda = \frac{1}{8}$ minimizes numerical viscosity effects [274]. With $\Lambda = \frac{1}{8}$ and typical grid spacing $\Delta x = \Delta y = 0.1$ fm, $\Delta\tau = 0.04$ fm/c, AZHYDRO generates only 0.3% additional entropy in central Au+Au collisions. This is negligible when compared with the $\mathcal{O}(10\%)$ entropy production by VISH2+1 for a fluid with real shear viscosity $\eta/s = 1/4\pi$.

By increasing the grid spacing in AZHYDRO and/or changing Λ , we can explore the effects of numerical viscosity on radial and elliptic flow. We find that numerical viscosity has little effect on the development of radial flow but reduces v_2 in very much the same way as does real shear viscosity. Since we gauge the effects of η/s on v_2 by comparing results from VISH2+1 for $\eta/s \neq 0$ to those for $\eta/s = 0$, we should explore how much in the latter case v_2 is already suppressed by numerical viscosity. We can do this by setting $\eta/s = 0$ and reducing the grid spacing until v_2 stops changing (i.e. until we have completely removed all numerical viscosity effects on v_2). In this way we have ascertained that for our standard grid spacing numerical viscosity suppresses the differential elliptic flow $v_2(p_T)$ by less than 2%.

8.7 Conclusions

While the elliptic flow v_2 generated in non-central heavy-ion collisions is very sensitive to the shear viscosity to entropy ratio η/s of the QGP, it is also significantly affected by (i) details of the initialization of the hydrodynamic evolution, (ii) bulk viscosity and sound speed near the quark-hadron phase transition, and (iii) the chemical composition and non-equilibrium kinetics during the late hadronic stage. Not all of these effects are presently fully under control. Recent attempts to extract the specific shear viscosity η/s phenomenologically, by comparing experimental elliptic flow data with viscous hydrodynamics, have established a robust upper limit [135, 127]

$$\left. \frac{\eta}{s} \right|_{\text{QGP}} < 5 \times \frac{1}{4\pi}, \quad (8.1)$$

tantalizingly close to the conjectured KSS bound [146], but further progress requires elimination of the above systematic uncertainties. Since some of these influence the build-up of elliptic flow in opposite directions, it is

quite conceivable that the QGP specific viscosity is in fact much closer to the KSS bound $(\eta/s)|_{\text{KSS}} = 1/4\pi$ than suggested by the upper limit (8.1). Ongoing improvements on the theory side should help to reduce or eliminate most of the above uncertainties, bringing us closer to a quantitative extraction of η/s for the quark-gluon plasma. The single largest uncertainty, however, is caused by our poor knowledge of the initial source eccentricity which varies by about 30% between models. As shown in [135], this translates into an $\mathcal{O}(100\%)$ uncertainty for η/s . It seems unlikely that theory can help to eliminate this uncertainty from first principles. It thus appears crucial to develop experimental techniques that may help us to pin down the initial source eccentricity phenomenologically, with quantitative precision at the percent level.

Chapter 9: η/s from Other Considerations and Extraction Methods

9.1 Shear viscosity and Knudsen number

The Knudsen number approach starts with fitting the experimental multiplicity scaling curve for v_2/ε as a function of $\frac{1}{S} \frac{dN}{dy}$ by a simple formula:

$$\frac{v_2}{\varepsilon} = \frac{v_2^{hydro}}{\varepsilon} \frac{1}{1 + K/K_0}. \quad (9.1)$$

The above empirical formula are phenomenologically obtained from a two-dimensional parton cascade model simulations [275, 276, 277] from which one can directly measure the elliptic flow v_2 by sampling the particle distribution, and also calculate the Knudsen number K^{26} . K_0 is the free parameter in this formula, and from two-dimensional parton cascade model simulation runs one finds $K_0 = 0.7$ for a dilute system.

Extracting the QGP viscosity requires an estimate of the Knudsen number from experimental data first. It is known that elliptic flow v_2 is developed at an early stage, roughly at a time scale \bar{R}/c_s for an EoS with constant speed of sound c_s [277]. At the time $\tau \sim \bar{R}/c_s$, the particle density can be estimated by $c\tau n \sim \frac{1}{S} \frac{dN}{dy}$, assuming that total particle number is conserved and the transverse size of the system does not vary significantly. Then one can connect the Knudsen number with the final multiplicity per unit area $(1/S)dN/dy$ as follows [275]:

$$\frac{1}{K} \equiv \frac{R}{\lambda} = \frac{\sigma n R}{1} = \frac{\sigma}{S} \frac{dN}{dy} c_s. \quad (9.2)$$

After fitting the experimental multiplicity scaling curve for v_2/ε (for Glauber initial eccentricity and CGC initial eccentricity, respectively) with eqs. (9.1) and (9.2), one finds $v_2^{hydro}/\varepsilon = 0.30 \pm 0.02$ and $\sigma = 4.3$ mb for Glauber initialization, and $v_2^{hydro}/\varepsilon = 0.22 \pm 0.01$ and $\sigma = 7.6$ mb for CGC initialization (using $c_s^2 = 1/3$) [277].

The shear viscosity to entropy ratio is estimated using the formula for a classical gas of massless particles with isotropic differential cross section [278]:

$$\frac{\eta}{s} = 0.316 \frac{T}{c\sigma n}. \quad (9.3)$$

One finds $\eta/s = 0.19$ for Glauber initialization and $\eta/s = 0.11$ for CGC initialization, with the inputs $T = 200$ MeV and $n = 3.9 \text{ fm}^{-3}$ [277]²⁷. Since the particle density evolves with time, eq. (9.3) shows that a constant cross section and constant η/s throughout the fireball evolution are mutually exclusive. The η/s value extracted from this method thus represents at best an average value, taken over the history of the medium. Detailed hydrodynamic simulations in our group [231] show that the evolution history (and thus this average) depends on the initialization (Glauber vs. CGC) and the EOS. The estimated η/s values from Ref. [277] thus have to be considered with caution.

²⁶Knudsen number K is defined as the ratio of the mean free path and the system size, $K \equiv \frac{\lambda}{R}$. For a parton cascade model simulated within a two-dimensional $R_x \times R_y$ box, the system size is estimated by $R = (\frac{1}{R_x^2} + \frac{1}{R_y^2})^{-1/2}$. The mean free path λ is inversely proportional to transport cross section σ and particle density n , $\lambda = \frac{1}{\sigma n}$, with $n = \frac{N}{4\pi R_x R_y}$ (N is the number of test particles in a Monte Carlo simulation).

²⁷ $n = 3.9 \text{ fm}^{-3}$ is estimated at the time when v_2 is developed [275].

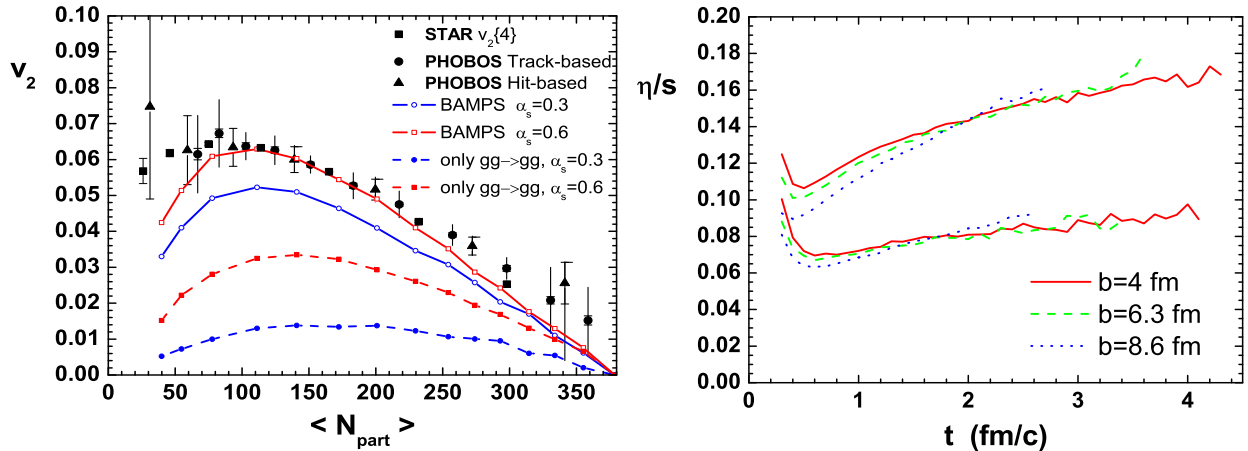


Figure 9.1: Left panel: elliptic flow $v_2(|y| < 1)$ from BAMPs [55](Boltzmann Approach of Multi-Parton Scattering) using $\alpha_s = 0.3$ and 0.6 , compared with the PHOBOS [279] and STAR [280] data. Right panel: The shear viscosity to entropy density ratio η/s at the central region during the entire expansion [55]. η/s values are extracted from the simulations at impact parameter $b = 4, 6.3,$ and 8.6 fm. The upper band shows the results with $\alpha_s = 0.3$ and the lower band the results with $\alpha_s = 0.6$

9.2 Shear viscosity from the parton cascade model

In contrast to the macroscopic hydrodynamic approach, the QGP fireball evolution can also be microscopically described by a Parton Cascade Model (PCM), solving the Boltzmann equation for colliding gluons. The earlier parton cascade model [52, 51] that only included $2 \rightarrow 2$ elastic gluon collisions was not able to achieve thermal equilibrium and to reproduce the large experimentally measured elliptic flow, unless unrealistically large scattering cross sections, far beyond the expectations of pQCD on which the parton cascade is based, were assumed [281]. Recently, a radiative parton cascade model including radiative $2 \leftrightarrow 3$ processes and their inverse has been developed to study, on a semiclassical level, the dynamics of gluon matter produced at RHIC energies [54, 282, 283, 284, 285]. This approach has shown that some well-known strongly coupled QGP phenomena (such as fast thermalization of the initial non-equilibrium system, large elliptic flow and a small shear viscosity to entropy ratio) can be achieved within a framework that is based on weakly coupled QCD [286].

The left panel of Fig. 9.1 shows the elliptic flow v_2 , calculated from the parton cascade model with only two body interactions ($gg \rightarrow gg$) and with multi-parton interactions ($gg \rightarrow gg, gg \rightarrow ggg$ and $ggg \rightarrow gg$, denoted as BAMPs²⁸ in the figure), using different values of the coupling constant α_s as input [55]. One finds that large elliptic flow v_2 , comparable to the experimental data, can be achieved within the perturbative QCD description if the radiative collision processes $gg \leftrightarrow ggg$ are included.

The shear viscosity η can be extracted from the Parton Cascade Simulation through the following formula (using the N-S approximation) [287]:

$$\eta \cong \frac{1}{5} n \frac{\langle E(\frac{1}{3} - v_z^2) \rangle}{\frac{1}{3} - \langle v_z^2 \rangle} \frac{1}{\sum R^{\text{tr}} + \frac{3}{4} n \partial_t (\ln \lambda)}. \quad (9.4)$$

²⁸Boltzmann Approach of Multi-Parton Scattering

Here n is gluon density, E is gluon energy, $v_z = \frac{p_z}{E}$ is the gluon velocity along the beam direction and λ is the gluon fugacity, $\lambda = n/n_{eq}$. $\sum R^{tr}$ denotes the total transport collision rate, the expression of which can be found in Ref [287].

The right panel of Fig. 9.1 shows the shear viscosity to entropy ratio η/s extracted from BAMPS, for different impact parameters and α_s values. One finds that η/s depends weakly on the gluon density or temperature (indicated by the time evolution on the horizontal axis), but depends strongly on α_s . For $\alpha_s = 0.6$, which best fits the experimental elliptic flow data, $\eta/s \simeq 0.08$, a value that is very close to the minimal KSS bound $1/4\pi$, is reached. The authors stated, however, that η/s may increase once hadronization and a subsequent hadron cascade are included [286].

The authors of Ref. [288] derived an improved expression for shear viscosity within the second order Israel-Stewart formalism, for a one-dimensionally expanding particle system. One finds that although the improved I-S expression increases the extracted η/s , when compared to eq. (9.4), the difference is within 20% for $\alpha_s = 0.3 - 0.6$ [287].

9.3 Shear viscosity and radiative energy loss

The estimation of the shear viscosity from radiative energy loss is inspired by the kinetic theory expression of shear viscosity η [278],

$$\eta = C\rho\langle p\rangle\lambda_{mfp} = C\langle p\rangle\frac{1}{\sigma_{tr}}, \quad (9.5)$$

where ρ is the particle density, $\langle p\rangle$ is the average particle momentum and λ_{mfp} is the mean free path. Again, the last expression replaces the mean free path by $\lambda_{mfp} = (\rho\sigma_{tr})^{-1}$ with particle density ρ and transport cross section σ_{tr} . In perturbative QCD and QED, the transport cross section σ_{tr} is dominated by small angle scattering and can be expressed by

$$\sigma_{tr} = \frac{4}{\langle E_{cm}^2\rangle} \int dk_{\perp}^2 k_{\perp}^2 \frac{d\sigma}{dk_{\perp}^2}, \quad (9.6)$$

where $\langle E_{cm}^2\rangle$ is the center of mass energy, with $\langle E_{cm}^2\rangle \approx 18T^2$ for a thermal medium with temperature T .

On the other hand, the transport parameter \hat{q} (which describes the per unit length energy loss of a fast parton traveling through the QGP by gluon bremsstrahlung), has a theoretical definition associated with the transverse momentum broadening of a fast parton through interaction with the medium:

$$\hat{q} = \rho \int dk_{\perp}^2 k_{\perp}^2 \frac{d\sigma}{dk_{\perp}^2}. \quad (9.7)$$

Here $\frac{d\sigma}{dk_{\perp}^2}$ is the differential cross section for elastic scattering in the medium, and ρ is the medium particle density.

Comparing eqs. (9.5) and (9.7), one finds that the shear viscosity to the entropy density ratio η/s can be expressed as [289]:

$$\frac{\eta}{s} \approx 1.25 \frac{T^3}{\hat{q}}, \quad (\text{for weak coupling}). \quad (9.8)$$

Here one set $C = 1/3$ [210, 211] and used $\langle p\rangle \approx 3T$, and $s \approx 3.6\rho$ for a thermal ensemble consisting of massless bosons.

In Ref. [289] the relationship between shear viscosity η and jet quenching parameter \hat{q} was formally derived within the weakly coupled QGP picture, for two different circumstances: **1**) the distribution of quasi-particles satisfies a linearized Boltzmann equation with a soft scattering collision term in leading-log approximation for a pure gluon gas [156]; **2**) the evolution of the quasi-particle distribution function satisfies

a Fokker-Planck equation, which does not contain a collision term but includes the effects of a random color field. The latter contributes a small anomalous shear viscosity [290, 291]. One finds that the coefficient 1.25 found in eq. (9.8) holds in both of these cases.

In the above weak coupling scenario (which describes the quark gluon plasma by nearly massless quasi-particles), one estimates that $\eta/s = 0.12 - 0.24$ for a lower value of $\hat{q}^{HT} = 1 - 2 \text{ GeV}^2/\text{fm}$, and $\eta/s = 0.008 - 0.024$ for a higher value of $\hat{q}^{ASW} = 10 - 30 \text{ GeV}^2/\text{fm}$, with $T \approx 340 \text{ MeV}$. The uncertainty of the estimated η/s mainly comes from the different values of \hat{q} obtained from different schemes, and the error bands in each estimate comes from whether one takes \hat{q} to be proportional to $\varepsilon^{4/3}$ or to T^3 . The authors of [289] pointed out that for the larger \hat{q} value, the η/s ratio derived from (9.8) strongly violates the KSS Bound, which they interpreted as a sign of break-down of the weakly-interacting quasi-particle picture underlying the relation (9.8).

However, eq. (9.8) is no longer true in the case of strong coupling. After checking the shear viscosity and \hat{q} from strongly coupled N=4 supersymmetric Yang-Mills (SYM) theory and for pion gases (where the strong coupling limit of QCD is exhibited by confinement), Majumder, Muller and Wang [289] also found that

$$\frac{\eta}{s} \gg 1.25 \frac{T^3}{\hat{q}}, \quad (\text{for strong coupling}). \quad (9.9)$$

So in the strong coupling limit, η/s can not be usefully derived from a measurement of \hat{q} . Considering eqs.(9.8) and (9.9) together, they conclude instead that *“The determination of both shear viscosity η and jet quenching parameter \hat{q} from experimental data would give a quantitative assessment of the strongly coupled nature of the quark gluon plasma produced in heavy ion collisions”* [289].

9.4 Shear viscosity and heavy quark diffusion

Heavy quarks are unique probes to study the transport properties of the QGP. Based on the property that the masses ($M_c = 1.3 \text{ GeV}$ and $M_b = 4.2 \text{ GeV}$) of heavy quarks are much larger than the medium temperature ($T \sim 300 \text{ MeV}$), Moore and Teaney proposed a simple model to study the motion of heavy quarks by the following stochastic equations [292]:

$$\frac{dp_i}{dt} = \xi_i(t) - \eta_D p_i, \quad \langle \xi_i(t) \xi_j(t') \rangle = k \delta_{ij} \delta(t - t'). \quad (9.10)$$

Here η_D is the drag coefficient, which measures the momentum loss per unit time, and ξ_i characterizes the uncorrelated random momentum kicks from the medium.

The diffusion coefficient D is defined as the probability of “starting a heavy quark at $x = 0$ at $t = 0$ and finding it at the mean squared position Dt at a later time”:

$$\langle x_i(t) x_j(t) \rangle = 2Dt \delta_{ij} \longrightarrow 6Dt = \langle x^2(t) \rangle. \quad (9.11)$$

One finds that D is related to the drag coefficient η_D at zero momentum [292]:

$$D = \frac{T}{M \eta_D(0)}. \quad (9.12)$$

After perturbatively calculating the heavy quark diffusion coefficient D and comparing it with the weakly-coupled QGP shear viscosity η at leading order, Moore and Teaney found that the heavy quark diffusion coefficient is related to the hydrodynamic diffusion coefficient $\frac{\eta}{e+p}$ by a factor of ~ 6 [292]. For later convenience, we rewrite this as follows (using $e + p = Ts$):

$$\frac{\eta}{s} \approx \frac{1}{6} T D \quad (\text{wQGP}). \quad (9.13)$$

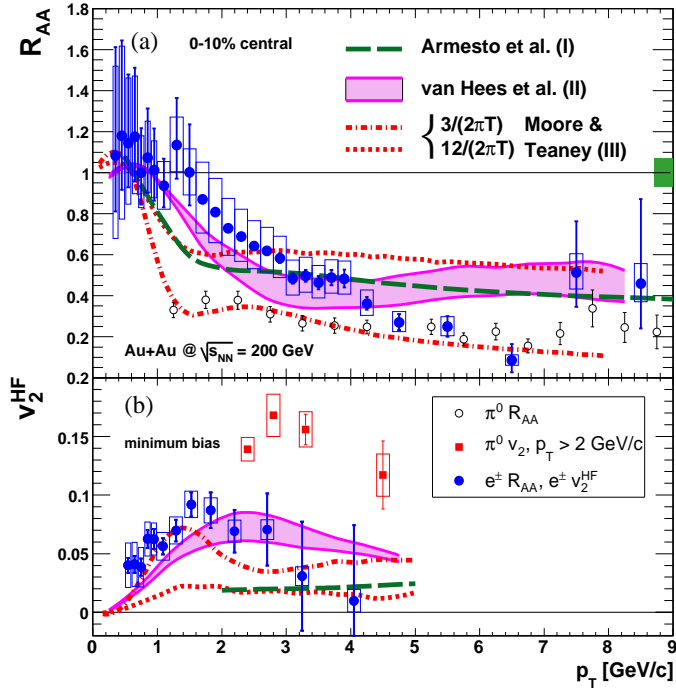


Figure 9.2: (a) R_{AA} of heavy-flavor electrons in 0-10% central collisions compared with π^0 data [293] and model calculations (curves I [294], II [295], and III [292]). (b) v_2^{HF} of heavy-flavor electrons in minimum bias collisions compared with π^0 data [296] and the same models. (Taken from the PHENIX data [297])

The heavy quark diffusion coefficient can also be calculated in strongly coupled $N = 4$ Super-Yang-Mills theory, using the AdS/CFT correspondence, which gives $D \simeq 1/(2\pi T)$ [298]. Recalling the remarkable result $\eta/s = 1/4\pi$ for a large class of strongly coupled theories that have a gravity dual ($N = 4$ SYM theory is one example among them), one finds the following simple relation between the heavy quark diffusion constant and the shear viscosity for a strongly coupled system:

$$\frac{\eta}{s} \approx \frac{1}{4\pi} D(2\pi T) = \frac{1}{2} TD \quad (N = 4 \text{ SYM}). \quad (9.14)$$

Fig. 9.2 shows the experimental quenching ratio R_{AA} (see Chap. 1.13) and v_2 for “non-photonic electrons” from semi-leptonic decays of heavy flavors (i.e. of hadrons carrying charm and bottom quarks) for Au+Au collisions at top RHIC energies, together with the theoretical predictions from different groups. The model that describes both R_{AA} and v_2 well is from van Hees et al. [295], leading to an estimate of the heavy quark diffusion constant $D \simeq (4 - 6)(2\pi T)$. Using the relations (9.13) and (9.14) for weakly and strongly coupled systems, respectively, one finds:

$$\frac{\eta}{s} = \begin{cases} (1.33 - 2)/4\pi & \text{for weak coupling,} \\ (4 - 6)/4\pi & \text{for strong coupling.} \end{cases} \quad (9.15)$$

A more detailed assessment of estimating η/s from the heavy quark diffusion constant D with different models can be found in the recent review article [299], to which we refer the interested reader.

9.5 Summary and comments

In Fig. 9.3, we summarize the estimated η/s from different methods, together with the lattice QCD estimates for a pure gluon plasma. One finds that all of these results fall in a relatively narrow band near the KSS bound at $1/4\pi$. This strongly indicates that the QGP created at RHIC energies is an almost perfect liquid.

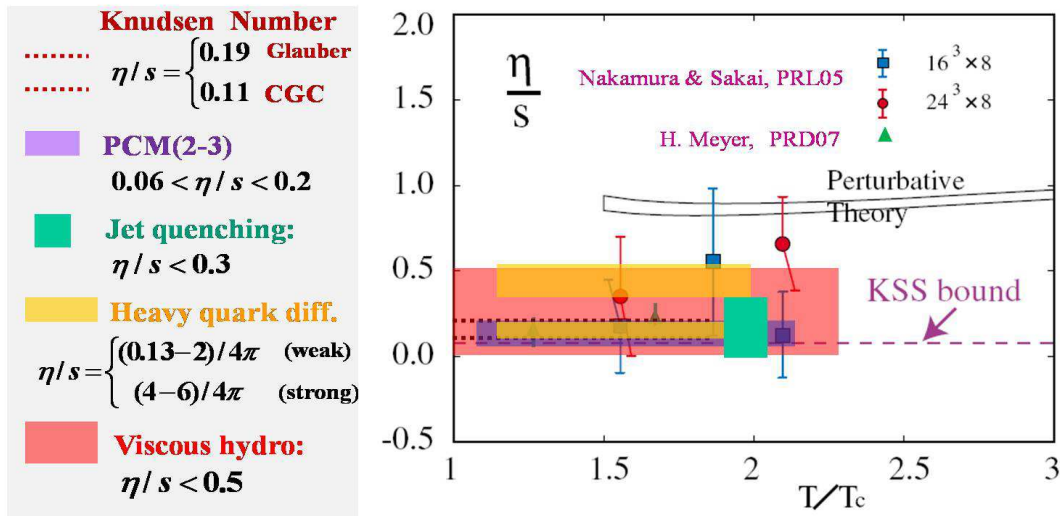


Figure 9.3: A summary for the estimated η/s from different method: **a)** from Knudsen number and multiplicity v_2 scaling (Ref. [277] and Chap. 9.1); **b)** from parton cascade model with $2 \rightarrow 2$ and $2 \rightarrow 3$ process (Ref. [55] and Chap. 9.2); **c)** from transport parameter \hat{q} of radiative energy loss (Ref. [289] and Chap. 9.3); **d)** from heavy quark diffusion constant D (Ref. [299] and Chap. 9.4); **e)** from viscous hydrodynamics (Ref. [135,127] and Chap. 8); **f)** SU(3) gluonic lattice QCD results from Nakamura and Sakai [162] and Meyer [163], respectively.

When interpreting the error bands in the figure, one must however pay attention to the assumptions and limitations of each method. For example, the narrow purple band is from the estimate based on parton cascade model, which simulates the dynamics of the pure SU(3) gluons [55]. To compare with the experimental data, it directly converts partons to hadrons, but totally neglects the effects from the phase transition and the succeeding hadronic expansion. Including these, the actual error band from the parton cascade model based estimate is very likely much larger than the current one. Although in the future the parton cascade model can be connected with the hadron cascade model to account for the highly viscous hadronic stage, this will not resolve generic difficulties of cascade models in treating the change of vacuum structure that occurs during the phase transition and reproducing a realistic EOS (see Chap. 1.12 for further discussion). As a result, the parton cascade model based approach also has difficulties to properly account for bulk viscous effects, which, as we showed in Chap. 6, should not be neglected when extracting the QGP shear viscosity.

The Knudsen number approach provides a simple way to estimate the shear viscosity to entropy ratio η/s from the experimental multiplicity scaling data for v_2/ε . However, it only gives an effective viscosity averaged over the whole evolution of the fireball, rather than the QGP viscosity, since the Knudsen number formula derived in Ref. [277] only deals with time averaged variables. On the other hand, the framework of this approach has also been challenged. For example, questions were raised about the basic assumption of this approach, which assumes a constant transport cross section σ during the whole fireball evolution and then extracts a constant η/s for a particular collision system. However, the Parton Cascade Model shows that a constant cross section σ corresponds an η/s that increases monotonically with time, while a constant η/s corresponds to a monotonically increasing σ [300]. This raises questions about the self-consistency of the Knudsen number approach.

The radiative energy loss and heavy quark diffusion approaches investigated both weakly and strongly coupled media and showed that the corresponding formulas for η/s are dramatically different. As emphasized

in Ref. [289], instead of using the different formulas to extract η/s , it is more preferable to use them to distinguish the strongly or weakly coupled nature of the QGP medium after both η/s and \hat{q} have been extracted from experimental data.

Simulations from current viscous hydrodynamic models show $\eta/s < 5/4\pi$. This error band is almost the largest, when compared with other estimates. However it is a pretty safe results, since it takes into account all kinds of uncertainties that currently persist (i.e. initial conditions, EOS, bulk viscosity, viscosity of the hadronic stage – see Chap. 8 for details). Compared with other methods, viscous hydrodynamics is a tool that directly attacks the problem for extracting the QGP viscosity. In the future it can be systematically improved through a controlled analysis of all presently persisting uncertainties. This is expected to further narrow down the uncertainty in η/s by a significant amount.

Chapter 10: Summary and Concluding Remarks

Ideal hydrodynamics has been a great success in describing and (in the case of elliptic flow) even predicting relativistic heavy ion collision data at RHIC energies. This has led to the well-known announcement that “RHIC scientists serve up the perfect liquid” – the quark-gluon plasma (QGP). To answer the question “*How perfect is the QGP fluid?*” quantitatively, one needs a dynamical framework which allows to include dissipative effects accurately and consistently. Causal viscous hydrodynamics is such a tool that not only improves the description of heavy-ion fireball dynamics in regions of parameter space where ideal hydrodynamics begins to fail, but also allows to extract even small values of η/s through detailed comparison with precise experimental data.

This thesis focused on causal viscous hydrodynamics for relativistic heavy ion collisions. The work included developing a numerical code to solve the causal viscous hydrodynamic equations and searching for possible signals for extracting the QGP viscosity. Based on the explicit form of the general 2nd-order Israel-Stewart (I-S) equations in 2+1-dimensions (derived by my advisor U. Heinz and myself [124]), assuming longitudinal boost-invariance but arbitrary dynamics in the 2-dimensional transverse plane, I subsequently developed a (2+1)-d viscous hydrodynamic code, called VISH2+1 (for “Viscous Israel-Stewart Hydrodynamics in 2+1 dimensions”) [125, 126]. This code has not only passed extensive tests against the well-established (2+1)-d ideal fluid code AZHYDRO and analytically known solutions for problems with reduced dimensionality during the early stage of my work [126] (see Appendix A. 2), but recently also passed detailed code verification tests (within the TECHQM Collaboration) against two other viscous hydrodynamics codes that were developed independently at the University of Washington and at Stony Brook later on (see Chap. 7.4).

Using VISH2+1, we numerically studied the effects from shear viscosity [125, 126] (Chap. 4) and bulk viscosity [130] (Chap. 6) on the hydrodynamic evolution of the QGP fireball, the final hadron spectra, and their elliptic flow coefficient v_2 . We found that shear viscosity reduces the longitudinal expansion, but accelerates transverse expansion, which leads to larger radial flow and flatter spectra when compared with an ideal fluid with identical initial and final conditions. Bulk viscosity reduces both longitudinal and transverse expansion, resulting in smaller radial flow and steeper spectra. Both shear and bulk viscosity suppress elliptic flow v_2 at low p_T . It turns out that v_2 is very sensitive to the QGP shear viscosity, and that in heavy ion collisions at RHIC energies even the conjectured lower bound, $\eta/s = 1/4\pi$, leads to a large suppression of v_2 . We explored the scaling behavior of v_2 with the initial source eccentricity ε_x , by computing v_2/ε_x as a function of charged hadron multiplicity in both ideal and viscous hydrodynamics, for Cu+Cu and Au+Au collisions at a variety of impact parameters and collision energies. We found that smaller systems and collisions at lower energies feature stronger shear viscosity effects, and that non-zero shear viscosity breaks the scaling of v_2/ε_x with charged multiplicity by small amounts that can perhaps be used to further constrain the QGP shear viscosity experimentally [127] (Chap. 5).

The first attempt to extract the QGP viscosity from RHIC elliptic flow data using viscous hydrodynamics comes from the work of Luzum and Romatschke. Their results indicate [135, 129]

$$\left. \frac{\eta}{s} \right|_{\text{QGP}} < 5 \times \frac{1}{4\pi}. \quad (10.1)$$

A more precise extraction of the QGP viscosity, however, requires to at least consider the following aspects in the future [129] (Chap. 8):

- **Better understanding of the initialization:** the largest contribution to the present uncertainty range for η/s comes from uncontrolled uncertainties in the initial conditions for the fireball eccentricity, more

specifically, the Glauber initialization vs. the Color Glass Condensate initialization. This issue can not be solved by hydrodynamics itself, but requires new experimental techniques to help us pin down the initial source eccentricity phenomenologically. In addition, it is important to implement event-by-event fluctuations in the initial source eccentricity in viscous hydrodynamic simulations to account for additional contributions to the elliptic flow v_2 .

- Constructing a better EOS: The non-equilibrium chemistry in the hadronic phase is known to affect the distribution of the hydrodynamic momentum anisotropy over the various hadron species and thus their elliptic flow, but has not yet been included in viscous hydrodynamic simulations. With the availability of new, more accurate lattice QCD data on the EOS, using almost physical quark masses, it is now possible and necessary to construct a new EOS that connects this latest lattice EOS above T_c with the non-equilibrium hadronic EOS below T_c .
- Viscous hydrodynamics + hadron cascade: The hadronic stage is highly viscous, to the extent that the framework of viscous fluid dynamics may break down. It is therefore necessary to match viscous hydrodynamics to a microscopic hadronic cascade below T_c . It is also important to investigate how well the late non-equilibrium hadronic stage can be reasonably simulated by viscous hydrodynamics with a temperature-dependent viscosity/entropy ratio that increases rapidly as the matter approaches freeze-out, and explore possibilities of extracting the viscosity of hadronic matter.
- Including effects from bulk viscosity: My recent research has shown that bulk viscosity also suppresses v_2 , thus adding to the effects from shear viscosity. It is therefore important to include bulk viscosity effects when extracting the QGP shear viscosity. However, relaxation times and initial values for the bulk pressure are required inputs in viscous hydrodynamic calculations, in addition to the transport coefficients and the EOS. Near T_c , the bulk viscosity ζ can exceed the shear viscosity η of the strongly interacting matter. If the relaxation time τ_Π for the bulk viscous pressure Π is short, it quickly loses memory of its initial value, but the relatively large peak value of ζ/s near T_c can lead to a significant viscous suppression of the elliptic flow v_2 , competing with shear viscous effects. If τ_Π grows rapidly near T_c , due to critical slowing down, the bulk viscous suppression effects on v_2 depend crucially on the initial value of Π : If Π is zero initially, bulk viscous effects on v_2 are almost negligible; if Π is initially large, however, as for the case of the N-S initialization, it remains relatively large throughout the evolution, suppressing the buildup of elliptic flow at a level that again competes with shear viscous effects. Additional research on initial conditions and relaxation times for the bulk viscous pressure is therefore necessary for a quantitative extraction of η/s from measured data.

In short, the field of viscous relativistic fluid dynamics is experiencing a fast and healthy development, with contributions from and collaborations among several different groups. As a result, we have reached a new threshold: we are in the process of quantitatively extracting the transport properties of the QGP, a new type of matter that we knew almost nothing about even a decade ago. What has been covered in this thesis is only the beginning of the story.

APPENDIX A:

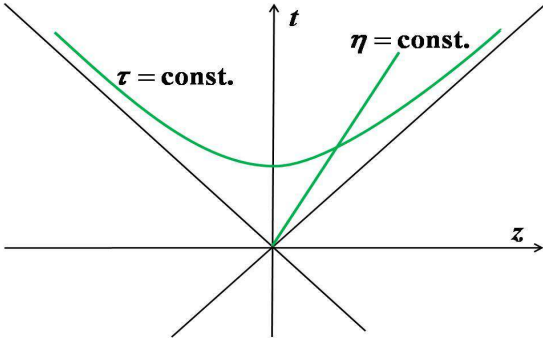
A.1 Coordinates and Transformations

The three spatial coordinates and time form a four dimensional coordinate system $x^\mu = (t, x, y, z)$, called *Cartesian coordinates*. Throughout this thesis, we use the metric tensor $g_{\mu\nu} = g^{\mu\nu} = \text{diag}(1, -1, -1, -1)$, such that four vectors (x^μ , for example) transform as follows:

$$x^\mu = (t, x, y, z), \quad x_\mu = g_{\mu\nu}x^\nu = (t, -x, -y, -z). \quad (\text{A.1})$$

One generally sets the z -axis parallel to the beam direction, and correspondingly calls the (x, y) plane the transverse plan (with x pointing in the direction of the impact parameter). Within the forward light-cone $|z| < t$, $\eta - \tau$ coordinates $x^m = (\tau, x, y, \eta)$ (with $\tau = \sqrt{t^2 - z^2}$ and $\eta = \frac{1}{2} \ln \frac{t+z}{t-z}$) prove more useful in high energy particle and nuclear physics. The metric in this coordinate system reads $g^{mn} = \text{diag}(1, -1, -1, -1/\tau^2)$, $g_{mn} = \text{diag}(1, -1, -1, -\tau^2)$.

Here we list the transformation between Cartesian and $\eta - \tau$ coordinates:



$$\begin{aligned} x^\mu &= (t, x, y, z) & x^m &= (\tau, x, y, \eta) \\ t &= \tau \cosh \eta & \tau &= \sqrt{t^2 - z^2} \\ z &= \tau \sinh \eta & \eta &= \arctan(z/t) \end{aligned}$$

A.2 Details of the viscous hydro code VISH2+1

A.2.1 Expressions for $\tilde{\pi}^{mn}$ and $\tilde{\sigma}^{mn}$

The expressions for $\tilde{\pi}^{mn}$ and $\tilde{\sigma}^{mn}$ in eq. (3.3) are

$$\tilde{\pi}^{mn} = \begin{pmatrix} \pi^{\tau\tau} & \pi^{\tau x} & \pi^{\tau y} & 0 \\ \pi^{\tau x} & \pi^{xx} & \pi^{xy} & 0 \\ \pi^{\tau y} & \pi^{xy} & \pi^{yy} & 0 \\ 0 & 0 & 0 & \tau^2 \pi^{\eta\eta} \end{pmatrix}, \quad (\text{A.2})$$

$$\begin{aligned}
\tilde{\sigma}^{mn} = & \begin{pmatrix} \partial_\tau u^\tau & \frac{\partial_\tau u^x - \partial_x u^\tau}{2} & \frac{\partial_\tau u^y - \partial_y u^\tau}{2} & 0 \\ \frac{\partial_\tau u^x - \partial_x u^\tau}{2} & -\partial_x u^x & -\frac{\partial_x u^y + \partial_y u^x}{2} & 0 \\ \frac{\partial_\tau u^y - \partial_y u^\tau}{2} & -\frac{\partial_x u^y + \partial_y u^x}{2} & -\partial_y u^y & 0 \\ 0 & 0 & 0 & -\frac{u^\tau}{\tau} \end{pmatrix} \\
& - \frac{1}{2} \begin{pmatrix} D((u^\tau)^2) & D(u^\tau u^x) & D(u^\tau u^y) & 0 \\ D(u^\tau u^x) & D((u^x)^2) & D(u^x u^y) & 0 \\ D(u^\tau u^y) & D(u^x u^y) & D((u^y)^2) & 0 \\ 0 & 0 & 0 & 0 \end{pmatrix} \\
& + \frac{1}{3} (\partial \cdot u) \begin{pmatrix} (u^\tau)^2 - 1 & u^\tau u^x & u^\tau u^y & 0 \\ u^\tau u^x & (u^x)^2 + 1 & u^x u^y & 0 \\ u^\tau u^y & u^x u^y & (u^y)^2 + 1 & 0 \\ 0 & 0 & 0 & 1 \end{pmatrix}.
\end{aligned} \tag{A.3}$$

Here $D = u^\tau \partial_\tau + u^x \partial_x + u^y \partial_y$ and $\partial \cdot u = \partial_\tau u^\tau + \partial_x u^x + \partial_y u^y + \frac{u^\tau}{\tau}$.

A.2.2 Velocity finding

As shown in [124], since we evolve all three components $\pi^{\tau\tau}$, $\pi^{\tau x}$, and $\pi^{\tau y}$ (one of which is redundant due to the constraint $\pi^{\tau m} u_m = 0$), the flow velocity and energy density can be found from the energy-momentum tensor components with the same efficient one-dimensional zero-search algorithm employed in ideal hydrodynamics [301, 302]. This is important since this step has to be performed after each time step at all spatial grid points in order to evaluate the EOS $p(e)$.

Using the output from the numerical transport algorithm, one defines the two-dimensional vector $\mathbf{M} = (M_x, M_y) \equiv (T^{\tau x} - \pi^{\tau x}, T^{\tau y} - \pi^{\tau y})$. This is (up to the substitution $p + \Pi \rightarrow p$) the ideal fluid part of the transverse momentum density vector; as such it is parallel to the transverse flow velocity $\mathbf{v}_\perp = (v_x, v_y)$. Introducing further $M_0 \equiv T^{\tau\tau} - \pi^{\tau\tau}$, one can write the energy density as

$$e = M_0 - \mathbf{v}_\perp \cdot \mathbf{M} = M_0 - v_\perp M, \tag{A.4}$$

where $v_\perp = \sqrt{v_x^2 + v_y^2}$ is the transverse flow speed and $M \equiv \sqrt{M_x^2 + M_y^2}$. One sees that solving for e requires only the magnitude of \mathbf{v}_\perp which is obtained by solving the implicit relation [301, 302, 124]

$$v_\perp = \frac{M}{M_0 + p(e = M_0 - v_\perp M) + \Pi}. \tag{A.5}$$

by a one-dimensional zero-search. The flow velocity components are then reconstructed using

$$v_x = v_\perp \frac{M_x}{M}, \quad v_y = v_\perp \frac{M_y}{M}. \tag{A.6}$$

Note that this requires direct numerical propagation of all three components ($\pi^{\tau\tau}$, $\pi^{\tau x}$ and $\pi^{\tau y}$) since the flow velocity is not known until after the velocity finding step has been completed. Hence the transversality constraint $\pi^{\tau m} u_m = 0$ cannot be used to determine, say, $\pi^{\tau\tau}$ from $\pi^{\tau x}$ and $\pi^{\tau y}$. However, it can be used after the fact to test the numerical accuracy of the transport code.

A.3 Tests of the viscous hydro code VISH2+1

A.3.1 Testing the ideal hydro part of VISH2+1

When one sets $\pi^{mn} = 0$ initially and takes the limit $\eta = 0$, VISH2+1 simulates the evolution of an ideal fluid, and its results should agree with those of the well-tested and publicly available (2+1)-dimensional

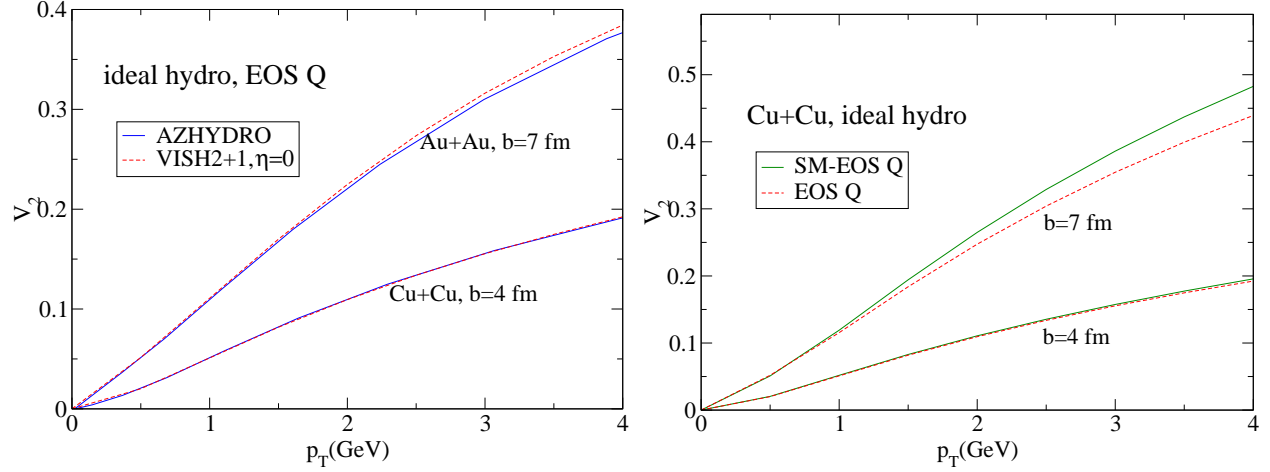


Figure A.1: *Left*: Differential elliptic flow $v_2(p_T)$ for π^- from $b = 4$ fm Cu+Cu collisions and $b = 7$ fm Au+Au collisions, using EOS Q. Results from VISH2+1 for $\eta = 0$ and $\pi^{mn} = 0$ (dashed lines) are compared with the ideal fluid code AZHYDRO (solid lines). *Right*: $v_2(p_T)$ for π^- from Cu+Cu collisions at impact parameters $b = 4$ and 7 fm, comparing VISH2+1 evolution with EOS Q (dashed) and SM-EOS Q (solid) in the ideal fluid limit $\eta = 0$, $\pi^{mn} = 0$.

ideal fluid code AZHYDRO [246]. Since VISH2+1 was written independently, using only the flux-corrected SHASTA transport algorithm from the AZHYDRO package [246, 274] in its evolution part, this is a useful test of the code. The left panel in Fig. A.1 shows that, for identical initial and final conditions as described in Chap. 3, the two codes indeed produce almost identical results. The small difference in the Au+Au system at $b = 7$ fm is likely due to the slightly better accuracy of AZHYDRO which, in contrast to VISH2+1, invokes an additional timesplitting step in its evolution algorithm.

When comparing our VISH2+1 results with AZHYDRO we initially found somewhat larger discrepancies which, however, could be traced back to different versions of the EOS used in the codes (EOS Q in AZHYDRO, the smoothed version SM-EOS Q in VISH2+1). In the left panel of Fig. A.1 this difference has been removed, by running also VISH2+1 with EOS Q. In the right panel we compare VISH2+1 results for EOS Q and for SM-EOS Q, showing that even the tiny rounding effects resulting from the smoothing procedure used in SM-EOS Q (which renders the EOS slightly stiffer in the mixed phase) lead to differences in the elliptic flow for peripheral collisions of small nuclei which exceed the numerical error of the code.

A.3.2 Comparison with analytical results for (0+1)-d boost-invariant viscous hydrodynamics

For boost-invariant longitudinal expansion without transverse flow, the relativistic Navier-Stokes equations read [211] (for zero bulk viscosity)

$$\frac{\partial e}{\partial \tau} + \frac{e + p + \tau^2 \pi^{\eta\eta}}{\tau} = 0, \quad (\text{A.7})$$

$$\tau^2 \pi^{\eta\eta} = -\frac{4}{3} \frac{\eta}{\tau}. \quad (\text{A.8})$$

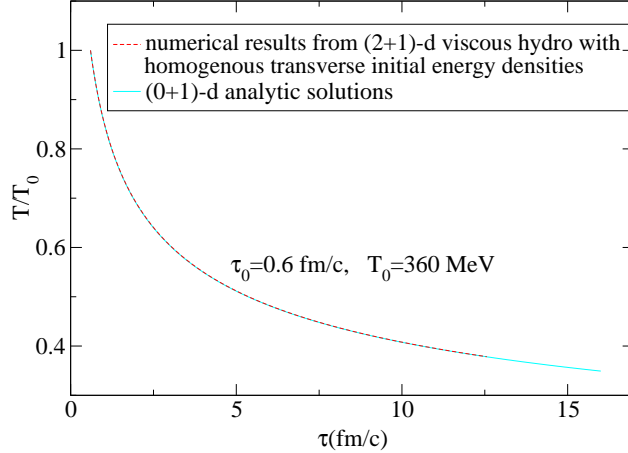


Figure A.2: Comparison between the analytical temperature evolution for (0+1)-d boost-invariant Navier-Stokes viscous hydrodynamics (solid line) and numerical results from VISH2+1 with homogeneous transverse initial energy density profiles (dashed line).

For an ideal gas EOS $p = \frac{1}{3}e \sim T^4$ this leads to the following analytic solution for the evolution of the temperature [211]:

$$\frac{T(\tau)}{T_0} = \left(\frac{\tau_0}{\tau}\right)^{1/3} \left[1 + \frac{2\eta}{3s\tau_0 T_0} \left(1 - \left(\frac{\tau_0}{\tau}\right)^{2/3}\right)\right]. \quad (\text{A.9})$$

To test our code against this analytical result we initialize VISH2+1 with homogeneous transverse density distributions (no transverse pressure gradients and flow) and use the Navier-Stokes identification $\pi^{mn} = 2\eta\sigma^{mn}$ in the hydrodynamic part of the evolution algorithm, sidestepping the part of the code that evolves π^{mn} kinetically. It turns out that in this case the relativistic Navier-Stokes evolution is numerically stable. Fig. A.2 compares the numerically computed temperature evolution from VISH2+1 with the analytic formula (A.9), for $\eta/s = 0.08$ and $T_0 = 360 \text{ MeV}$ at $\tau_0 = 0.6 \text{ fm}/c$. They agree perfectly.

A.3.3 Reduction of VISH2+1 to relativistic Navier-Stokes theory for small η and τ_π

Having tested the hydrodynamic part of the evolution algorithm in Appendix A.3.1, we would like to demonstrate also the accuracy of the kinetic evolution algorithm that evolves the viscous pressure tensor components. A straightforward approach would be to take VISH2+1, set the relaxation time τ_π as close to zero as possible, and compare the result with a similar calculation as in Appendix A.3.1 where we sidestep the kinetic evolution algorithm and instead insert into the hydrodynamic evolution code directly the Navier-Stokes identity $\pi^{mn} = 2\eta\sigma^{mn}$. Unfortunately, this naive procedure exposes us to the well-known instability and acausality problems of the relativistic Navier-Stokes equations. The suggested procedure only works if a set of initial conditions and transport coefficients can be found where these instabilities don't kick in before the freeze-out surface has been reached.

We found that sufficiently stable evolution of the relativistic Navier-Stokes algorithm (i.e. of VISH2+1 with the identification $\pi^{mn} = 2\eta\sigma^{mn}$) can be achieved for standard initial density profiles in Cu+Cu collisions and the simple ideal gas equation of state EOS I by choosing a very small and temperature dependent specific shear viscosity $\frac{\eta}{s} = 0.01 \frac{T}{200 \text{ MeV}} = \frac{T}{2 \text{ GeV}}$. For the Israel-Stewart evolution we use a relaxation time which is correspondingly short: $\tau_\pi = \frac{3\eta}{sT} = 0.03 \text{ fm}/c$.

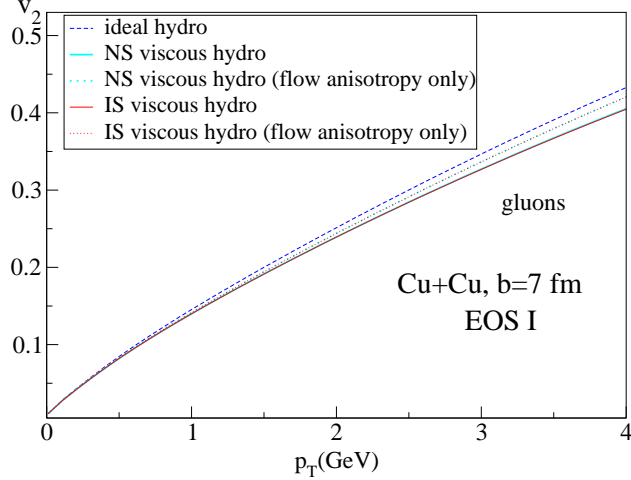


Figure A.3: Differential elliptic flow $v_2(p_T)$ for gluons from $b = 7$ fm Cu+Cu collisions, calculated with ideal hydrodynamics (blue dashed line), relativistic Navier-Stokes (NS) hydrodynamics (light blue lines), and Israel-Stewart (IS) viscous hydrodynamics with $\frac{\eta}{s} = \frac{T}{2 \text{ GeV}}$ and $\tau_\pi = 0.03$ fm/c (red lines), using EOS I. The lines for NS and IS viscous hydrodynamics are almost indistinguishable. Solid lines show the full results from viscous hydrodynamics, dotted lines neglect viscous corrections to the spectra and take only the flow anisotropy effect into account.

Figure A.3 shows the differential elliptic flow $v_2(p_T)$ for gluons in $b = 7$ fm Cu+Cu collisions evolved with these parameters. The dashed line gives the ideal fluid result. The solid and dotted lines show the total elliptic flow and the anisotropic flow contribution to $v_2(p_T)$, respectively, similar to the left panel Fig. 4.9. There are two solid and dotted lines with different colors, corresponding to Israel-Stewart and Navier-Stokes evolution; they are indistinguishable, but clearly different from the ideal fluid result. We conclude that, for small shear viscosity η/s and in the limit $\tau_\pi \rightarrow 0$, the second-order Israel-Stewart algorithm reproduces the Navier-Stokes limit and that, therefore, VISH2+1 evolves the kinetic equations for π^{mn} accurately.

A.4 Hydrodynamics vs. blast wave model

As discussed in Chap. 4.3, the viscous corrections to the final pion spectra from the hydrodynamic model have a different sign (at least in the region $p_T > 1$ GeV) than those originally obtained by Teaney [240]. In this Appendix we try to explore the origins of this discrepancy. We will see that the sign and magnitude of viscous corrections to the (azimuthally averaged) particle spectra are fragile and depend on details of the dynamical evolution and hydrodynamic properties on the freeze-out surface. Fortunately, they same caveat does not seem to apply to the viscous corrections to elliptic flow where hydrodynamic and blast wave model calculations give qualitatively similar answers.

Following Teaney's procedure, we calculate π^{mn} in the Navier-Stokes limit $\pi^{mn} = 2\eta\sigma^{mn}$. We do this both in the blast wave model and using the results for σ^{mn} from VISH2+1. For the blast wave model we assume like Teaney freeze-out at constant τ with a box-like density profile $e(r) = e_{\text{dec}}\theta(R_0 - r)$, where $e_{\text{dec}} = 0.085$ GeV/fm³ is the same freeze-out energy density as in the hydrodynamic model for EOS I, and $R_0 = 6$ fm. The velocity profile in the blast wave model is taken to be linear, $u_r(r) = a_0 \frac{r}{R_0} \theta(R_0 - r)$, with $a_0 = 0.5$; freeze-out is assumed to occur at $\tau_{\text{dec}} = 4.1$ fm/c. R_0 , a_0 and τ_{dec} are somewhat smaller than in Ref. [240] since we study Cu+Cu instead of Au+Au collisions. We concentrate here on a discussion of π^{rr} for illustration; the expression for σ^{rr} is found in Ref. [124], Eq. (A11c). While π^{rr} from VISH2+1 differs

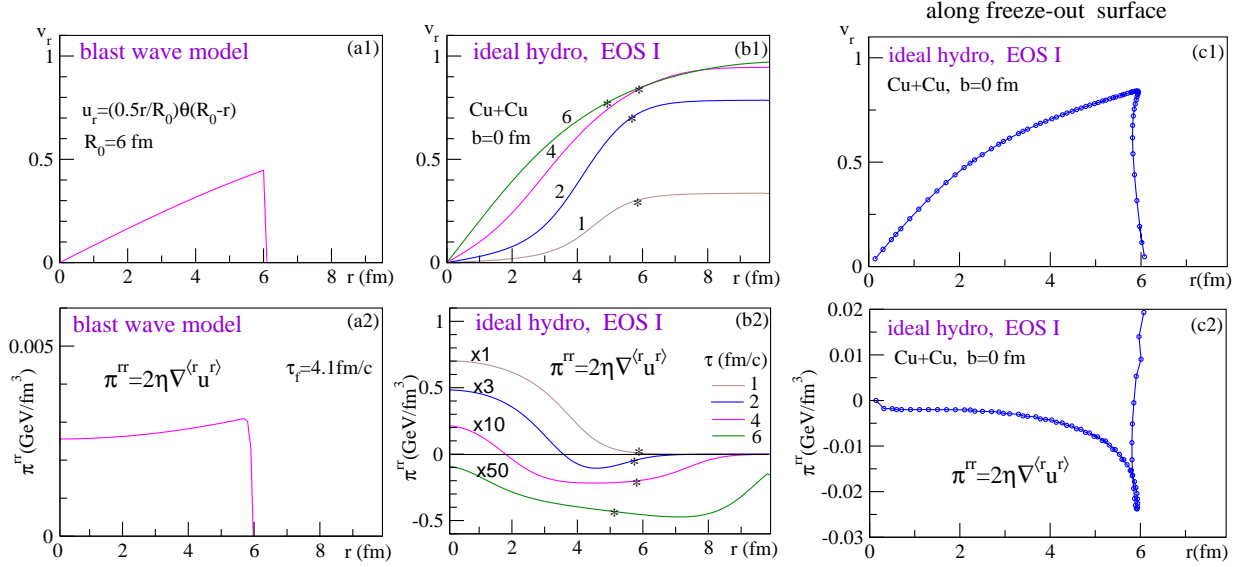


Figure A.4: *Top row*: Velocity profiles from the blast wave model (left) and from the hydrodynamic model with EOS I at fixed times (middle) and along the decoupling surface (right). *Bottom row*: The corresponding profiles for the transverse shear viscous pressure π^{rr} in the Navier-Stokes limit, $\pi^{rr} = 2\eta\nabla^{(\mu} u^{\nu)}$. Calculations are for central Cu+Cu collisions, and the curves in the middle panels correspond to the times $\tau = 1, 2, 4,$ and $6 \text{ fm}/c$. See text for discussion.

from $2\eta\sigma^{rr}$ due to the finite relaxation time τ_π (see Sec. 4.6), we have checked that the signs of these two quantities are the same on the freeze-out surface so that our discussion provides at least a qualitatively correct analysis of the viscous spectra corrections in the two models.

In Fig. A.4 we compare the freeze-out profiles for the radial flow velocity and $2\eta\sigma^{rr}$ from the blast wave model. In spite of qualitative similarity of the velocity profiles, the freeze-out profiles of $2\eta\sigma^{rr}$ are entirely different and even have the opposite sign in the region where most of the hydrodynamic particle production occurs (left and right columns in Fig. A.4). The middle column shows that at fixed times τ , the hydrodynamic profile for $2\eta\sigma^{rr}$ shows some similarity with the blast wave model in that $2\eta\sigma^{rr}$ is positive throughout most of the interior of the fireball. What matters for the calculation of the spectra via Eq. (3.5), however, are the values of $2\eta\sigma^{rr}$ on the freeze-out surface Σ where they are negative, mostly due to radial velocity derivatives. This explains the opposite sign of the viscous correction to the spectra in the hydrodynamic model and shows that, as far as an estimate of these viscous corrections goes, the blast wave model has serious limitations.

A.5 Cooling rates for ideal and viscous heavy-ion fireballs

In the early expansion stage of a heavy-ion collision, shear viscosity leads to a reduction of the longitudinal and an increase of the transverse pressure. The reduced longitudinal pressure decreases the work done by longitudinal expansion, thereby reducing the initial cooling rate of the fireball. This leads to a somewhat increased lifetime of the quark-gluon plasma phase. The increased transverse pressure, on the other hand, causes larger transverse acceleration and stronger radial flow of the matter than in ideal fluid dynamics. Due to the larger transverse flow, the center of the viscous fireball cools more quickly during the late stages than an ideal fluid, thereby slightly reducing the total fireball lifetime until freeze-out for central and near-central

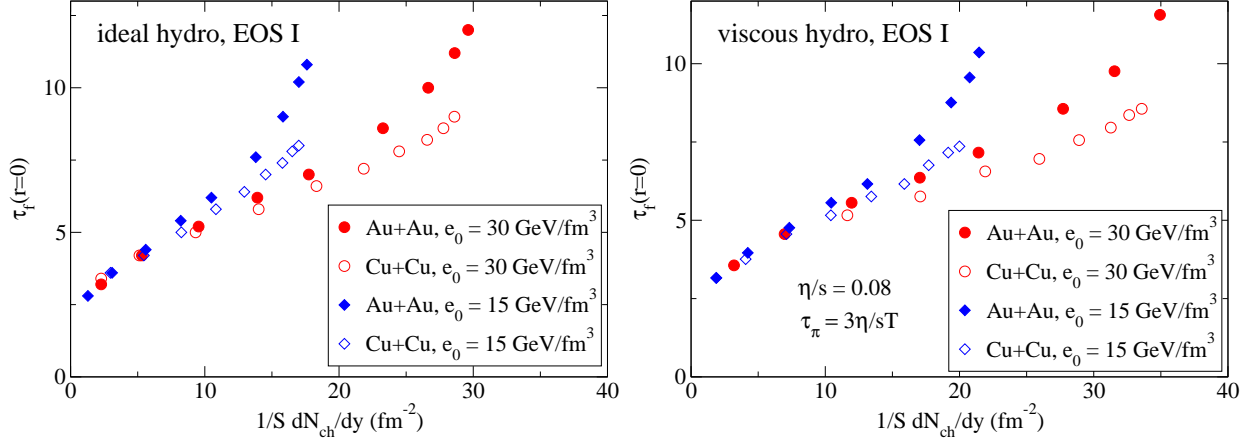


Figure A.5: Central freeze-out times for Au+Au and Cu+Cu collisions with differential initial peak energy densities $e_0 \equiv e(0, 0; b=0)$ as a function of final charged hadron multiplicity density. Points belonging to one series correspond to different impact parameters, with central (peripheral) collisions corresponding to large (small) multiplicity densities. Left: ideal fluid dynamics. Right: viscous fluid dynamics with $\eta/s = 0.08$ and $\tau_\pi = 3\eta/sT$.

collisions (see Fig. A.5). The viscous fireballs created in peripheral collisions don't live long enough for this mechanism to manifest itself; they live longer than their ideal counterparts, due to the decreased initial cooling rate arising from the smaller longitudinal pressure (left points in Fig. A.5).

For an equation of state (EOS) with a first-order quark-hadron phase transition, the mixed phase matter is free of pressure gradients and hence not accelerated. Velocity gradients in the mixed phase generate, however, viscous pressure components whose gradients continue to accelerate the viscous fluid even while it passes through the mixed phase where the thermal pressure gradients vanish. As a result, the viscous fluid spends less time in the mixed phase than the ideal one.

In ideal hydrodynamics, a first-order phase transition with a mixed phase (MP) generates large velocity gradients near the QGP-MP and MP-HG (HG = hadron gas) interfaces. In viscous fluids such gradients generate viscous pressures that act against building up large velocity gradients. In consequence, all prominent structures in ideal hydrodynamics that arise from discontinuities in the speed of sound in ideal hydrodynamics are washed out by viscous effects. Shear viscosity thus effectively turns a first-order phase transition into a smooth cross-over transition.

APPENDIX B: Glossary

RHIC: Relativistic Heavy Ion Collider
LHC: Large Hadron Collider
CGC : Color Glass Condensate
QGP: the quark gluon plasma
HRG: hadron resonance gas
MP: Mixed phase
EOS : equation of state
PCE-EOS: partially chemical equilibrium EOS (for the HRG phase)

N-S equation: Navier-Stokes equation
I-S equation: Israel-Stewart equation
O-G equation: Öttinger-Gremla equation
VISH2+1: Viscous Israel-Stewart Hydrodynamics in 2+1 dimensions
AZHYDRO: AZimuthally asymmetric (ideal) Hydrodynamics in 2+1 dimensions

$g^{\mu\nu}$: metric tensor
 τ : longitudinal proper time
 η : space time rapidity
 γ : Lorentz contraction factor
 u^μ : four velocity

A : atomic number
 b : impact parameter
 R : nuclear radius
 $e_0(r = 0, b = 0)$: initial peak energy density value at $r = 0$
 e_{dec} : decoupling energy density
 τ_0 : initial time
 τ_f : freeze-out time
 c_s : speed of sound
 T_{cr} : critical temperature
 T_{dec} : decoupling temperature

ε_x : spatial eccentricity
 ε_p : momentum anisotropy
 v_T : transverse flow velocity
 N_{ch} : produced charged hadrons
 y : momentum rapidity
 p_T : particle transverse momentum
 v_2 : elliptic flow coefficient
 S : overlap area

$T^{\mu\nu}$: energy momentum tensor
 N^μ : conserved charge flow
 $f(x, p)$: distribution function

$f_0(x, p)$: equilibrium distribution function

$\delta f(x, p)$: non-equilibrium part in the distribution function $f = f_0 + \delta f$

e : energy density

p : pressure

T : temperature

s, \mathcal{S} : entropy density, total entropy

$\Delta \mathcal{S}$ entropy production

$\pi^{\mu\nu}$: shear pressure tensor

Π : bulk pressure

q^μ : heat flow

ζ : bulk viscosity

η : shear viscosity

λ : heat conductivity

τ_π : relaxation time for shear pressure tensor

τ_Π : relaxation time for bulk pressure

$\lambda_1, \lambda_2, \lambda_3$: other 2nd order transport coefficients in the viscous equation for $\pi^{\mu\nu}$

$\sigma^{\mu\nu}, \nabla^{\langle\mu} u^{\nu\rangle}$: velocity stress tensor

$\Omega^{\mu\nu}$: vorticity tensor

BIBLIOGRAPHY

- [1] T. D. Lee and G. C. Wick, “Vacuum stability and vacuum excitation in a spin 0 field theory,” *Phys. Rev.* **D9** (1974) 2291.
- [2] J. C. Collins and M. J. Perry, “Superdense matter: neutrons or asymptotically free quarks?,” *Phys. Rev. Lett.* **34** (1975) 1353.
- [3] H. G. Baumgardt *et al.*, “Shock waves and Mach cones in fast nucleus-nucleus Collisions,” *Z. Phys.* **A273** (1975) 359–371.
- [4] S. Nagamiya and M. Gyulassy, “High-energy nuclear collisions,” *Adv. Nucl. Phys.* **13** (1984) 201–315.
- [5] J. W. Harris and B. Muller, “The search for the quark-gluon plasma,” *Ann. Rev. Nucl. Part. Sci.* **46** (1996) 71–107, hep-ph/9602235.
- [6] **BRAHMS** Collaboration, I. Arsene *et al.*, “Quark gluon plasma an color glass condensate at RHIC? The perspective from the BRAHMS experiment,” *Nucl. Phys.* **A757** (2005) 1–27, nucl-ex/0410020.
- [7] B. B. Back *et al.*, “The PHOBOS perspective on discoveries at RHIC,” *Nucl. Phys.* **A757** (2005) 28–101, nucl-ex/0410022.
- [8] **STAR** Collaboration, J. Adams *et al.*, “Experimental and theoretical challenges in the search for the quark gluon plasma: The STAR collaboration’s critical assessment of the evidence from RHIC collisions,” *Nucl. Phys.* **A757** (2005) 102–183, nucl-ex/0501009.
- [9] **PHENIX** Collaboration, K. Adcox *et al.*, “Formation of dense partonic matter in relativistic nucleus nucleus collisions at RHIC: Experimental evaluation by the PHENIX collaboration,” *Nucl. Phys.* **A757** (2005) 184–283, nucl-ex/0410003.
- [10] N. Armesto *et al.*, “Heavy ion collisions at the LHC - last call for predictions,” *J. Phys.* **G35** (2008) 054001, 0711.0974.
- [11] U. W. Heinz and M. Jacob, “Evidence for a new state of matter: An assessment of the results from the CERN lead beam programme,” nucl-th/0002042.
- [12] M. Gyulassy, “The QGP discovered at RHIC,” nucl-th/0403032.
- [13] M. Gyulassy and L. McLerran, “New forms of QCD matter discovered at RHIC,” *Nucl. Phys.* **A750** (2005) 30–63, nucl-th/0405013.
- [14] B. Muller and J. L. Nagle, “Results from the relativistic heavy ion collider,” *Ann. Rev. Nucl. Part. Sci.* **56** (2006) 93–135, nucl-th/0602029.
- [15] C. Wong, “Introduction to high energy heavy-ion collisions,” *World Scientific* (1994).
- [16] P. Arnold and C.-X. Zhai, “The three loop free energy for pure gauge QCD,” *Phys. Rev.* **D50** (1994) 7603–7623, hep-ph/9408276.
- [17] P. Arnold and C.-x. Zhai, “The three loop free energy for high temperature QED and QCD with fermions,” *Phys. Rev.* **D51** (1995) 1906–1918, hep-ph/9410360.
- [18] J. O. Andersen and M. Strickland, “Resummation in hot field theories,” *Ann. Phys.* **317** (2005) 281–353, hep-ph/0404164.
- [19] A. D. Linde, “Phase transitions in gauge theories and cosmology,” *Rept. Prog. Phys.* **42** (1979) 389.
- [20] A. D. Linde, “Infrared problem in thermodynamics of the yang-Mills Gas,” *Phys. Lett.* **B96** (1980) 289.
- [21] A. Bazavov *et al.*, “Equation of state and QCD transition at finite temperature,” 0903.4379.
- [22] M. Cheng *et al.*, “The QCD equation of state with almost physical quark masses,” *Phys. Rev.* **D77** (2008) 014511, 0710.0354.
- [23] Y. Aoki, Z. Fodor, S. D. Katz, and K. K. Szabo, “The QCD transition temperature: Results with physical masses in the continuum limit,” *Phys. Lett.* **B643** (2006) 46–54, hep-lat/0609068.
- [24] U. W. Heinz and P. F. Kolb, “Early thermalization at RHIC,” *Nucl. Phys.* **A702** (2002) 269–280, hep-ph/0111075.
- [25] E. V. Shuryak, “What RHIC experiments and theory tell us about properties of quark-gluon plasma?,” *Nucl. Phys.* **A750** (2005) 64–83, hep-ph/0405066.

- [26] P. F. Kolb and U. Heinz, “Hydrodynamic description of ultrarelativistic heavy ion collisions,” in *Quark-Gluon Plasma 3*, edited by R. C. Hwa and X.-N. Wang (World Scientific, Singapore) (2003) 634, nucl-th/0305084.
- [27] P. Huovinen, “Hydrodynamical description of collective flow,” in *Quark-Gluon Plasma 3*, edited by R. C. Hwa and X.-N. Wang (World Scientific, Singapore) (2003) 600, nucl-th/0305064.
- [28] E. V. Shuryak and I. Zahed, “Rethinking the properties of the quark gluon plasma at T approx. T(c),” *Phys. Rev.* **C70** (2004) 021901, hep-ph/0307267.
- [29] J. Liao and E. V. Shuryak, “What do lattice baryonic susceptibilities tell us about quarks, diquarks and baryons at $T > T_c$?,” *Phys. Rev.* **D73** (2006) 014509, hep-ph/0510110.
- [30] A. Ipp, K. Kajantie, A. Rebhan, and A. Vuorinen, “Unified description of deconfined QCD equation of state,” *J. Phys.* **G34** (2007) S631–S634.
- [31] A. Peshier, *private communication*.
- [32] U. W. Heinz, “Concepts of heavy-ion physics,” hep-ph/0407360.
- [33] <http://qgp.phy.duke.edu/>.
- [34] H. Satz, “Parton percolation in nuclear collisions,” hep-ph/0212046.
- [35] P. Arnold, J. Lenaghan, and G. D. Moore, “QCD plasma instabilities and bottom-up thermalization,” *JHEP* **08** (2003) 002, hep-ph/0307325.
- [36] P. Arnold, J. Lenaghan, G. D. Moore, and L. G. Yaffe, “Apparent thermalization due to plasma instabilities in quark gluon plasma,” *Phys. Rev. Lett.* **94** (2005) 072302, nucl-th/0409068.
- [37] T. Hirano and M. Gyulassy, “Perfect fluidity of the quark gluon plasma core as seen through its dissipative hadronic corona,” *Nucl. Phys.* **A769** (2006) 71–94, nucl-th/0506049.
- [38] C. Nonaka and S. A. Bass, “Space-time evolution of bulk QCD matter,” *Phys. Rev.* **C75** (2007) 014902, nucl-th/0607018.
- [39] S. A. Bass, “Microscopic reaction dynamics at SPS and RHIC,” *Nucl. Phys.* **A698** (2002) 164–170, nucl-th/0104040.
- [40] L. D. McLerran and R. Venugopalan, “Computing quark and gluon distribution functions for very large nuclei,” *Phys. Rev.* **D49** (1994) 2233–2241, hep-ph/9309289.
- [41] L. D. McLerran and R. Venugopalan, “Gluon distribution functions for very large nuclei at small transverse momentum,” *Phys. Rev.* **D49** (1994) 3352–3355, hep-ph/9311205.
- [42] W. Poschl and B. Muller, “Real time dynamics of colliding gauge fields and the ‘glue burst’,” *Phys. Rev.* **D60** (1999) 114505, nucl-th/9812066.
- [43] S. A. Bass, B. Muller, and W. Poschl, “Lattice gauge description of colliding nuclei,” *J. Phys.* **G25** (1999) L109–L115, nucl-th/9808011.
- [44] K. Geiger, “Space-time description of ultrarelativistic nuclear collisions in the QCD parton picture,” *Phys. Rept.* **258** (1995) 237–376.
- [45] R. B. Clare and D. Strottman, “Relativistic hydrodynamics and heavy ion reactions,” *Phys. Rept.* **141** (1986) 177–280.
- [46] H. Sorge, H. Stoecker, and W. Greiner, “Poincare invariant Hamiltonian dynamics: modeling multi - hadronic interaction in a phase space approach,” *Annals Phys.* **192** (1989) 266–306.
- [47] S. A. Bass *et al.*, “Microscopic models for ultrarelativistic heavy ion collisions,” *Prog. Part. Nucl. Phys.* **41** (1998) 255–369, nucl-th/9803035.
- [48] M. Bleicher *et al.*, “Relativistic hadron hadron collisions in the ultra- relativistic quantum molecular dynamics model,” *J. Phys.* **G25** (1999) 1859–1896, hep-ph/9909407.
- [49] E. Iancu and R. Venugopalan, “The color glass condensate and high energy scattering in QCD,” hep-ph/0303204.
- [50] T. Lappi and L. McLerran, “Some features of the glasma,” *Nucl. Phys.* **A772** (2006) 200–212, hep-ph/0602189.
- [51] B. Zhang, “ZPC 1.0.1: A parton cascade for ultrarelativistic heavy ion collisions,” *Comput. Phys. Commun.* **109** (1998) 193–206, nucl-th/9709009.
- [52] D. Molnar and M. Gyulassy, “New solutions to covariant nonequilibrium dynamics,” *Phys.Rev.C* **62** (2000) 054907, nucl-th/0005051.
- [53] U. W. Heinz and P. F. Kolb, “Two RHIC puzzles: early thermalization and the HBT problem,” hep-ph/0204061.
- [54] Z. Xu and C. Greiner, “Thermalization of gluons in ultrarelativistic heavy ion collisions by including three-body interactions in a parton cascade,” *Phys. Rev. C* **71** (2005) 064901, hep-ph/0406278.
- [55] Z. Xu, C. Greiner, and H. Stoecker, “PQCD calculations of elliptic flow and shear viscosity at RHIC,” *Phys. Rev. Lett.* **101** (2008) 082302, arXiv:0711.0961 [nucl-th].
- [56] U. W. Heinz, “Kinetic theory for nonabelian plasmas,” *Phys. Rev. Lett.* **51** (1983) 351.
- [57] U. W. Heinz, “Quark - gluon transport theory. part 1. the classical theory,” *Ann. Phys.* **161** (1985) 48.
- [58] U. W. Heinz, “Quark - gluon transport theory. part 2. color response and color correlations in a quark-gluon plasma,” *Ann. Phys.* **168** (1986) 148.

- [59] H.-T. Elze and U. W. Heinz, “Quark - gluon transport theory,” *Phys. Rept.* **183** (1989) 81–135.
- [60] E. S. Weibel, “Spontaneously growing transverse waves in a plasma due to an anisotropic velocity distribution,” *Phys. Rev. Lett.* **2** (1959) 83.
- [61] S. Mrowczynski, “Stream instabilities of the quark gluon plasma,” *Phys. Lett.* **B214** (1988) 587.
- [62] S. Mrowczynski, “Plasma instability at the initial stage of ultrarelativistic heavy ion collisions,” *Phys. Lett.* **B314** (1993) 118–121.
- [63] A. Rebhan, P. Romatschke, and M. Strickland, “Hard-loop dynamics of non-Abelian plasma instabilities,” *Phys. Rev. Lett.* **94** (2005) 102303, hep-ph/0412016.
- [64] P. Arnold, G. D. Moore, and L. G. Yaffe, “The fate of non-abelian plasma instabilities in 3+1 dimensions,” *Phys. Rev. D* **72** (2005) 054003, hep-ph/0505212.
- [65] A. Rebhan, P. Romatschke, and M. Strickland, “Dynamics of quark-gluon plasma instabilities in discretized hard-loop approximation,” *JHEP* **09** (2005) 041, hep-ph/0505261.
- [66] P. Romatschke and R. Venugopalan, “The unstable Glasma,” *Phys. Rev. D* **74** (2006) 045011, hep-ph/0605045.
- [67] P. Romatschke and R. Venugopalan, “Collective non-Abelian instabilities in a melting color glass condensate,” *Phys. Rev. Lett.* **96** (2006) 062302, hep-ph/0510121.
- [68] U. W. Heinz, “Early collective expansion: relativistic hydrodynamics and the transport properties of QCD matter,” 0901.4355.
- [69] D. A. Teaney, “Viscous hydrodynamics and the quark gluon plasma,” 0905.2433.
- [70] Z.-W. Lin, C. M. Ko, B.-A. Li, B. Zhang, and S. Pal, “A multi-phase transport model for relativistic heavy ion collisions,” *Phys. Rev. C* **72** (2005) 064901, nucl-th/0411110.
- [71] B. Zhang, L.-W. Chen, and C. M. Ko, “Equation of state of the hot dense matter in a multi-phase transport model,” 0705.3968.
- [72] J.-Y. Ollitrault, “Anisotropy as a signature of transverse collective flow,” *Phys. Rev. D* **46** (1992) 229–245.
- [73] W. Reisdorf and H. G. Ritter, “Collective flow in heavy-ion collisions,” *Ann. Rev. Nucl. Part. Sci.* **47** (1997) 663–709.
- [74] J. Rafelski and B. Muller, “Strangeness production in the quark - gluon plasma,” *Phys. Rev. Lett.* **48** (1982) 1066.
- [75] J. Sollfrank and U. W. Heinz, “The role of strangeness in ultrarelativistic nuclear collisions,” nucl-th/9505004.
- [76] T. Matsui and H. Satz, “ J/ψ suppression by quark-gluon plasma formation,” *Phys. Lett.* **B178** (1986) 416.
- [77] L. Kluberg and H. Satz, “Color deconfinement and charmonium production,” 0901.3831.
- [78] L. D. McLerran and T. Toimela, “Photon and dilepton emission from the quark - gluon plasma: some general considerations,” *Phys. Rev. D* **31** (1985) 545.
- [79] C. Gale and K. L. Haglin, “Electromagnetic radiation from relativistic nuclear collisions,” hep-ph/0306098.
- [80] X.-N. Wang and M. Gyulassy, “Gluon shadowing and jet quenching in A + A collisions at $\sqrt{s} = 200$ GeV,” *Phys. Rev. Lett.* **68** (1992) 1480–1483.
- [81] X.-N. Wang, Z. Huang, and I. Sarcevic, “Jet quenching in the opposite direction of a tagged photon in high-energy heavy-ion collisions,” *Phys. Rev. Lett.* **77** (1996) 231–234, hep-ph/9605213.
- [82] M. Gyulassy, I. Vitev, X.-N. Wang, and B.-W. Zhang, “Jet quenching and radiative energy loss in dense nuclear matter,” nucl-th/0302077.
- [83] A. Kovner and U. A. Wiedemann, “Gluon radiation and parton energy loss,” hep-ph/0304151.
- [84] S. Jeon and V. Koch, “Event-by-event fluctuations,” hep-ph/0304012.
- [85] “The frontiers of nuclear science, a long range plan,” 0809.3137.
- [86] P. Jacobs *et al.*, “Phases of QCD: Summary of the Rutgers long range plan town meeting,” 0705.1930.
- [87] “RHIC scientists serve up perfect liquid,” <http://www.bnl.gov/rhic/milestones.htm>.
- [88] **STAR** Collaboration, C. Adler *et al.*, “Elliptic flow from two- and four-particle correlations in Au + Au collisions at $\sqrt{s_{NN}} = 130$ GeV,” *Phys. Rev. C* **66** (2002) 034904, nucl-ex/0206001.
- [89] **PHENIX** Collaboration, S. S. Adler *et al.*, “Elliptic flow of identified hadrons in Au + Au collisions at $\sqrt{s_{NN}} = 200$ GeV,” *Phys. Rev. Lett.* **91** (2003) 182301, nucl-ex/0305013.
- [90] **STAR** Collaboration, J. Adams *et al.*, “Particle dependence of azimuthal anisotropy and nuclear modification of particle production at moderate p_T in Au + Au collisions at $\sqrt{s_{NN}} = 200$ GeV,” *Phys. Rev. Lett.* **92** (2004) 052302, nucl-ex/0306007.
- [91] **STAR** Collaboration, J. Adams *et al.*, “Azimuthal anisotropy at RHIC: The first and fourth harmonics,” *Phys. Rev. Lett.* **92** (2004) 062301, nucl-ex/0310029.
- [92] **CERES/NA45** Collaboration, G. Agakichiev *et al.*, “Semi-hard scattering unraveled from collective dynamics by two-pion correlations in 158-A-GeV/c Pb + Au collisions,” *Phys. Rev. Lett.* **92** (2004) 032301, nucl-ex/0303014.

- [93] P. F. Kolb, J. Sollfrank, and U. W. Heinz, “Anisotropic transverse flow and the quark-hadron phase transition,” *Phys. Rev.* **C62** (2000) 054909, hep-ph/0006129.
- [94] P. R. Sorensen, “Kaon and Lambda production at intermediate p_T : insights into the hadronization of the bulk partonic matter created in Au + Au collisions at RHIC,” *Ph.D thesis(2003)*, nucl-ex/0309003.
- [95] **STAR** Collaboration, J. Adams *et al.*, “Multi-strange baryon elliptic flow in Au + Au collisions at $\sqrt{s_{NN}} = 200$ GeV,” *Phys. Rev. Lett.* **95** (2005) 122301, nucl-ex/0504022.
- [96] P. Huovinen, P. F. Kolb, U. W. Heinz, P. V. Ruuskanen, and S. A. Voloshin, “Radial and elliptic flow at RHIC: further predictions,” *Phys. Lett.* **B503** (2001) 58–64, hep-ph/0101136.
- [97] U. W. Heinz, “Thermalization at RHIC,” *AIP Conf. Proc.* **739** (2005) 163–180, nucl-th/0407067.
- [98] P. Braun-Munzinger, D. Magestro, K. Redlich, and J. Stachel, “Hadron production in Au Au collisions at RHIC,” *Phys. Lett.* **B518** (2001) 41–46, hep-ph/0105229.
- [99] P. Braun-Munzinger, K. Redlich, and J. Stachel, “Particle production in heavy ion collisions,” nucl-th/0304013.
- [100] **PHENIX** Collaboration, A. Adare *et al.*, “Scaling properties of azimuthal anisotropy in Au + Au and Cu + Cu collisions at $\sqrt{s_{NN}} = 200$ GeV,” *Phys. Rev. Lett.* **98** (2007) 162301, nucl-ex/0608033.
- [101] R. J. Fries, B. Muller, C. Nonaka, and S. A. Bass, “Hadronization in heavy ion collisions: recombination and fragmentation of partons,” *Phys. Rev. Lett.* **90** (2003) 202303, nucl-th/0301087.
- [102] R. J. Fries, B. Muller, C. Nonaka, and S. A. Bass, “Hadron production in heavy ion collisions: fragmentation and recombination from a dense parton phase,” *Phys. Rev.* **C68** (2003) 044902, nucl-th/0306027.
- [103] V. Greco, C. M. Ko, and P. Levai, “Parton coalescence and antiproton/pion anomaly at RHIC,” *Phys. Rev. Lett.* **90** (2003) 202302, nucl-th/0301093.
- [104] V. Greco, C. M. Ko, and P. Levai, “Parton coalescence at RHIC,” *Phys. Rev.* **C68** (2003) 034904, nucl-th/0305024.
- [105] D. Molnar and S. A. Voloshin, “Elliptic flow at large transverse momenta from quark coalescence,” *Phys. Rev. Lett.* **91** (2003) 092301, nucl-th/0302014.
- [106] **PHENIX** Collaboration, S. S. Adler *et al.*, “High transverse momentum η meson production in $p + p$, $d + Au$ and $Au + Au$ collisions at $\sqrt{s_{NN}} = 200$ GeV,” *Phys. Rev.* **C75** (2007) 024909, nucl-ex/0611006.
- [107] **STAR** Collaboration, J. Adams *et al.*, “Evidence from $d + Au$ measurements for final-state suppression of high p_T hadrons in Au + Au collisions at RHIC,” *Phys. Rev. Lett.* **91** (2003) 072304, nucl-ex/0306024.
- [108] **STAR** Collaboration, J. Adams *et al.*, “Distributions of charged hadrons associated with high transverse momentum particles in $p + p$ and Au + Au collisions at $\sqrt{s_{NN}} = 200$ GeV,” *Phys. Rev. Lett.* **95** (2005) 152301, nucl-ex/0501016.
- [109] **STAR** Collaboration, C. Adler *et al.*, “Centrality dependence of high p_T hadron suppression in Au+Au collisions at $\sqrt{s_{NN}} = 130$ GeV,” *Phys. Rev. Lett.* **89** (2002) 202301, nucl-ex/0206011.
- [110] **PHENIX** Collaboration, S. S. Adler *et al.*, “Suppressed π^0 production at large transverse momentum in central Au + Au collisions at $\sqrt{s_{NN}} = 200$ GeV,” *Phys. Rev. Lett.* **91** (2003) 072301, nucl-ex/0304022.
- [111] **STAR** Collaboration, J. Adams *et al.*, “Transverse momentum and collision energy dependence of high p_T hadron suppression in Au + Au collisions at ultrarelativistic energies,” *Phys. Rev. Lett.* **91** (2003) 172302, nucl-ex/0305015.
- [112] M. Gyulassy and X.-N. Wang, “Multiple collisions and induced gluon Bremsstrahlung in QCD,” *Nucl. Phys.* **B420** (1994) 583–614, nucl-th/9306003.
- [113] **STAR** Collaboration, C. Adler *et al.*, “Disappearance of back-to-back high p_T hadron correlations in central Au+Au collisions at $\sqrt{s_{NN}} = 200$ GeV,” *Phys. Rev. Lett.* **90** (2003) 082302, nucl-ex/0210033.
- [114] J. Casalderrey-Solana, E. V. Shuryak, and D. Teaney, “Conical flow induced by quenched QCD jets,” *J. Phys. Conf. Ser.* **27** (2005) 22–31, hep-ph/0411315.
- [115] J. Casalderrey-Solana, E. V. Shuryak, and D. Teaney, “Hydrodynamic flow from fast particles,” hep-ph/0602183.
- [116] G. Y. Qin, A. Majumder, H. Song, and U. Heinz, “Energy and momentum deposited into a QCD medium by a jet shower,” 0903.2255.
- [117] J. M. Maldacena, “The large N limit of superconformal field theories and supergravity,” *Adv. Theor. Math. Phys.* **2** (1998) 231–252, hep-th/9711200.
- [118] O. Aharony, S. S. Gubser, J. M. Maldacena, H. Ooguri, and Y. Oz, “Large N field theories, string theory and gravity,” *Phys. Rept.* **323** (2000) 183–386, hep-th/9905111.
- [119] D. T. Son and A. O. Starinets, “Viscosity, black holes, and quantum field theory,” *Ann. Rev. Nucl. Part. Sci.* **57** (2007) 95–118, 0704.0240.
- [120] S. S. Gubser, S. S. Pufu, F. D. Rocha, and A. Yarom, “Energy loss in a strongly coupled thermal medium and the gauge-string duality,” 0902.4041.
- [121] K. M. O’Hara, S. L. Hemmer, M. E. Gehm, S. R. Granade, and J. E. Thomas, “Observation of a strongly interacting degenerate fermi gas of atoms,” *Science* **12** (2002) 2179.

- [122] A. Turlapov, J. Kinast, B. Clancy, L. Luo, J. Joseph, and J. E. Thomas, “Is a gas of strongly interacting atomic fermions a nearly perfect fluid?,” *J Low Temp. Phys.* **150** (2008) 567.
- [123] “Future science at the relativistic heavy ion collider,” <http://www.bnl.gov/physics/rhiciiscience/>.
- [124] U. W. Heinz, H. Song, and A. K. Chaudhuri, “Dissipative hydrodynamics for viscous relativistic fluids,” *Phys. Rev. C* **73** (2006) 034904, nucl-th/0510014.
- [125] H. Song and U. W. Heinz, “Suppression of elliptic flow in a minimally viscous quark-gluon plasma,” *Phys. Lett.* **B658** (2008) 279–283, 0709.0742.
- [126] H. Song and U. W. Heinz, “Causal viscous hydrodynamics in 2+1 dimensions for relativistic heavy-ion collisions,” *Phys. Rev. C* **77** (2008) 064901, 0712.3715.
- [127] H. Song and U. W. Heinz, “Multiplicity scaling in ideal and viscous hydrodynamics,” *Phys. Rev. C* **78** (2008) 024902, 0805.1756.
- [128] U. W. Heinz and H. Song, “Causal relativistic hydrodynamics for viscous fluids,” *J. Phys.* **G35** (2008) 104126, 0806.0352.
- [129] H. Song and U. W. Heinz, “Extracting the QGP viscosity from RHIC data – a status report from viscous hydrodynamics,” 0812.4274.
- [130] H. Song and U. W. Heinz, “Causal viscous hydrodynamics in 2+1 dimensions for relativistic heavy-ion collisions II : with shear and bulk viscosity,” *in preparation* (2009).
- [131] R. Baier, P. Romatschke, and U. A. Wiedemann, “Dissipative hydrodynamics and heavy ion collisions,” *Phys. Rev. C* **73** (2006) 064903, hep-ph/0602249.
- [132] R. Baier and P. Romatschke, “Causal viscous hydrodynamics for central heavy-ion collisions,” *Eur. Phys. J.* **C51** (2007) 677–687, nucl-th/0610108.
- [133] P. Romatschke, “Causal viscous hydrodynamics for central heavy-ion collisions. II: Meson spectra and HBT radii,” *Eur. Phys. J.* **C52** (2007) 203–209, nucl-th/0701032.
- [134] P. Romatschke and U. Romatschke, “Viscosity information from relativistic nuclear collisions: How perfect is the fluid observed at RHIC?,” *Phys. Rev. Lett.* **99** (2007) 172301, 0706.1522.
- [135] M. Luzum and P. Romatschke, “Conformal relativistic viscous hydrodynamics: applications to RHIC results at $\sqrt{s_{NN}} = 200$ GeV,” *Phys. Rev. C* **78** (2008) 034915, 0804.4015.
- [136] M. Luzum and P. Romatschke, “Viscous hydrodynamic predictions for nuclear collisions at the LHC,” 0901.4588.
- [137] K. Dusling and D. Teaney, “Simulating elliptic flow with viscous hydrodynamics,” *Phys. Rev. C* **77** (2008) 034905, 0710.5932.
- [138] K. Dusling and S. Lin, “Dilepton production from a viscous QGP,” *Nucl. Phys.* **A809** (2008) 246–258, 0803.1262.
- [139] K. Dusling, “Photons as a viscometer of heavy ion collisions,” 0903.1764.
- [140] D. Molnar and P. Huovinen, “Dissipative effects from transport and viscous hydrodynamics,” *J. Phys.* **G35** (2008) 104125, 0806.1367.
- [141] P. Huovinen and D. Molnar, “The applicability of causal dissipative hydrodynamics to relativistic heavy ion collisions,” *Phys. Rev. C* **79** (2009) 014906, 0808.0953.
- [142] A. K. Chaudhuri, “Saturation of elliptic flow and shear viscosity,” 0708.1252.
- [143] A. K. Chaudhuri, “Viscous fluid dynamics in Au+Au collisions at RHIC,” 0801.3180.
- [144] A. K. Chaudhuri, “Multiplicity, mean p_T , p_T -spectra and elliptic flow of identified particles in Pb+Pb collisions at LHC,” *Phys. Lett.* **B672** (2009) 126–131, 0803.0643.
- [145] L. P. Csernai, J. I. Kapusta, and L. D. McLerran, “On the strongly-interacting low-viscosity matter created in relativistic nuclear collisions,” *Phys. Rev. Lett.* **97** (2006) 152303, nucl-th/0604032.
- [146] P. Kovtun, D. T. Son, and A. O. Starinets, “Viscosity in strongly interacting quantum field theories from black hole physics,” *Phys. Rev. Lett.* **94** (2005) 111601, hep-th/0405231.
- [147] O. Hirshfelder, C. Curtis, and R. Bird, “Molecular theory of gases and liquids,” *Wiley-Interscience, U.S.* (1964).
- [148] J. Frenkel, “Kinetic theory of liquids,” *Dover Publications, U.S.* (1955).
- [149] W. Vincenti and C. Kruger, “Introduction to physical gas dynamics,” *Krieger, Malabar, FL* (1975).
- [150] S. Chapman and T. G. Cowling, “The mathematical theory of non-uniform gases, 3rd ed.,” *Cambridge University Press, Cambridge, England* (1970).
- [151] R. E. Graves and B. M. Argrow, “Bulk viscosity: past to present,” *J. ThermoPhys. and Heat Trans.* **13** (1999) 337.
- [152] K. Meier, A. Laesecke, and S. Kabelac, “Transport coefficients of the Lennard-Jones model fluid. III. Bulk viscosity,” *J. Chem. Phys.* **122** (2005) 014503.
- [153] J. I. Kapusta, “Viscous properties of strongly interacting matter at high temperature,” 0809.3746.
- [154] S. Jeon, “Computing spectral densities in finite temperature field theory,” *Phys. Rev. D* **47** (1993) 4586–4607, hep-ph/9210227.

- [155] S. Jeon, “Hydrodynamic transport coefficients in relativistic scalar field theory,” *Phys. Rev.* **D52** (1995) 3591–3642, hep-ph/9409250.
- [156] P. Arnold, G. D. Moore, and L. G. Yaffe, “Transport coefficients in high temperature gauge theories: (I) Leading-log results,” *JHEP* **11** (2000) 001, hep-ph/0010177.
- [157] P. Arnold, G. D. Moore, and L. G. Yaffe, “Transport coefficients in high temperature gauge theories. II: Beyond leading log,” *JHEP* **05** (2003) 051, hep-ph/0302165.
- [158] H. Defu, “Shear viscosity of hot QCD from transport theory and thermal field theory in real time formalism,” hep-ph/0501284.
- [159] M. A. York and G. D. Moore, “Second order hydrodynamic coefficients from kinetic theory,” 0811.0729.
- [160] R. Kubo *J. Phys. Soc. Japan* **12** (1957) 570.
- [161] F. Karsch and H. W. Wyld, “Thermal green function and transport coefficients on the lattice,” *Phys. Rev.* **D35** (1987) 2518.
- [162] A. Nakamura and S. Sakai, “Transport coefficients of gluon plasma,” *Phys. Rev. Lett.* **94** (2005) 072305, hep-lat/0406009.
- [163] H. B. Meyer, “A calculation of the shear viscosity in SU(3) gluodynamics,” *Phys. Rev.* **D76** (2007) 101701, 0704.1801.
- [164] H. B. Meyer, “A calculation of the bulk viscosity in SU(3) gluodynamics,” *Phys. Rev. Lett.* **100** (2008) 162001, 0710.3717.
- [165] A. Hosoya and K. Kajantie, “Transport coefficients of QCD matter,” *Nucl. Phys.* **B250** (1985) 666.
- [166] A. Hosoya, M.-A. Sakagami, and M. Takao, “Nonequilibrium thermodynamics in field theory: Transport coefficients,” *Ann. Phys.* **154** (1984) 229.
- [167] G. Baym, H. Monien, C. J. Pethick, and D. G. Ravenhall, “Transverse interactions and transport in relativistic quark-gluon and electromagnetic plasmas,” *Phys. Rev. Lett.* **64** (1990) 1867–1870.
- [168] H. B. Meyer, “The Yang-Mills spectrum from a 2-level algorithm,” *JHEP* **01** (2004) 030, hep-lat/0312034.
- [169] N. Demir and S. A. Bass, “Shear-viscosity to entropy density ratio of a relativistic hadron gas at RHIC: approaching the AdS/CFT bound?,” 0812.2422.
- [170] M. Prakash, M. Prakash, R. Venugopalan, and G. Welke, “Nonequilibrium properties of hadronic mixtures,” *Phys. Rept.* **227** (1993) 321–366.
- [171] D. Davesne, “Transport coefficients of a hot pion gas,” *Phys. Rev.* **C53** (1996) 3069–3084.
- [172] J. Noronha-Hostler, J. Noronha, and C. Greiner, “Transport coefficients of hadronic matter near T_c ,” 0811.1571.
- [173] K. Itakura, O. Morimatsu, and H. Otomo, “Shear viscosity of a hadronic gas mixture,” *Phys. Rev.* **D77** (2008) 014014, 0711.1034.
- [174] M. I. Gorenstein, M. Hauer, and O. N. Moroz, “Viscosity in the excluded volume hadron gas model,” *Phys. Rev.* **C77** (2008) 024911, 0708.0137.
- [175] P. Arnold, C. Dogan, and G. D. Moore, “The bulk viscosity of high-temperature QCD,” *Phys. Rev.* **D74** (2006) 085021, hep-ph/0608012.
- [176] K. Paech and S. Pratt, “Origins of bulk viscosity at RHIC,” *Phys. Rev.* **C74** (2006) 014901, nucl-th/0604008.
- [177] D. Kharzeev and K. Tuchin, “Bulk viscosity of QCD matter near the critical temperature,” *JHEP* **09** (2008) 093, 0705.4280.
- [178] F. Karsch, D. Kharzeev, and K. Tuchin, “Universal properties of bulk viscosity near the QCD phase transition,” *Phys. Lett.* **B663** (2008) 217–221, 0711.0914.
- [179] S. S. Gubser, A. Nellore, S. S. Pufu, and F. D. Rocha, “Thermodynamics and bulk viscosity of approximate black hole duals to finite temperature quantum chromodynamics,” *Phys. Rev. Lett.* **101** (2008) 131601, 0804.1950.
- [180] S. S. Gubser, S. S. Pufu, and F. D. Rocha, “Bulk viscosity of strongly coupled plasmas with holographic duals,” *JHEP* **08** (2008) 085, 0806.0407.
- [181] G. D. Moore and O. Saremi, “Bulk viscosity and spectral functions in QCD,” *JHEP* **09** (2008) 015, 0805.4201.
- [182] G. Policastro, D. T. Son, and A. O. Starinets, “The shear viscosity of strongly coupled $N = 4$ supersymmetric Yang-Mills plasma,” *Phys. Rev. Lett.* **87** (2001) 081601, hep-th/0104066.
- [183] A. Buchel, J. T. Liu, and A. O. Starinets, “Coupling constant dependence of the shear viscosity in $N=4$ supersymmetric Yang-Mills theory,” *Nucl. Phys.* **B707** (2005) 56–68, hep-th/0406264.
- [184] S. C. Huot, S. Jeon, and G. D. Moore, “Shear viscosity in weakly coupled $\mathcal{N}=4$ Super Yang-Mills theory compared to QCD,” *Phys. Rev. Lett.* **98** (2007) 172303, hep-ph/0608062.
- [185] E. Witten, “Anti-de Sitter space and holography,” *Adv. Theor. Math. Phys.* **2** (1998) 253–291, hep-th/9802150.
- [186] E. Witten, “Anti-de Sitter space, thermal phase transition, and confinement in gauge theories,” *Adv. Theor. Math. Phys.* **2** (1998) 505–532, hep-th/9803131.

- [187] S. R. Das, G. W. Gibbons, and S. D. Mathur, “Universality of low energy absorption cross sections for black holes,” *Phys. Rev. Lett.* **78** (1997) 417–419, hep-th/9609052.
- [188] M. Natsuume, “String theory and quark-gluon plasma,” hep-ph/0701201.
- [189] A. Buchel, R. C. Myers, and A. Sinha, “Beyond $\eta/s = 1/4\pi$,” *JHEP* **03** (2009) 084, 0812.2521.
- [190] M. Brigante, H. Liu, R. C. Myers, S. Shenker, and S. Yaida, “The viscosity bound and causality violation,” *Phys. Rev. Lett.* **100** (2008) 191601, 0802.3318.
- [191] U. Gursoy, E. Kiritsis, G. Michalogiorgakis, and F. Nitti, “Thermal transport and drag force in improved holographic QCD,” 0906.1890.
- [192] A. Karch, E. Katz, D. T. Son, and M. A. Stephanov, “Linear confinement and AdS/QCD,” *Phys. Rev.* **D74** (2006) 015005, hep-ph/0602229.
- [193] K. Kajantie, T. Tahkokallio, and J.-T. Yee, “Thermodynamics of AdS/QCD,” *JHEP* **01** (2007) 019, hep-ph/0609254.
- [194] A. Buchel, “Bulk viscosity of gauge theory plasma at strong coupling,” *Phys. Lett.* **B663** (2008) 286–289, 0708.3459.
- [195] A. Muronga, “Second order dissipative fluid dynamics for ultra-relativistic nuclear collisions,” *Phys. Rev. Lett.* **88** (2002) 062302, nucl-th/0104064.
- [196] A. Muronga, “Causal theories of dissipative relativistic fluid dynamics for nuclear collisions,” *Phys. Rev.* **C69** (2004) 034903, nucl-th/0309055.
- [197] A. Muronga and D. H. Rischke, “Evolution of hot, dissipative quark matter in relativistic nuclear collisions,” nucl-th/0407114.
- [198] W. Israel and J. M. Stewart, “Thermodynamics of nonstationary and transient effects in a relativistic gas,” *Phys. Lett.* **58A** (1976) 213.
- [199] C. Eckart, “The thermodynamics of irreversible processes. iii. relativistic theory of the simple fluid,” *Phys. Rev.* **58** (1940) 919.
- [200] L. D. Landau and E. M. Lifshitz, “Fluid mechanics,” *Pergamon, Oxford*, (1963).
- [201] W. Israel, “Nonstationary irreversible thermodynamics: a causal relativistic theory,” *Ann. Phys. (N.Y.)* **100** (1976) 310.
- [202] W. Israel and J. M. Stewart, “Transient relativistic thermodynamics and kinetic theory,” *Ann. Phys. (N.Y.)* **118** (1979) 341.
- [203] B. Betz, D. Henkel, and D. H. Rischke, “From kinetic theory to dissipative fluid dynamics,” 0812.1440.
- [204] R. Baier, P. Romatschke, D. T. Son, A. O. Starinets, and M. A. Stephanov, “Relativistic viscous hydrodynamics, conformal invariance, and holography,” *JHEP* **04** (2008) 100, 0712.2451.
- [205] M. Grmela and H. C. Ottinger, “Dynamics and thermodynamics of complex fluids I: Development of a general formalism,” *Phys. Rev. E* **56** (1997) 6620.
- [206] H. C. Ottinger and M. Grmela, “Dynamics and thermodynamics of complex fluids II: illustrations of a general formalism,” *Phys. Rev. E* **56** (1997) 6633.
- [207] H. C. Ottinger and M. Grmela, “General projection operator formalism for the dynamics and thermodynamics of complex fluids,” *Phys. Rev. E* **57** (1998) 1416.
- [208] K. Dusling, *private communication*.
- [209] D. H. Rischke, “Fluid dynamics for relativistic nuclear collisions,” nucl-th/9809044.
- [210] S. R. deGroot, W. A. van Leeuwen, and C. G. van Weert, “Relativistic kinetic theory,” *North-Holland, Amsterdam* (1980).
- [211] P. Danielewicz and M. Gyulassy, “Dissipative phenomena in quark gluon plasmas,” *Phys. Rev. D* **31** (1985) 53–62.
- [212] A. Muronga, “Relativistic dynamics of non-ideal fluids: viscous and heat-conducting fluids I. general aspects and 3+1 formulation for nuclear collisions,” *Phys. Rev.* **C76** (2007) 014909, nucl-th/0611090.
- [213] A. Muronga, “Relativistic dynamics of non-ideal fluids: viscous and heat-conducting fluids II. transport properties and microscopic description of relativistic nuclear matter,” *Phys. Rev.* **C76** (2007) 014910, nucl-th/0611091.
- [214] W. A. Hiscock and L. Lindblom, “Stability and causality in dissipative relativistic fluids,” *Ann. Phys.* **151** (1983) 466–496.
- [215] W. A. Hiscock and L. Lindblom, “Generic instabilities in first-order dissipative relativistic fluid theories,” *Phys. Rev.* **D31** (1985) 725–733.
- [216] W. A. Hiscock and L. Lindblom, “Linear plane waves in dissipative relativistic fluids,” *Phys. Rev.* **D35** (1987) 3723–3732.
- [217] I. Muller *Z. Phys.* **198** (1967) 329.
- [218] P. Romatschke, “New developments in relativistic viscous hydrodynamics,” 0902.3663.
- [219] H. Grad *Commun. Pure App. Math* **2** (1949) 381.
- [220] https://wiki.bnl.gov/TECHQM/index.php/Causal_viscous_hydrodynamics._the_different_2nd_order_formalisms.

- [221] K. Dusling, “Status of viscous hydrodynamic simulations,” *Acta Phys. Polon.* **B40** (2009) 963–972.
- [222] J. D. Bjorken, “Highly relativistic nucleus-nucleus collisions: the central rapidity region,” *Phys. Rev.* **D27** (1983) 140–151.
- [223] P. F. Kolb, J. Sollfrank, and U. W. Heinz, “Elliptic and hexadecupole flow from AGS to LHC energies,” *Phys. Lett.* **B459** (1999) 667–673, nucl-th/9906003.
- [224] P. F. Kolb, U. W. Heinz, P. Huovinen, K. J. Eskola, and K. Tuominen, “Centrality dependence of multiplicity, transverse energy, and elliptic flow from hydrodynamics,” *Nucl. Phys.* **A696** (2001) 197–215, hep-ph/0103234.
- [225] D. Kharzeev and M. Nardi, “Hadron production in nuclear collisions at RHIC and high density QCD,” *Phys. Lett.* **B507** (2001) 121–128, nucl-th/0012025.
- [226] D. Kharzeev, E. Levin, and M. Nardi, “QCD saturation and deuteron nucleus collisions,” *Nucl. Phys.* **A730** (2004) 448–459, hep-ph/0212316.
- [227] H.-J. Drescher, A. Dumitru, A. Hayashigaki, and Y. Nara, “The eccentricity in heavy-ion collisions from color glass condensate initial conditions,” *Phys. Rev.* **C74** (2006) 044905, nucl-th/0605012.
- [228] T. Hirano and Y. Nara, “Hydrodynamic afterburner for the color glass condensate and the parton energy loss,” *Nucl. Phys.* **A743** (2004) 305–328, nucl-th/0404039.
- [229] T. Hirano, U. W. Heinz, D. Kharzeev, R. Lacey, and Y. Nara, “Hadronic dissipative effects on elliptic flow in ultrarelativistic heavy-ion collisions,” *Phys. Lett.* **B636** (2006) 299–304, nucl-th/0511046.
- [230] A. Kuhlman, U. W. Heinz, and Y. V. Kovchegov, “Gluon saturation effects in relativistic U + U collisions,” *Phys. Lett.* **B638** (2006) 171–177, nucl-th/0604038.
- [231] S. Moreland, *private communication*.
- [232] S. D. Katz, “Equation of state from lattice QCD,” *Nucl. Phys.* **A774** (2006) 159–168, hep-ph/0511166.
- [233] M. Laine and Y. Schroder, “Quark mass thresholds in QCD thermodynamics,” *Phys. Rev.* **D73** (2006) 085009, hep-ph/0603048.
- [234] P. F. Kolb, P. Huovinen, U. W. Heinz, and H. Heiselberg, “Elliptic flow at SPS and RHIC: From kinetic transport to hydrodynamics,” *Phys. Lett.* **B500** (2001) 232–240, hep-ph/0012137.
- [235] P. F. Kolb and R. Rapp, “Transverse flow and hadro-chemistry in Au + Au collisions at $\sqrt{s_{NN}} = 200$ -GeV,” *Phys. Rev.* **C67** (2003) 044903, hep-ph/0210222.
- [236] D. Teaney, “Chemical freezeout in heavy ion collisions,” nucl-th/0204023.
- [237] P. Huovinen, “Chemical freeze-out temperature in hydrodynamical description of Au+Au collisions at $\sqrt{s_{NN}} = 200$ GeV,” *Eur. Phys. J.* **A37** (2008) 121–128, 0710.4379.
- [238] T. Hirano and K. Tsuda, “Collective flow and two pion correlations from a relativistic hydrodynamic model with early chemical freeze out,” *Phys. Rev.* **C66** (2002) 054905, nucl-th/0205043.
- [239] F. Cooper and G. Frye, “Comment on the single particle distribution in the hydrodynamic and statistical thermodynamic models of multiparticle production,” *Phys. Rev.* **D10** (1974) 186.
- [240] D. Teaney, “Effect of shear viscosity on spectra, elliptic flow, and Hanbury Brown-Twiss radii,” *Phys. Rev.* **C68** (2003) 034913, nucl-th/0301099.
- [241] A. Monnai and T. Hirano, “Effects of bulk viscosity at freezeout,” 0903.4436.
- [242] S. Bhattacharyya, V. E. Hubeny, S. Minwalla, and M. Rangamani, “Nonlinear fluid dynamics from gravity,” *JHEP* **02** (2008) 045, 0712.2456.
- [243] M. Natsuume and T. Okamura, “Causal hydrodynamics of gauge theory plasmas from AdS/CFT duality,” *Phys. Rev.* **D77** (2008) 066014, 0712.2916.
- [244] J.-W. Chen and J. Wang, “Bulk viscosity of a gas of massless pions,” 0711.4824.
- [245] A. Buchel, “Relaxation time of non-conformal plasma,” 0908.0108.
- [246] *AZHYDRO can be downloaded from URL: <http://www.physics.ohio-state.edu/~froderma/>.*
- [247] A. K. Chaudhuri and U. W. Heinz, “Hydrodynamical evolution of dissipative QGP fluid,” *J. Phys. Conf. Ser.* **50** (2006) 251–258, nucl-th/0504022.
- [248] D. A. Teaney, “Viscosity and thermalization,” *J. Phys.* **G30** (2004) S1247–S1250, nucl-th/0403053.
- [249] G. Kestin and U. W. Heinz, “Hydrodynamic radial and elliptic flow in heavy-ion collisions from AGS to LHC energies,” 0806.4539.
- [250] **NA49** Collaboration, C. Alt *et al.*, “Directed and elliptic flow of charged pions and protons in Pb + Pb collisions at 40-A-GeV and 158-A-GeV,” *Phys. Rev.* **C68** (2003) 034903, nucl-ex/0303001.
- [251] **STAR** Collaboration, S. A. Voloshin, “Energy and system size dependence of charged particle elliptic flow and v_2/ε scaling,” *J. Phys.* **G34** (2007) S883–886, nucl-ex/0701038.
- [252] **STAR** Collaboration, S. A. Voloshin, “Energy and system size dependence of elliptic flow: using rapidity gaps to suppress non-flow contribution,” *AIP Conf. Proc.* **870** (2006) 691–694, nucl-ex/0610038.

- [253] R. C. Hwa and K. Kajantie, “Diagnosing quark matter by measuring the total entropy and the photon or dilepton emission rates,” *Phys. Rev.* **D32** (1985) 1109.
- [254] R. S. Bhalerao, J.-P. Blaizot, N. Borghini, and J.-Y. Ollitrault, “Elliptic flow and incomplete equilibration at RHIC,” *Phys. Lett.* **B627** (2005) 49–54, nucl-th/0508009.
- [255] H. Heiselberg and A.-M. Levy, “Elliptic flow and HBT in non-central nuclear collisions,” *Phys. Rev.* **C59** (1999) 2716–2727, nucl-th/9812034.
- [256] S. A. Voloshin and A. M. Poskanzer, “The physics of the centrality dependence of elliptic flow,” *Phys. Lett.* **B474** (2000) 27–32, nucl-th/9906075.
- [257] H.-J. Drescher, A. Dumitru, C. Gombeaud, and J.-Y. Ollitrault, “The centrality dependence of elliptic flow, the hydrodynamic limit, and the viscosity of hot QCD,” *Phys. Rev.* **C76** (2007) 024905, 0704.3553.
- [258] D. Kharzeev and E. Levin, “Manifestations of high density QCD in the first RHIC data,” *Phys. Lett.* **B523** (2001) 79–87, nucl-th/0108006.
- [259] G. Torrieri and I. Mishustin, “Instability of boost-invariant hydrodynamics with a QCD inspired bulk viscosity,” *Phys. Rev.* **C78** (2008) 021901, 0805.0442.
- [260] https://wiki.bnl.gov/TECHQM/index.php/Code_verification_for_viscous_hydrodynamics.
- [261] U. W. Heinz and G. Kestin, “Jozso’s legacy: chemical and kinetic freeze-out in heavy- ion collisions,” *Eur. Phys. J. ST* **155** (2008) 75–87, 0709.3366.
- [262] U. Heinz and G. Kestin, “Universal chemical freeze-out as a phase transition signature,” *PoS CPOD2006* (2006) 038, nucl-th/0612105.
- [263] H. Song and U. Heinz, *unpublished notes*.
- [264] D. Teaney, J. Lauret, and E. V. Shuryak, “Collective flow in ultra-relativistic heavy ion collisions,” *Ph.D thesis* (2001).
- [265] F. Karsch and E. Laermann, “Thermodynamics and in-medium hadron properties from lattice QCD,” hep-lat/0305025.
- [266] P. Huovinen, “Anisotropy of flow and the order of phase transition in relativistic heavy ion collisions,” *Nucl. Phys.* **A761** (2005) 296–312, nucl-th/0505036.
- [267] M. Bluhm, B. Kampfer, R. Schulze, D. Seipt, and U. Heinz, “A family of equations of state based on lattice QCD: impact on flow in ultrarelativistic heavy-ion collisions,” *Phys. Rev.* **C76** (2007) 034901, 0705.0397.
- [268] M. Cheng *et al.*, “The transition temperature in QCD,” *Phys. Rev.* **D74** (2006) 054507, hep-lat/0608013.
- [269] P. Huovinen, *private communication*.
- [270] **STAR** Collaboration, J. Adams *et al.*, “Identified particle distributions in p + p and Au + Au collisions at $\sqrt{s_{NN}} = 200$ GeV,” *Phys. Rev. Lett.* **92** (2004) 112301, nucl-ex/0310004.
- [271] T. Hirano, U. W. Heinz, D. Kharzeev, R. Lacey, and Y. Nara, “Elliptic flow from a hybrid CGC, full 3D hydro and hadronic cascade model,” *J. Phys.* **G34** (2007) S879–882, nucl-th/0701075.
- [272] D. Teaney, “A hydrodynamic description of heavy ion collisions at the SPS and RHIC,” nucl-th/0110037.
- [273] A. Poskanzer, *private communication*.
- [274] J. P. Boris and D. L. Book *J. Comput. Phys.* **11** (1973) 38.
- [275] R. S. Bhalerao, J.-P. Blaizot, N. Borghini, and J.-Y. Ollitrault, “Elliptic flow and incomplete equilibration at RHIC,” *Phys. Lett.* **B627** (2005) 49–54, nucl-th/0508009.
- [276] C. Gombeaud and J.-Y. Ollitrault, “Elliptic flow in transport theory and hydrodynamics,” *Phys. Rev. C* **77** (2008) 054904, nucl-th/0702075.
- [277] H.-J. Drescher, A. Dumitru, C. Gombeaud, and J.-Y. Ollitrault, “The centrality dependence of elliptic flow, the hydrodynamic limit, and the viscosity of hot QCD,” *Phys. Rev. C* **76** (2007) 024905, 0704.3553.
- [278] A. J. Kox, S. R. De Groot, and W. A. Van Leeuwen *Physica* **84A** (1976) 155.
- [279] **PHOBOS** Collaboration, B. B. Back *et al.*, “Centrality and pseudorapidity dependence of elliptic flow for charged hadrons in Au + Au collisions at $\sqrt{s_{NN}} = 200$ GeV,” *Phys. Rev.* **C72** (2005) 051901, nucl-ex/0407012.
- [280] **STAR** Collaboration, J. Adams *et al.*, “Azimuthal anisotropy in Au + Au collisions at $\sqrt{s_{NN}} = 200$ GeV,” *Phys. Rev.* **C72** (2005) 014904, nucl-ex/0409033.
- [281] D. Molnar and M. Gyulassy, “Saturation of elliptic flow at RHIC: Results from the covariant elastic parton cascade model MPC,” *Nucl. Phys.* **A697** (2002) 495–520, nucl-th/0104073.
- [282] Z. Xu and C. Greiner, “Transport rates and momentum isotropization of gluon matter in ultrarelativistic heavy-ion collisions,” *Phys. Rev.* **C76** (2007) 024911, hep-ph/0703233.
- [283] Z. Xu and C. Greiner, “Elliptic flow of gluon matter in ultrarelativistic heavy- ion collisions,” *Phys. Rev.* **C79** (2009) 014904, 0811.2940.
- [284] B. Zhang, “Recent results from parton cascade and microscopic transport,” 0809.0446.

- [285] B. Zhang, “Kinetic equilibration from a radiative transport,” 0903.2055.
- [286] Z. Xu, C. Greiner, and H. Stocker, “QCD plasma thermalization, collective flow and extraction of shear viscosity,” *J. Phys.* **G35** (2008) 104016, 0807.2986.
- [287] Z. Xu and C. Greiner, “Shear viscosity in a gluon gas,” *Phys. Rev. Lett.* **100** (2008) 172301. arXiv:0710.5719 [nucl-th].
- [288] A. El, A. Muronga, Z. Xu, and C. Greiner, “Shear viscosity and out of equilibrium dissipative hydrodynamics,” 0812.2762.
- [289] A. Majumder, B. Muller, and X.-N. Wang, “Small shear viscosity of a quark-gluon plasma implies strong jet quenching,” *Phys. Rev. Lett.* **99** (2007) 192301, hep-ph/0703082.
- [290] M. Asakawa, S. A. Bass, and B. Muller, “Anomalous viscosity of an expanding quark-gluon plasma,” *Phys. Rev. Lett.* **96** (2006) 252301, hep-ph/0603092.
- [291] M. Asakawa, S. A. Bass, and B. Muller, “Anomalous transport processes in anisotropically expanding quark-gluon plasmas,” *Prog. Theor. Phys.* **116** (2007) 725–755, hep-ph/0608270.
- [292] G. D. Moore and D. Teaney, “How much do heavy quarks thermalize in a heavy ion collision?,” *Phys. Rev.* **C71** (2005) 064904, hep-ph/0412346.
- [293] **PHENIX** Collaboration, S. S. Adler *et al.*, “Measurement of single electron event anisotropy in Au + Au collisions at $\sqrt{s_{NN}} = 200$ GeV,” *Phys. Rev.* **C72** (2005) 024901, nucl-ex/0502009.
- [294] N. Armesto, M. Cacciari, A. Dainese, C. A. Salgado, and U. A. Wiedemann, “How sensitive are high- p_T electron spectra at RHIC to heavy quark energy loss?,” *Phys. Lett.* **B637** (2006) 362–366, hep-ph/0511257.
- [295] H. van Hees, V. Greco, and R. Rapp, “Heavy-quark probes of the quark-gluon plasma at RHIC,” *Phys. Rev.* **C73** (2006) 034913, nucl-th/0508055.
- [296] **PHENIX** Collaboration, S. S. Adler *et al.*, “Identified charged particle spectra and yields in Au + Au collisions at $\sqrt{s_{NN}} = 200$ GeV,” *Phys. Rev.* **C69** (2004) 034909, nucl-ex/0307022.
- [297] **PHENIX** Collaboration, A. Adare *et al.*, “Energy loss and flow of heavy quarks in Au+Au collisions at $\sqrt{s_{NN}} = 200$ GeV,” *Phys. Rev. Lett.* **98** (2007) 172301, nucl-ex/0611018.
- [298] J. Casalderrey-Solana and D. Teaney, “Heavy quark diffusion in strongly coupled $N = 4$ Yang Mills,” *Phys. Rev.* **D74** (2006) 085012, hep-ph/0605199.
- [299] R. Rapp and H. van Hees, “Heavy quark diffusion as a probe of the quark-gluon plasma,” 0803.0901.
- [300] D. Molnar, “The ‘minimal’ viscosity and elliptic flow at RHIC,” 0806.0026.
- [301] D. H. Rischke, S. Bernard, and J. A. Maruhn, “Relativistic hydrodynamics for heavy ion collisions. 1. General aspects and expansion into vacuum,” *Nucl. Phys.* **A595** (1995) 346–382, nucl-th/9504018.
- [302] D. H. Rischke, Y. Pursun, and J. A. Maruhn, “Relativistic hydrodynamics for heavy ion collisions. 2. Compression of nuclear matter and the phase transition to the quark - gluon plasma,” *Nucl. Phys.* **A595** (1995) 383–408, nucl-th/9504021.